Dynamic Modeling and Control of Multi-Terminal HVDC Grids

Rault Pierre

N° d'ordre : 230

ECOLE CENTRALE DE LILLE

THESE

Présentée en vue
d'obtenir le grade de

DOCTEUR

En

Spécialité : Génie Électrique

Par

RAULT Pierre

DOCTORAT DELIVRE PAR L'ECOLE CENTRALE DE LILLE

Titre de la thèse :
Modélisation Dynamique et Commande des Réseaux à Courant Continu Multi-Terminaux Haute Tension

Dynamic Modeling and Control of Multi-Terminal HVDC Grids

Soutenue le 20 Mars 2014 devant le jury d'examen :

Président	*(le nom du président ne peut être arrêté que le jour de la soutenance)*
Rapporteur	*Stephen, FINNEY, Professeur, University of Strathclyde*
Rapporteur	*Xavier, ROBOAM, Professeur, Université de Toulouse*
Examinateur	*Carlos, MOREIRA, Professeur assistant, INESC Porto*
Examinateur	*Thierry, VAN CUTSEM, Professeur, Université de Liège*
Examinateur	*Benoît, ROBYNS, Professeur, HEI*
Invité	*Marc, PETIT, Professeur adjoint, Supélec*
Directeur de thèse	*Xavier, GUILLAUD, Professeur, École Centrale de Lille*
Encadrant	*Frédéric, COLAS, Ingénieur de recherche, A&M ParisTech*
Encadrant	*Samuel, NGUEFEU, Ingénieur sénior, RTE-CNER*

Thèse préparée dans le Laboratoire L2EP

Ecole Doctorale SPI 072 (Lille I, Lille III, Artois, ULCO, UVHC, EC Lille)
PRES Université Lille Nord-de-France

ABSTRACT

Offshore wind power could help European countries to reach their objectives in terms of renewable energy. Since offshore wind farms may be located far from the shore, HVDC transmission is the only viable solution to connect it to the shore. The connection of wind farm could be coupled with DC interconnections and reinforcements between AC systems to improve power transit flexibility and reliability. Before the achievement of such DC grids, control principles and protection scheme must be considered.

This thesis deals with control and stability of Multi-terminal HVDC (MTDC) grid used to connect wind farms to several onshore injection points. This work discusses both the primary control methods to provide DC grid power balance and coordinated control methods to dispatch power as scheduled by TSOs.

The literature review on primary control methods allows choosing the droop voltage method as the best candidate to control the DC grid. An in-depth analysis highlights the influence of the droop parameter and the DC storage elements on the DC grid dynamics and this leads to a methodology to size the droop parameter. Next the stability of DC grid alone is assessed by small signal stability analyses. Also, interaction origins between AC and DC systems are traced using modal analysis.

Since, primary control act as converter level using local measurements, a master controller is proposed to manage the DC grid power flows. Based on steady study state considerations, this controller computes references to send to converter stations in order to restore the system at nominal value and to satisfy TSOs wishes: interconnections schedule power transits and wind power sharing.

Finally, methods developed along the thesis are assessed on a multi-terminal mock-up. This is an hardware-in-the-loop mock-up where AC systems are simulated in real time and cables and some converters are real at low scale. The low scale mock-up is homothetic to a full scale system: electrical elements are the same in per unit, DC storage is also homothetic and converter's controllers are tuned to achieve identical time responses. The mock-up is monitored by a SCADA system in which the coordinated control is implemented.

KEYWORDS

Control, Modeling, Modal analysis, High Voltage Direct Current (HVDC), Multi-Terminal DC (MTDC), Interactions AC-DC, Load-Flow, SCADA, Hardware In the Loop (HIL),Voltage Source Converter (VSC),

RÉSUMÉ ÉTENDU

Ici serra écrit un résumé substantiel en français (5 à 7 pages)

MOTS CLÉS :

SYMBOLS AND ABBREVIATIONS

1. Symbols

A	System matrix (state space representation)
B	Input matrix (state space representation)
c	Linear capacitance
C	Output matrix (state space representation)
C	Capacitance
D	Direct feedthrough matrix (state space representation)
G	Conductance
g	Linear conductance
H	Inertia constant
H_c	Electrostatic constant
i	Current
I	Current (steady state)
k	DC voltage droop parameter
L	Inductance
l	Linear inductance
L_s	VSC's phase reactor inductance
L_T	VSC's transformer leakage inductor
P	Active power
PI	Proportional Integral (controller)
Q	Reactive power
R	Frequency droop parameter
R	Resistance
r	Linear resistance
R_s	VSC's phase reactor resistance
R_T	VSC's transformer resistance of Joule losses
S	Apparent power
s	Laplace operator
$t_{r5\%}$	Time response at 5% of the final value
u	DC voltage
U	DC voltage (Static value)
v	Phase to ground voltage
x	State vector (state space representation)
Y	Admittance (DC grid)
δ	Voltage phase angle or rotor angle
ω	Angular frequency
ϕ	Displacement angle
Π	Line model represented by a "PI" section

2. Subscripts

a	First phase a quantity
abc	Three phase AC quantity in the stationary frame
AC	Alternating current quantity
b	Second phase quantity
base	Base quatity
c	Third phase quantity
c	Cable quantity
d	d component in the dq frame
DC	Direct current quantity
dq	Quantity in the dq frame
g	Quantity at the PCC between converter and AC grid
m	Modulated quantity
N	Nominal quantity
q	q component in the dq frame
s	Source quantity
α	α component in the $\alpha\beta$ stationary frame
$\alpha\beta$	Tow phase quantity in the $\alpha\beta$ stationary frame
β	β component in the $\alpha\beta$ stationary frame
0	Quantity at operating point

3. Upper-scripts

*	Reference quantity
T	Transpose of a matrix

4. Abbreviations

AC	Alternating Current
AVM	Average Value Model
DAE	Differential-Algebraic Equation
DC	Direct Current
DSP	Digital Signal Processor
EMT	ElectroMagnetic Transient
FACTS	Flexible AC Transmission System
HIL	Hardware In the Loop
MTU	Master Terminal Unit
PCC	Point of Common Coupling
PI	Proportional Integral

PLC	Programmable Logic Controller
RTU	Remote Terminal Unit
SCADA	Supervisory Control and Data Acquisition
SCR	Short Circuit Ratio
SPS	Special Protection Plan
SVC	Static Var Compensator
STATCOM	Static Synchronous Compensator
SSSA	Small Signal Stability Analysis

CONTENTS

INTRODUCTION

1 CONTEXT AND MOTIVATION FOR A DC GRID

The world is facing today a global energy transition challenge since developed and emerging countries need more and more energy for their economy growth in a framework of limited and poorly distributed energy resources . In the meantime, the climate change owing to greenhouse gas emission leads to change the energy pattern with more climate-friendly energy resources such as hydro, wind or solar.

In that context, the European leaders agreed to develop in Europe a global leadership to tackle climate change: European economy should become a model for sustainable development in the 21st century despite major political, social, and economic efforts have to be expended to reach this objective. Two key targets are fixed by the European Council in 2008 [EUR08]:

- A reduction of at least 20 % in greenhouse gases by 2020.
- A 20 % share of renewable energies in EU energy consumption by 2020.

To reach these targets, large offshore wind farms are expected in the coming years, notably in the North Sea due to shallow water. Following EWEA's recommendations (see Figure 1) [FIC09], the European Transmission System Operators (TSO) represented by ENTSO-E have sketched a grid development plan for the next ten years [ENT10]. The scenario proposed by ENTSO-E until 2020 is the creation of 9600 km of new HVDC lines in Europe, which should be compared to the 32500 km of new and refurbished HVAC lines. As regards to HVDC transmission lines, some of them are expected to be structured as a multi-terminal DC grid, seen as a cost-effective solution which enhances reliability and improves flexibility.

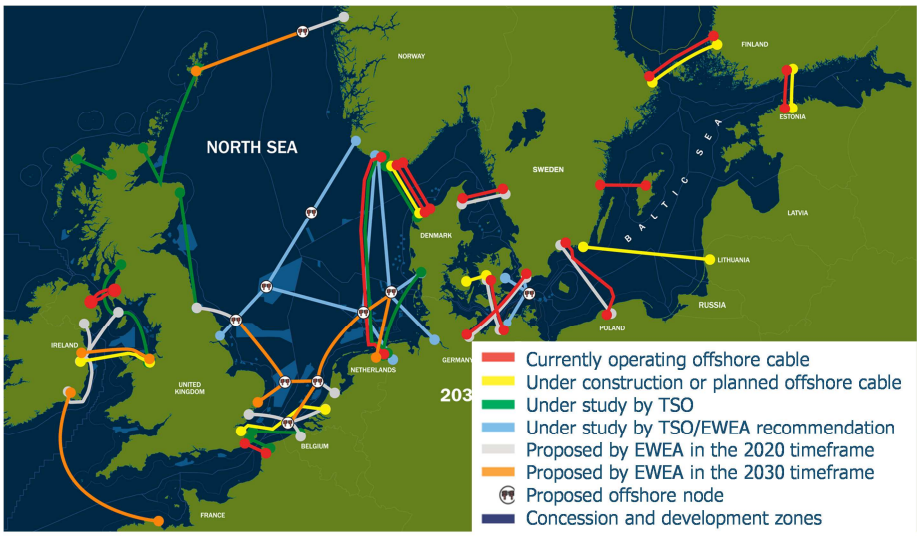

Figure 1: EWEA's 20 year offshore network development master plan [FIC09]

MTDC transmissions are expected to provide additional features compared to VSC-HVDC point-to-point links:

- More flexibility of power dispatch location
- Optimize assets between wind power and trade transfer capability [LIU11a]
- Smoothing wind power fluctuations (mitigation of wind power which is produced from different area) [DES12a]

- Frequency support to onshore grids [SIL12]
- More reliability (can operate or at least partially operate even if one element is out of service)

At present, most of HVDC transmissions are point to point schemes, only two multi-terminal HVDC (MTDC) transmissions are existing worldwide. The first one is in Europe between Italy, Sardinia and Corsica (SACOI) and the second one is in North America between Quebec and New England. Both are LCC-MTDC schemes, the first was initially a point to point HVDC link between Italy and Sardania, then a third terminal was added in Corsica in 1986, making the first MTDC grid. The second was first commissioned for a five terminals MTDC grid and finally reduced to three terminal following unexpected problems; it delivers power from hydro-power plant to load centers located 1,500 km away, from the northern of Quebec to New England [LON90]. These two MTDC schemes are LCC-HVDC. With LCC station the power flow reversal at one terminal is not as easy as with VSC since the substation's current cannot be reversed. In the SACOI transmission scheme, mechanical switches are used to interchange DC converter's terminals to be able to change its power flow direction [LON90].

With VSC based converter stations, the power flow can be controlled in both directions without changing the DC voltage polarity, therefore MTDC with VSC seems to be a better solution. Some research groups see in the MTDC grids the key solution to accommodate more renewable energy and to balance the power over large areas [FRI13] [DES13]. Others do not believe in huge MTDC from the scratch, they imagine that MTDC will be an extension or reinforcement of point to point HVDC links [DES12a]. In [ASP11] and [LIU11a] they have thought about a scenario of step by step evolution from preexisting HVDC links toward MTDC grids. Taking cost and technical complexity into consideration, the later seems more realistic, the gap to reach a pan-European DC network in a near future is still too large.

Point to point VSC-HVDC link technology is already in operation to connect offshore wind farms to the onshore grid [TEN13]. Several recent studies have explored combined solutions as a cost effective solution to connect offshore wind and several onshore AC areas [LEV12]:

- Kriegers Flak project. A 1600 MW wind farm split in Danish, German and Swedish seas. All wind farms shall be connected to their respective on-shore grids and among themselves. When the wind power harvested is not at its maximal value, transmission cables can be used to provide additional transfer capacity between these countries (see Figure 2) [ENE09].
- COBRA cable project. This project was initially a 700 MW interconnection between the Netherlands and Denmark. Studies propose to couple this project with a German's wind farm located in the same region [DEC11].
- Moray Firth HVDC Hub project. In this project, it is intended to connect existing and planned wind farms and the Shetland Islands to the Scottish's grid.

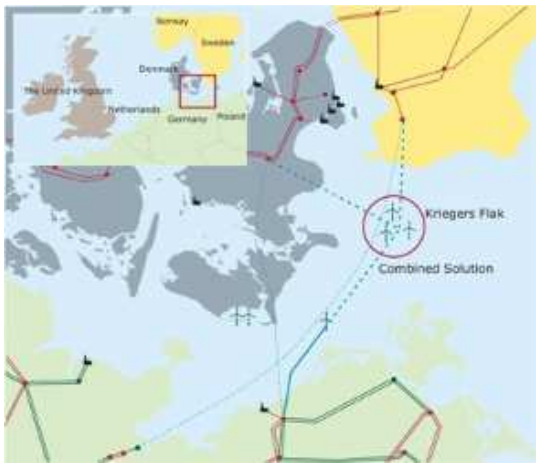

Figure 2: Kriegers Flak project [ENE09]

Key challenges remain before achieving such DC grid projects [ASP11] [BEE13]. Firstly power flow and DC voltage control methods should be developed for dispatching properly the flows of energy during normal and disturbed condition. Secondly, a very fast protection scheme must be elaborated to detect all faults occurring especially in the DC grid before the whole DC system collapses. Thirdly, equipment such as DC circuit breakers should be built to physically isolate faulted parts. Finally, there is a need for standardization in order to cope with devices from different manufacturers.

2 PROJECT OBJECTIVES AND OUTLINE OF THIS THESIS

As part of the TWENTIES project, particularly DEMO3 WP11, the aim of this work is to assess main the drivers for the development of offshore DC grids in order to facilitate the integration of the offshore wind energy in the European networks.

The TWENTIES project was funded by European Commission's Directorate-General for Energy under its seventh Framework Programme (FP7), it aims to advance the development of new technology to facilitate the integration of wind energy into the European electricity system [TWE13]. The TWENTIES project gathers electrical companies, wind energy manufacturers and research institutions, it is coordinated by the Spanish TSO, REE, and organized around six demonstration projects grouped together in three task forces, the whole organization is shown in Figure 3. The French TSO RTE is leading one of these demonstrations; the DEMO3 which is subdivided into two work packages, namely WP5 and WP11. The DEMO3 objective is to assess the technical and economic feasibility of submarine DC grids; WP5 is looking at research and theoretical issues while WP11 focuses in practical features such as algorithms development and physical equipment design to build and operate a small-scale demonstrator.

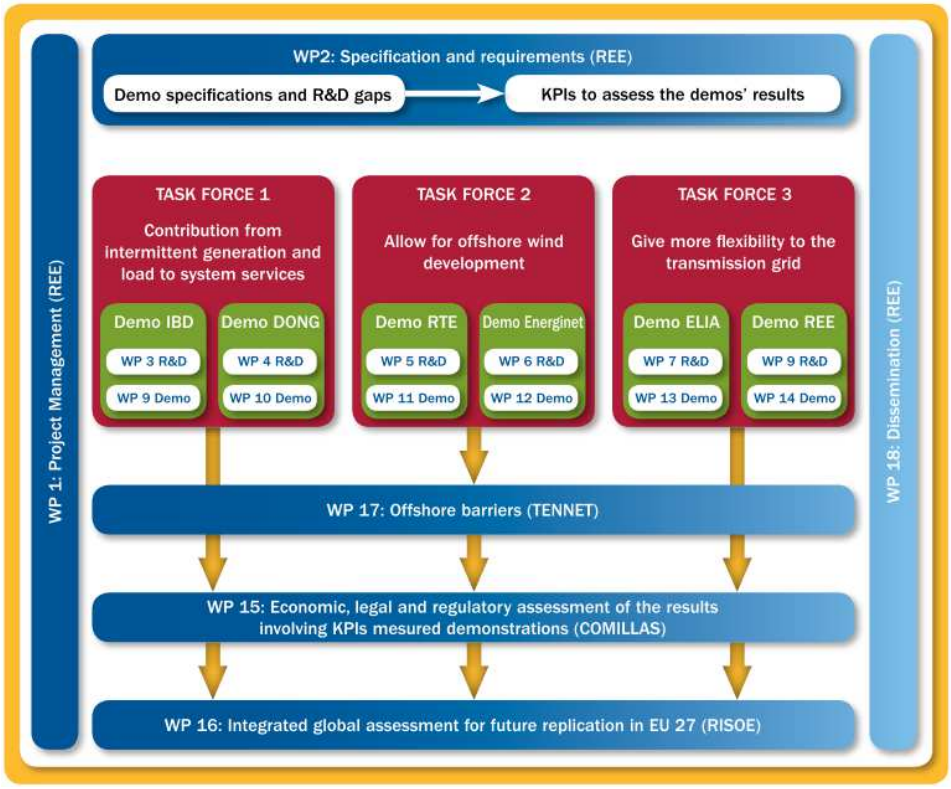

Figure 3: TWENTIES project structure

Assessing the HVDC grid feasibility by a demonstration was the objective of Work Package 11; this includes the DC breaker issue which is Alstom Grid's concern, while RTE is in charge of the overall DC grid operation. For this purpose, two PhD theses were lunched, one focused on protection aspects and another on control and stability issues. The first one was conducted by Miss Justine Descloux in collaboration between the G2ELab (Grenoble Electrical Engineering laboratory) and RTE, her thesis is entitled "Protection of Multi-Terminal High Voltage Direct Current Grids" [DES13a]. The second one deals with control and stability of multi-terminal DC grids. It is realized in association between the L2EP (Electrotechnology and Power Electronics Laboratory) and RTE and is matter of this work. Both, protection and control strategies were tested on a DC grid mock-up implemented in the L2EP Laboratory.

The aim of this work is to assess DC grid control strategies used to harvest offshore wind energy towards several mainland network injection points. This work answers the question "how to control a DC grid to face wind power intermittency and forecast production errors without fast communication?" This work develops and discusses control strategies used to dispatch DC grid power flows at short-term and long-term. In-depth analyses were performed to find which elements mainly drive the DC system dynamics, to assess the DC grid control stability and evaluate possible interactions with connected AC systems.

The outline of this thesis is organized as follows:

Chapter 1 is an introduction of DC transmission scheme; it explains why DC instead of AC, the differences between Voltage Source Converter (VSC) and Line Commutated Converter (LCC), and how VSC based transmissions are currently controlled.

Chapter 2 is an introduction for small signal stability analysis (SSSA) with DC systems. As a step before DC grid SSSA, linearized VSC models as well as DC cable models are introduced. These models are validated by time and frequency domain simulations. Finally, as an example of application, a SSSA is performed on a VSC-HVDC point-to-point link.

Chapter 3 is focused on DC grid control methods. Firstly there is a comparison between DC and AC systems. Then, control methods of the literature are discussed and some considerations on DC system dynamics are pointed out. Finally a novel method to tune converter station DC voltage controllers is proposed to equally divide up the power balance role and achieve the desired dynamics.

Chapter 4 deals with stability issues of DC grids connected to AC systems. This chapter is divided in two main sections; one is dealing with the DC grid behavior and the other is analyzing interactions caused by its connection to AC systems. Once validated the DC grid state space model is used to performed eigenvalues analysis to retrieve mode origins, and by the way of parametric studies, evaluate the sensibility of some parameters on the DC system dynamics. In the second section, a methodology based on a step-by-step approach enables to trace the mode evolutions due to the AC and DC system coupling. Frequency support from the DC grid as well as connection of asynchronous AC systems by a DC grid is also investigated.

Chapter 5 discusses the role of a dispatch center. Static methods used to calculate suitable set points for achieving the desired power flow are presented. These methods are assessed by time domain simulation with realistic wind production profile and for more severe events such as converter station tripping.

Chapter 6 deals with experimental tests. The first section shows how a small-scale DC grid could be designed to be representative of a unitary scale system. The second section is an experimental validation of control methods theoretically discussed throughout this thesis.

Conclusions and perspectives chapter summarizes the work findings, recommends some improvements and suggests further investigations.

3 SCIENTIFIC CONTRIBUTION OF THIS WORK

The main contributions of this work are summarized below:

- The development of a generic VSC model associated with its controllers tuned to achieve specific dynamics (Chapter 1).
- A methodology to linearize a generic VSC model with its controllers (Chapter 2).
- A novel linear cable model dedicated to small signal stability analysis has been found. This model improves the bandwidth of the classical Π model by modeling the coupling between the core and the screen conductors (Chapter 2).
- A consideration on droop controlled DC grid has led to a simplified model which highlights the DC grid storage and the droop value as main drivers of the DC grid dynamics (Chapter 3).
- A methodology to design droop value based on dynamic criterions (Chapter 3).
- A methodology to build DC grid state space model (Chapter 4).

- An in-depth analysis performed on DC grid eigenvalues has shown a clear separation between modes referred as DC grid modes and modes referred as converter control loops. The dynamics linked to the DC voltage are also retrieved (Chapter 4).
- The sensibility analyses on DC grid parameters assessed by modal analysis have revealed that (Chapter 4):
    - the droop value has mainly an influence on the DC voltage dynamics and a small impact on DC grid modes,
    - the converter stations capacitors have an influence in both DC voltage dynamics and DC grid modes,
    - smoothing reactors and DC line feeder inductors have an influence in the DC grid modes but not in the DC voltage dynamics. Furthermore, high values could make the system unstable.
- A comparison with the results of modal analysis performed on each system independently has enabled to clearly identify the changes of modes stemming from the coupling between AC and DC systems (Chapter 4).
    - Modes of each independent system have almost experienced no change when both systems are connected together.
    - There are some modal evolutions when the DC grid is supporting the frequency: DC voltage mode as well as inter-area and local modes are impacted by the frequency support.
- The electromechanical mode shape analysis performed on two asynchronous AC grids and connected by a DC grid revealed that both AC grid electromechanical states are influenced by the same modes only if grid side converter stations are endowed with a frequency droop controller (Chapter 4).
- A DC load flow algorithm without slack bus has been developed; the power deviation is dispatched on several buses following DC grid operator requirements (Chapter 5).
- The benefits of DC grid coordinated controller have been assessed to dispatch wind power production, follow onshore power transmission plan, rearrange power flow after a converter outage and alleviate AC congestions (Chapter 5).
- A methodology to design a small-scale DC system with same dynamics than a unitary one is detailed (Chapter 6).
- Experimental validations of control strategies on a small-scale DC grid are presented (Chapter 6).

4 LIST OF PUBLICATION DERIVED FROM THIS WORK

This work has resulted in the following publications:

P. Rault, X. Guillaud, F. Colas, and S. Nguefeu, "Method for Small Signal Stability Analysis of VSC-MTDC grids," in *Proc. IEEE Power and Energy Society General Meeting*, 2012.

P. Rault, X. Guillaud, F. Colas, and S. Nguefeu, "Challenges when operating DC grids," *Revue E tijdschrift*, Dec. 2012.

P. Rault, X. Guillaud, F. Colas, and S. Nguefeu, "Investigation on interactions between AC and DC grids," in *Proc. IEEE Grenoble PowerTech*, 2013.

S.A. Amara, F. Colas, X. Guillaud, P. Rault, and S. Nguefeu, "Laboratory-based test bed of a three terminals DC networks using Power Hardware In the Loop," in *15th European Conf. Power Electronics and Applications, Lille, France*, 2012.

J. Descloux et al., "HVDC Meshed grid : Control and Protection of a Multiterminal HVDC System," in *CIGRE General Session, Paris, France*, 2012.

S. Nguefeu, P. Rault, W. Grieshaber, and F. Hassan, "DEMO 3 requirement specifications: detailed specifications for a DC network and detailed specifications for ALSTOM Grid's DC breaker," Status report for European Commission, Deliverable D11.1. FP7 Twenties project EC-GA n° 249812, April 2012.

S. Nguefeu et al., "Description of a Protection Plan for DC Networks – Preliminary Results towards the real-time experimentation of a small-scale model of a DC network and the 120 kV DC breaker prototype tests," Status report for European Commission, Deliverable D11.2. FP7 Twenties project EC-GA n° 249812, 2012.

S. Nguefeu et al., "Testing results from DC network mock-up and DC breaker prototype," Status report for European Commission, Deliverable D11.3. FP7 Twenties project EC-GA n° 249812, Sep. 2013.

CHAPTER 1: HVDC State of the Art

1.1 DC VERSUS AC TRANSMISSION

Nowadays, bulk power systems mainly use AC overhead lines. However with technology evolution and inescapable constraints, DC transmissions are gaining ground. In this subsection the reason of DC instead of AC is discussed, the first part deals with the limitations of AC transmission and the second with a comparison between both transmission modes.

1.1.1. Power transmission with HVAC cable

The Cigré Working group B1.07 performed a statistic study related to the implementation of AC underground cables in the power system; the results of their investigation is summarized in Figure 1-1 [SWI07]. This study compares the length of underground cables against total circuit length for voltage level above 50 kV. It has been noted that there are very few underground cables in the power transmission grid, only 6.7 % for voltage level between 50 kV and 109 kV, and this figure decreases as far as the voltage level grows. This working group analyzed several underground cable projects in order to find why this solution was chosen, they concluded that, in most of the cases underground cables are used when overhead lines cannot be installed, because of space constraints such as densely populated urban areas or technical reasons like crossing a wide river.

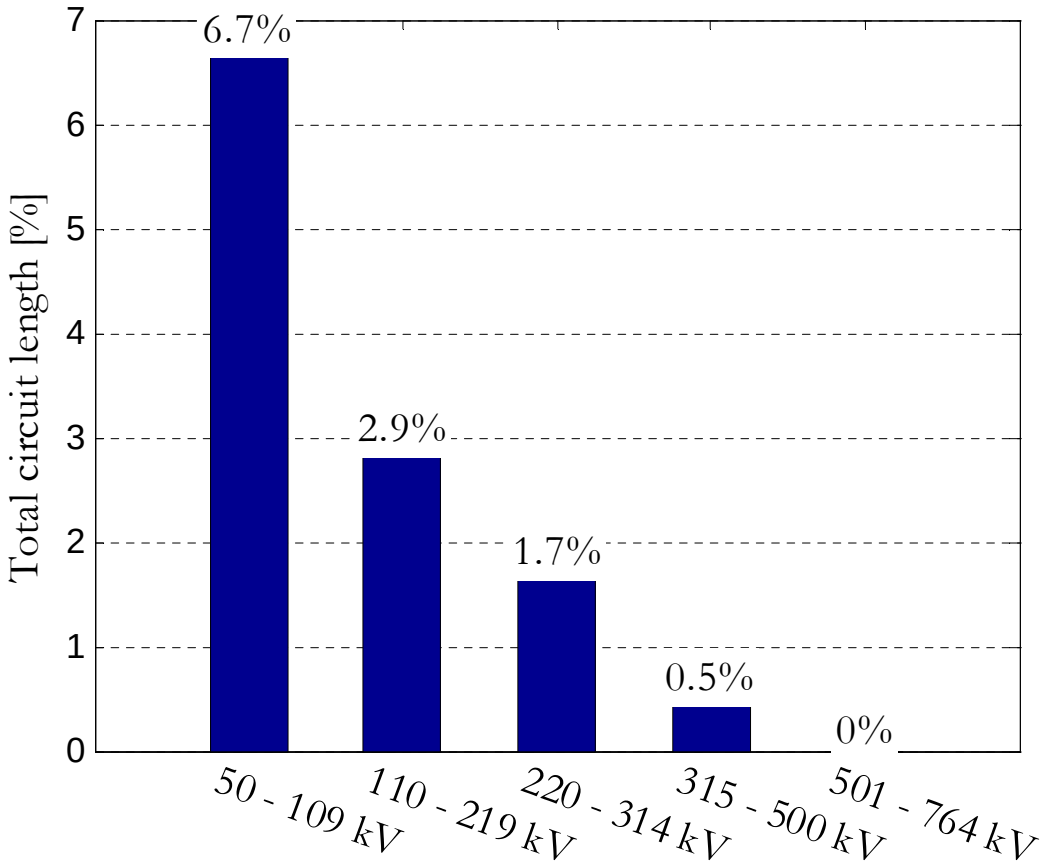

Figure 1-1: Percentage of the total circuit length that is underground

One of the major drawbacks of power transmission with HVAC underground or submarine cables is the reactive power generated by the cable itself, which limits the real power

transfer capacity. This reactive power is generated by the cable's shunt capacitance which is much larger than in the case of overhead lines because of the cable's insulation. Moreover, the cable capacitance increases with the cable length which limits the transmission distance. N. Negra and P. Monjean, respectively in [NEG06] and [MON12], have been interested in the problem of maximal transmissible real power as the cable length increases, for three voltage levels i.e. 132, 220 and 400 kV which are classical voltage levels for transmission grid.

The selected HVAC link configuration considered in their example is three single-core cables with cooper core and XLPE insulation, sufficiently distant to neglect their interactions. Cable data are summarized in Table 1-1.

Table 1-1: HVAC Cable parameters [NEG06]

	132 kV	220kV	400kV
Cable section [mm²]	1000	1000	1200
Nominal current [A]	1055	1055	1323
Resistance [Ω/km]	0.048	0.048	0.0455
Inductance [mH/km]	0.34	0.37	0.39
Capacitance [µF/km]	0.23	0.18	0.18

For this study, the HVAC cable is connected at the receiving end at an infinite bus. The maximal admissible active power which could flow through the HVAC cable is calculated from the current carrying capacity (ampacity) and the reactive power current provided by the cable.

$$P_{max} = \sqrt{3} U_N . \sqrt{I_N^2 - I_{reactive}^2} \quad \textbf{(1.1)}$$

Where P_{max} is the maximal admissible active power, U_N is the nominal voltage level, I_N is the nominal cable current and $I_{reactive}$ is the reactive current part generated by the cable. The reactive current part is calculated using the following formula:

$$I_{reactive} = 2\pi f \,.\, c \,.\, d \,.\, \frac{U_N}{\sqrt{3}} \quad \textbf{(1.2)}$$

Where f is the frequency, c the cable shunt capacitance per unit length and d the cable length. Considering this formula the cable self-inductance is neglected. Even if in [SHA11] this assumption has definitively an importance in the amount of transmittable power, the general conclusions are not modified.

Study results are presented in Figure 1-2. This figure illustrates the problem of active power limitation in HVAC cables when the cable length increases. Two case studies are explored: when there is compensation at one cable end and at both cable ends. The compensation is sized in order to reach the maximal active power through the cable.

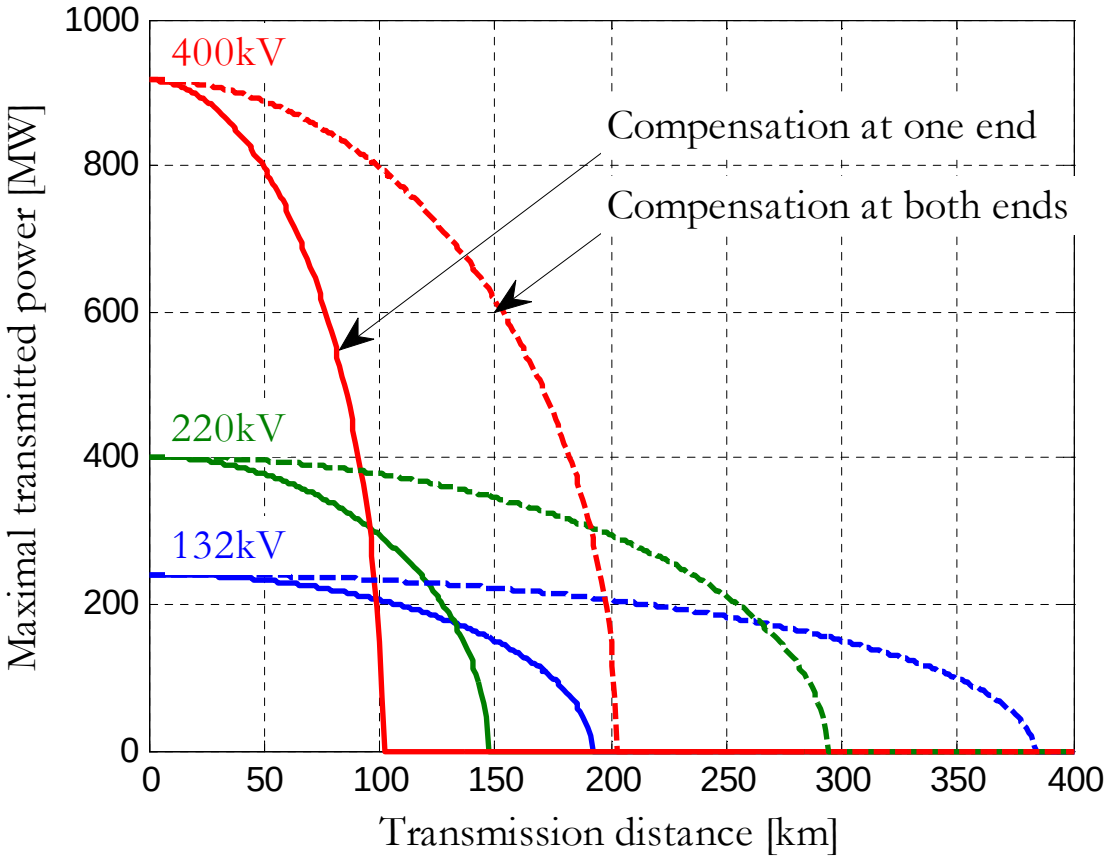

Figure 1-2: Maximal transmitted power through an underground cable as a function of the cable length, for AC voltage levels of 400 kV, 320 kV and 132 kV, with reactive power compensation at one end or at both ends

As expected the cable length is limited owing to the reactive power generated by the cable itself. If the voltage level is higher, there are more reactive power generated, and therefore the critical distance is shorter.

The active power transmission capacity through HVAC cable can be improved by using reactive compensation devices which consume the surplus of reactive power, such as shunt reactors, SVC or STATCOM. For underground cables it is possible to install compensation units between cable sections, however, for submarine cables, they can be added only at both cable ends, because it is not possible to install such devices under water.

In summary, focusing in a technical point of view, i.e. without economic aspects, HVAC cables are not suitable for transmission system. In some specific cases, they are used for short distances when overhead lines are not possible. For offshore wind farm connection, this result shall be moderated, because the transmitted power is not yet in the range of gigawatts and their distance to the shore does not exceed 50 km.

1.1.2. DC versus AC

The choice between AC and DC for long distances often follows economic rationales; Figure 1-3 illustrates the costs of a transmission with regard to the distance and its type, AC or DC. AC-DC substations increase significantly the investment cost when the line length is short. As the transmission distance increases the DC solution becomes more and more profitable because DC link need less conductors than AC link for the same power transfer capability. In [BAH08], the author provides an estimate of 30 % of cost saving in line building, taking into account that HVDC needs less conductors and smaller transmission towers and has lower line losses. In addition long distance AC lines require compensation devices which also increase the transmission cost. The distance at which the DC becomes cheaper than AC, is called the break-even distance (around 40 km for cable and 500 km for overhead line [BAH08]).

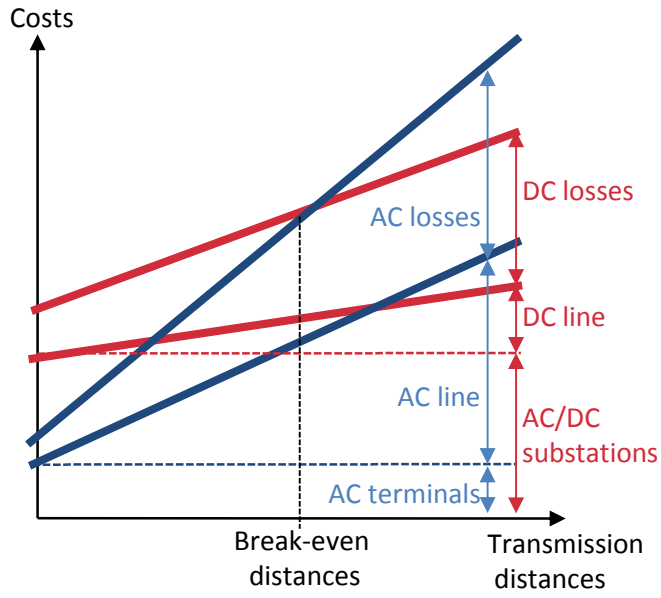

Figure 1-3: Sensitivity of length of connection on transmission costs [SIE11]

As regard to cable transmission, unlike HVAC, HVDC has no length limitation. For submarine transmission between continental substations, the reactive compensation can only be located onshore, thus beyond a certain distance, HVDC is the only technically feasible solution since intermediate compensation devices are no practically feasible.

The Table 1-2 presents some advantages and drawbacks of HVDC over HVAC.

Table 1-2: Advantages of HVDC over HVAC [OKB12]

Advantages	Drawbacks
• More power per conductor • Smaller transmission tower • Two conductors instead of three • 30% of cost saving in line building • Lower transmission losses • No charging current in steady state • No reactive power transfer • No skin effect • No synchronous operation required • Asynchronous interconnections • Isolation and even mitigation of electromechanical oscillations • Controllability of active power • No transmission length limitation • Isolation of AC faults [BEE13]	• Converters are expensive • Converters generate harmonics • Converter losses are significant • Converters are fragile • Heavy offshore substations [MON12] • Lower reliability • DC grids are not easy to operate • No DC breakers exist today • VSC-HVDC is a quite new technology even though LCC-HVDC technology is nearly 60 years old • Multi-voltage level i.e. connection involving different DC voltage levels needs DC-DC converters

1.2 TECHNOLOGIES USED FOR HVDC PROJECT

1.2.1. Evolution of HVDC projects

In order to show the evolution of HVDC technology, a brief history of HVDC project is given in Table 1-3. The first operational HVDC transmission was designed by René Thury, it had transferred the power harvested by hydro turbines in the Gorzente River to supply the city of Genoa in Italy. At one cable end, the hydro plant side, six dynamos are connected in series in order to raise the DC voltage up to 6 kV; at the other end, the power was consumed by motors also connected in series [WIK13]. In 1951, in Russia, the first HVDC transmission using mercury-arc valve has been designed. This valve is controllable at the closure thanks to a low voltage arc which heats and vaporizes the mercury, enabling electrons to flow from a power electrode to another.

Today, these components are obsolete; none of them are in operation. They have been replaced by silicon solid state HVDC converter, i.e. thyristor and more recently transistor based. The first full-thyristor project is a back to back project named Eel River in 1972. It has been developed to connect the asynchronous grids of Hydro Quebec and NB Power [IEE13]. Thyristor based converters are still in operation, their voltage and current rating has increased with time. Recent commissioned projects (e.g. Xiangjiaba – Shanghai) show that DC links using thyristors have a great interest with long distance and large power transfer. However, electricity transmission using thyristor converter stations has several limitations, which will be presented later (see part 1.2.2). A new technology of silicon solid state component called IGBT appeared into the power system. The first commercial HVDC link with IGBT is named Directlink, was built in 2000 to trade electricity between two regions of Australia. Recently a new topology of IGBT converter station, i.e. MMC enables to step up the voltage level by using a strategy which

allows subdividing the DC link voltage into several voltage levels (e.g. Trans Bay Cable and INELFE).

Table 1-3: A few HVDC projects [TAY07] [INE12]

Name	Date [year]	Length [km]	Voltage [kV]	Power [MW]	Type
Gorzente River (Italy)	1889	120	14	0.63	Thury
Lyon-Moutiers (France)	1906	200	±75	30	Thury
Moscow – Kashira (Russia)	1951	100	±100	30	Mercury
English Channel (France-UK)	1961	64	±100	160	Mercury
Eel River (Canada)	1972	0	80	320	Thyristor
Square Butte (USA)	1977	749	250	500	Thyristor
Cross Channel (France-UK)	1986	70	±270	2000	Thyristor
Directlink (Australia)	2000	59	80	180	IGBT
Trans Bay Cable (USA)	2010	85	200	400	IGBT (MMC)
Xiangjiaba – Shanghai (China)	2010	1980	±800	6400	Thyristor
INELFE (France-Spain)	2014	60	±320	2000	IGBT (MMC)

1.2.2. Thyristor based LCC transmission

Today, most of the HVDC schemes in operation are LCC transmissions, they are chosen because thyristor can withstand tens of kilovolts and handle several kilo amps. In this subsection, the thyristor structure and operation will first be presented, then the principle of LCC converter station will be explained, finally the LCC HVDC scheme will be shown.

Thyristor structure and operation [BAL12]

The thyristor, also called silicon controlled rectifier (SCR) is a semiconductor device composed of four layers alternatively doped P-N-P-N (Figure 1-4b). The thyristor is a three-pin device, two of them are used as power terminals (the anode (A) and the cathode (K)) and the third is used to control the switch (gate (G)) (Figure 1-4a). This device is able to be blocked for both positive and negative voltage, making it proper for alternative applications. The High voltage blocking capability is obtained thanks to the high doping gradient between the P+(anode)/N-drift junction and the P(gate)/N-drift junction. When its voltage is positive, it can be triggered into the on-state, by sending a positive current pulse on the gate (Figure 1-4c). Once the thyristor is conducting, it cannot be reopened until the voltage becomes negative (what is often obtained when anode-to-cathode current becomes negative). Hence, the structure of the thyristor is composed of two coupled bipolar transistors, enabling to stay in the on-state as long as a current is passing through it (process called regenerative action).

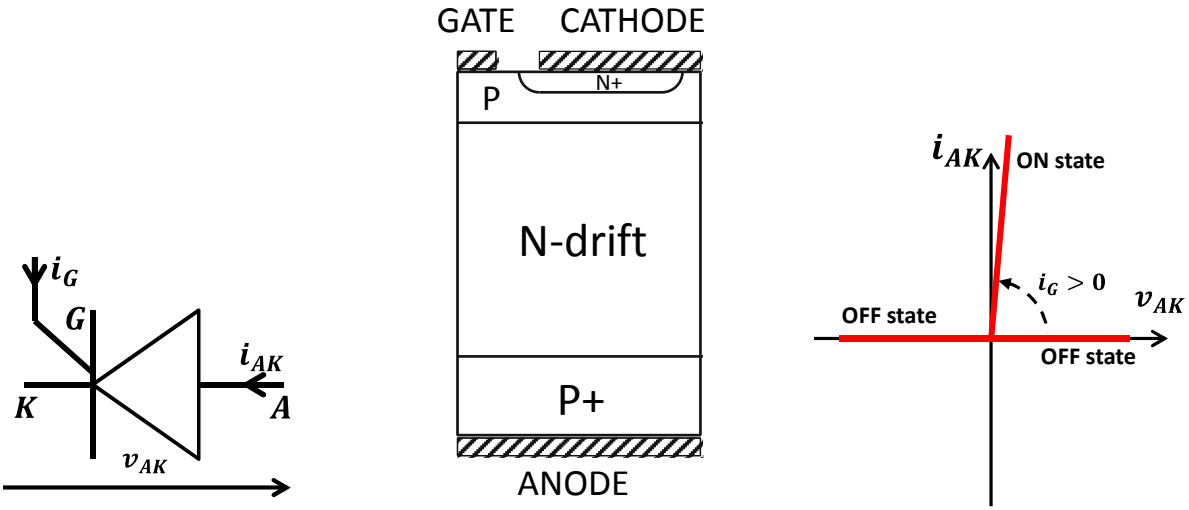

(a) Schematic symbol (b) Doping profile (c) VI characteristic

Figure 1-4: Thyristor

Today, thyristors available on the market can hold an anode to cathode voltage of 8 kV and current of 5 kA, which offers good characteristic for power applications. For HVDC projects, thyristors are stacked in series in order to step up the voltage level. This is possible thanks to light-triggered thyristor, enabling gate control with optical fiber.

Operating principles of a LCC converter station scheme [KUN94]

The LCC (Line Commutated Converter) is a Graëtz bridge, where "diodes" are controllable at the closure. To explain the operating principle of the LCC converter station, an idealized example is presented in Figure 1-5a. In an idealized case, the DC current is constant and the AC voltage source is really strong. Unlike diodes, a thyristor starts conducting when its forward anode to cathode is voltage positive and a signal is sent to its gate. So, contrary to the diode-based Graëtz bridge, the DC voltage level can be controlled by delaying the gate signal. By adjusting this delay, called the ignition delay angle, the average DC voltage level and the AC current phase are modified.

As an example, the case where the ignition delay angle is set at 15° is presented in Figure 1-5b, the DC voltage is plotted in the upper figure and the AC current through the phase is plotted in the lower figure. Active power transferred between the AC and DC side depends on ignition delay angle however the same control variable change the reactive power too. Therefore, additional reactive power compensation devices are needed to supply reactive power at the LCC connection point since phase currents at the AC side always lag the corresponding AC phase-to-ground voltages.

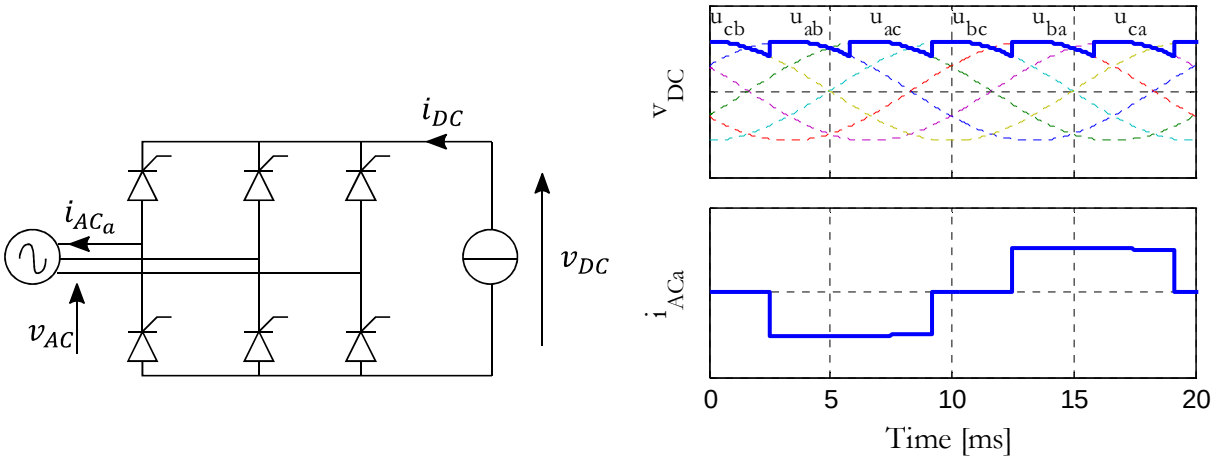

(a) Topology

(b) Direct voltage and AC current in the phase a waveforms with ignition delay angle of 15°

Figure 1-5: Ideal 6 pulses thyristor converter

The previous example is idealized; in reality AC grids can be represented by a voltage source in series with reactors which represents AC grid impedances seen from the LCC connection point. Since current cannot step change instantaneously through a reactor, when a signal is sent to a thyristor gate, the fired thyristor will conduct but the previous one will also conduct until the current though it decreases to zero. This commutation time, also called overlap, depends on the AC grid impedance and on the direct current magnitude.

In order to operate with positive direct current, thyristors must be in the opposite direction from one end of the link to the other end. So according to the arrangement of converter thyristors, the converter may either be a rectifier (i.e. positive DC voltage and negative DC current) or an inverter (i.e. positive DC voltage and positive DC current). Operating ignition angle for the rectifier ranges between 0° and 90°, while for the inverter the ignition angle is between 90° and 180°. Useful parameters are summarized in Table 1-4 for both operating modes.

Table 1-4: LCC useful parameters

Rectifier	Inverter
α: ignition delay angle	$\beta = \pi - \alpha$: ignition delay angle
μ: overlap angle	μ: overlap angle
δ: extinction delay angle	$\gamma = \pi - \delta$: extinction delay angle

To obtain a higher DC voltage, two or more thyristors bridges can be connected in series. To supply each additional bridge, an AC voltage source with independent ground reference is needed, this is obtained thanks to transformers. In practice, when there are two bridges in series, one transformer is YY connected while the other is $Y\Delta$ connected in order to obtain a phase shift of 30° between the two AC voltages. This leads to a 12 pulses arrangement and then fifth and seventh harmonics are eliminated on the AC side. Moreover, on the DC side, DC voltage ripple is reduced and sixth and eighth harmonics are eliminated.

One of the main drawbacks of the LCC is the commutation failure issue, it happens when the AC grid is not enough strong or have been weakened by an AC short circuit. This phenomenon occurs when a valve cannot be extinguished owing to the current across it not returning to zero, because of high DC current or high value of AC phase reactor. For this reason, LCC substation is not suitable to connect offshore wind farm.

Operating principles of a LCC-HVDC transmission scheme [AND05]

LCC can be implemented in different kinds of power transmission applications, such as back to back for the connection of two asynchronous AC grids, submarine or underground cable power transfer and long distance overhead lines power transfer. For power transmission, both monopole (with ground return) and bipole transmission or even symmetrical monopole strategies work, however the use of metallic return is often preferred. Indeed, many grid codes prohibit monopolar with earth or sea return as environmental consequences on gas or oil pipes (corrosion), telephone networks (interferences) magnetic fields are out of control. For a given rated current, bipolar schemes divide by 2 the voltage constraint on the cable, while allowing half power transmission in case of disturbance of one converter pole.

A classical LCC transmission scheme is presented in Figure 1-6. There are two converter stations at both DC link ends, one acts as a rectifier and the other as an inverter. These converters are composed of several bridges in series to operate with a high DC voltage. Each of these converters is connected to the AC grid through a transformer to have voltage sources with independent reference (for each six-pulse bridge) and to have proper AC voltage to suit the rated DC voltage. Because this type of converter consumes 60% of reactive power as regard to the active power transferred, capacitor banks are needed to compensate this reactive power: capacitor cells are turned on or off to achieve a satisfactory power factor. Close to capacitor banks there are harmonic filters to reduce low frequency harmonics rejected by the LCC (a LCC of n pulses generates harmonic orders of n±1 on the AC side). The last essential component is the DC reactor, it is used to smooth the DC line current and provide harmonic reduction.

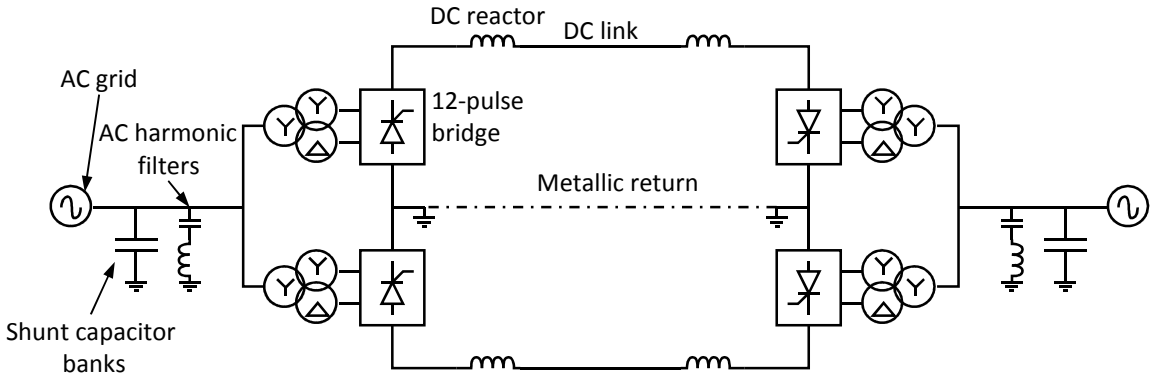

Figure 1-6: LCC-HVDC transmission scheme [AND05]

Usually LCC-HVDC transmission operates at a constant DC voltage and an adjustable constant current order set by the dispatch center. The firing angle order sent to each converter follows characteristics presented in Figure 1-7, the stable operating point corresponds to the curves intersection. Commonly, the rectifier controls the DC current and the inverter controls

the DC voltage. The voltage loop dynamics is slower than the current loop dynamics to avoid interactions between them. The power transfer reversal is realized by changing the voltage polarity and keeping same current direction.

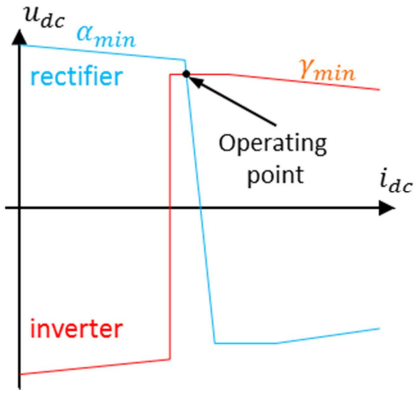

Figure 1-7: Converter control characteristics

1.2.3. IGBT based VSC transmission

Due to some advantages such as power transfer reversal without having to change the DC voltage polarity, self-commutated Voltage Source Converter (VSC) based transmissions are preferred to LCC in some transmission cases. This technology is based on a component which can switch on and off freely: the IGBT. A lot of converter topologies have been designed for electric drives, however for transmission scheme, only few of them are utilized [BAH07]. In this subsection, the IGBT structure and operation principles are first described, then the conventional (PWM based) VSC and the new MMC topology is described, finally a brief presentation of VSC-HVDC transmission scheme is presented.

IGBT structure and operation [BAL12] [BER00]

The IGBT (Insulated Gate Bipolar Transistor) is a combination of bipolar transistor and MOS (Metal Oxide Semiconductor) transistor, using the MOS transistor to control the bipolar transistor (Figure 1-8a). Figure 1-8b is a half cross section structure which illustrates an IGBT structure. On the left side, there is a MOSFET - N channel (N+/P/N-base) controlled by the gate potential and on the right side there is a PNP bipolar transistor (P+region/ N-buffer N-base /P+). By applying a positive potential to the gate, thanks to electrostatic effects, that pushes back holes of the P zone, and creates a path for electrons, enabling currents to flow through the formatted N-channel. This current excites the P+ region which produces a current in the opposite direction which controls the base of the PNP bipolar transistor. In summary, IGBT is a PNP bipolar transistor with its base current controlled by the voltage applied to the MOS gate. Therefore, this switch can be turned on in the first quadrant by applying a positive voltage to the gate and turned off by stopping this voltage. In addition, it is possible to control the switch gain with the gate voltage level, and therefore limit di/dt and dv/dt during commutations.

The IGBT structure is asymmetric, allowing lower on-state voltage drop and higher forward voltage blocking capability at the expense of reverse voltage blocking capability performances decreased.

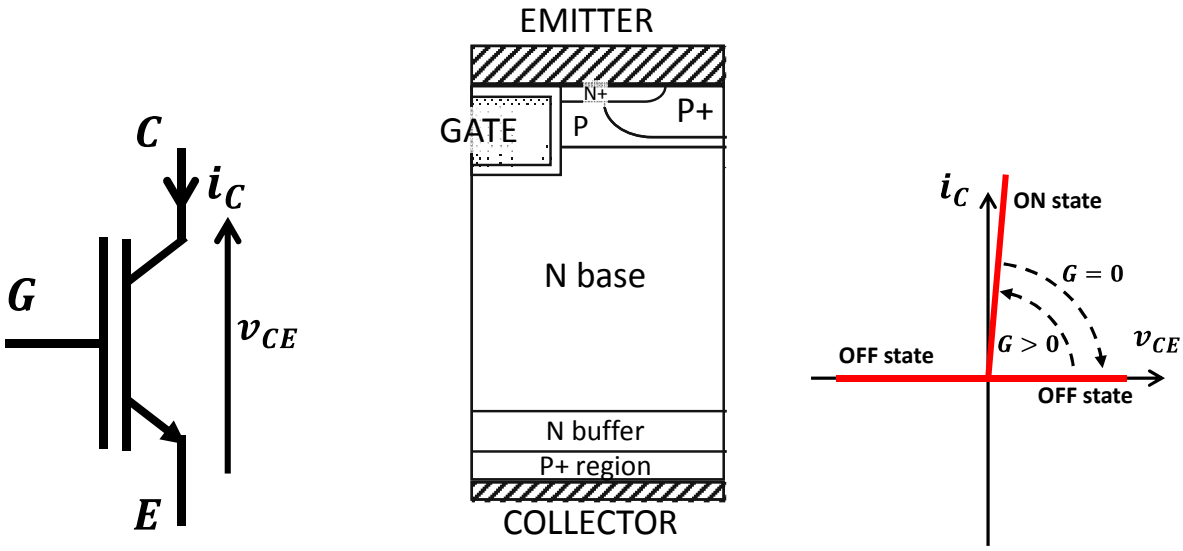

(a) Schematic symbol (b) Doping profile (c) VI characteristic

Figure 1-8: IGBT

IGBT modules are now available with 6.5 kV forward voltage blocking capability and current handling of 1 kA. For HVDC application, to improve performances and redundancy, IGBTs are staked in series and parallel [ABB13].

Operating principles of conventional VSC scheme

The basic structure arrangement of a two-level VSC is presented in Figure 1-9a. Thanks to IGBT switch-on and switch-off capability, each valve can switch more than once per cycle. In order to deal with negative current and IGBT low reverse voltage blocking capability, a diode is added in anti-parallel. At any time, the phase-to-phase voltage at the converter output (u_m) can be either equal to the DC voltage or equal to the opposite of the DC voltage, following the states of switches. So this converter topology enables to create an AC voltage source, by an appropriate switch control strategy.

The Pulse Width Modulation technique is used to reduce harmonics, a trade-off between the switching frequency (i.e. commutation losses) and the harmonic content must be considered. There are a large number of control strategies for two-level VSC [HOL92], the simplest and the most famous technique is the triangular comparison technique. The voltage waveform using the latter technique is presented in Figure 1-9b. The reference voltage is compared against a triangular signal (see upper figure), resulting in a modulated switching pattern (see lower figure), the fundamental of which is equal to the reference signal.

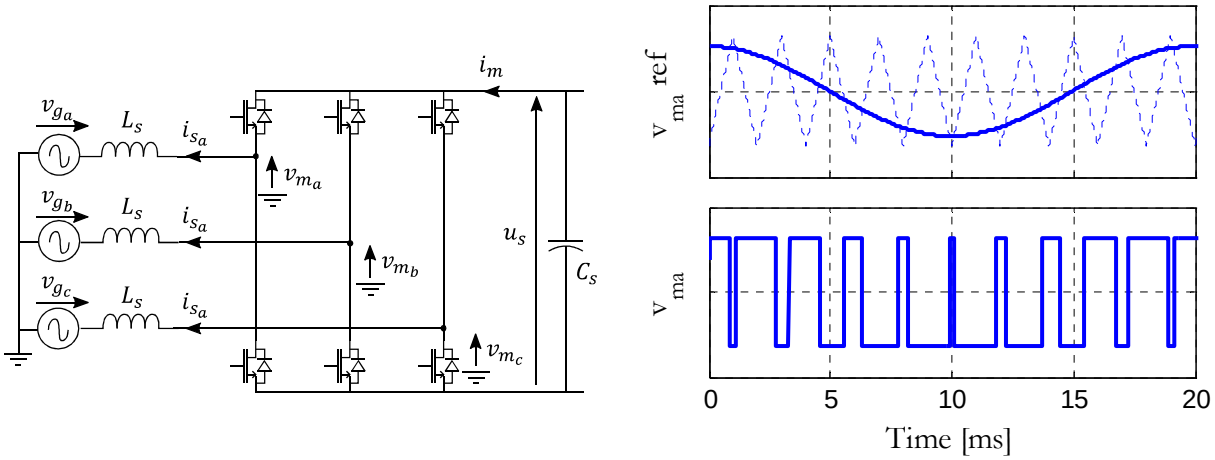

(a) Topology

(b) AC voltage with triangular comparison technique

Figure 1-9: Two-level VSC

Thanks to the voltage angle and magnitude control capability it is possible to manage the current through the line reactor, thus both active and reactive power can be controlled independently.

To keep controllability, terminal voltage of commutation cells must be positive otherwise the diodes conduct and it is no more possible to choose the commutation instant. To avoid this problem the DC voltage should be higher than the peak AC voltage of the voltage source; otherwise the two-level VSC works as a diode based Graëtz bridge. So in case of severe DC undervoltage, the AC side will supply the DC side without any possible control. Without fast DC or AC protection scheme, current through diodes will rapidly exceed the maximal admissible current.

A way to reduce harmonics without increasing switching losses is to subdivide the DC voltage into several voltage levels. As an example, the Neutral Point Clamped (NPC) converter topology is presented in Figure 1-10a. This is a three-level VSC, thanks to the two additional diodes which clamp the voltage to the half of the DC voltage as shown in Figure 1-10b. Contrary to misleading appearances, the number of IGBTs is not increased due to the fact that each IGBT valve withstands only half the voltage level of those of the two-level, so the number of switches into each IGBT stack valve can be divided by two, therefore the total sum of semiconductor devices in a converter station is still the same. Thanks to this topology, there is less harmonic content and switching losses are reduced because each switch commute two times less than for the two-level.

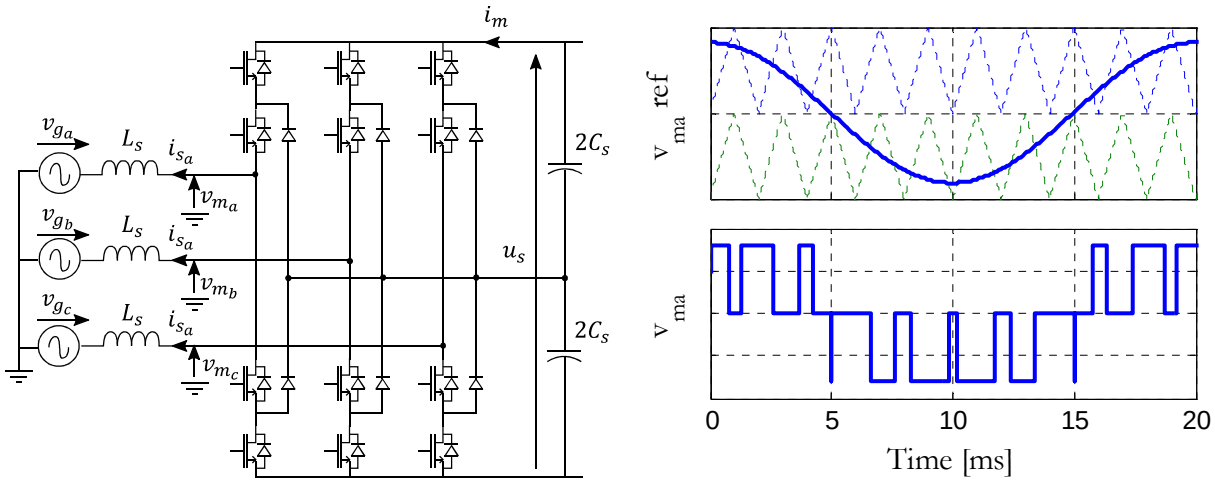

(a) Topology

(b) AC voltage with triangular comparison technique

Figure 1-10: Neutral Point Clamped Converter

Although losses in higher multi-level topologies should be even lower thanks to lower voltage excursion resulting from the switching, they also have negative aspects such as complex commutation process, unequal capacitor voltage balance which makes higher multi-level converters non suitable for HVDC applications. More advantages and drawbacks on conventional VSC topologies for transmission operation can be retrieved in [AND02].

Operating principles of a MMC station scheme

The new Modular Multilevel Converter (MMC) overcomes limitations of conventional multilevel VSC [LES03]. MMC is attractive for HVDC applications thanks to its modular structure which enables [PER12]:

- Smaller switching frequency of individual semiconductors (i.e. around ten times lower than two or three-level [MAC11]) improves the efficiency by decreasing switching losses.
- Smother voltage waveforms due to low voltage step. So harmonic filters can be removed or smaller in size. By increasing the number of sub-modules harmonic rejections are improved.
- Each individual switch has lower voltage which improves switching losses and experiences lower dv/dt.
- Scalable to any DC voltage. The MMC DC terminal voltage can be upgraded by adding submodules in series in each leg.
- Better reliability by adding sub-modules.

MMC topology is presented in Figure 1-11a. It is a combination of sub-modules in series for each phase. A detail of the content of one sub-module is given in this Figure 1-11c. Each sub-module is a DC chopper, when the upper switch is on and the lower is off, the DC capacitor is connected in series, therefore its voltage is added to the arm voltage, otherwise (i.e. the upper switch is off and the lower is on) the capacitor is disconnected and the sub-module voltage is

zero. Therefore the voltage of each arm of the MCC can be controlled independently of each other.

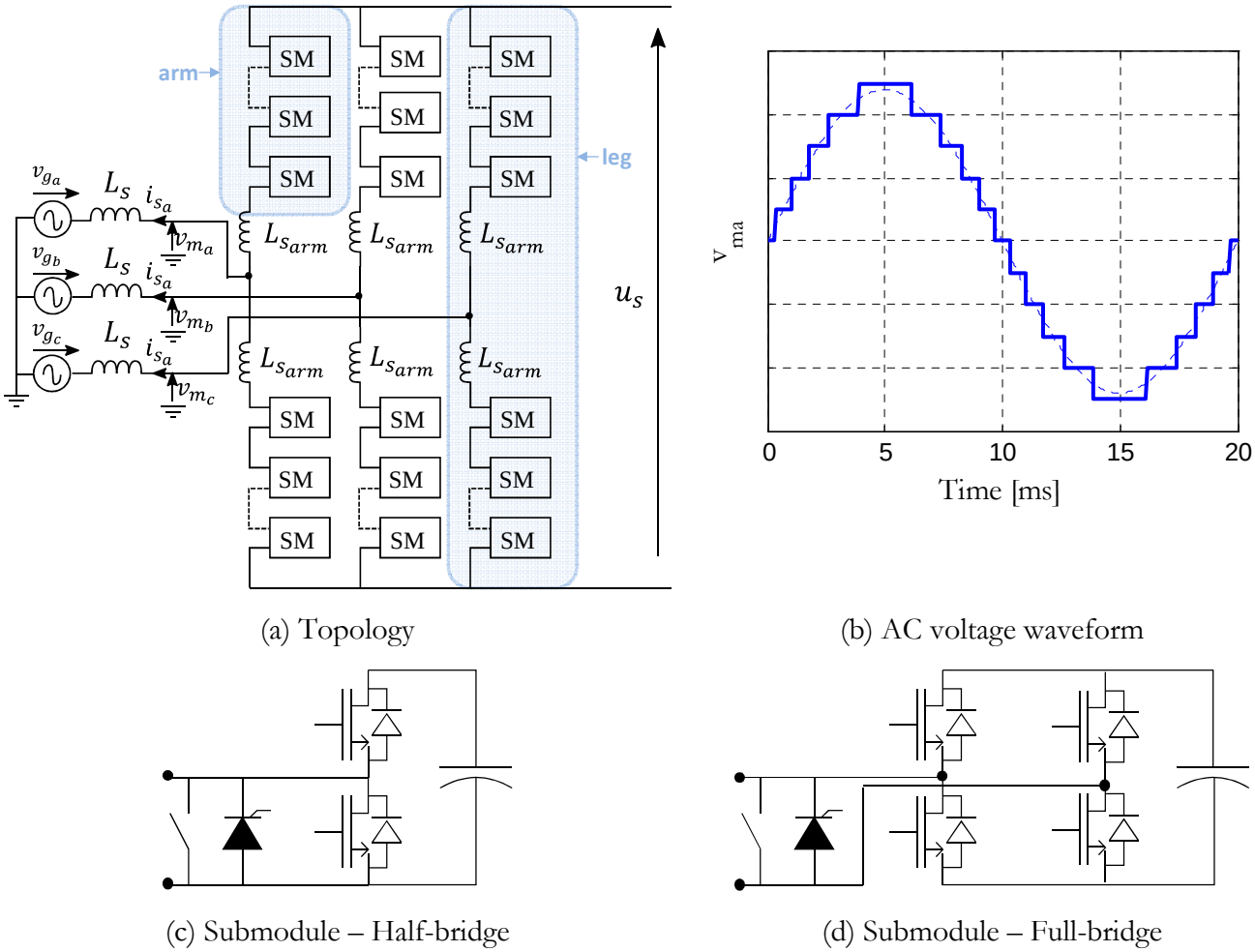

(a) Topology

(b) AC voltage waveform

(c) Submodule – Half-bridge

(d) Submodule – Full-bridge

Figure 1-11: Modular Multilevel Converter (MMC)

The control of this topology is more complex than for two-level VSC due to the huge number of variables to monitor and control. Improvements in informatics and telecommunications have permitted to manage this topology. The modulation technique used to control MCC can be either based on PWM techniques [LES03] or staircase type method where the nearest voltage level is chosen [PER12]. The latter technique is presented in Figure 1-11b for an MMC comprising five submodules per arm.

In order to operate in good condition, the large number of submodule capacitors must have a balanced voltage. This function is achieved by an additional controller which monitors the submodule capacitor voltage and chooses which submodule must be switched ON (resp. OFF) according to the arm current sign [PER12]. The open loop control of arm voltages leads to a circulating current owing to voltage mismatch between legs, it can be canceled by adding a supplementary controller [PER12].

MCC topology with submodules including four controllable switches, called H-bridge or full-bridge presented in Figure 1-11d, is under study because it has current blocking aptitude

when a DC faults occurs [ADA12a]. Switching losses brought by additional switches, are the main drawback of this topology as regard to the MMC with sub-modules including two switches only.

MCCs have already been developed or are under development by three main manufacturers ABB, Alstom and Siemens [MAC11] [JAC10] [DOR08].

Summary on VSC topology

In Table 1-5 there is a summary of conclusions drawn by Adam et al.

Table 1-5: Comparisons of VSC-HVDC topologies [ADA12a]

	Two-level	NPC	MMC	H-bridge MMC
Reactive power capability	Limited by DC link voltage	Limited by DC link voltage and capacitor voltage balancing	Limited by DC link voltage and arm inductance voltage drop	Limited by DC link voltage and arm inductance voltage drop
Power flow	100% bidirectional	100% bidirectional (with some restrictions due to modulation index margin for capacitor balance)	100% bidirectional	100% bidirectional
Harmonic filters and interfacing reactors	Relatively large	Relatively large	Could be eliminated	Could be eliminated
Conversion losses	Very high	high	low	Moderate
Switch stress	high	better	low	low
AC fault ride through capability	Yes	yes	yes	yes
DC fault ride through capability	Poor	poor	good	excellent

Conclusions drawn on VSC topologies may change because of recent advances in semiconductor devices such as Silicon Carbide (SiC) which are not yet available for HVDC applications. Those devices are expected to improve significantly VSC substations because they can handle higher temperature (i.e 500°C instead of 150°C for silicon) [BAD12].

In normal operation, from a macroscopic point of view, i.e. AC grid phase reactor current control, DC voltage control, active and reactive power control, the behaviors of any VSC topology are similar. Their behaviors differ in case of abnormal operations, for losses, and harmonics. Therefore, for studies focused on power management in normal operation such as dynamic stability phenomena, two-level converters are representative of any VSC topology. Indeed, for the sake of simplicity, computation time saving and development time saving, for those kinds of study, two-level converters can be simulated instead of MMC [PER12] [TEE09].

Operating principles of a VSC-HVDC transmission scheme

A point-to-point VSC-HVDC transmission is composed of two VSC substations connected at each ends of the DC-link (see Figure 1-12).

As for LCC transmission, the DC link can be either overhead or underground, monopolar or bipolar. But, as explained before, the bipolar solution is preferred if N-1 is requested. On the DC side, capacitors enable to maintain the DC voltage. On the AC side, the converter is connected to the AC grid by an interface transformer which enables to define a specific voltage at converter side. The phase reactors associated with transformer's leakage inductances filter injected grid currents and allow their control. Optional AC filters are tuned to filter PWM harmonics; also they could improve the PQ diagram by supplying reactive power.

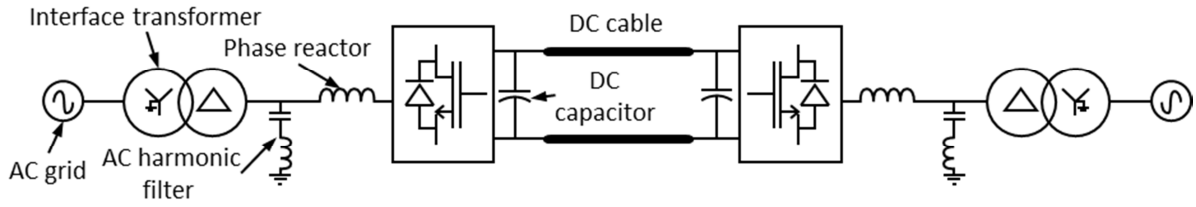

Figure 1-12: VSC-HVDC transmission scheme

As previously seen in LCC-HVDC transmission, one of the converters is controlling the DC bus voltage while the other controls the power transfer. Similarly to the LCC technology, the receiving side often controls the dc voltage while the sending side controls the power transfer. VSC can control quasi-independently active and reactive power, so it is possible to control AC voltage level or the reactive power at each end within the limit of the converter rating (see 1.3.5).

For passive or islanded network (e.g. offshore wind farm), this converter can generate its own AC voltage from scratch, at any voltage level and frequency [TWE11a].

1.2.4. Comparison of LCC and VSC transmission schemes

The main dissimilarities between LCC and VSC transmissions are summarized in Table 1-6.

Table 1-6: Comparison between LCC-HVDC and VSC-HVDC [AND05] [CIG10] [SEL12]

	LCC-HVDC	VSC-HVDC
Harmonics	Important filter banks are required to guarantee the harmonic rejection	Fast switching reduces the harmonic content and small filters can be used on the AC side. With MMC technology, the filter is nearly not needed
AC fault	If a fault is occurring close to the converter, it can induce commutation failures	VSC can ride through AC fault.
DC fault	Thyristors control the DC current, then the DC fault current can be controlled too.	AC breaker for point to point line. DC breakers are needed in MTDC systems.
Active power control	Current sign cannot be inverted through the thyristors, so the power transfer reversal supposes to change the voltage sign which may not be instantaneous	Fast control of active power in both directions

Reactive power control	Naturally, the LCC HVDC consumes reactive power. This is compensated by shunt capacitor banks. The reactive power control is not easy.	VSC can continuously generate or absorb reactive power, within apparent power limitation.
Black start capability	Not possible	Possible
AC side short circuit ratio	A strong AC grid is mandatory because LCC switches through an external voltage source.	No short circuit ratio is required.
Power rating	Up to 3500 MW per monopole	Up to 1000 MW per monopole
Cost (1000 MW)	95 M€ ± 20%	85 M€ ± 20%
Losses (1000 MW)	0.75% per converter station	0.9% to 1.75% per converter station, depending on the technology used two-level converter, MCC,…
Footprint (400MW)	27 000m² (100%)	20 700m² (77%) if two-level 15 675m² (58%) if MMC

1.3 CLASSICAL CONTROL PRINCIPLES OF VSC

Figure 1-13 shows the schematic diagram of a VSC substation controlled in dq synchronous frame. In this subsection, for the sake of simplicity, the VSC AC filter is reduced to a simple phase reactor, containing the VSC phase reactor and the transformer leakage inductance. Regarding the AC voltage generated by the converter, only the fundamental frequency is considered.

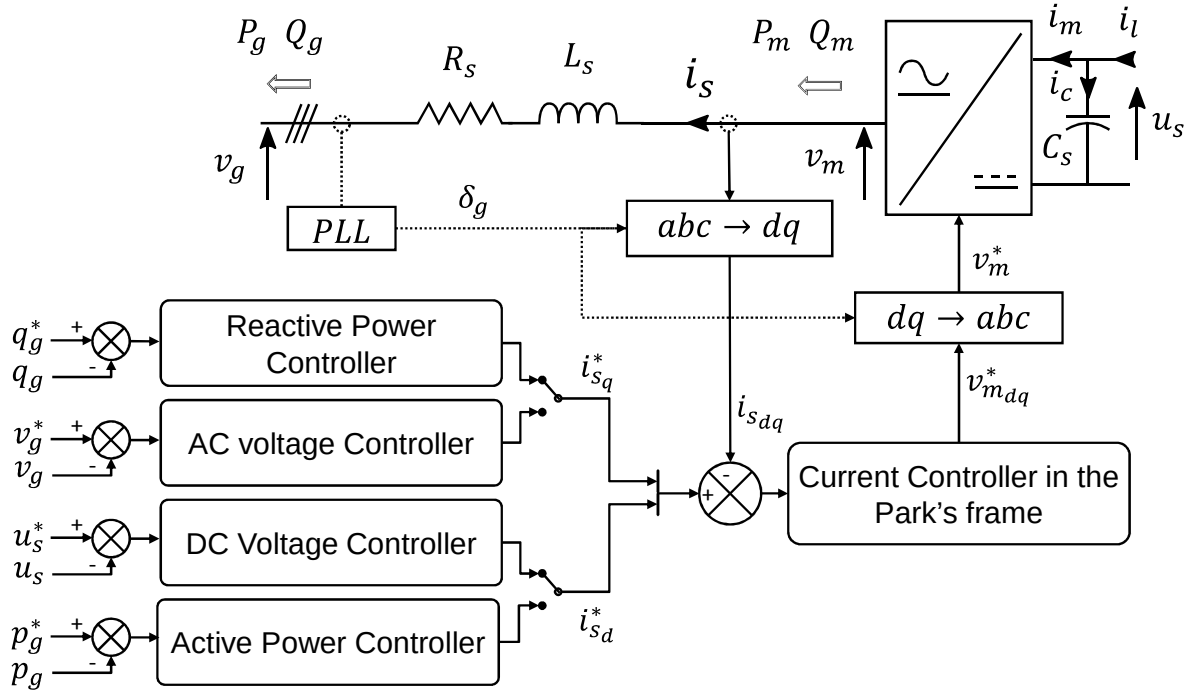

Figure 1-13: Single line diagram of RL filtered VSC and its associated control

The case where the converter is connected to a grid which imposes the frequency is considered. The Phase Lock Loop (PLL) allows synchronizing the dq rotating frame (also called

Park's frame) with the grid voltage at the Point of Common Coupling (PCC) with the grid. Thus, the active and reactive power can be independently controlled by current components. Additional controllers are used to achieve specific functions:

- the q-axis current reference (i_{sq}^*) can either be given by a reactive power controller which controls the reactive power exchange at the PCC or by an AC voltage controller which controls the AC voltage.
- The d-axis current reference (i_{sd}^*) can either be given by an active power controller which controls the active power exchange at the PCC or by a DC voltage controller which controls the DC voltage level by acting on power transfer through the VSC.

The structures of generic controllers are presented in this subsection. First, basic current control loop scheme is detailed, and then outer controllers are described.

1.3.1. Current control

The role of the current control loop (also called inner control loop) is to achieve a current control through the AC filter. The equivalent diagram of the AC filter and its phasor diagram are presented in Figure 1-14. v_g represents the PCC voltage, v_m the fundamental component of the voltage at converter side, R_s and L_s the phase reactor parameters and i_s the phase reactor current.

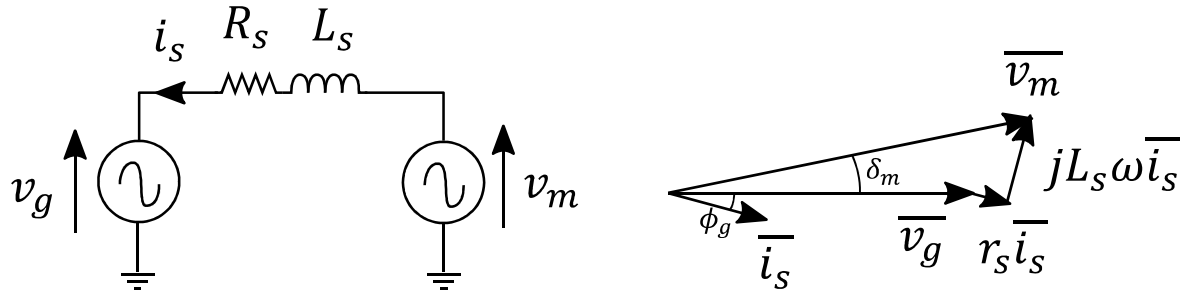

(a) Equivalent diagram of L-filter VSC (b) Fresnel's diagram

Figure 1-14: Current control principle

The AC phase reactor current behavior is governed by the following differential equation:

$$\frac{d\,\overline{i_s}}{dt} = \frac{1}{L_s}\left(\overline{v_m} - \overline{v_g} - r_s\overline{i_s}\right) \quad \textbf{(1.3)}$$

Where:

$\overline{i_s}$	Is the phasor current through the phase reactor [A]
$\overline{v_m}$	Is the phasor voltage at converter side [V]
$\overline{v_g}$	Is the phasor voltage at grid side [V]
r_s	Is the phase reactor resistance [Ω]
L_s	Is the phase reactor inductance [H]

Since classical PI controller introduces a phase shift when controlling sinusoidal quantities, the dq rotating frame is introduced to achieve zero steady state error. This rotating frame turns with the same angular velocity than the AC grid; it is locked on the direct sequence voltage vector. A Phase Lock Loop (PLL) is used to track the grid voltage angle. The relation which transforms quantities from the stationary reference frame to the dq rotating frame is called Concordia-Park transformation (see Figure 1-15).

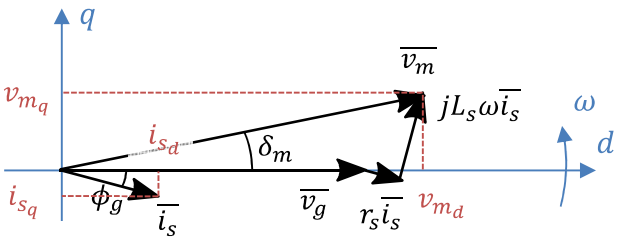

Figure 1-15: dq frame of current control

In this frame the current equation (1.3) becomes [HAI09a]:

$$\begin{cases} \dfrac{di_{s_d}}{dt} = \dfrac{1}{L_s}\left(v_{m_d} - v_{g_d} - R_s i_{s_d} + i_{s_q}\omega L_s\right) \\ \dfrac{di_{s_q}}{dt} = \dfrac{1}{L_s}\left(v_{m_q} - v_{g_q} - R_s i_{s_q} - i_{s_d}\omega L_s\right) \end{cases} \tag{1.4}$$

The decoupled current controller, presented in Figure 1-16, is designed from (1.4). This structure of controller enables to cancel the coupling between the d and q axes. Thanks to this decoupling, d and q currents can be controlled independently. The dynamics can be tuned by using the properties of second order polynomials.

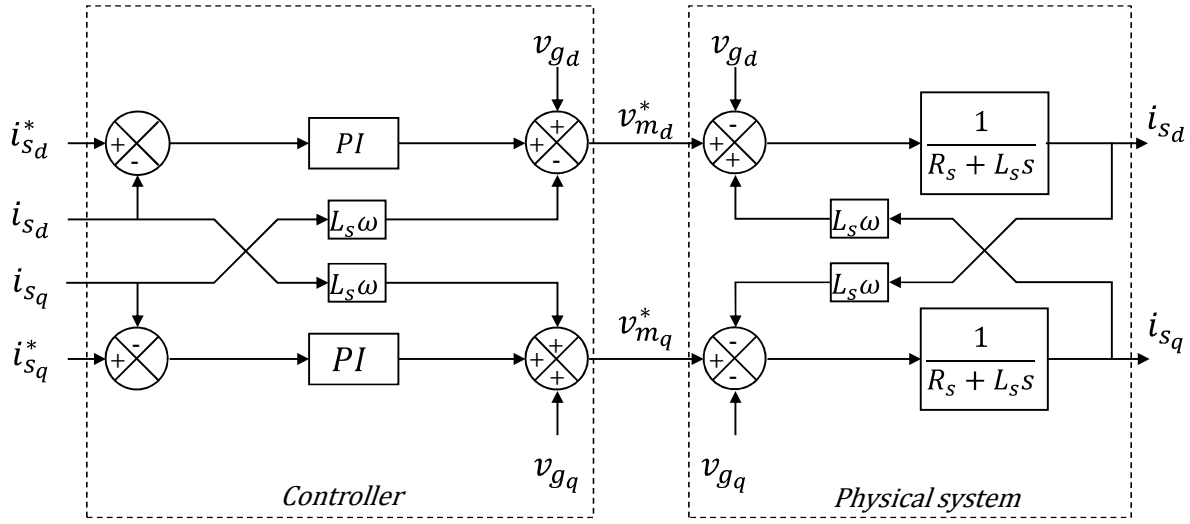

Figure 1-16: Current control loops in the dq frame

1.3.2. Power control

The active and reactive powers in the dq-frame are expressed by [YAZ10]:

$$\begin{cases} P = v_d i_d + v_q i_q \\ Q = v_q i_d - v_d i_q \end{cases} \quad (1.5)$$

In this study, the PLL has been designed to align the voltage d-axis with the grid voltage vector, therefore (1.5) can be simplified as follows:

$$\begin{cases} P = v_d i_d \\ Q = -v_d i_q \end{cases} \quad (1.6)$$

Nevertheless, additional power controllers are often preferred because, for transmission grid application, the important quantity is the power (or the AC voltage). Indeed, outer power loop controllers guarantee active and reactive power transfer at the PCC, especially when the AC filter is not a simple RL circuit. Figure 1-17 shows the basic arrangement of active and reactive power controllers. Using power controller enables to set the active and reactive power dynamics responses. In some cases, the power controller has a feed-forward action (dotted arrow in the figure) which shunts the power controller dynamics by directly feeding the reference into the current controller. With this feature, power controllers enable to guarantee that the active and reactive power exchange at the PCC and the power reference change dynamics are close to those of the current loop.

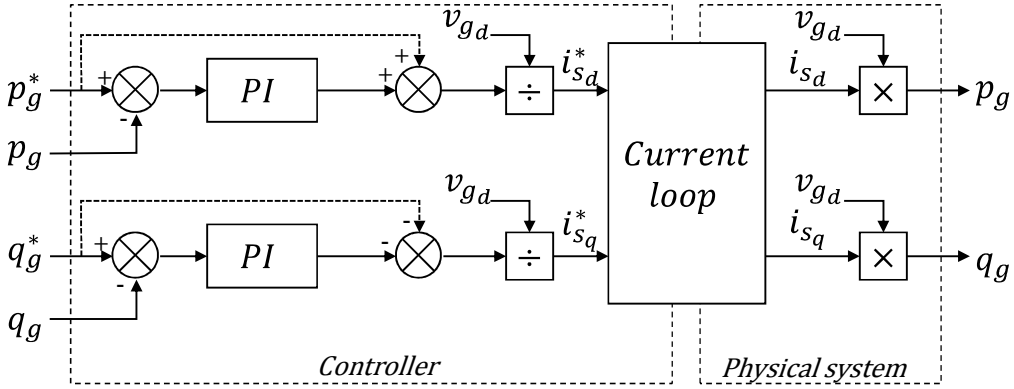

Figure 1-17: Active and reactive power control loops

1.3.3. DC Voltage control

For one converter, the DC voltage equation can be written as:

$$\frac{du_s}{dt} = \frac{1}{C_s}(i_l - i_m) \quad (1.7)$$

Where:

i_l Is the load current [A]

i_m Is the incoming converter current [A]

C_s Is the converter station capacitor [F]

u_s Is the DC voltage [V]

There are two typical ways to control the DC voltage, either the directly controlling the DC voltage or the square of this voltage. The first method is based on the DC current control and the second on the power management. The controller arrangement of the first method is presented in Figure 1-18.

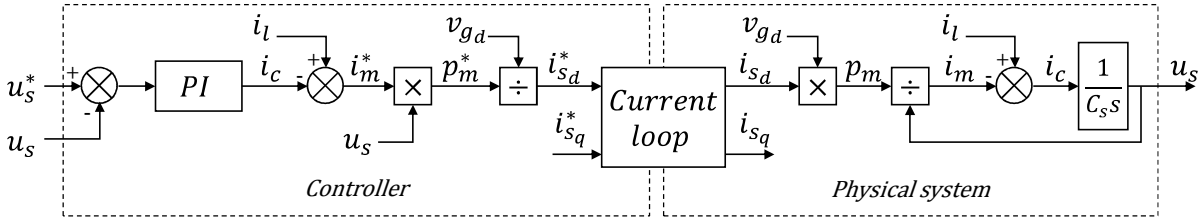

Figure 1-18: DC voltage control loop

The command structure has been designed by inverting the physical system. By experience, the compensation of the load current i_l can bring instabilities because of the measurement delays. So, in practice this current is not compensated, its variation is seen as a perturbation and will be corrected by the PI controller. As regards AC voltage and DC voltage compensation, they are often replaced by their nominal value because, in power system, they should be maintained close to this value.

1.3.4. AC voltage control

Although, for stiff AC grids the PQ control is preferred, for some weak AC grids the control of the PCC voltage could be required by the TSO [EIR11]. In this case, instead of controlling the reactive power the converter controls the AC voltage by acting on the current component which is associated to reactive power. For the sake of simplicity, this ability is not considered in this study.

1.3.5. Capability chart [COL10]

As explained before, active and reactive power can be controlled independently as long as they are not exceeding the operating limits fixed by the converter and the DC line rating. The three main quantities which limit the VSC range of operation are:

(1) The maximal admissible AC current feeding in the converter
(2) The maximal converter voltage on the AC side
(3) The maximal DC current

The first limit is calculated from the maximal current through the converter which is equivalent to the maximal admissible current through the phase reactor ($I_{s\,max}$). At a given V_g PCC voltage, this current limit yields to the following power limitation:

$$S_g = \sqrt{P_g^2 + Q_g^2} < S_{g\,max} = 3V_g I_{s\,max} \tag{1.8}$$

The second limit is related to the maximal AC voltage on the converter side ($V_{m\,max}$). This voltage depends on the DC voltage level, the converter topology and the modulation strategy (i.e. modulation index). The limitation caused by this voltage limit can be determined with the power flow equations through the RL filter:

$$\begin{cases} P_g = 3\dfrac{V_g V_m \sin(\delta_{mg})}{L_s \omega} \\ Q_g = 3\dfrac{-V_g^2 + V_g V_m \cos(\delta_{mg})}{L_s \omega} \end{cases} \quad \textbf{(1.9)}$$

Where:

$\delta_{mg} = \delta_m - \delta_g$ Is the voltage angle difference of v_m and v_g [rad]

V_m Is the rms value of the converter voltage v_m [V]

V_g Is the rms value of the grid voltage v_g [V]

Eliminating $\sin(\delta_{mg})$ and $\cos(\delta_{mg})$ from (1.9), leads to a circle equation in the PQ diagram:

$$P_g^2 + \left(Q_g + 3\frac{V_g^2}{L_s \omega}\right)^2 < \left(3\frac{V_g V_{m\,max}}{L_s \omega}\right)^2 \quad \textbf{(1.10)}$$

The last limitation is the maximal DC load current ($i_{l\,max}$) which could be the cable ampacity in case of a point to point HVDC link. Neglecting switching and phase reactor losses, the third limitation can be written as:

$$|P_g| < u_s . i_{l\,max} \quad \textbf{(1.11)}$$

All these limits are reported in Figure 1-19, for a PCC voltage level at the nominal value (solid line) and another at a PCC voltage level of 90% (dotted line), the normal operating range of the VSC should be inside this PQ diagram. Thus, PQ diagram is strongly dependent on the AC grid voltage: decreasing this value extends limit 2 but in the same time shortens limit 1. A way to improve the VSC's operating range is the integration of an OLTC transformer to change the AC voltage level as a function of the wanted operating point.

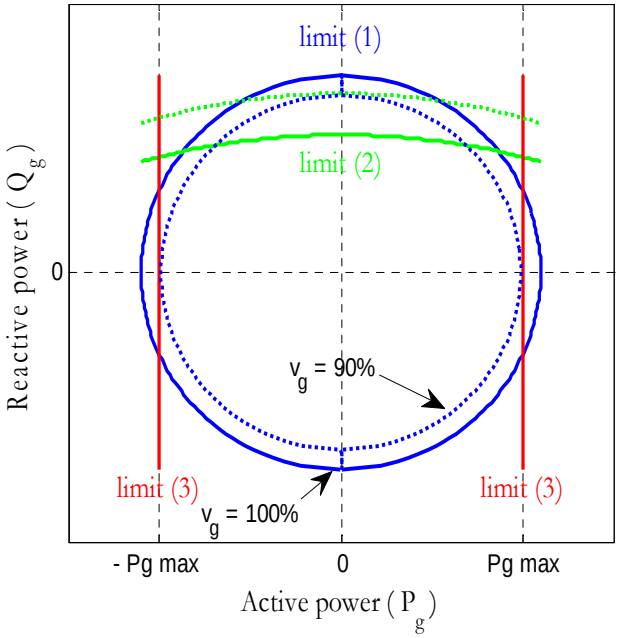

Figure 1-19: PQ diagram of a VSC

1.4 SUMMARY

In this introduction chapter the critical distance where HVDC is more attractive than HVAC was justified by an analytical approach on a simple case. Evolution of HVDC technology over time has shown a great improvement of valves which leads to new converter structures. Currently, both LCC and VSC are in operation, they operate differently due to the inherent characteristics of their components. Today, LCC is better known, it is more robust and it can withstand higher power, however, this converter station cannot be connected to AC network with low short circuit ratio and fast power flow reversal is not possible. VSC does not have these drawbacks and therefore it is more suitable than LCC to build up an offshore DC grid.

Although, the trend is to use modular multilevel converters for VSC HVDC ongoing transmission projects, a simple two-level VSC is considered in this work since basic control principles are similar. The VSC structure has small effects on power flow behavior only harmonics, dynamics and operational limits may differ.

CHAPTER 2: Small-Signal Stability Analysis of an HVDC Link

2.1 CHAPTER INTRODUCTION

In [KUN04], authors define stability as the ability of a system, for a given operating point, to regain a state of equilibrium after a physical disturbance. The classification of power system stability problems still refers to AC systems, such as rotor angle stability, frequency stability and voltage stability.

There are several simulation tools used to evaluate the system stability depending on the phenomenon time frame. In general, Electro Magnetic Transient (EMT) simulations are used to evaluate the system response when it is subject to severe disturbances such as short circuit which cause large deviations in the power system. Models required for this kind of simulation should be accurate in order to represent the system non-linearity. EMT programs are used to accurately represent electromagnetic transients, they are also well suited to simulate switching devices such as converters [BEE13]. One major drawback of this kind of simulation is the computation cost, i.e. several minutes to simulate less than one second. For VSC-HVDC studies, detailed EMT models are used either to simulate faults on the DC grid [DES12] or considered as reference models to validate simplified models [COL10a]. When a slower dynamics phenomenon such as the electromechanical behavior has to be studied, the phasor theory can be applied. In those simulations where electromagnetic effects are neglected, models can be simplified and therefore simulated with larger time steps, which significantly improves the computation time. In [YAO08], the author proposes a dynamic phasor model of a VSC-HVDC link.

Traditionally, the ability of a power system to remain stable when it is subject to small disturbances is studied on a linearized model. The main advantage is the possibility to use powerful techniques of control theory developed for the linear system. It allows assessing the system stability, identifying the origin of oscillations and proposing methodologies to tune controllers in order to reach sufficient stability margin. As an example, in power systems this method is widely used to tune Power System Stabilizers (PSS) in order to damp electromechanical oscillations of generators.

Introduction of FACTS and HVDC is considered as a way to improve the stability and the flexibility of power systems: such as an increase of transmission capability, improvement of static and dynamic stability and decrease of transmission losses [GRU99]. Small-signal stability analysis (SSSA) with power electronics is mainly studied since Ainsworth identified stability problems due to control of LCC [AIN67]. Recent works, notably PhD thesis have investigated Small signal stability of VSC-HVDC system inserted into an AC system: [ZHA10] analyzes the control strategy of a VSC-HVDC link connected to weak AC grids, [LAT11] and [PRE13] investigate control strategies of VSC-HVDC transmission in order to improve damping of electromechanical modes of AC systems. The emphasis of these works was mainly on AC system behavior, special VSC-HVDC controls have been designed to improve AC system performances, such as Power Oscillation Damping (POD).

The core of our study is the DC system; AC ancillary services are not considered in the first step in order to keep the focus on the power flow control in the DC side.

SSSA is a well-known tool in the field of power system stability and control analysis. It has proven its effectiveness in AC system and seems to be an interesting tool to study DC systems

stability and control. This chapter proposes a methodology for a SSSA of VSC-HVDC links, which is a step toward MTDC modeling and control assessment. This chapter is organized as follows: the first part is about modeling of VSC converter, the second part presents an original cable model usable for SSSA and the last part exhibits the basics of SSSA with a VSC-HVDC link example.

2.2 MODELLING VSC WITH ITS CONTROLLERS

In this part, a methodology to model VSC-HVDC converter station for dynamic study is presented. For the sake of simplicity the considered VSC is RL-filtered, instead of LCL. Indeed, except for harmonic and reactive power generation the general dynamics is similar for both AC filter structures. Moreover, most advanced converter station, e.g. MMC, are simply RL-filtered. More information on modeling of VSC with LCL filter is available in [LIN98a].

Until the end of this subsection, the converter is considered as ideal, it is simulated by its averaged model in order not to take into account harmonics which are not a matter of interest of this thesis.

The VSC used here as an illustration example is a converter station rated at 1000 MVA, 320 kVrms phase to phase AC voltage and a DC voltage of ±320 kV; more parameters are reported in Appendix A.

2.2.1. Linear model of a current controlled VSC

Modelling

The VSC, modeled with its current control loops as presented in Figure 1-16, is the base structure for any grid connected VSC model. As already said in the previous chapter, the control of the current is achieved in the dq rotating frame. Neglecting switching losses, the real power at the AC converter side and the DC side is the same. With this assumption the power relation between AC and DC side is defined as follows:

$$v_{m_d} i_{s_d} + v_{m_q} i_{s_q} = u_s i_m \tag{2.1}$$

This equation is non-linear owing to the multiplication between variables. This equation is linearized by using the Taylor's development limited at the order one. Each quantity is defined by an operating point denoted by capital letter and the subscript 0, and a small variation denoted by the Greek symbol Δ. The previous equation becomes:

$$\begin{aligned}\left(V_{m_d0} + \Delta v_{m_d}\right)\left(I_{s_d0} + \Delta i_{s_d}\right) + \left(V_{m_q0} + \Delta v_{m_q}\right)\left(I_{s_q0} + \Delta i_{s_q}\right) \\ = (U_{s0} + \Delta u_s)(I_{m0} + \Delta i_m)\end{aligned} \tag{2.2}$$

In steady state, the real power is:

$$V_{m_d0} I_{s_d0} + V_{m_q0} I_{s_q0} = U_{s0} I_{m0} \tag{2.3}$$

Developing (2.2), keeping only small variations around the steady state yields:

$$\begin{aligned}\Delta v_{m_d} I_{s_d0} + \Delta i_{s_d} V_{m_d0} + \Delta v_{m_d} \Delta i_{s_d} + \Delta v_{m_q} I_{s_q0} + \Delta i_{s_q} V_{m_q0} \\ + \Delta v_{m_q} \Delta i_{s_q} = \Delta u_s I_{m0} + \Delta i_m U_{s0} + \Delta u_s \Delta i_m\end{aligned} \tag{2.4}$$

By neglecting terms of second degree and higher, this equation becomes linear:

$$\Delta v_{m_d} I_{s_d 0} + \Delta i_{s_d} V_{m_d 0} + \Delta v_{m_q} I_{s_q 0} + \Delta i_{s_q} V_{m_q 0} = \Delta u_s I_{m0} + \Delta i_m U_{s0} \quad \textbf{(2.5)}$$

The bloc diagram of the VSC associated with its inner controller is presented in Figure 2-1.

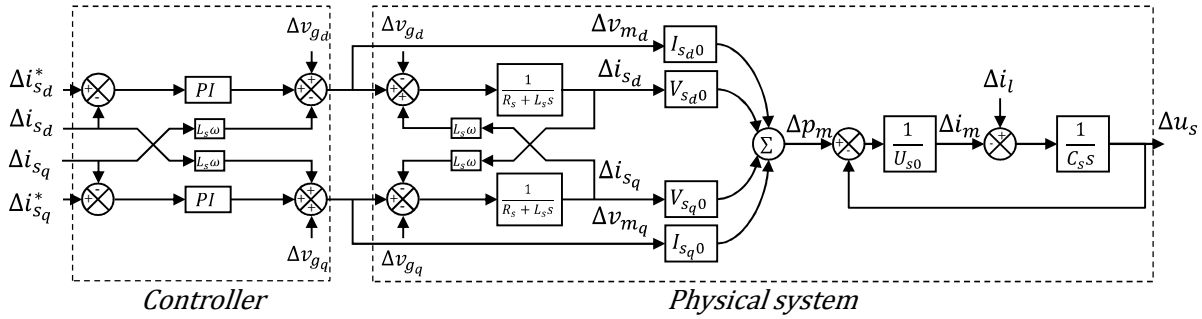

Figure 2-1: Linearized block diagram of the current controlled VSC

Validation

In order to validate the state space model of the dq frame controlled VSC, a simulation of the converter connected to a 900 MW resistor at the DC side (nominal voltage) is performed. The scenario is a step change on reference $i_{s_d}^*$ at t = 0.2 s. Results achieved on Matlab/Simulink® for the state space model (State-Space) and on EMTP-RV® for the average model (EMT), are compared in Figure 2-3. The operating point is computed by EMTP-RV® before the step change. It is used as the input of the state space model and added to state space outputs in the time domain simulation in order to retrieve full quantities.

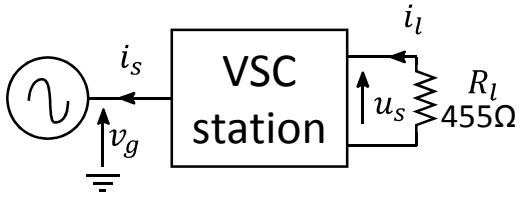

Figure 2-2: Test system used to validate the VSC state space model with the current controller

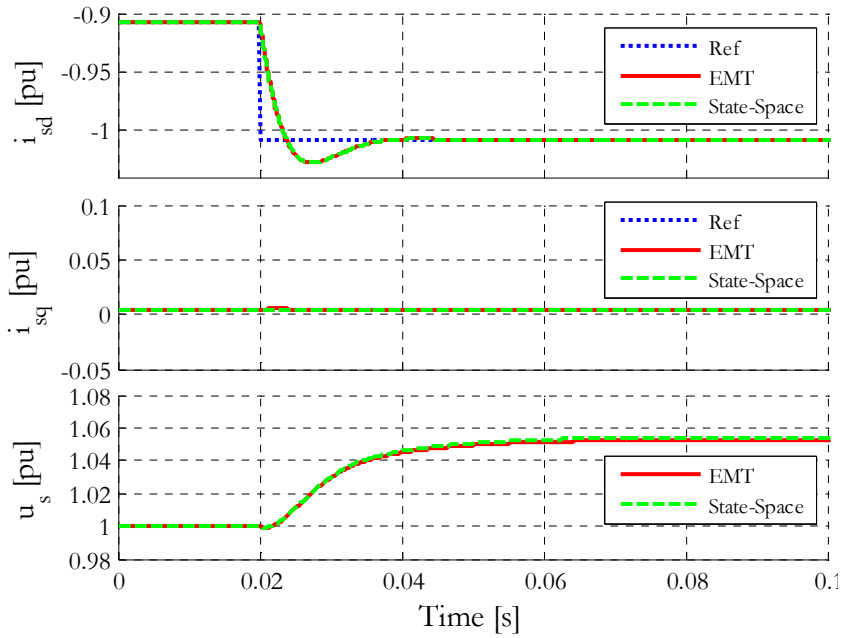

Figure 2-3: State space model validation of the vector current controlled VSC

Both waveforms from average and linearized models cannot be differentiated, thus the linear model for the current controlled VSC state space model is validated.

2.2.2. Linearization of the power controller

In the previous chapter it is mentioned that active and reactive powers can be controlled directly by adjusting d and q components but additional power controllers are often used. In this paragraph the power controllers is state space modeled with feed-forward action.

Modeling

Both reactive and active power controllers have same structure, except for the negative sign on the reactive power controller which comes from the reactive power definition. Therefore, only the active power controller's state space model is shown.

The active power equation seen in Chapter 1 (1.6) is linearized as follows:

$$P_{g0} + \Delta p_g = \left(V_{g_d0} + \Delta v_{g_d}\right)\left(I_{s_d0} + \Delta i_{s_d}\right) \tag{2.6}$$

Developing (2.6), neglecting terms of second and higher orders, and deleting steady state in both equation sides, yields:

$$\Delta p_g = \Delta v_{g_d} I_{s_d0} + \Delta i_{s_d} V_{g_d0} \tag{2.7}$$

The state space model of the active power controller is built from (2.7) and Figure 1-15. It is represented by the bloc diagram on Figure 2-4.

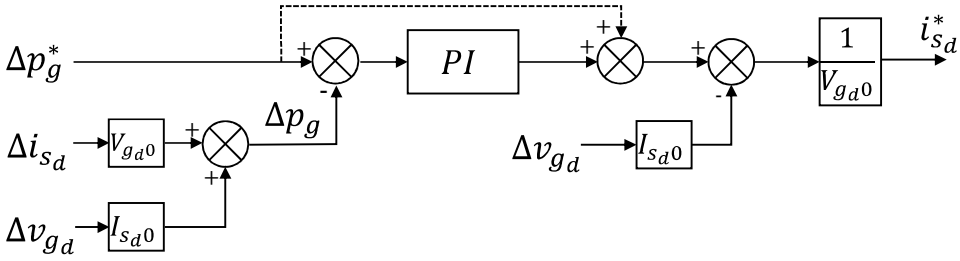

Figure 2-4: Bloc diagram of the linearized active power controller

Validation

In order to validate the state space model of the power controlled VSC, a simulation of the converter connected to an ideal DC voltage source is achieved. The scenario is a step on p_g^* at t = 0.2 s. Results achieved on Matlab/Simulink® for the state space model (State-Space) and on EMTP-RV® for the average model (EMT), are compared in Figure 2-6. Both controller structures are investigated, i.e. the configurations with and without feed forward action.

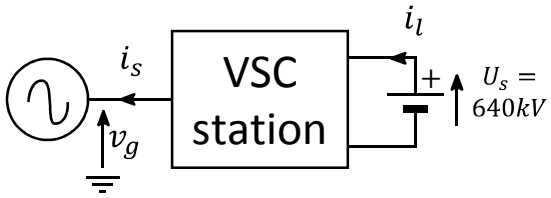

Figure 2-5: Test system used to validate the VSC state space model with power control

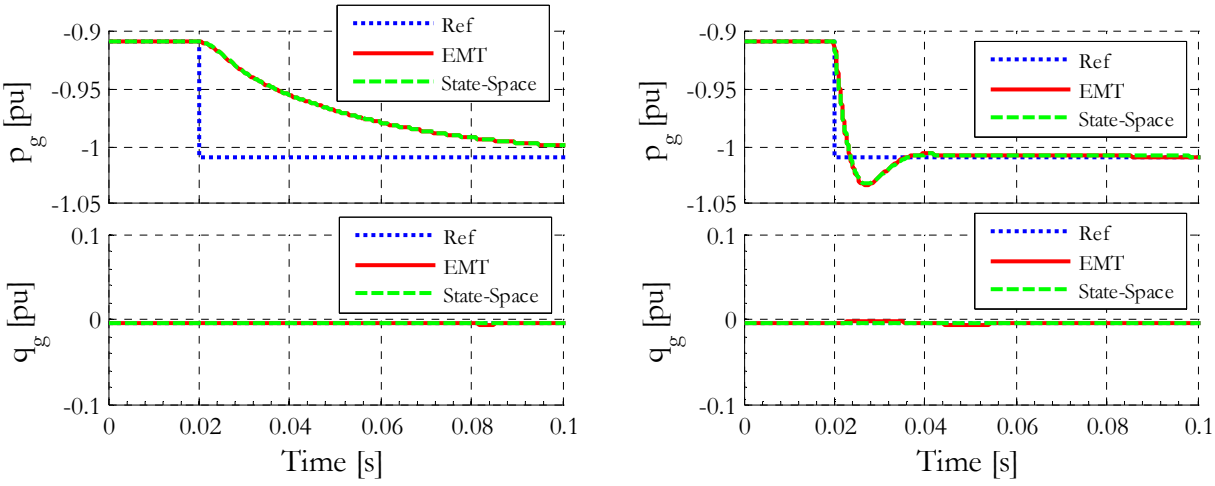

(a) No feed-forward action (b) With feed-forward action

Figure 2-6: State space model validation of the power controlled VSC

There is no notable difference between results from the state space model and from the average model, therefore the power controller state space is validated. Concerning the choice of the controller's structure, the time response with feed forward action is similar to that without feed forward action; the power control dynamics is retrieved in both cases.

2.2.3. Linearization of the DC voltage controller

In this paragraph the DC voltage controller presented in part 1.3.3 is linearized. In this study the DC voltage controller is tuned based on the substation's capacitor which controls the stored energy in the DC side.

Modeling

The model of the DC voltage controller is presented on a converter alone. An IP controller is used instead of a classical PI controller in order to avoid the overshoot when applying a reference step (see Figure 2-7). Either with PI or IP controller the power loop has same polynomial characteristic so the loop's dynamics remains the same.

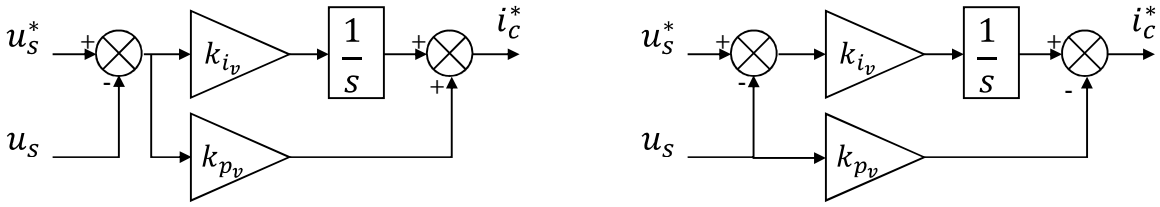

(a) PI controller (b) IP controller

Figure 2-7: Controller's structures

Neglecting the phase reactor and the shunt conductance capacitance losses, AC and DC relations can be written as follows:

$$(I_{m0} + \Delta i_m)(U_{s0} + \Delta u_s) \approx \left(I_{s_d0} + \Delta i_{s_d}\right)\left(V_{g_d0} + \Delta v_{g_d}\right) \quad \textbf{(2.8)}$$

Using the same approach as previously, the DC voltage controller is linearized as shown in Figure 2-8.

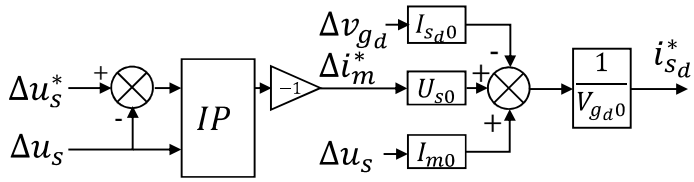

Figure 2-8: Bloc diagram of the linearized DC voltage controller

Validation

To validate the model, an unloaded converter is simulated, i.e. without DC load (see Figure 2-9), a voltage reference step is applied at t = 0.2 s. Time domain simulations are achieved on Matlab/Simulink® for the state space model (State-Space) and on EMTP-RV® for the average model (EMT). Results are compared in Figure 2-10 and Both controller structures are investigated: PI and IP controllers.

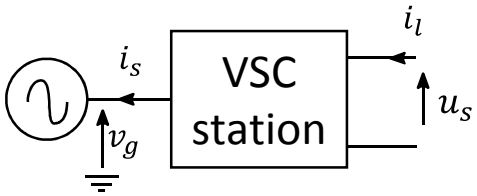

Figure 2-9: Test system used to validate the VSC state space model with dc voltage control

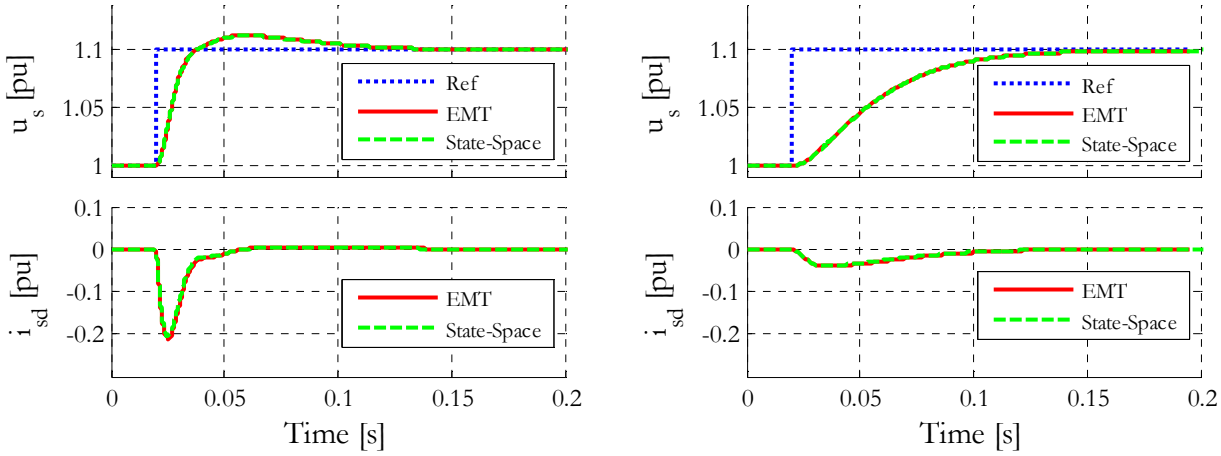

(a) Controller PI (b) Controller IP

Figure 2-10: State space model validation of voltage controlled VSC

There is no difference between results from the state space model and from the average model; therefore the voltage controlled state space VSC model is validated. With PI controller there is an overshoot due to the controller structure which comes from the zero on the transfer function while with the IP the DC voltage reaches smoothly the reference within the wanted time response.

2.3 CABLE MODELLING IN VIEW OF STABILITY ANALYSIS

The main objective of this subsection is to obtain a DC cable model which could be used for small-signal stability studies, i.e. a transfer function. The transfer function order should be accurate enough to represent the cable behavior for a certain frequency range and as simple as possible to not overload the stability analysis and to easily identify the main interactions. In order to achieve accurate results for stability studies, the cable model will be valid from DC to the fastest converter control loops dynamics, i.e. the current control loop dynamics. For converter in the range of hundreds of megawatts, the current loop dynamics is commonly around 10 milliseconds.

2.3.1. Choice of cable technology

Several technologies of cable are available for HVDC transmission [EUR12]:

- Mass Impregnated Cable (MI)

The copper conductor is covered by oil and resin-impregnated paper. This technology is well-known, traditionally used for underground transmission. It is available

for voltages up to 600kV and transmission capacity over 1100MW in one cable. This cable has no length limitation. Thanks to very high oil viscosity, it has no risk of oil leakage. However, it has limited overload capability due to high temperature drift.

- Low pressure oil-filled Cable

The copper conductor is covered by a paper impregnated with low viscosity oil which is conducted through a duct along the cable. This technology is available as well for AC or DC voltages up to 600kV. Its length is limited to 50 km due to oil flow and there is a risk of oil leakage in case of cable damage. This technology is therefore not suitable for submarine cable transmissions.

- XLPE Cable

The copper or aluminum conductor is covered by a solid insulation layer made of cross-linked polyethylene (XLPE). This technology becomes more and more attractive because of its low material and processing costs. The conductor's temperatures can grow up to 90°C without insulation damaging and can run under DC voltages up to 320 kV and transmission capacity over 1000 MW using two cables of inverse polarities. Despite these advantages, due to problem of break down polarity reversal with polymeric insulated cable [HAN03], this cable technology is not used in LCC-HVDC projects. However, with VSC-HVDC transmission scheme the DC voltage is never reversed (except during DC faults), so XLPE insulation cable can be used.

Nowadays, for VSC-HVDC applications and voltages higher than 320 kV, the preferred cable insulation is MI and for voltage lower than 320 kV it is XLPE. Both MI and XLPE cable are expected to increase in voltage and capacity in the near future.

Future long distance undersea VSC-HVDC power transmission will be certainly XLPE insulated cable due to many advantages over MI Cable. Although XLPE can handle lower voltage than MI, cables with XLPE are generally mechanically more robust, quicker to build, lighter which enables to carry longer cable leading to less joints. XLPE cables can operate at higher temperature which allows carrying more current in the same conductor section [ENT11]. In view of that, the choice of cable technology in this study is naturally XLPE. An example of XLPE cable is presented in Figure 2-11.

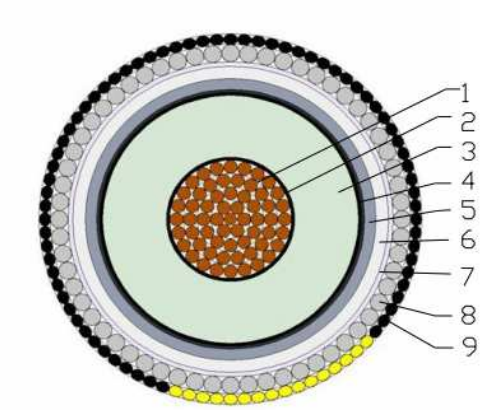

1. Stranded copper conductor, longitudinally sealed
2. Semiconducting tape + extruded layer
3. XLPE based special insulation compound
4. Semiconducting layer + Longitudinal water penetration barrier
5. Lead alloy sheath
6. Polyethylene sheath
7. Polypropylene bedding
8. Galvanised steel wires armour
9. Polypropylene serving

Figure 2-11: Example of single core XLPE Cable cross-section [EUR12]

The cable cross-section shows the different layers which form the XLPE cable. The conductor, which is in this case, a copper conductor could also be aluminum. The insulation and both semiconductor layers are extruded simultaneously, the second semiconducting layer serves as water barrier in case of cable damage. The cable sheath is made of metallic alloy. Additional layers strengthen the cable and provide protection against moisture, abrasions and frictions [EUR12].

2.3.2. Cable data

The cable generation data routine from EMTP-RV software has been used to compute the data for different cable modeling.

The DC link use as reference to justify the modeling is two symmetrical monopoles with shield conductor of a 100 km long, ±320 kV and 1000 MW power transfer capability. The DC cable layout is presented in Figure 2-12, each cable is laid at a depth of 1.33 m and there is a 50 cm space between the positive and the negative cable poles, for thermal reasons. The shield of each cable is grounded at each cable end. In this study the cable model has been simplified, keeping only the conductor, the XLPE insulation and the shield. In the cable generation routine, the conductor section is assumed full instead of stranded, so compared to the real cable with same diameter, Joule losses will be underestimated, however cable capacitance and inductance are similar to the real cable.

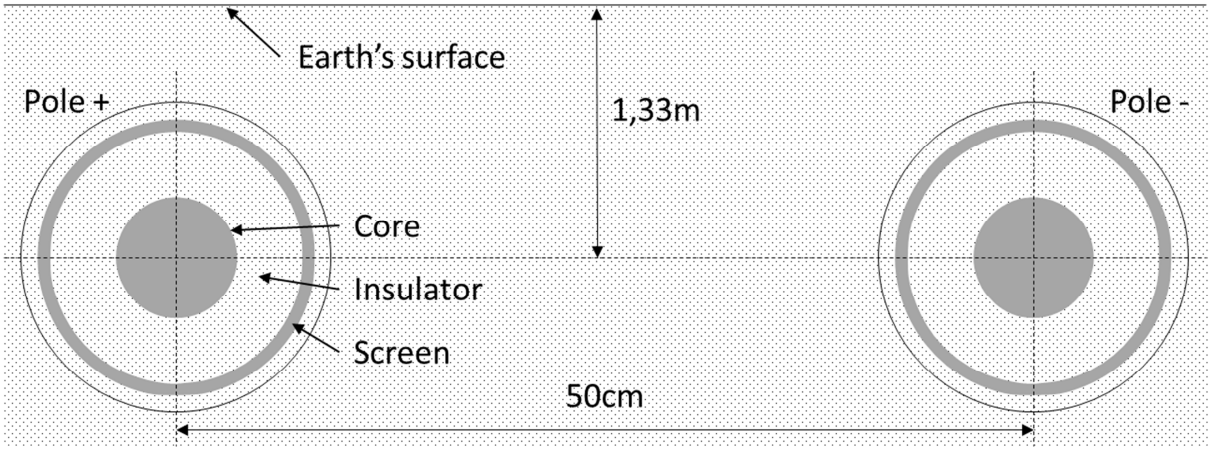

Figure 2-12: Cable layout

The cable model considered as reference is obtained by an accurate frequency dependent model, available in the EMTP-RV library, i.e. WideBand model [KOC08].

2.3.3. Frequency data of the Π model

The objective of this first step is to determine at which frequency the admittance and the impedance matrices of the Π model should be calculated. Admittance and impedance matrices are obtained for different frequencies by using the cable generation data routine from the EMTP-RV software. These matrices are entered in a multiphase Π section, for different frequencies, and compared in the frequency domain to the reference case (i.e Wideband model). The comparison has been done for data calculated at 10 μHz and data obtained at 1 kHz, using the test system of the Figure 2-13. This test system is composed of the 100 km pair of cables which connect, at one end, a 50 μF shunt capacitor equivalent to a VSC DC capacitor, and at the other end, an impedance meter. This device computes the impedance by injecting 1 A at the scanned frequency and measures the voltage between the positive and the negative nodes [EMT12].

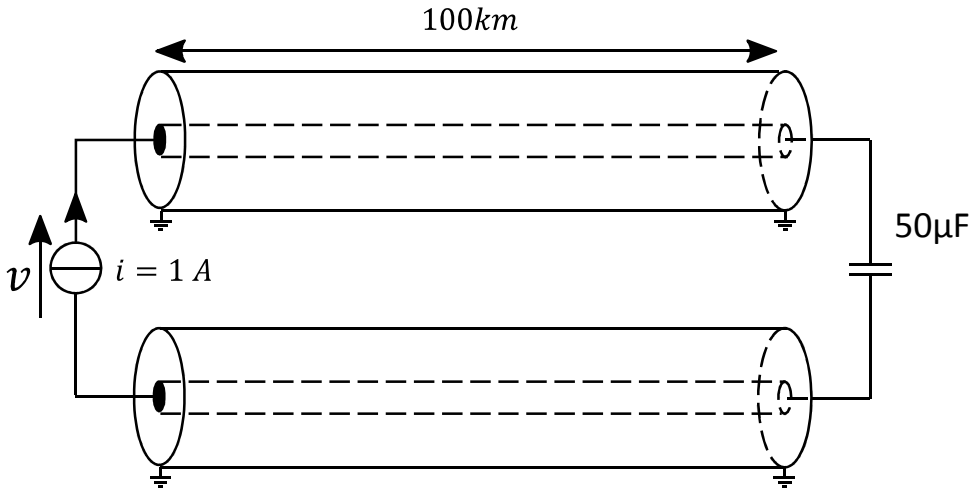

Figure 2-13: Cable impedance measuring system

A frequency scan is achieved with EMTP-RV from 10 μHz (almost DC) to 10 kHz, for the three cables models. The magnitude and the phase of the computed impedance results are compared in Figure 2-14.

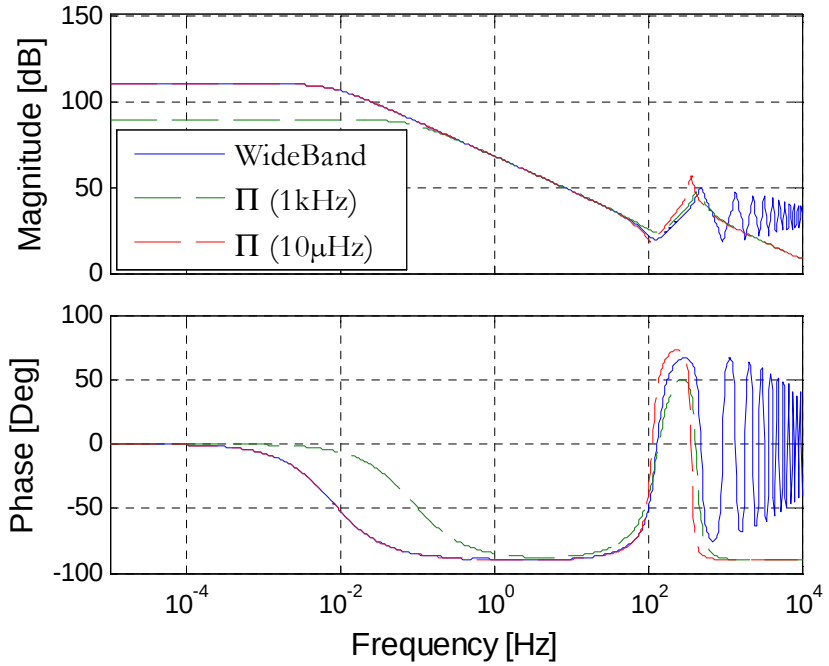

Figure 2-14: Frequency scan – model comparison for data obtained at 1 kHz and 10 μHz

Figure 2-14 shows that the Π model with data obtained at 10 μHz seems more similar to the reference than the one with data obtained at 1 kHz. Indeed, as expected the one obtained at 10 μHz fits the reference case at low frequencies while the other does not, but for frequencies between 1 Hz and 100 Hz the three curves are merged, then for frequencies from 100 Hz to 300 Hz the three curves are quite similar, finally for higher frequencies none corresponds to the reference case. As a conclusion, the frequency range of validity of the Π model obtained at 10 μHz is clearly larger than the one obtained at 1 kHz.

Knowing the fastest control loop is the phase reactor current loop with a time response of 10 ms (i.e. undamped natural frequency around 50Hz), the Π model obtained at 10 μHz is suitable for dynamic studies.

2.3.4. Multiphase Π model simplification

In the previous paragraph, the multiphase Π section model represents all relationships between conductors. Now, the multiphase Π model is simplified in order to reduce the number of state variables in the model.

The classical Π section

The intuitive approximation consists of neglecting the screen and the proximity effects between the two cables, then the cable model is reduced to two classical Π sections, one for each pole (see Figure 2-15a). The line impedance is obtained by the core self-inductance as well as the core resistance, the admittance in each Π section end are the core-screen capacitance and conductance divided by two. The Bode plot of this model is compared to the reference model in Figure 2-15b.

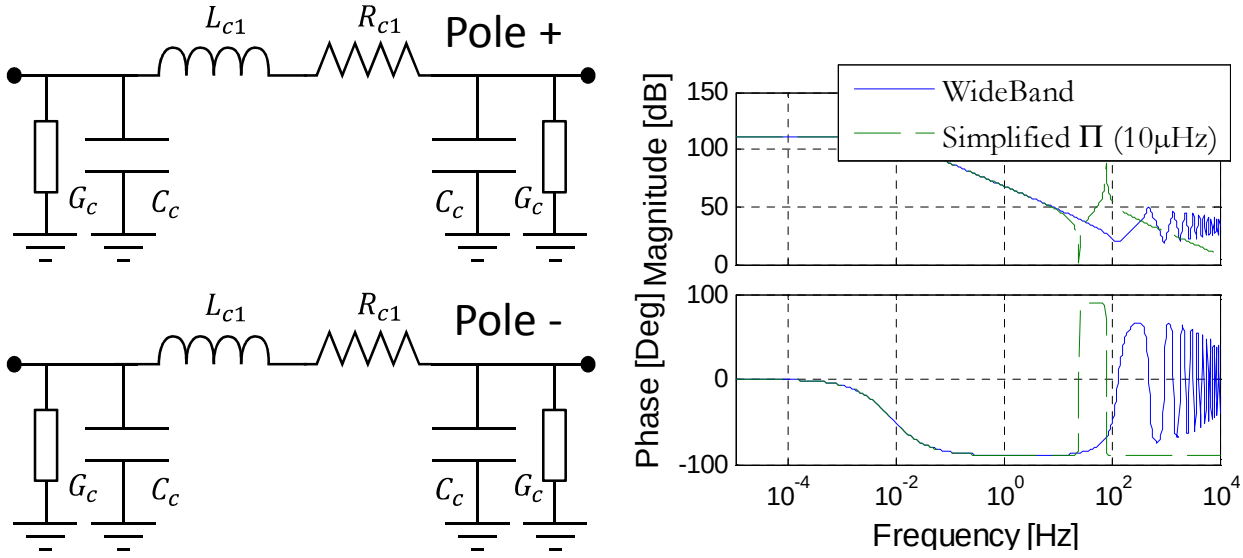

(a) Schematic (b) Bode plot

Figure 2-15: Classical Π section

This frequency scan shows that the first resonance in the classical Π section appears at a lower frequency than the WideBand Model. The Highest frequency limit of model validity is 20 Hz, a too narrow band compared with the current loop dynamics. This model is not acceptable.

The classical Π section with coupling between core and screen

To overcome this problem, a little bit more sophisticated model is introduced. The new simplified model takes into account the coupling between the core and the screen but not the coupling between the two poles. The coupling between the core and the screen is represented by the mutual inductance between these two conductors (see Figure 2-16a). The screen impedance is

composed of the screen self-inductance and its resistance. The Bode plot of this model is compared to the reference model in Figure 2-16b.

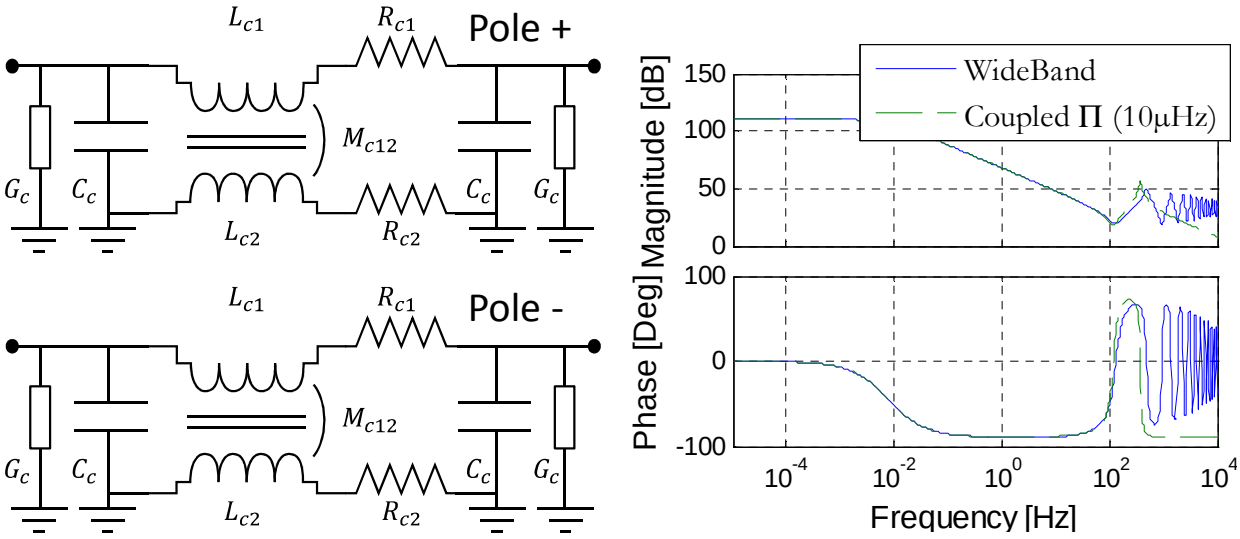

(a) Schematic (b) Bode plot

Figure 2-16: Classical Π section with core and screen modeled

The results obtained with this model are clearly better than with the first model, they are similar to those obtained with the EMTP-RV's multiphase Π section, so there is no important loss of information due to this simplification. Since the model range of validity is equivalent to that of the multiphase Π section, this model can be used for DC stability studies.

Time domain validation

An extra validation was achieved in the time domain in order to compare the results of this two cable models. The simulation consists of two AC-DC converters, connected at the ends of the pair of cables studied until now, one converter controls the DC voltage and the other controls the power flow (see Figure 2-17). The scenario is a change from 50 MW to 0 MW, in the power controlled converter station. Results obtained on EMTP-RV are shown in Figure 2-18.

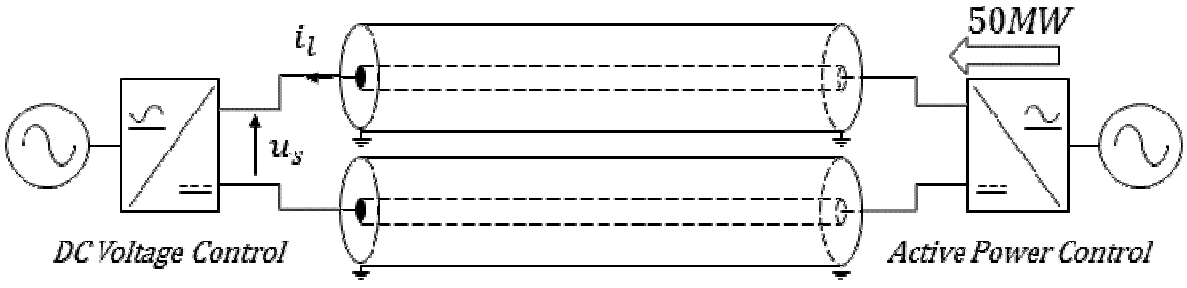

Figure 2-17: Test system for time domain cable modelling validation

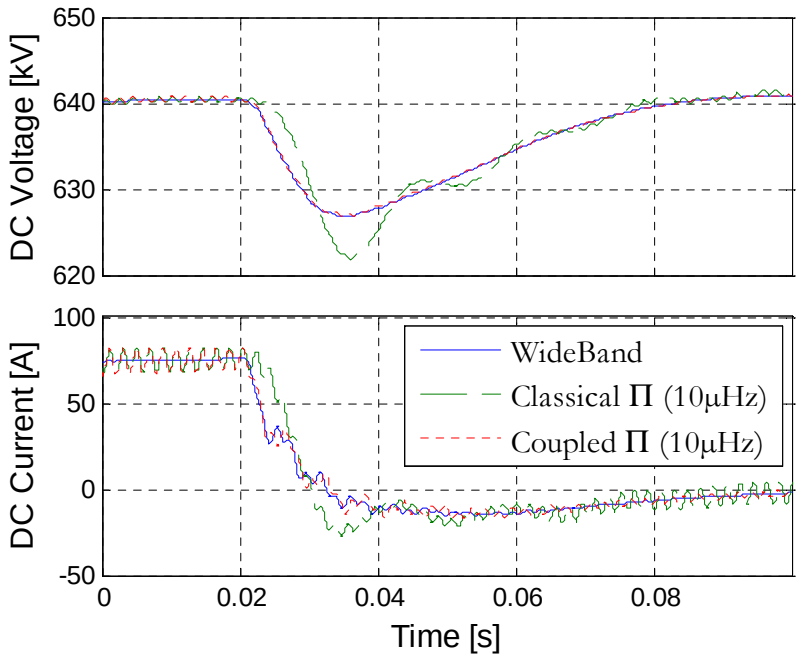

Figure 2-18: Time domain simulation – Drop of power transfer (50MW)

Time domain results confirm that when using classical Π model, there are oscillations which do not exist in the reference model. Using the Π core-screen coupled model the dynamics is close to the reference model except for fast oscillations which are more damped in the reference model.

Π model improvement

The Π core-screen coupled model can be improved by putting in series several cells. As an example, the previous case was simulated with five cells instead of one. Results are visible both in the frequency domain (Figure 2-19a) and in the time domain (Figure 2-19b).

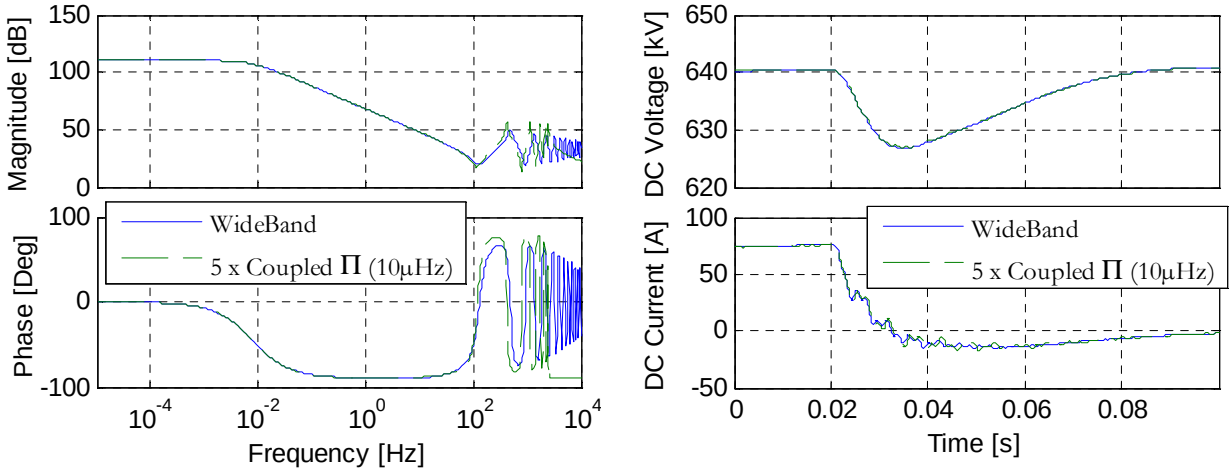

(a) Bode plot (b) Time domain

Figure 2-19: Five classical Π sections with core and screen modeled

As expected, the similarity to the reference model is improved by putting in series Π sections: i.e. the frequency range of validity is increased, and in the time domain fast oscillations are more damped, like the reference model.

2.3.5. State-space modeling of a cable pair

The goal of this subsection is to build a state space model for a pair of cables with opposite DC voltage polarities. To do this, the state space model of one core-screen coupled Π section is first established and then the output voltage is multiplied by two to take into account the two cables. Indeed, if positive and negative poles are supposed to have same length and identical parameters and no asymmetric studies are foreseen. The positive pole of the Π core-screen coupled model is recapped in Figure 2-20 with currents and voltages represented.

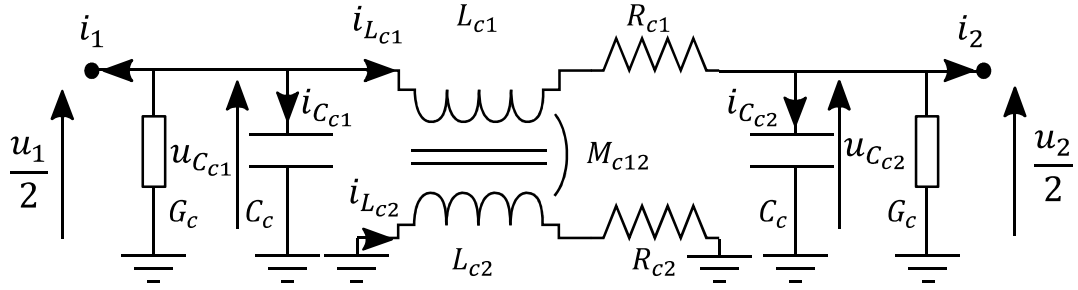

Figure 2-20: positive pole of the Π core-screen coupled model

In the following the state space model of this special Π section is presented. The pole's differential equations are:

$$\frac{du_{C_{c1}}}{dt} = \frac{1}{C_{c1}} i_{C_{c1}} \tag{2.9}$$

$$\frac{du_{C_{c2}}}{dt} = \frac{1}{C_{c2}} i_{C_{c2}} \tag{2.10}$$

$$\phi_1 = L_{c1} i_{L_{c1}} + M_{c12} i_{L_{c2}} \tag{2.11}$$

$$u_{L_{c1}} = \frac{d\Phi_1}{dt} = L_{c1} \frac{di_{L_{c1}}}{dt} + M_{c12} \frac{di_{L_{c2}}}{dt} \tag{2.12}$$

$$u_{L_{c2}} = \frac{d\Phi_2}{dt} = L_{c2} \frac{di_{L_{c2}}}{dt} + M_{c12} \frac{di_{L_{c1}}}{dt} \tag{2.13}$$

Combining (2.12) and (2.13) yields:

$$\frac{di_{L_{c1}}}{dt} = \frac{u_{Lc1}\, L_{c2}}{L_{c1}L_{c2} - M_{c12}^2} - \frac{u_{L_{c2}} M_{c12}}{L_{c1}L_{c2} - M_{c12}^2} \tag{2.14}$$

$$\frac{di_{L_{c2}}}{dt} = \frac{u_{Lc2}\, L_{c1}}{L_{c1}L_{c2} - M_{c12}^2} - \frac{u_{L_{c1}} M_{c12}}{L_{c1}L_{c2} - M_{c12}^2} \tag{2.15}$$

Algebraic equations are as follows:

$$i_{C_{c1}} = -i_1 - i_{L_{c1}} - G_c u_{c_{c1}} \tag{2.16}$$

$$i_{C_{c2}} = -i_2 + i_{L_{c1}} - G_c u_{c_{c1}} \tag{2.17}$$

$$u_{L_{c1}} = -R_{c1} i_{L_{c1}} - u_{C_{c2}} + u_{c_{c1}} \tag{2.18}$$

$$u_{L_{c2}} = -R_{c2} i_{L_{c2}} \tag{2.19}$$

Arranging these differential and algebraic equations yields to a four-order system which represents the pair of cables:

$$\frac{d}{dt}\begin{bmatrix} u_{C_{c1}} \\ u_{C_{c2}} \\ i_{L_{c1}} \\ i_{L_{c2}} \end{bmatrix} = \begin{bmatrix} -\frac{G_c}{C_c} & 0 & -\frac{1}{C_c} & 0 \\ 0 & -\frac{G_c}{C_c} & \frac{1}{C_c} & 0 \\ \frac{L_{c2}}{L_{c1}L_{c2} - M_{c12}^2} & \frac{-L_{c2}}{L_{c1}L_{c2} - M_{c12}^2} & \frac{-R_{c1}L_{c2}}{L_{c1}L_{c2} - M_{c12}^2} & \frac{R_{c2}M_{c12}}{L_{c1}L_{c2} - M_{c12}^2} \\ \frac{-M_{c12}}{L_{c1}L_{c2} - M_{c12}^2} & \frac{M_{c12}}{L_{c1}L_{c2} - M_{c12}^2} & \frac{R_{c1}M_{c12}}{L_{c1}L_{c2} - M_{c12}^2} & \frac{-R_{c2}L_{c1}}{L_{c1}L_{c2} - M_{c12}^2} \end{bmatrix} \begin{bmatrix} u_{C_{c1}} \\ u_{C_{c2}} \\ i_{L_{c1}} \\ i_{L_{c2}} \end{bmatrix} + \begin{bmatrix} -\frac{1}{C_c} & 0 \\ 0 & -\frac{1}{C_c} \\ 0 & 0 \\ 0 & 0 \end{bmatrix} \begin{bmatrix} i_1 \\ i_2 \end{bmatrix} \tag{2.20}$$

$$\begin{bmatrix} u_1 \\ u_2 \end{bmatrix} = \begin{bmatrix} 2 & 0 & 0 & 0 \\ 0 & 2 & 0 & 0 \end{bmatrix} \begin{bmatrix} u_{C_{c1}} \\ u_{C_{c2}} \\ i_{L_{c1}} \\ i_{L_{c2}} \end{bmatrix}$$

The state space model is compared with the equivalent circuit model in the frequency domain in Figure 2-21. Results of both simulations are identical, therefore the model is validated.

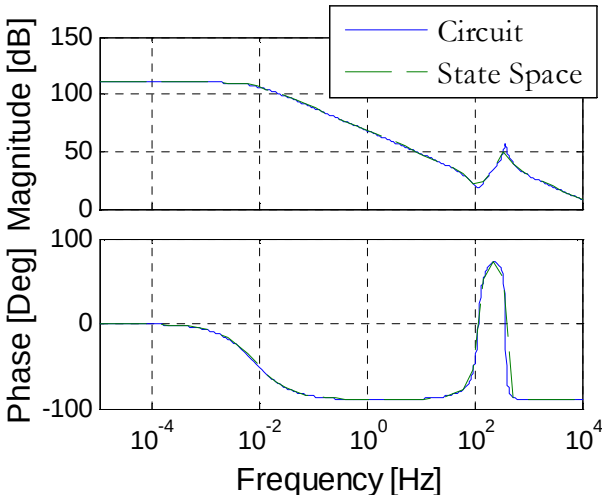

Figure 2-21: Validation of the Coupled Π cable state space model

2.4 STABILITY STUDY ON A HVDC LINK

The VSC-HVDC point-to-point link is one of the DC transmission schemes used today to transport energy over long distances. In this part, a 1 GW, 100 km long DC transmission system is considered. The model of the DC transmission scheme is composed of two VSCs and their controllers and the DC cable model. In [ALS11] and in [VEC11] the authors propose methods to build the whole state space model of a MTDC grid from elementary subsystems.

The DC link studied is shown in Figure 2-22. There is one substation which is power controlled, a pair of DC cables of 100 km long, and at the other end a substation which controls the DC voltage. Between each substation and the DC cable, smoothing reactors are inserted, these are simple inductors in series with the cables, they are used to filter the DC current and protect converters against inrush currents in case of DC fault. In this example, AC grids are supposed to have an infinite Short Circuit Ratio (SCR).

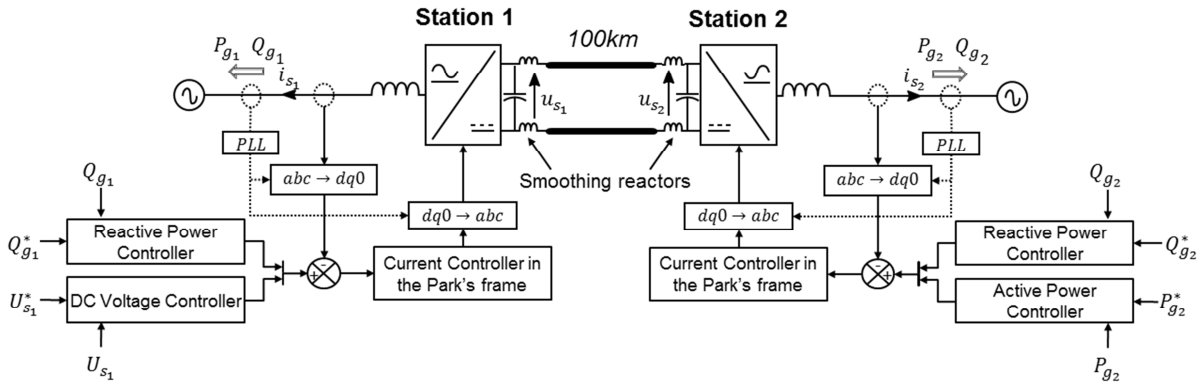

Figure 2-22: Point-to-point VSC-HVDC link

2.4.1. Basic principles of model association

In this part the principle of model association is briefly presented. Two generic subsystems ΣA and ΣB are the parts of the global system Σ. The state space model of ΣA is defined by:

$$\Sigma A = \begin{cases} \frac{d}{dt}\begin{bmatrix} x_{a_1} \\ x_{a_2} \end{bmatrix} = \boldsymbol{A_a}\begin{bmatrix} x_{a_1} \\ x_{a_2} \end{bmatrix} + \boldsymbol{B_a}\begin{bmatrix} u_{a_1} \\ u_{a_2} \end{bmatrix} \\ \begin{bmatrix} y_{a_1} \\ y_{a_2} \end{bmatrix} = \boldsymbol{C_a}\begin{bmatrix} x_{a_1} \\ x_{a_2} \end{bmatrix} + \boldsymbol{D_a}\begin{bmatrix} u_{a_1} \\ u_{a_2} \end{bmatrix} \end{cases} \quad \textbf{(2.21)}$$

And the state space model of ΣB is defined by:

$$\Sigma B = \begin{cases} \frac{d}{dt}\begin{bmatrix} x_{b_1} \\ x_{b_2} \end{bmatrix} = \boldsymbol{A_b}\begin{bmatrix} x_{b_1} \\ x_{b_2} \end{bmatrix} + \boldsymbol{B_b}\begin{bmatrix} u_{b_1} \\ u_{b_2} \end{bmatrix} \\ \begin{bmatrix} y_{b_1} \\ y_{b_2} \end{bmatrix} = \boldsymbol{C_b}\begin{bmatrix} x_{b_1} \\ x_{b_2} \end{bmatrix} + \boldsymbol{D_b}\begin{bmatrix} u_{b_1} \\ u_{b_2} \end{bmatrix} \end{cases} \quad \textbf{(2.22)}$$

In this example, both systems have two inputs, two states variables and two outputs, their state matrices are denoted by the subscript a for the subsystem ΣA and by the subscript b for the subsystem ΣB. In the global system, the inputs of subsystem ΣA are linked to the outputs of subsystem ΣB by:

$$\begin{bmatrix} u_{a_1} \\ u_{a_2} \end{bmatrix} = \boldsymbol{T_{ab}}\begin{bmatrix} y_{b_1} \\ y_{b_2} \end{bmatrix} \quad \textbf{(2.23)}$$

Where $\boldsymbol{T_{ab}}$ is the transfer matrix between the outputs of subsystem ΣB and the inputs of subsystem ΣA. For instance, $u_{a_1} = y_{b_2}$ and $u_{a_2} = 3y_{b_1}$ yield to:

$$\boldsymbol{T_{ab}} = \begin{bmatrix} 0 & 1 \\ 3 & 0 \end{bmatrix} \quad \textbf{(2.24)}$$

In the same way, in the global system, the inputs of subsystem ΣB are linked to the outputs of subsystem ΣA by:

$$\begin{bmatrix} u_{b_1} \\ u_{b_2} \end{bmatrix} = \boldsymbol{T_{ba}} \begin{bmatrix} y_{a_1} \\ y_{a_2} \end{bmatrix} \tag{2.25}$$

Where $\boldsymbol{T_{ba}}$ is the transfer matrix between the outputs of subsystem ΣA and the inputs of subsystem ΣB.

From each subsystem the global system Σ is built as follows:

$$\Sigma = \begin{cases} \dfrac{d}{dt}\begin{bmatrix} x_{a_1} \\ x_{a_2} \\ x_{b_1} \\ x_{b_2} \end{bmatrix} = \boldsymbol{A}\begin{bmatrix} x_{a_1} \\ x_{a_2} \\ x_{b_1} \\ x_{b_2} \end{bmatrix} + \boldsymbol{B}\begin{bmatrix} u_{a_1} \\ u_{a_2} \\ u_{b_1} \\ u_{b_2} \end{bmatrix} \\ \boldsymbol{Y} = \boldsymbol{C}\begin{bmatrix} x_{a_1} \\ x_{a_2} \\ x_{b_1} \\ x_{b_2} \end{bmatrix} + \boldsymbol{D}\begin{bmatrix} u_{a_1} \\ u_{a_2} \\ u_{b_1} \\ u_{b_2} \end{bmatrix} \end{cases} \tag{2.26}$$

The state variables of the global system are the juxtaposition of subsystem state variables. Keeping the order of subsystems arrangement in the global system allows retrieving subsystem state variables in the global system. Inputs are also a juxtaposition of subsystem inputs, even if some inputs may not be useful at all. State space matrices $\boldsymbol{A}$, $\boldsymbol{B}$, $\boldsymbol{C}$ and $\boldsymbol{D}$ are linear combinations of state space matrices of each subsystem. Here, only the constitution of matrix $\boldsymbol{A}$ is presented, the formation of others is based on the same principle (see Appendix E.1). If the direct feed forward matrix $\boldsymbol{D}$ of subsystems is null, then matrix $\boldsymbol{A}$ is defined by:

$$\boldsymbol{A} = \begin{bmatrix} \boldsymbol{A_a} & \boldsymbol{B_a T_{ab} C_b} \\ \boldsymbol{B_b T_{ba} C_a} & \boldsymbol{A_b} \end{bmatrix} \tag{2.27}$$

Diagonal elements are the subsystem $\boldsymbol{A_i}$ matrices, and extra diagonal elements represent the coupling between the subsystems.

2.4.2. Modeling a VSC-HVDC link

Each linearized subsystem of the VSC-HVDC link has already been modeled as state space models in the previous parts. As presented in [VEC11], inputs and outputs of each subsystem are connected together to form a global closed-loop model. The closed-loop model of the VSC-HVDC link is shown in Figure 2-23.

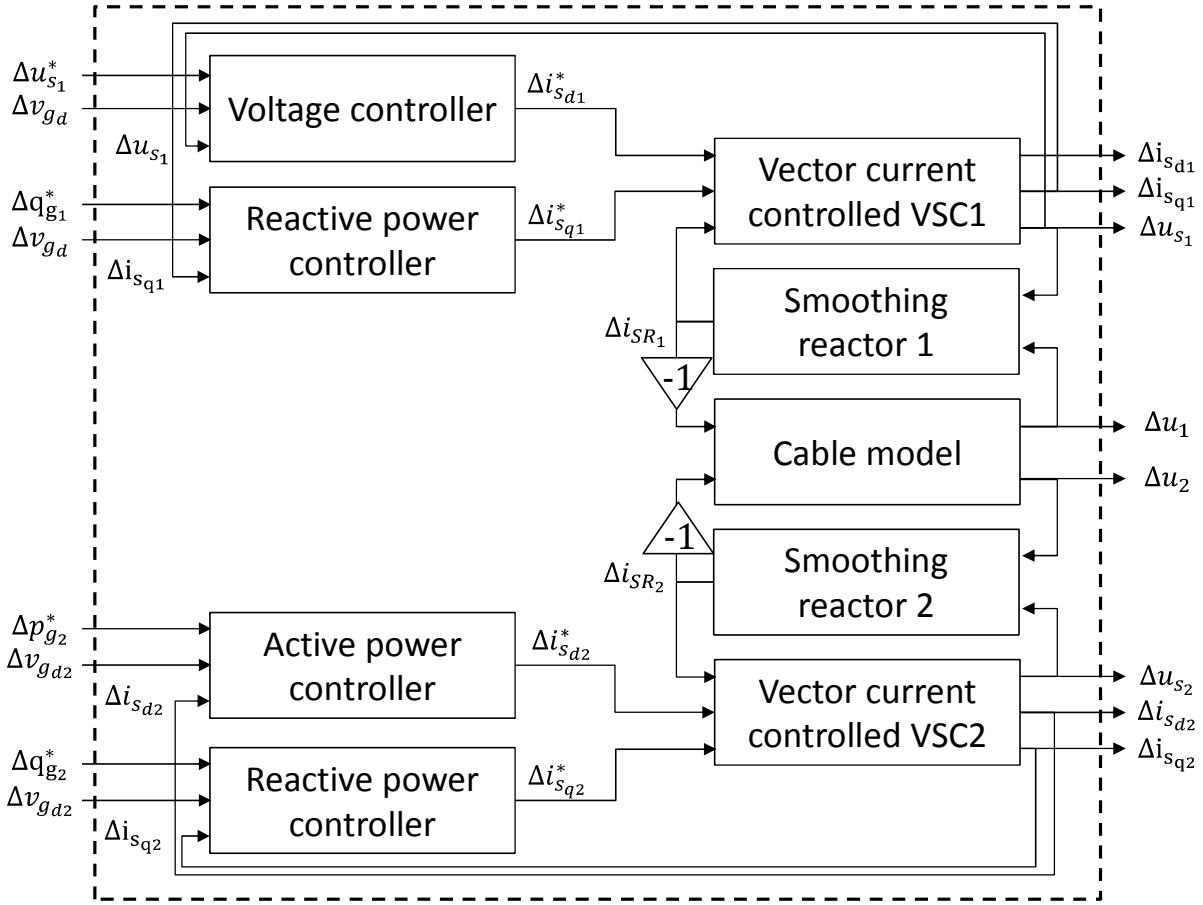

Figure 2-23: Closed-loop model of the point-to-point VSC-HVDC link

A routine based on the method described in 2.4.1 and presented in Appendix E.2, has been used to link the inputs and the outputs of each individual subsystem.

Station controllers are tuned by the pole placement method, current control loops as inner loops are tuned to achieve a response time of 10 ms and outer control loops, i.e. active, reactive and voltage control loops are tuned 10 times slower than inner control loops in order to avoid interactions between the loops. More explanations on controller tuning methods are available in Appendix B.

As mentioned earlier, the state space model is built around an operating point given by EMTP-RV® and the two models (State-Space and EMT) are compared in the time domain, results are displayed in Figure 2-24. Initially the DC link was transmitting 900 MW from Station 2 to Station 1 when applying a reference step of -100 MW at 0.02 s on converter Station 2.

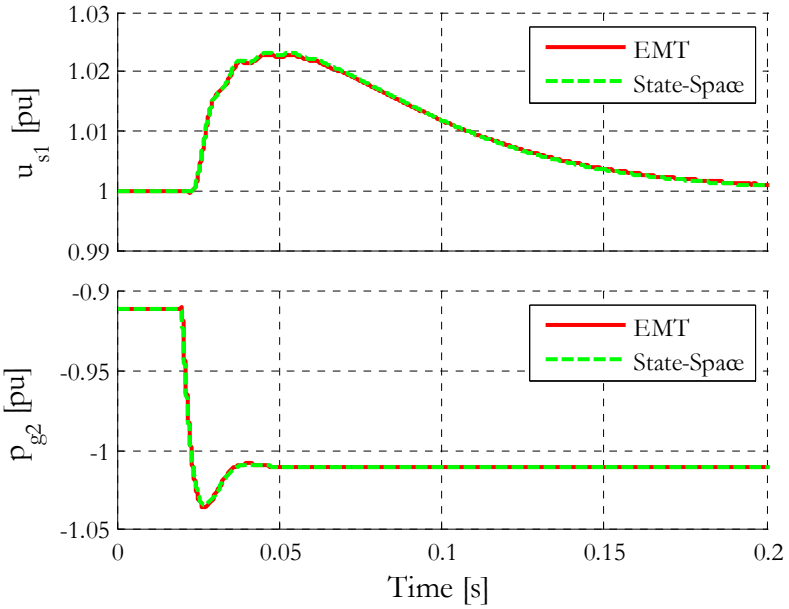

Figure 2-24: State space model validation of the VSC-HVDC link – Reference step of 100MW on Station 2

Results from the average model and the state-space model are similar; therefore the state-space model is validated. When Station 2 changes its power flow, there is an excess of power into the DC cable which leads to an increase of the DC voltage owing to the energy stored in the DC capacitors. Seeing that the DC voltage attempts to grow the DC voltage controller of the first station changes its power flow to maintain the DC voltage at the reference value, this has the effect of balancing the power transfer. The station which is endowed with the voltage regulation is sometimes described as the system slack bus in reference to load flow programs.

2.4.3. Stability analysis of a VSC-HVDC link

Now that the state-space model is built and validated, system roots can be obtained, thus all instruments dedicated to small-signal stability analysis can be employed to characterize and achieve stability analysis on the system.

Modal analysis

Eigenvalues of the state matrix are computed and presented in Table 2-1. Frequency and damping ratios of oscillating modes are also reported in this table. Then, participation factors are used to retrieve physical states which are involved in the participation of the mode. Only, physical states with participation factors above 30% are reported in the table. For more information on physical states nomenclature see Appendix E.5. Finally, using participation factor results, eigenvalues are sorted according to their origin.

Table 2-1: System modes of a VSC-HVDC link

	eigenvalues	Freq.	Damp.	Dominant States		Comment
1	- 60 ± j 4290	682	0.014	Line12_D_uc1 Line12_D_uc2 Line12_D_il1 station1_D_il station2_D_il	0.94 0.94 1.00 0.46 0.46	DC grid
2	-5.4 ± j 3020	480	0.0018	Line12_D_uc1 Line12_D_uc2 station1_D_il station2_D_il	0.89 0.89 1.00 1.00	
3	-71.7 ±j 747	119	0.096	Line12_D_il1 station1_D_us station1_D_il station2_D_us station2_D_il	0.88 1.00 0.46 0.85 0.47	
4	-9.14	-	-	Line12_D_il2	1.00	
6	-193 ± j 238	37.9	0.63	station1_Xid station1_D_isd	0.93 1.00	Station 1
7	-200 ± j 225	35.8	0.67	station1_Xiq station1_D_isq	0.93 1.00	
8	-29.8	-	-	station1_Xq	1.00	
9	-31 ± j 9.51	1.51	0.96	station1_D_us station1_Xiv station2_D_us	0.43 1.00 0.42	
11	-200 ± j 225	35.8	0.67	station2_Xid station2_D_isd	0.93 1.00	Station 2
12	-200 ± j 225	35.8	0.67	station2_Xiq station2_D_isq	0.93 1.00	
13	-29.8	-	-	station2_Xp	1.00	
14	-29.8	-	-	station2_Xq	1.00	

The number of eigenvalues – 20 – is obviously equal to the number of origin states, 8 per converter (i.e. 4 for current control loops, 2 for power or voltage controller, 1 for the substation's DC capacitor and 1 for smoothing reactor) and 4 for the DC cable.

Modes which are classified as DC grid modes are participating in states associated with the DC cable (Line12_D_uc1, Line12_D_uc2 are the states related to the cable end DC voltage, Ligne12_D_il1 is related to the core current and Line12_D_il2 is related to the screen current), states related to the current through the smoothing reactor (station1_D_il and station2_D_il) and then states related to station DC voltage (station1_D_us and station2_D_us). In conclusion, each of these modes involves DC elements. Most of them correspond to complex interactions between DC elements since they are involved in many states.

Modes which are classified as Station 1 modes are the d-axis current control loop mode (6), the q-axis current control loop mode (7), the DC voltage control mode (9) and the reactive power control loop mode (8). Modes related to reactive power control are at the set value given by the pole placement (i.e. 200 ± j 225 rad/s for current loops and -30 rad/s for power loops).

The mode related to d-axis control loop is slightly different from the theoretical, perhaps because of the voltage control loop. According to the pole placement method, eigenvalues of the DC voltage control loop should have been two real eigenvalues at 50 s^{-1} .However, the involvement of Station 2 capacitor and the DC cable capacitors (if the participation threshold of 30 % is decreased, the DC cable capacitor states are observed among dominant states) explains why this mode is not at the expected value.

Modes which are classified as Station 2 modes are the d-axis current control loop mode (11), the q-axis current control loop mode (12), the active power control loop mode (13) and the reactive power control loop mode (14). All these modes are at the set value given by the pole placement (i.e. 200 ± j 225 rad/s for current loops and -30 rad/s for power loops)

As a general comment, modes can be easily sorted because the states the most influenced by them are well split depending on their origin. There is no much interaction between systems since DC cables modes have very fast oscillations with regard to converter modes.

Root locus

As an example a root locus is plotted with the evolution of the current loop time response in Figure 2-25, the whole root locus is plotted in the left side and in the right side there is a zoom corresponding to the doted square in the larger figure. This plot shows the dynamics evolution of the system when the current loop time response changes. In the left figure, roots referred to DC cable are almost not dependent on the current loop time response. In the right figure, as expected, as far as the time response increases the system becomes less damped until falling unstable. The VSC-HVDC link average model was simulated with two different current loop time responses, one at each side of the stability limits. The simulation with time response value corresponding to the root on the right side (i.e. $t_{r5\%}$ =0.34 s) diverges while the one with time response value corresponding to the root on the left side (i.e. $t_{r5\%}$ =0.28 s) is clearly oscillating but finally converges. Calculating participation factors on the unstable mode shows that the voltage control loop is involved in it.

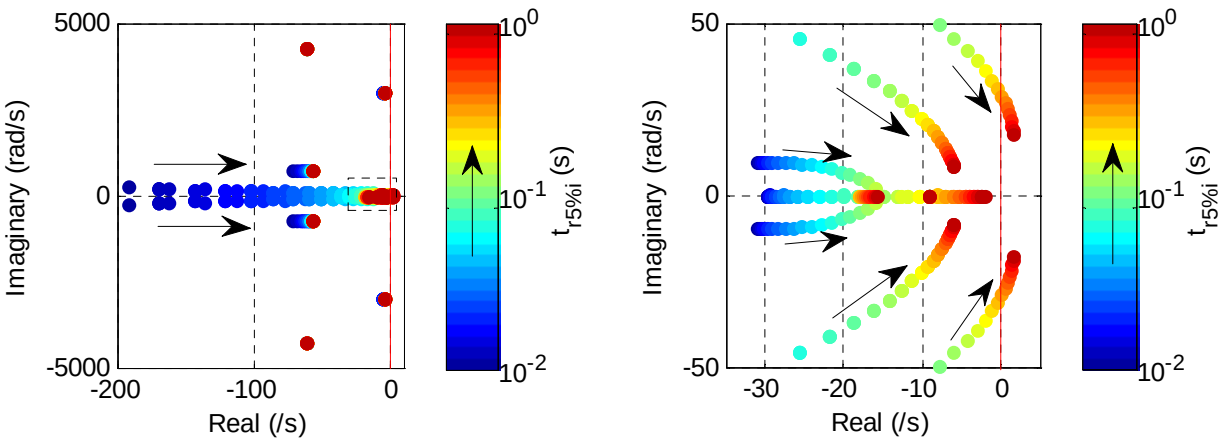

(a) Zoom (b)

Figure 2-25: Root locus of the VSC-HVDC link – evolution with the current loop time response

2.5 CONCLUSION

This chapter has presented and validated mathematical models of VSC-HVDC components and analysis methods on a simple point-to-point HVDC scheme. This chapter has presented basics for DC grid modelling and analysis.

In this chapter, a methodology to build a state space model of a converter and its associated controllers as well as a state space model for a DC cable has been presented. Based on comparison with an accurate cable model, a special Π model has been designed for SSSA purposes; it includes the coupling between the core and the screen conductors. Then, SSSA was achieved on a VSC-HVDC point-to-point link, which enables to retrieve the system's modes and their origin. Finally, an example of root evolution according to the current loop time response was achieved.

As conclusion, for this didactic case study, when studying the VSC-HVDC alone there is no stability problem, except for unrealistic parameters. The matter of this chapter was to bring in the methodological principles on a simple DC system, in order to introduce further studies in multi-terminal DC grids.

CHAPTER 3: Control of an MTDC system

3.1 INTRODUCTION

This chapter is focused on HVDC transmission systems with three to five terminals because they are the most plausible projects in the foreseeable future. As already said in the introduction, as part of TWENTIES project DEMO3, this thesis aims to demonstrate the controllability of MTDC transmissions which connect offshore wind farms to onshore grids. Discussions on control principles are the matter of this chapter.

The first part of this chapter is dedicated to considerations on the DC grid; first of all, actual discussions on the definition of DC grid topologies are presented and then differences and similarities between AC and DC systems are outlined. The second part is a literature review on methodology to control DC grids. The third part emphasizes the general dynamics of the droop controlled DC grid through a simplified analytical approach. In the fourth part, a methodology to size the droop parameter and its consequences are exposed. Finally, the chapter key points are summarized in a conclusion.

3.2 CONSIDERATIONS ON DC GRIDS

3.2.1. Topologies of DC grids

Two kinds of DC grid topologies can be differentiated: radial and meshed grids. Radial grids (see Figure 3-1a) could be an extension of a point-to-point HVDC link. For example, it could be initially an HVDC link which connects a wind farm to the shore, and then the wind farm is connected by another HVDC link to another onshore point. This kind of topology enables to inject wind energy at two different on-shore grid points and power exchange from an on-shore point to the other if the DC transmission line is not fully in used. The main drawback of this topology is that when one of the transmission lines is unavailable, the power cannot be transferred to the corresponding converter. This problem can be avoided by building an additional DC link which leads to a meshed grid (see Figure 3-1b). This topology is more reliable because it enables to operate with a link out of service; the power can be delivered using another path; however its cost is higher.

(a) Radial DC grid (b) Meshed DC grid

Figure 3-1: DC grid topologies

In the Cigré B4.58 working group as well as in the Twenties Work Package WP5, a difference is considered between multi-terminal DC systems (MTDC) and DC grids. A MTDC is defined as a radial DC network, and a DC grid as meshed DC network. The main difference between both systems is the redundancy; a radial DC network cannot operate normally if there is a cable outage while it seems possible with a meshed DC grid, to survive in degraded mode after

a cable loss. In this work, the terminology MTDC and DC grid has the same signification; they are used when there are at least three terminals connected to the DC network.

3.2.2. Analogies between AC and DC system

In this subsection, the similarities and differences between AC and DC systems are pointed out in order to see how already existing control methods used in AC systems could be adapted to the control of a DC system.

AC system dynamics is characterized by the kinetic energy stored in synchronous rotating machines connected to it. For DC systems, the energy is stored under an electrostatic form since it corresponds mainly to the energy stored in converter station capacitors (and in the core-to-screen capacitor of DC cables, to a certain extent):

$$E_c = \frac{1}{2} C_s u_s^2 \tag{3.1}$$

Where:

$\mathrm{u_s}$ is the DC voltage [V]

$\mathrm{C_s}$ is the converter station capacitor value [F]

E_c is the energy stored in a converter station capacitor [J]

The DC grid power mismatches lead to charging or discharging capacitors, which results in modification of the DC voltage level. The same phenomenon exists in AC systems, power imbalances lead to speed variation of electrical rotating machines and thus the frequency. This signal has been used by several generation units to adjust their power reference in order to reestablish the power balance between production and consumption. Similarly, the power balance of the DC grid could be achieved by controlling the DC voltage level.

In power systems, the inertia of a synchronous machine is commonly defined by an inertia constant (H) to normalize the kinetic inertia of each generator with respect to its nominal power [KUN94], thus it can be possible to compare units with different ratings. The same philosophy could be applied to DC systems; the electrostatic energy stored in the substation's capacitor can be weighted by the substation base power. This leads to an electrostatic constant which is homogeneous to a time:

$$H_c = \frac{\frac{1}{2} C_s u_s^2}{P_{base}} \tag{3.2}$$

Where:

P_{base} is the base power of the converter station [W]

H_c is the electrostatic constant [s]

Thanks to the electrostatic constant, the converter station energy can be compared to the kinetic inertia of conventional rotating units. The numerical application on leading HVDC converter stations [JAC10] leads to an electrostatic constant close to 30-40 ms (i.e. 30-40 kJ/MVA) which is a very small value compared to conventional unit inertia constant (i.e.

3 s for hydropower plants, 2.5 s to 10 s for thermal power plants and several seconds for nuclear power plants [KUN94]).

Looking at the energy stored into the whole AC grids, it is the sum of all energy stored in rotating machines. The stored energy compared to the transmitted power drives the evolution speed when the system is subject to a disturbance. Therefore, in continental AC systems, AC grids are connected together to share the primary reserve and to make the overall system stronger. Thus, the sudden loss of one element has a small impact on the grid behavior. In islanded AC networks, there are considerably less generation units so the loss of one element leads to higher variations even if their size is relatively smaller than in the case of continental grids. In such networks, the frequency is more volatile than in huge AC systems such as the pan-European grid. In terms of number of connection points, a DC network could be assimilated to an islanded system. Since the energy stored in this system is very small, the voltage may be extremely volatile. To control the voltage level, it is necessary to have a very high speed closed system for the voltage control which is allowed by the fast dynamics of the power electronic converters.

The analogy between of AC and DC systems is summarized in Table 3-1. In this table quantities in the AC system are associated to their DC system counterpart.

Table 3-1: Analogy between AC and DC systems [BAR10]

AC	DC
Frequency ω	DC voltage level u_s
Impedance of connection X	Resistance of connection R
Active power transfer $\frac{V^2 \sin(\delta)}{X}$	Power transfer $u_s \frac{\Delta u_s}{R}$
Constant of mechanical inertia $H = \frac{1}{2} J \frac{\omega_{base}^2}{S_{base}}$	Electrostatic Constant $H_c = \frac{1}{2} C_s \frac{U_{s\,base}^2}{P_{base}}$

3.2.3. Voltage drops across the cable

In AC grids, the system frequency is common everywhere while for DC systems the DC voltage map is not uniform because of DC cable resistance. Figure 3-2 shows the DC per unit voltage drop across the cable as a function of the cable length at nominal power. This pair of cables has already been presented in Chapter 2, i.e. ±320 kV – 1000 MW symmetrical monopole application. The cable conductor is annealed copper with a section of 2500mm², its resistivity changes with the conductor's temperature. The EMTP-RV cable data generator handles only solid conductors while the cable core is stranded, this explains why the cable model described in Chapter 2 presents a core cross-section of 3200 mm² instead of the 2500 mm² given by the manufacturer. Numerical application results are displayed in Figure 3-2 for four different resistances: three resistances based on a 2500 mm² section and calculated at different temperatures and the resistance obtained from the EMTP-RV cable model generator. As a result, the voltage drop at nominal power transfer is less than 1% for a cable length lower than 300 km.

It should be noted that even if the cable resistance of the cable model is underestimated, the difference is not important with respect to the study objectives.

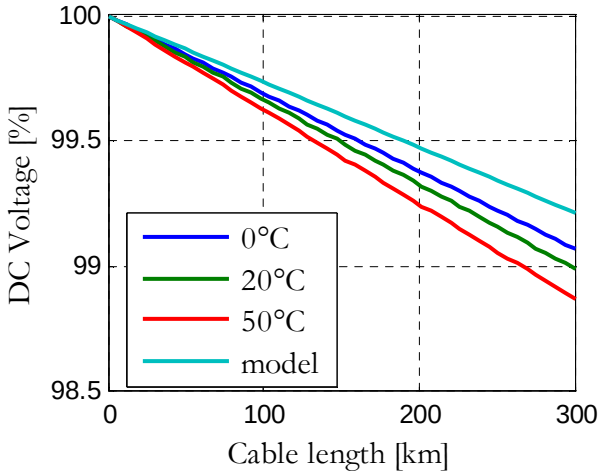

Figure 3-2: Voltage drop at nominal power as a function of the cable length

(XLPE cable – ±320 kV – 1000 MW)

3.3 LITERATURE REVIEW ON PRIMARY CONTROL METHODS

To date, various strategies have been investigated in the literature to control MTDC grids, since this is also the main subject treated when talking about MTDC. These methods are local (i.e. at converter station level) and autonomous, i.e. do not rely on communication. Thus, these methods are able to react quickly in case of network event and they can operate properly in case of a communication failure. In the literature, they are often referred to as primary DC voltage control methods in reference to the primary frequency control which maintains the balance between production and demand in AC grids. The time frame of this control starts from the converter control outer loop response time (around 100ms) to several seconds.

In the literature, to balance the power DC flows, some papers are dealing with DC current based control [BAR10] and the majority with power base control. In [BEE13] there is a discussion on that topic, the author compares both strategies. As results, differences are almost hidden by the line thickness. The author argues that DC current control is more linear since the DC voltage deviation is directly proportional to the current deviation due to the inherent capacitor relationships, and that power control is more intuitive for TSO and can be directly implemented with basic converter control. The author did not say if he was in favor of one solution. From a power system point of view, it seems better to consider the power based control option since matters of exchange are MWs.

Two control method philosophies are distinguishable in the literature for the voltage control. These methods are either based on the Master-Slave method or on the Voltage Droop method. The first category is when only one converter is controlling the DC voltage at any given time. The second category is when more than one converter is controlling the DC voltage at the

same time. These control methods are illustrated below by the means of a simple scenario on a three-terminal DC grid presented in the next subsection:

3.3.1. Test system

The objective of this paragraph is to provide a common case study to distinguish control methods. This test system is composed of three converter stations, two stations are onshore and one is offshore. The two onshore stations are rated at 1500 MW and are directly linked by a 75 km long DC cable. A 800 MW offshore wind farm is connected to the two onshore stations. The topology of the DC grid test system is presented in Figure 3-3.

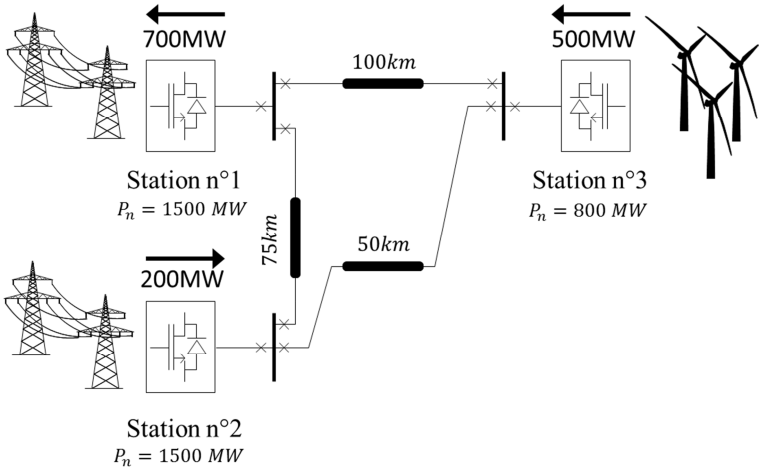

Figure 3-3: Three terminal DC grid test system

The control must achieve:

- the wind farm power transfer to the on-shore grid,
- a power transfer between the two on-shore injection points.

Control methods are assessed on a common scenario. For all cases, the initial operating point is the same, the wind farm is producing 500 MW and the power transfer between the two on-shore converter stations is 200 MW. All the wind power is supposed to be transmitted to Station 1.

Converter stations are symmetric monopolar VSC stations with a nominal DC voltage of ±320 kV. Their DC capacitors are sized in order to have an electrostatic constant equal to 10.24 ms (obtained from a station of 1 GW which has a DC capacitor of 50 μF). They are connected by three ±320 kV pairs of DC cables. Cable lengths are reported on Figure 3-3. Converter station parameters are summarized in Table 3-2.

Table 3-2: Three-terminal DC grid – converter stations parameters

	Nominal DC voltage [kV]	Nominal power [MW]	Operating point [MW]	DC capacitor value [μF]
Station 1	±320 kV	1500	700	75
Station 2	±320 kV	1500	-200	75
Station 3	±320 kV	800	-500	40

The simulated scenario used to assess control methods performances is a sudden 140 MW wind power decrease. This event may occur when a feeder breaker trips in the wind farm.

3.3.2. Master-Slave method

The Master-Slave method is a simple extension of the existing control method used to control point-to-point HVDC links (see part 1.2.3). Indeed, there is only one converter controlling the DC bus voltage to a constant value and the others are controlling their power they inject into (or absorb from) the DC grid. With this method the power balance is achieved by only one converter, therefore the AC grid connected to this substation has to be strong enough to accommodate with such power variations. Furthermore in case of this particular substation failure, the DC system collapses.

This control method should be well adapted to the connection of several wind farms to the AC mainland grid at a single injection point, since each offshore wind farm injects all the power harvested by its wind turbines into the DC grid while the on-shore station absorbs all the power delivered by wind farms.

To illustrate this method, the test system presented in part 3.3.1 is considered. Station 1 is controlling the DC voltage and Station 2 and Station 3 are controlling their power flow. Operating principles are reported in Figure 3-4, as PV characteristics. In this figure, the initial operating point is given by the orange crosses. Following the wind farm feeder outage, the power delivered by the wind farm is 360 MW, this loss of production is only withstood by Station 1 whose power flow is decreasing from 700 MW to 560 MW. Moreover, the DC voltage remains at the previous level because it is stiffly controlled by Station 1. The new operating point is represented by purple circles in Figure 3-4.

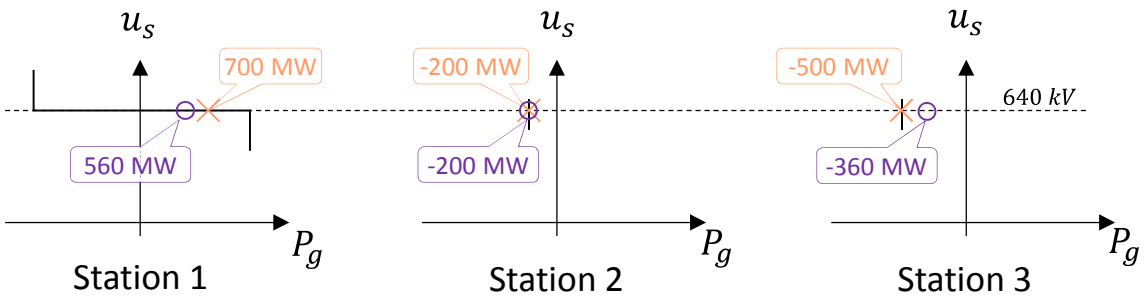

Figure 3-4: PV characteristics with the master-slave method

3.3.3. Voltage Droop method

The voltage droop method is inspired by the primary frequency control [BAR10]. In AC systems, to maintain the balance between production and demand, some production units are equipped by a controller which regulates their output power according to the frequency by following a power-frequency characteristic which is commonly called droop control. As said in the previous section, the frequency counterpart in the DC system is the DC voltage level, hence following the same principle the power flow can be controlled by a PV droop (i.e. power-voltage droop):

$$\Delta p_g = \frac{1}{k}\Delta u_s \tag{3.3}$$

Where:

k is the droop value [V/W] or [pu/pu]

Δp_g is deviation of power injected into the AC grid [W] or [pu]

Δu_s is deviation of DC voltage [V] or [pu]

This method increases the reliability and reduces the stress on the DC system, however, due to the proportional controller, the DC voltage level is not strictly maintained at a constant value. Hence, like for AC system, an additional control is needed to restore the system at the nominal values after a change occurred in the DC system. This is the matter of Chapter 5.

This control method should be well adapted to larger DC grids since the power balance is achieved by several stations. Furthermore, this method is interesting when there are several connection points to mainland grids, because the power could be split into these different injection points.

The portion of the power deviation which is flowing through a converter station is defined by its droop value (for instance k=0.02 kV/MW) with regard to the droop value of other converter stations. For example, if the droop value of a first station is twice the droop value of a second station, the portion of a power deviation which flows through the first station must be half the amount of the second station.

To illustrate this method, the test system presented in part 3.3.1 is considered. Station 1 and Station 2 are endowed with the droop control while Station 3 is controlling its power flow. Operating principles are reported in Figure 3-5, as PV characteristics. In these PV characteristics initial operating points are given by the orange crosses. These operating points are indicative; they do not take into account the DC grid losses and the cable voltage drops.

Following a feeder outage in the wind farm, the power delivered by the wind farm is 360 MW ($p_{g_3} = -360\ MW;\ \Delta p_{g_3} = 140\ MW$). This loss of production is equally shared between the two on-shore converter stations since they have the same droop value:

$$p_{g_1} = p_{g_{10}} + \Delta p_{g3}\frac{k_2}{k_1 + k_2} = 700 - \frac{140}{2} = 630\ MW$$

$$p_{g_2} = p_{g_{20}} + \Delta p_{g3}\frac{k_1}{k_1 + k_2} = -200 - \frac{140}{2} = -270\ MW$$

Since the PV characteristics of the droop controlled stations are slopes, changing the power operating point leads to a change of the DC voltage operating point too. In this case, the DC voltage level is lower since there is less power transfer with regard to the previous operating point. Considering that the slope is defined in per unit by the k coefficient, a change of 70 MW on Station 1 leads to a voltage deviation of:

$$\Delta u_s = 70\ MW \times 0.02 = 1.4\ kV = 0.002\ pu \tag{3.4}$$

The new operating point is represented by purple circles in Figure 3-5.

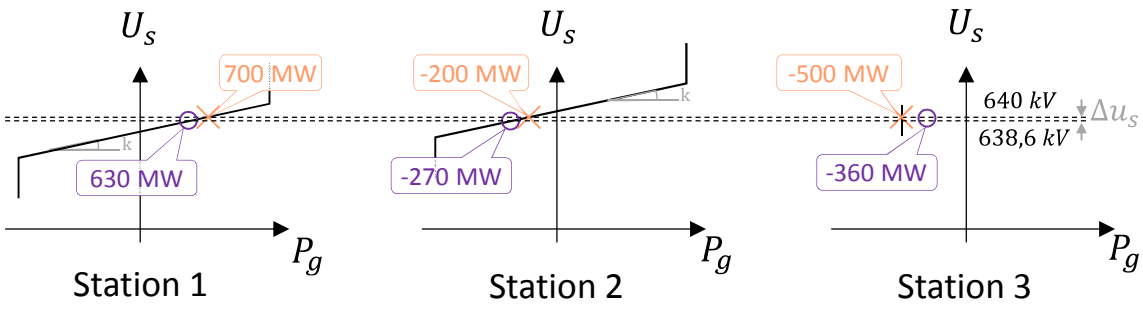

Figure 3-5: PV characteristics with voltage droop method

3.3.4. Variant control methods

Following control strategies arise from the master-slave and the voltage droop methods:

Voltage margin method

The voltage margin method can be considered as an extension of the master-slave method: the master role may be successively devoted to different substations depending on the level of power in each station. This method was first introduced in [SAK83] and then by [NAK99] for LCC based MTDC. Then this method has been tested in a three terminal back-to-back prototype based on GTO converters [SEK00]. Finally, this method is introduced for the control of a VSC MTDC grid in [HAI08a]. Fake power limits are introduced in PV curves to define the power sharing.

This control method may be used as backup system, i.e. the slack role is changed when the substation, which controls the DC voltage, reaches its power limits. This method might not be suitable for large DC grids because, at any given time, only one converter is controlling the DC voltage.

To illustrate this method, the test system presented in part 3.3.1 is considered. Station 1 and Station 2 are endowed with step-form PV characteristics while Station 3 is controlling its power flow. Operating principles are reported in Figure 3-6, as PV characteristics. In this figure the initial operating point is given by the orange crosses.

Following the feeder outage in the wind farm, the power delivered by the wind farm is 360 MW.

1. Before the event, Station 1 was controlling the DC voltage
2. Station 1 controls the DC voltage from 700 MW to 600 MW trying to balance the DC grid power,
3. Then it stops controlling the DC voltage, the DC power balance is in deficit of 40 MW, and therefore the DC voltage starts to decrease.
4. The DC voltage level reaches the Station 2 DC voltage threshold (e.g. 0.95 pu). Station 2 starts controlling the DC voltage and successfully recover the DC grid power balance.
5. The power balance is reached; Station 2 is controlling the DC voltage and the power injected on the DC grid is increased from 200 MW to 240 MW.

The new operating point is represented by purple circles in Figure 3-6.

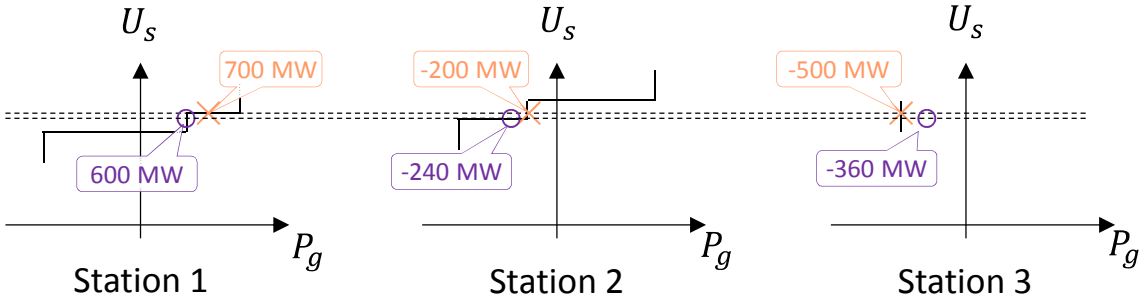

Figure 3-6: PV characteristics with voltage margin method

Dead band droop method

The dead band droop control is a mix between the voltage margin method and the droop voltage method [DIE12]. With low power deviations the balance role is assumed by the stations which are classically droop controlled, but for severe deviations, when the DC voltage reaches a first critical limit, stations which were initially constant power controlled switch to droop control to support the DC voltage and contribute to the balance effort. This method is well adapted for wind farms, in this way the wind farms produce power delivered by wind in normal operation and help to the power balance when the DC voltage is outside the bounds.

To illustrate this method, the scenario presented in part 3.3.1 is tested with the droop control method. Station 1 and Station 2 are endowed with the droop control while Station 3 is controlling its power flow with a dead-band droop control. There is no change, except that Station 3 controls the DC voltage if it exceeds the bounds. Operating principles are reported in Figure 3-7, as PV characteristics. Following the wind farm feeder outage, the operating points are the same as in section 3.3.3, because the voltage bounds are not exceeded. If the voltage level has grown over the maximal voltage limit, then the wind farm would have decreased its power flow. For instance, if Station 1 trips the wind farm can help Station 2 to control the DC voltage by decreasing its power (blue diamond).

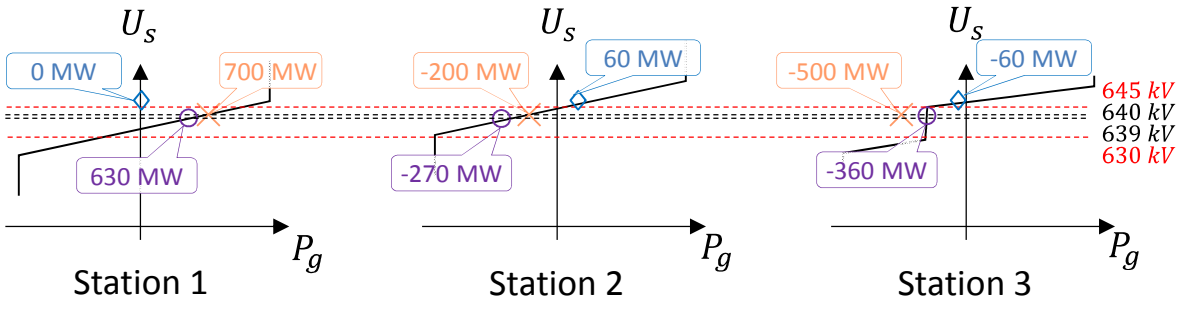

Figure 3-7: PV characteristics with dead-band droop method

Piecewise droop method

The piecewise droop method is also called undead-band droop control and has firstly been presented in [VRA12]. This method is based on piecewise droop characteristics; it enables to define different droop values according to the voltage level, i.e. for small and large power deviations. This method seems interesting for on-shore converters, since the DC voltage operating range can be limited.

To illustrate this method, the scenario presented in part 3.3.1 is tested. Station 1 and Station 2 are endowed with the droop control while Station 3 is controlling its power flow. Within a defined DC voltage interval (from 638 kV to 643 kV) the droop value is set to the same value as in section 3.3.3. When running out this interval and exceeding the upper threshold the droop values are set lower in order to limit the voltage deviation. Operating principles are reported in Figure 3-8, as PV characteristics. Following the feeder outage in the wind farm, the operating points are the same as in section 3.3.3, because voltage thresholds are not exceeded. If the voltage level was over the high voltage threshold, Station 2 would control the DC voltage with a lower voltage deviation than within the thresholds with regard to the same power deviation. For instance, if the wind farm station is lost, Station 1 and Station 2 have the same power flow as if the same droop was used since they have same droop value for a given voltage, see blue diamond on the figure. However, the DC voltage would be 637 kV instead of 635 kV if the same droop value was used.

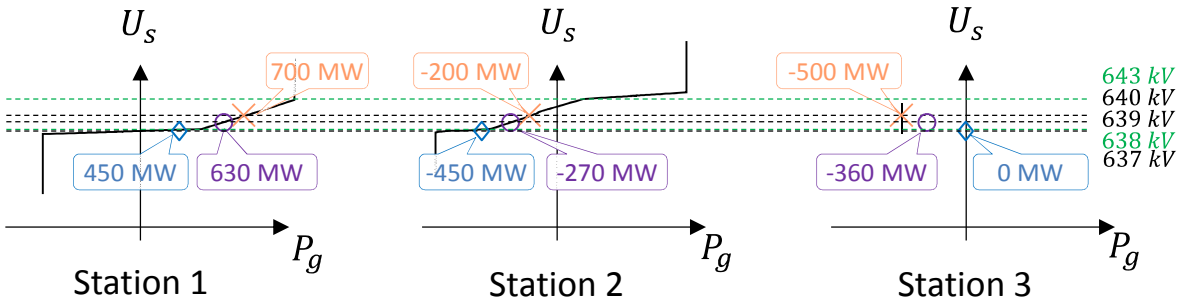

Figure 3-8: PV characteristics with piecewise droop method

3.3.5. Conclusion on primary control methods

In this part, MTDC control methods found in the literature have been presented. There are two operation modes: the normal operation with small power deviations and emergency situations with larger deviations. For normal operation, the voltage droop method presents good performances in respect to power transmission applications. Indeed, the abilities of this method are similar to the primary frequency control in AC systems, such as smooth control and power sharing among different converters. For abnormal operation, variant control methods seem interesting since they allow different control modes adapted to the DC grid situation. All in one, variant control methods are classical methods with back-up ability.

3.4 DYNAMIC BEHAVIOR OF DROOP CONTROLLED DC GRIDS

The aim of this subsection is to understand the general behavior of the DC grid when it is droop controlled. In [XU09], the DC voltage closed loop transfer function is obtained by simplifying the DC grid model as an equivalent capacitor and by neglecting the current control loop dynamics. This transfer function is obtained when only one converter is endowed with a droop controller. In this work, the DC system is simplified as much as possible to keep only the general behavior. Firstly the droop controlled converter station model is simplified, secondly by the way of an example based on the three-terminal DC grid, a simplified MTDC model is obtained and finally this model is generalized for any other multi-terminal droop controlled DC grid.

3.4.1. Voltage droop controller

As mentioned in section 3.3.3, each converter station endowed with DC voltage droop control adjusts linearly its power flow according to the voltage level to share the DC grid power mismatch. The voltage droop controller presented in Figure 3-9 allows the voltage source converter to follow the PV droop characteristics. The power deviation ($\Delta p^*_{DC\,g}$) is stemmed from the DC voltage deviation. Indeed, multiplying the inverse of the voltage droop parameters (k) by the difference between the measured DC voltage (u_s) and the DC voltage set point (U^*_{s0}) leads to a power deviation. The VSC power reference (p^*_g) is the sum of the power set point (P^*_{g0}) and the power deviation ($\Delta p^*_{DC\,g}$). In practice the power set point (P^*_{g0}) and the voltage set point (U^*_{s0}) are given by a DC grid supervisor which calculates appropriate set points for all converter stations to achieved a desired power flow. Therefore, just after the supervisor had sent set points, the steady-state measured voltage and power must be at the reference values if the system has not evolved and set points have been correctly calculated. In this condition, the power deviation ($\Delta p^*_{DC\,g}$) must be a null value.

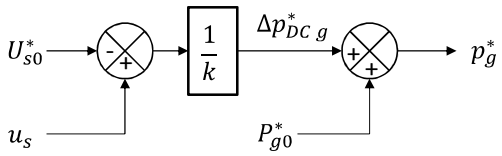

Figure 3-9: DC voltage droop controller

3.4.2. Simplified model of a voltage droop controlled VSC

The model of a voltage droop controlled substation is simplified in order to keep the essential with regards to the voltage control. The general model of a substation given in Chapter 2 part 2.2 has been simplified as follows:

- Suppression of all parts related to reactive power control
- The dynamics of the current loops are neglected, set at unitary gain
- The phase reactor resistance and reactance are neglected therefore the active power at the PCC becomes equal to the active power at the converter side.

Figure 3-10 displays the small signal model of a voltage droop controlled VSC considering aforementioned assumptions. Quantities denoted with asterisk superscript refer to reference sent by the coordinated control system of the DC grid. The DC voltage and the power reference are defined in per unit with regards to the converter base. Quantities which are into the dashed border zone are SI quantities while the outside quantities are in per unit of the converter base.

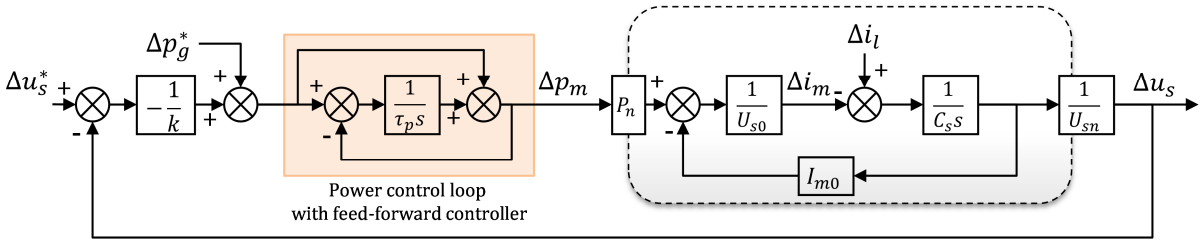

Figure 3-10: Simplified model of a droop controlled VSC station

In the particular case where the converter station is not connected, the steady state DC current (I_{m0}) as well as the load current (i_l) are null. In this condition:

$$\frac{\Delta u_s}{\Delta u_s^*}(s) = \frac{1 + \tau_p s}{\left(1 + \tau_p s\right)\left(1 + \frac{k\, U_{s0}\, U_{sn}\, C_s}{P_n}\right)} \tag{3.5}$$

Where:

Δu_s is the DC voltage deviation [pu]

Δu_s^* is the DC voltage set point deviation [pu]

P_n is the nominal active power of the ith substation [W]

k is the droop parameter of the ith substation [pu]

U_{s0} is the operation point DC voltage [V]

U_{s_n} is the nominal DC voltage [V]

C_s is the converter station DC capacitor value [μF]

τ_p is the time constant of the power loop [s]

Even if this transfer function has two poles, one is compensated by the zero, so the DC voltage control dynamics is similar to a first order transfer function. In fact owing to the simplification of the current control loop, as presented in Figure 3-10, the power controller has no action in the voltage control loop since the output is equal to the input due to the feed-forward action. Thus, in this case, the power control loop can be neglected too.

3.4.3. Application to the three-terminal DC system

The proposed model is generalized to a three-terminal DC system in order to retrieve its general behavior. DC lines are simplified and smoothing reactors are not considered; there is only an equivalent capacitor which represents the DC cable insulation capacitances. The DC grid can be represented by an equivalent capacitor (C_{eq}) which is the sum of the substation's capacitors and the cable capacitances:

$$C_{eq} = \sum_{i=1}^{N} C_{s_i} + \sum_{i=1}^{N_c} C_{cable_i} \tag{3.6}$$

Where:

N is the number of converter stations

N_c is the number of cable in the DC grid

C_{s_i} is the ith converter station capacitor value [F]

C_{cable_i} is the ith cable capacitance [F]

C_{eq} is the DC grid equivalent capacitor value [F]

In those conditions, if three VSC stations are connected to the same DC grid, the DC voltage is given by:

$$u_s = -\frac{1}{C_{eq}} \int_0^t \left(i_{m_1} + i_{m_2} + i_{m_3}\right) dt \tag{3.7}$$

However, VSC stations are controlling the power and not the DC current, so:

$$u_s = -\frac{1}{C_{eq}} \int_0^t \frac{\left(p_{m_1} + p_{m_2} + p_{m_3}\right)}{u_s} dt \tag{3.8}$$

Considering small variations, (3.8) can be linearized as presented in Chapter 2 part 2.2.1:

$$\Delta u_s = -\frac{1}{C_{eq}} \int_0^t \left(\frac{p_{m_1} - \Delta u_s I_{m_1 0}}{U_{s0}} + \frac{p_{m_2} - \Delta u_s I_{m_2 0}}{U_{s0}} + \frac{p_{m_3} - \Delta u_s I_{m_3 0}}{U_{s0}} \right) dt \tag{3.9}$$

Using the aforementioned simplified model of droop controlled station, the simplified small signal model of the three-terminal DC grid is represented on Figure 3-11. The two on-shore grid side converters (Stations 1 & Station 2) are droop controlled while the wind farm converter (Station 3) injects all the available wind power into the DC grid.

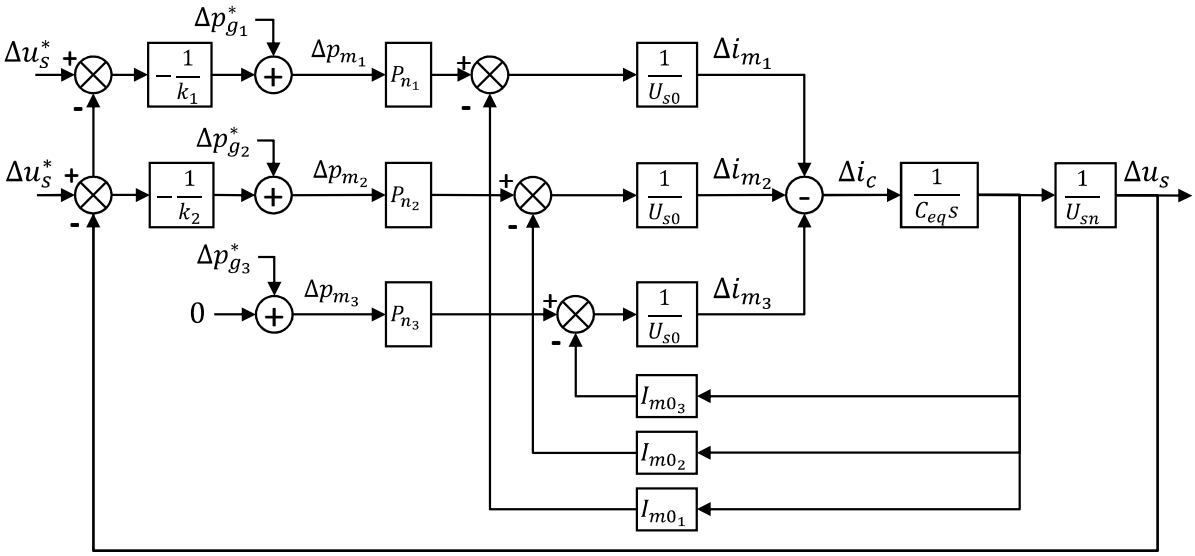

Figure 3-11: Simplified model of the three-terminal DC grid – 1

The power balance is expressed by the sum of substations output power; at an equilibrium point this sum must be null if the losses are neglected. Moreover, if voltage drops are also neglected, the sum of out-coming currents into the simplified DC grid is null, this leads to considerably simplify the model, see Figure 3-12:

$$I_{m0_1} + I_{m0_2} + I_{m0_3} = 0 \tag{3.10}$$

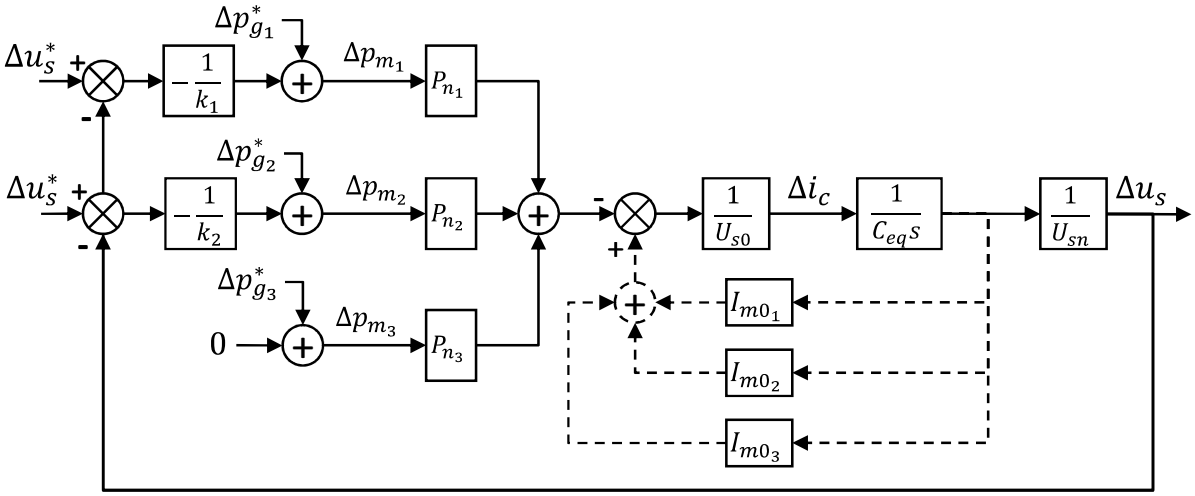

Figure 3-12: Simplified model of the three-terminal DC grid – 2

From the block diagram Figure 3-12, the DC voltage deviation which occurs after a change of power reference (i.e. $\Delta P p_{g_i}^*$) can be defined by the following formula:

$$\Delta u_s = -\frac{\dfrac{1}{\dfrac{P_{n_1}}{k_1} + \dfrac{P_{n_2}}{k_2}}}{1 + \dfrac{U_{s0} U_{s_n} C_{eq} s}{\dfrac{P_{n_1}}{k_1} + \dfrac{P_{n_2}}{k_2}}} \frac{P_{n_i}}{U_{sn}} \Delta p_{g_i}^* \tag{3.11}$$

Where:

Δu_s is the DC voltage deviation [pu]

$\Delta p^*_{g_i}$ is the power deviation of the ith substation [pu] (with regards to the substation's nominal power)

P_{n_i} is the nominal active power of the ith substation [W]

k_i is the droop parameter of the ith substation [pu]

U_{s0} is the operation point DC voltage [V]

U_{s_n} is the nominal DC voltage [V]

C_{eq} is the equivalent DC capacitor [µF]

This formula is a simple first order transfer function, which describes the DC voltage behavior. The numerator indicates the final voltage deviation with regards to the power deviation, the denominator represents the DC voltage dynamics. The capacitor value plays a role only on dynamics while the droop value acts on both dynamics and steady state voltage deviation.

3.4.4. Validation

To obtain this formula some assumptions have been done, a comparison with a detailed model is necessary to validate this simplified model. The reference model is composed of WideBand cable models, smoothing reactors at the converter DC terminals, non-linearized controllers, converter modeled as averaged model. The scenario presented in part 3.3.1 has been simulated with two different droop values: for 1.065 pu/pu and for 0.213 pu/pu (i.e. 1.065/5). Results are plotted in Figure 3-13 for both droop values.

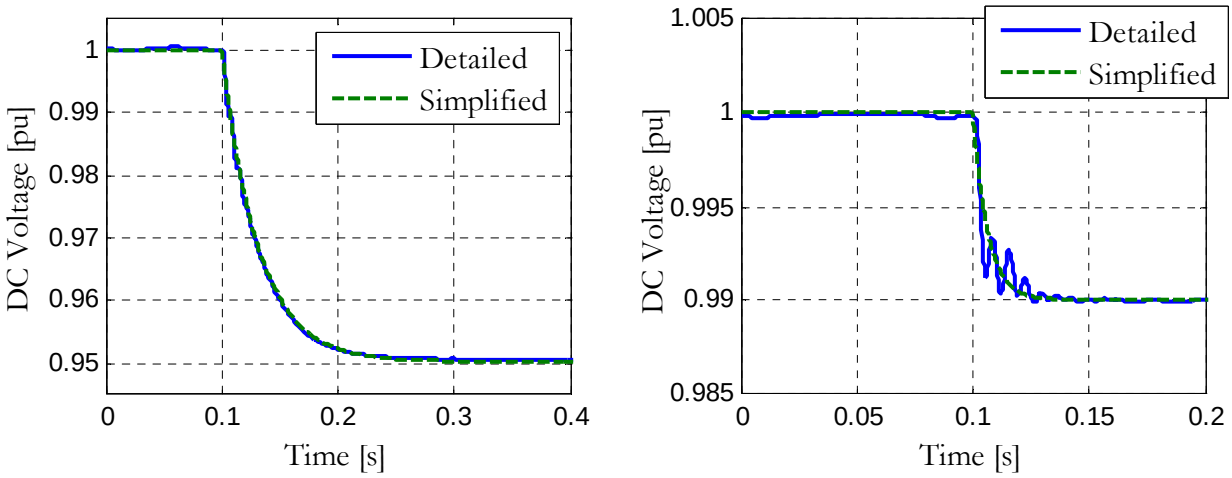

(a) droop value of 1.064 (b) droop value of 0.213

Figure 3-13: loss of 140 MW on the three-terminal DC grid – DC voltage waveform – Comparison between the detailed model (i.e. EMTP-RV) and the simplified model

For a droop value set at 1.065 pu/pu the theoretical response time is 100 ms and the DC voltage deviation in steady state is 5%, results from the simplified model match exactly the DC voltage of the detailed model. Regarding results with droop parameters equal to 0.213 pu/pu, the theoretical response time of 20 ms is given by the simplified model, however even if the response

time is in the same range, the behavior of the DC voltage from the detailed model does not look like a first-order transfer function. This is due to the response time of the DC voltage which is too close to the response time of VSC current controllers. The assumption which considers that the current loop dynamics is much faster than the DC voltage, is not true in that case. In addition, knowing the power deviation for a droop controlled converter station is proportional to the DC voltage, these oscillations will be transmitted to the AC system connected to the converter; this effect has to be avoided.

As conclusion, the DC voltage behavior can be obtained accurately by a first order transfer function if its response time is much lower than the current loops response time.

3.4.5. Generalization to any topology

In the previous paragraph a simplified model for a voltage droop controlled three-terminal DC grid has been developed. In this paragraph, it is generalized for any topology, which means any converter station number and any number of substations which are participating to the power balance effort. Generalizing the formula (3.11) leads to:

$$\Delta u_s = -\frac{\dfrac{1}{\sum_{j=1}^{N'} \dfrac{P_{n_j}}{k_j}}}{1 + \dfrac{U_{s0} U_{s_n} C_{eq}}{\sum_{j=1}^{N'} \dfrac{P_{n_j}}{k_j}}} P_{n_i} \Delta p_{g_i}^* \tag{3.12}$$

Where:

Δu_s	is the DC voltage deviation [pu]
$\Delta p_{g_i}^*$	is the power deviation of the ith substation [pu] (with regards to the substation's nominal power)
P_{n_i}	is the nominal active power of the ith substation [W]
k_i	is the droop parameter of the ith substation [pu]
U_{s0}	is the DC voltage at operating point [V]
U_{s_n}	is the nominal DC voltage [V]
N	is the number of substation
N'	is the number of substation which participates to the voltage control
C_{eq}	is the equivalent DC capacitor [µF]

The numerator of this transfer function deals with steady state voltage deviation and the denominator deals with the DC voltage dynamics.

If converter stations have the same electrostatic constant (see (3.2)), if DC cable capacitances are neglected and the DC voltage at operating point is at its nominal value, then the DC voltage control loop dynamics can be simplified as follows:

$$\Delta u_s = -\frac{\frac{k}{\sum_{j=1}^{N'} P_{n_j}}}{1 + k\frac{U_{s_n}^2 \left(\sum_{j=1}^{N} C_{s_j}\right) s}{\sum_{j=1}^{N'} P_{n_j}}} P_{n_i} \Delta p_{g_i}^* \quad \textbf{(3.13)}$$

$$\Delta u_s = -\frac{\frac{k}{\sum_{j=1}^{N'} P_{n_j}}}{1 + 2k\left(\sum_{j=1}^{N} \frac{1}{2} C_{s_j} \frac{U_{s_n}^2}{P_{nj}} P_{n_j}\right)\frac{1}{\sum_{j=1}^{N'} P_{n_j}}} P_{n_i} \Delta p_{g_i}^* \quad \textbf{(3.14)}$$

$$\tau = 2kH_c\left(\frac{\sum_{j=1}^{N} P_{nj}}{\sum_{j=1}^{N'} P_{nj}}\right) \quad \textbf{(3.15)}$$

Where:

$\mathrm{H_c}$ is the electrostatic constant [s]

τ is the time constant of the DC voltage dynamics [s]

From (3.12) and (3.15), some conclusions can be drawn on the behavior of an MTDC system:

- The droop value influences the dynamics. Higher value of k leads to higher value of τ which means lower dynamics.
- The droop value also influences the steady state voltage deviation. Higher value of k leads to higher voltage variation with regard to the same power deviation.
- The DC storage influences the DC voltage dynamics. In other words, if substations have higher capacitor values (i.e. higher H_c) or if there are more capacitors brought by additional connected substations (N) which are not participating to the voltage control, the dynamics will be slower.
- The number of stations which participate to the voltage control (N') also influences the dynamics. Making one more station participating to the voltage control leads to decrease the DC voltage time constant.
- The number of stations which participate to the voltage control (N') also influences the steady state voltage deviation. Making one more station participating to the voltage control leads to decrease the DC voltage variation with regard to the same power deviation.

In brief, the simplified formula enables to predict the general behavior of any DC grid without the need to simulate it. Thanks to this approach, two major parameters which drive the DC voltage behavior have been identified: the capacitor value and the droop parameter.

3.5 SIZING THE DROOP VALUE

3.5.1. Previous works

In the majority of papers the droop is set at a value close to 5 % (i.e. typical value for frequency droop controllers), nevertheless there are some studies which deal with design of droop value: it could be based on steady states criterions in [XU09] [CHA13a] and [DES12a], on an error inferior to a certain limit over a bandwidth in [PRI11]. In [KAR02], the droop parameter and the capacitor value are designed to achieve a given damping ratio and a desired voltage deviation at nominal load.

In [XU09], the droop parameters are designed following a methodology based on the DC grid resistances to achieved the desired power sharing between two onshore converters. Droop values are fictively changing the DC grid resistances seen from converter stations and therefore changing the power flows. This method is suitable only for a specific topology. In fact, to apply this methodology, the whole power must flow through the same bus, because the calculation of droop parameters is based on resistances from the common bus to the stations. Furthermore, an error in the line resistance evaluation, due to the conductor heating for instance, will change the expected power dispatch.

In the same way, in [DES12a] the control of specific grid structures (i.e. point-to-point HVDC links connected by a cable linking the middles of the transmission cables) is achieved by controlling the voltage of strategic remote nodes. For each on-shore station, the droop parameter is designed to harvest the wind power of its associated wind farm. This strategy is not generic and relies on remote measurements.

The adaptive droop control method is also based on the droop method. Unlike previous methods, this control cannot be described by a static PV curve since the droop parameter evolves over time as a function of the possible converter contingencies and the proximity of the converter operating point with regards to its limits [CHA13a]. With this method, converters will never reach their limits, even with severe disturbances such as converter outage, because the droop value of each converter is pre-computed in order to remain between limits for the worst event which can occur at this moment. The main drawback of this method is that the power deviation sharing is not decided by TSOs, since an algorithm decides the droop values.

In [PRI11], it was developed a methodology based on singular values to obtain a maximum voltage error of 10 % over a bandwidth and the stability is assessed by eigenvalues analysis. However in this study the DC model is very simplified: converters are assimilated to simple current injectors and it does not take into account the dynamics of converters while the obtained DC dynamics is in the same bandwidth as the current loops.

In [KAR02] it was developed a methodology to size the capacitor value on damping criterions. This study investigates the connection of several loads and renewable energy sources at the same low voltage DC grid (700 V). By neglecting converter control loops the DC system is simplified as a second order transfer function, taking into account the droop parameter as well as the capacitor value. However the polynomial characteristic is only used to achieve a certain damping and no attention is paid to the overall response time. This method leads to a capacitor

value of 199 μF/kW, i.e. an electrostatic constant of 48 s, a value not imaginable for HVDC application.

3.5.2. Proposed methodology

In this part, a methodology to design the droop value is proposed. This methodology is based on the simplified model seen in subsection 3.4. It has been seen in this subsection that the voltage response time depends on the converter station capacitors (i.e. electrostatic constant H_c), on the droop parameter k and on the number of stations which are controlling the DC voltage (N'). Moreover, the voltage deviation which comes from a given power deviation is defined by the droop value k and N'.

The choice of the voltage droop parameter is a trade-off between response time and final voltage deviation. However, the DC voltage control loop is an outer control loop embedding the current control loop. Therefore, the system stability is improved when the voltage control loop is slower. Based on this consideration the droop value was sized to achieve a desired response time by rearranging (3.15):

$$k = \frac{\tau}{2H_c}\left(\frac{\sum_{j=1}^{N'} P_{nj}}{\sum_{j=1}^{N} P_{nj}}\right) \tag{3.16}$$

In control engineering, the common practice is to have outer control loops ten times slower than inner control loops in order to avoid unwanted interactions between both nested loops. According to manufacturers, the response time for the current control loop is around 10 ms, therefore the DC voltage control loop response time should be around 100 ms (it means time constant τ = 0.033 s). Considering the three-terminal DC grid presented in part 3.3.1, dealing with H_c=10 ms, the droop value on Station 1 and Station 2 is calculated as follows:

$$k = \frac{0.033}{2 \times 0.01024}\left(\frac{P_{n_1} + P_{n_2}}{P_{n_1} + P_{n_2} + P_{n_3}}\right) = 1.27 \text{ pu/pu} \tag{3.17}$$

3.5.3. Maximal power deviation

By designing the droop constant according to dynamic consideration, the voltage deviation was not considered at all. However, to work properly, the DC grid voltage must remain within specific bounds (e.g. ± 5 %). For a given maximal admissible voltage deviation, the maximal power deviation which could occur in a DC grid is obtained by considering the numerator of (3.12):

$$\Delta P_{max} = \Delta u_{s\,max} \frac{\sum_{j=1}^{N'} P_{nj}}{k} \tag{3.18}$$

Where:

$\Delta u_{s\,max}$ is the maximal DC voltage deviation [pu]

ΔP_{max} is the maximal power variation which could occur in the DC grid (obtained as a function of the admissible voltage deviation and a given droop value) [MW]

The maximal power variation which could occur in a DC grid without exceeding the voltage limits is a function of the droop value k and the nominal power of the stations which are controlling the DC voltage. Hence, the choice of the droop design has an influence on the maximal admissible power deviation. Note that, the maximal power variation does not take into account the substation power limits.

Combining (3.16) and (3.18), the maximal power deviation which could occur in the three-terminal DC grid can be calculated for different values of the response time ($t_{r_{5\%}}$) and storage (H_c):

$$\Delta P_{max} = \Delta u_{s\,max} \frac{3 \times 2H_c \sum_{j=1}^{N} P_{nj}}{t_{r_{5\%}}} \tag{3.19}$$

The droop value of the two onshore converter stations is tuned to achieve a desired DC voltage control loop response time for a given storage. The DC grid storage is expressed by the station electrostatic constant. The maximal sudden power deviation which could happen in DC grid without exceeding 5 % voltage variation is displayed on a 3D graph in Figure 3-14a and in 2D graph in Figure 3-14b. The maximal power variation is calculated for electrostatic constant ranging from 10 ms to 50 ms and desired response time ranging from 40 ms to 100 ms.

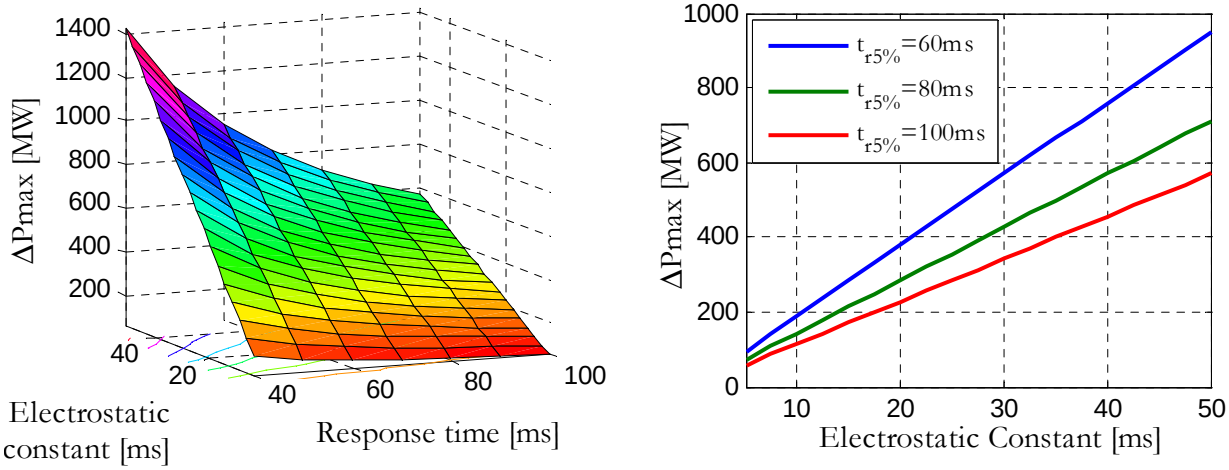

(a) 3D view

(b) 2D view

Figure 3-14: Three-terminal HVDC droop controlled system – Maximal power for a 5 % voltage drop – as a function of the response time

In Figure 3-14, the maximal power variation which could occur in the DC system is very sensitive to the stored energy (H_c) and the voltage control dynamics. For a given response time, a higher capacitor value is needed to handle a higher power deviation. However, higher electrostatic constant value is more expensive and also leads to higher short circuit peak currents [DES13]. Another way to increase the maximal power variation is to decrease the response time, however this value cannot be lowered indefinitely because of converter control dynamic limits and furthermore, connected AC grids would be more solicited.

In the previous analysis the maximal voltage deviation was imposed at ± 5 %, however, according to (3.18) this parameter is as important as the droop parameter. The time response of

the voltage loop is imposed at 100 ms to ensure no interaction between the VSC station current control loops and the DC voltage control. The maximal power deviation is calculated as a function of both the stored energy and the maximal voltage deviation; results are shown in Figure 3-15. As expected the maximal power deviation is linear to the admissible voltage variation. Thus, for a given voltage control loop time response, it is possible to handle more power deviation in the DC system by increasing the storage and maximal admissible voltage deviation. The maximal voltage level is defined by DC cable insulation and IGBT voltage blocking capability. While the minimal voltage level is defined by the minimal modulation index, the maximal current through cables and the minimal DC voltage supply used to drive to IGBTs which is a fraction of the HVDC value seen by the converters. It is expected that new multilevel converters can handle higher DC voltage deviation than two-level converters.

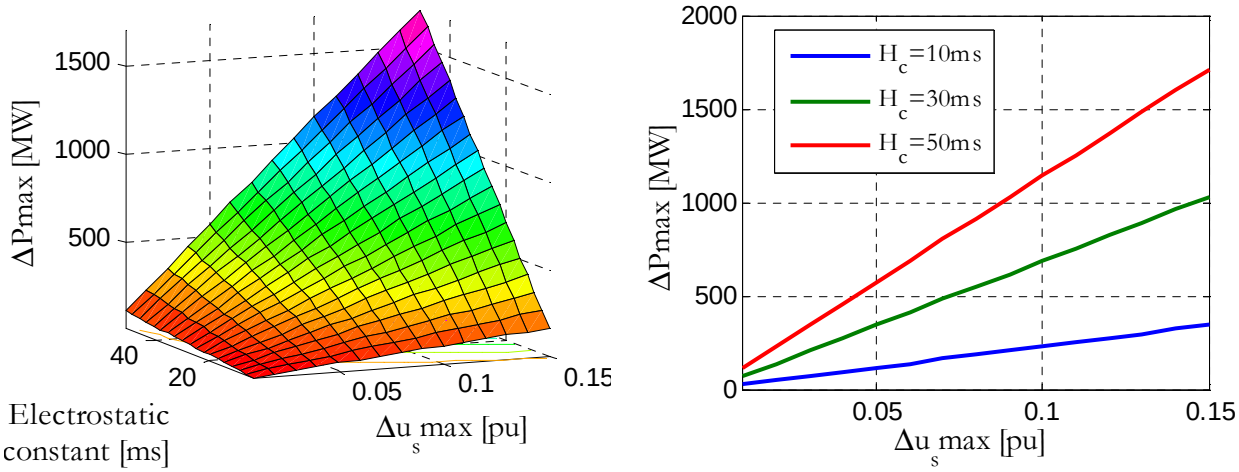

(a) 3D view (b) 2D view

Figure 3-15: Three-terminal HVDC droop controlled system – DC voltage control loop response time set at 100 ms – as a function of maximal voltage and electrostatic constant

3.6 RESCUE OPERATION

The notion of N-1 criterion is defined for AC systems in [UCT04] as follows: "The N-1 CRITERION is a rule according to which elements remaining in operation after failure of a single network element (such as transmission line / transformer or generating unit, or in certain instances a bus-bar) must be capable of accommodating the change of flows in the network caused by that single failure".

Two scenarios may be analyzed: the trip of a substation which only controls its power flow or a station which participates to the DC voltage control. First, the trip of one offshore wind farm converter station is considered. This kind of station is not controlling the DC voltage, its loss leads to DC grid power deficit, since it was injecting power in it, and thus the lowest voltage level limit is the critical point.

For instance if the voltage deviation is limited at 5 %, taking the three terminal DC grid as example with the previous droop parameter (k=1.27 pu/pu), from (3.18) the maximal power deviation which could occur in the DC grid is given by:

$$\Delta P_{max} = \Delta u_{s\,max} \frac{P_{n_1} + P_{n_2}}{k} = 0.05 \frac{1500 + 1500}{1.27} = 118\ MW \ll P_{n_3} \quad \textbf{(3.20)}$$

The maximal power is much lower than the nominal power of Station 3. To increase ΔP_{max}, the k parameter has to be decreased.

$$k = \Delta u_{s\,max} \frac{P_{n_1} + P_{n_2}}{P_{n_3}} = 0.05 \frac{1500 + 1500}{800} = 0.19\ pu/pu \quad \textbf{(3.21)}$$

To obtain the same response time with this value of k and with the loss of Station 3 capacitor, that supposes to increase DC grid stored energy:

$$H_c = \frac{\tau}{2k}\left(\frac{P_{n_1} + P_{n_2}}{P_{n_1} + P_{n_2}}\right) = \frac{0.033}{2 \times 0.19} = 87\ ms \quad \textbf{(3.22)}$$

The capacitor value must be multiplied by 9 to have 100 ms of response time when Station 3 is disconnected. With these values of H_c and k, the response time in normal operation is 126 ms.

Secondly, the trip of an onshore converter (Station 1) which was participating to the DC voltage control is considered. In this case, equation (3.18) must be adapted since there is only one station which was controlling the DC voltage:

$$\Delta P_{max} = \Delta u_{s\,max} \frac{P_{n_2}}{k} = 0.05 \frac{1500}{1.27} = 59\ MW \ll P_{n_1} \quad \textbf{(3.23)}$$

For a given droop value, ΔP_{max} is much lower than for normal operation. Like previously, it is possible to design the droop value to achieve a desired static voltage deviation:

$$k = \Delta u_{s\,max} \frac{P_{n_2}}{P_{n_1}} = 0.05 \frac{1500}{1500} = 0.05\ pu/pu \quad \textbf{(3.24)}$$

This leads to significantly increase the stored energy:

$$H_c = \frac{\tau}{2k}\left(\frac{P_{n_2}}{P_{n_3} + P_{n_2}}\right) = \frac{0.033}{2 \times 0.05}\left(\frac{1500}{2300}\right) = 215\ ms \quad \textbf{(3.25)}$$

The capacitor value must be multiplied by 21 with regard to the initial case. The loss of onshore station is the most critical event. In normal operation the theoretical response time is 82 ms. If this station was delivering power into AC grid, the operating point could be calculated at lower voltage level to accept higher growing voltage variations, and therefore higher power variation. Also, the tripped station power can be reported on both remaining onshore stations and wind farm stations thanks to the dead-band droop control strategy.

In the literature, there are some simulations where a loss of a substation is tested [HAI08] [WAN12] [GON12a]. In these simulations, the DC grid storage is often much larger and the droop value is set at much lower value than it is proposed in the previous subsection. Doing so lower DC voltage deviation are obtained, and thus DC grid can cope with an important power deviation such as a station trip. The dynamics of power exchange is not the matter of interest of these studies.

Since there are few stations with large nominal power the loss of one station represents a large fraction of the total load, therefore the N-1 station operation is very difficult. Using

advanced control strategy, such as dead-band control strategy on wind farm converters and piecewise droop control strategy on on-shore converters will help the DC grid to survive, but AC grids must cope with higher power ramps rates and wind farms must be able to change their power very quickly. In case of outage of a converter which was exporting power towards AC grids, there will be an excess of energy which could be temporally consumed by additional DC loads such as DC chopper. In case of loss of a converter which was importing power towards the DC grid, lower DC voltage will release more energy from DC capacitors and thus limiting the power ramp at remained stations. To sum up, N-1 becomes possible only if the stored energy is significantly increased and voltage deviation could be larger. The N-1 ability must be tested on a case-by-case basis, the simplified model must be adapted to each situation, to check if the steady state voltage does not exceed limits, if the dynamics is respected and if power limits of remaining stations are not overstepped.

3.7 CONCLUSION

In this chapter, several methods for primary control of DC grid are investigated. The droop control method, which mimics the primary frequency control, presents good performance when the DC grid is connected at several injection points to AC grids (either synchronous or asynchronous) due to power sharing capability. Then a simplified analysis on a droop controlled DC grid highlighted that the main dynamics of DC voltage as well as substation power flow look like first order transfer functions which depend on the equivalent DC capacitor and the droop parameter. From this, a methodology to size the droop parameter is proposed; it imposes a DC voltage dynamics to enable a smooth control.

Also, the simplified model enables to determine the maximal power variation which could occur in the DC grid without exceeding operational DC voltage limits. Thanks to this model, it was proven that it is not possible to lose one station with capacitor values equivalent to actual ones. To be able to cope with converter station contingencies, converter station capacitors must be greatly oversized with regard to those of actual VSC stations.

To sum up, with droop control, power exchanges have same dynamics than the DC voltage. These dynamics are defined by the equivalent DC capacitor value and the droop parameter. The maximal power deviation depends on the droop value and the authorized voltage deviation. It could be improved by authorizing much DC voltage deviation, by increasing the DC grid storage or by a quicker converter control (MMC are expected to be faster than two-level PWM converters).

CHAPTER 4: Small Signal Stability Analysis of a DC grid

4.1 INTRODUCTION

Chapter 2 has presented a small signal stability analysis (SSSA) applied on a point-to-point HVDC link and Chapter 3 has presented the concept of MTDC grid and the management of the DC voltage thanks to droop control. Chapter 4 proposes an extension of the SSSA to a MTDC grid connected to a small AC grid. This chapter treats first the DC grid itself and then the combined AC-DC system. The analysis on the DC grid itself enables to assess the main drivers which act on the DC grid behavior while the second analysis on the combined AC-DC system aims to identify possible interactions between both AC and DC systems once they are connected.

Classical SSSA is a tool used for in-depth modal analysis. But currently, few studies are dealing with SSSA of Multi-terminal DC grids. In [ALS11], [CHA13] and [CHA11c], a root locus is plotted to assess the stability of an AC-DC system. Parametric studies have been reported for various short-circuit levels of the AC grids [ALS11], for converter control parameters [KAL12], for frequency droop value [CHA13], for DC voltage droop value [CHA13a]. In those approaches, however, it is difficult to find the origins and the couplings between the different modes.

This chapter proposes a step-by-step approach, involving progressively more and more devices implicated in an MTDC system to easily identify their impacts: converter control loops have already been studied in Chapter 2, then the DC grid is studied alone, finally the same DC grid is connected to an AC grid. For didactic purposes the same methodology as in Chapter 2, is used to build the state space model of the MTDC system. However, AC-DC state space model is not obtained with the same manner since the considered AC systems have already been modeled by the University of Liege (ULg) in a home-made library developed in the Matlab/Simulink® environment [VOU04]. Both modeling approaches lead to the same state space model.

In section 4.2, a five-terminal DC grid, used as test system, is first described, modeled as a state space model and then validated by a time domain simulation. In section 4.3, a modal analysis is performed on this test system. Each mode is identified according to its related states and parametric studies on relevant parameters are performed in order to show their impact on the stability and dynamics. A special attention is given to the DC voltage mode identified in Chapter 3. Section 4.4 deals with what occurs when a DC system is connected to an AC system. Modes of this AC system are identified without the DC grid connection for different power flow patterns. Then modes of the coupled AC-DC system are compared to those of the AC system alone and those of the DC system alone. In this section the frequency support from the DC grid and the connection to asynchronous areas are also considered.

4.2 MODELLING METHODOLOGY OF A DC GRID

4.2.1. Five-terminal DC grid test system description and characteristics

As already said in Chapter 3, the DC grid should be built step-by-step, and therefore, topologies with three to five terminals are more likely possible in the near future than a pan European DC grid. The proposed DC test system used to assess control performances of the DC grid is presented in Figure 4-1. It is a five terminal DC grid which connects three offshore wind farms (WF1, WF2 and WF3) to two AC grid injection points (GS1 and GS2). Recall that this

work is a part of the TWENTIES demo 3, the objective of the test system is to illustrate both operation and protection of a DC grid. For the second topic, it is expected that radial and meshed grid will not behave in the same manner, namely for fault current [NGU11].

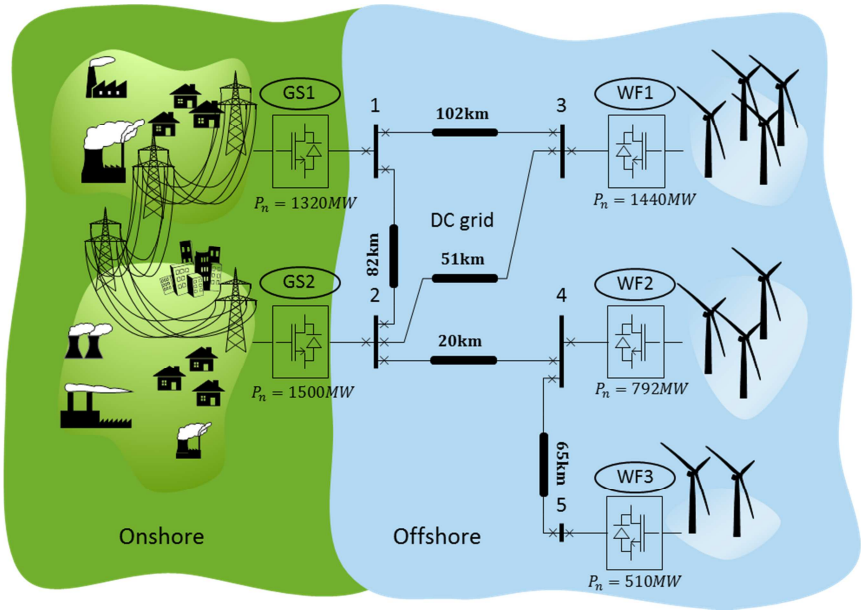

Figure 4-1: Five-terminal DC grid test system

Wind farms have nominal power in the same range than actual granted wind farm projects [FIC09] and onshore converter stations are sized to transmit the wind power production to the AC grid. The nominal voltage of converter station is set at ±320 kV, the state-of-the-art DC voltage level for VSC-HVDC transmission [INE11]. Regarding the converter station DC capacitor value, it is designed in order to have 10 ms electrostatic constant (as in Chapter 3). Converter station parameters of the five-terminal DC grid are summarized in Table 4-1. Note that nominal powers of stations derive from the small scale DC grid presented in Chapter 6, which explains why nominal powers are not round numbers.

Table 4-1: Five-terminal DC grid test system – converter station parameters

Converter station	Nominal voltage [kV]	Nominal power [MW]	DC capacitor [µF]
GS1	±320 kV	1320	66
GS2	±320 kV	1500	75
WF1	±320 kV	1440	72
WF2	±320 kV	792	40
WF3	±320 kV	510	26

Transmission channels are pairs of ±320 kV DC cables, with XLPE insulation technology (see Chapter 2 part 2.4.2). Two cable copper sections are used in the DC grid: The 2500 mm² copper section is used in almost the entire DC grid except for the DC transmission channel between WF2 and WF3 (i.e. DC cables between node 4 and 5) which are two parallel cables of 500 mm² copper section. DC cable ampacity varies with regard to the laying arrangement and the climate where it is installed. Based on ABB HVDC Light® cable data [ABB06], cables with a 500 mm² section have a nominal power set at 400 MW per pair of cables and cables with

2500 mm² section have a nominal power set at 1000 MW per pair of cables. DC cable main parameters are reported in Table 4-2, for more cable data see Appendix C.

Table 4-2: Five-terminal DC grid test system – DC link parameters

Transmission	Length [km]	Cable section [mm²]	Nominal power [MW]	Rated voltage [kV]
DC link 12	82	2500	1000	±320 kV
DC link 13	102	2500	1000	±320 kV
DC link 23	51	2500	1000	±320 kV
DC link 24	20	2500	1000	±320 kV
DC link 45	65	2*500	2*(400)	±320 kV

4.2.2. Voltage droop design of the five-terminal DC grid

In order to deliver the wind power to the AC grid, only grid side converter stations are equipped with a voltage droop controller, offshore station are controlling their power flow to supply the whole wind power into the DC grid.

Considering the same droop value, the method to size the droop value introduced in Chapter 3 is applied to the five-terminal DC grid to achieve 100 ms response time for the DC voltage dynamics. From (3.3), the droop parameter of the two onshore stations is:

$$\begin{aligned} k &= \frac{\tau}{2H_c}\left(\frac{\sum_{j=1}^{N'} P_{nj}}{\sum_{j=1}^{N} P_{nj}}\right) \\ &= \frac{0.033}{2\times 0.010}\left(\frac{1320+1500}{1320+1500+1440+792+510}\right) \\ &= 0.82 \end{aligned} \quad (4.1)$$

From (3.4) and considering 5 % as maximal voltage deviation, the maximal power deviation which could be managed in the DC grid is:

$$\Delta P_{max} = 0.05\frac{1320+1500}{0.82} = 172\ MW \quad (4.2)$$

4.2.3. State-space modeling of the five-terminal DC grid

In this part, the principles developed in Chapter 2 are used to model the five-terminal DC grid. As presented in Chapter 2, the closed-loop model of the DC system is composed of several subsystems which are connected together. The five-terminal DC grid system composition is presented in Figure 4-2. For the sake of clarity, links between subsystems are not reported in this figure. Each converter station is composed of the converter station itself, the converter station control and its associated smoothing reactor (SR). Then, converter stations are connected together by DC links.

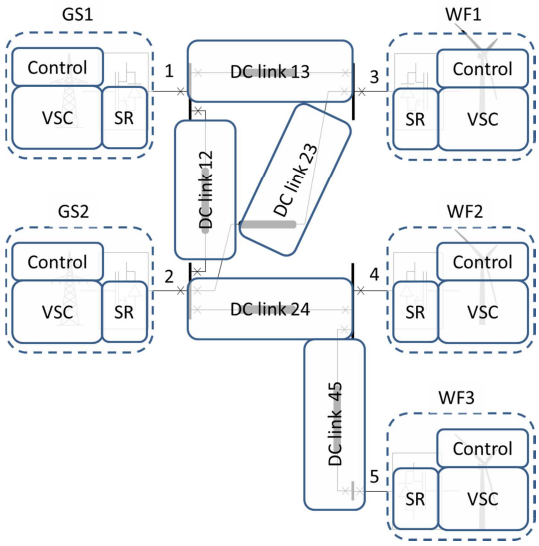

Figure 4-2: Closed-loop model of the five-terminal DC grid

The model of the DC voltage droop controlled VSC is shown in Figure 4-3. This model is composed of the DC voltage droop controller (see Chapter 3 Figure 3-9) connected to the linearized model of the power controlled VSC model (see Chapter 2 in Figure 2-1 and in Figure 2-4).

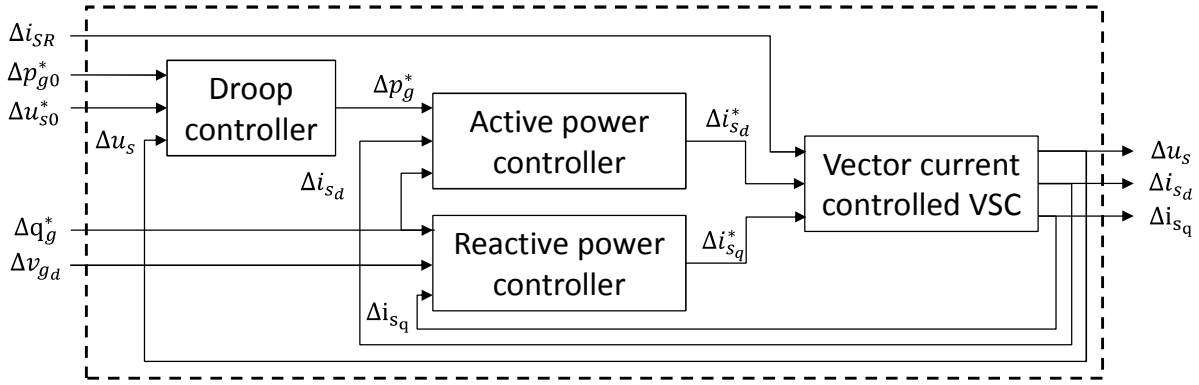

Figure 4-3: Linearized DC voltage droop controlled VSC

Thanks to the modification of DC cable models and smoothing reactor models, it is now possible to combine all the models. The overall state space model of the five-terminal DC grid is built using the routine presented in Appendix E.4. It has 64 state variables:

- six DC cables with 4 states
- five stations with 8 states (i.e. 2 states for the d-axis current control loop, 2 states for the q-axis current loop, 1 state for the active power controller, 1 state for the reactive power controller, 1 state for the converter station capacitor and 1 state for the station smoothing reactor).

To validate this state space model, a set point change of 172 MW step is done at 0.1 s on WF3. The state space model is simulated in time domain on the Matlab/Simulink® environment. The simulation used as reference, is a more detailed simulation (EMT) done on the EMTP-RV® environment using WideBand cable models and average converter models. The DC voltage of GS1 (u_{s1}) and the active power of the GS1 (p_{g1}) and GS2 (p_{g2}) are shown in Figure 4-4. In this

figures, quantities are in per unit with regard to the station power and voltage rating. The operating point is added to the deviations obtained by the simulation of state space model, to facilitate comparison with results from the reference simulation. Results from the linearized simulation match exactly results obtained by the reference model, therefore the state space model can be considered as validated.

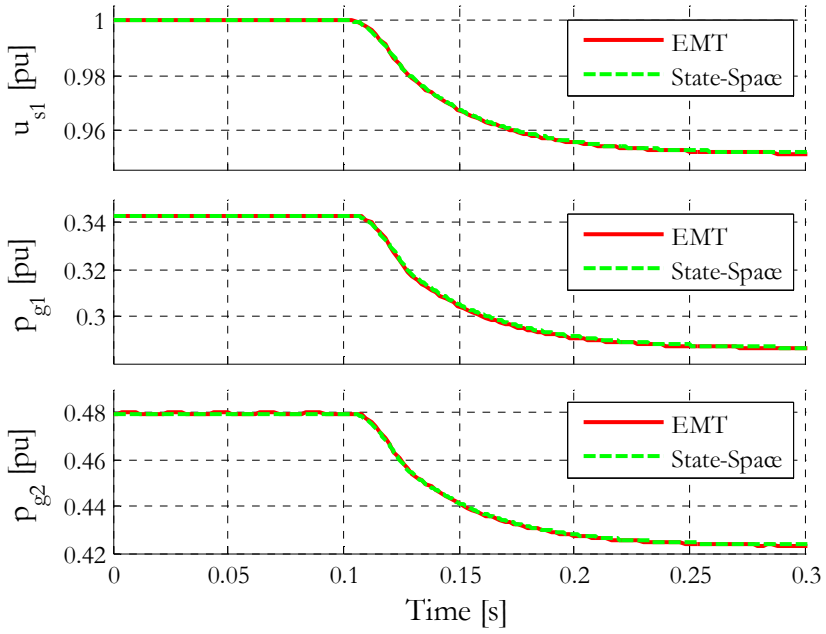

Figure 4-4: Validation of the five-terminal DC grid – step change of 172 MW in WF5

4.3 SMALL SIGNAL STABILITY ANALYSIS ON A DC GRID

4.3.1. Eigenvalues analysis of the DC system

Eigenvalues of the five-terminal DC grid are computed and only a selection of them is displayed in Table 4-3 for the sake of clarity (all eigenvalues are reported in Appendix F.1). In this table, states which are the most involved in the mode evolution are reported as well as their relative participation.

Table 4-3: Eigenvalues of the five-terminal DC grid

	Eigenvalues	Freq.	Damp.	Dominant States		Comment
DC1	-191 ± j 7820	1240	0.024	Line24_D_il1 Line45a_D_uc1 Line45b_D_uc1	1.00 0.40 0.40	DC grid
DC9	-95.2 ± j 686	109	0.14	Line12_D_il1 Line23_D_il1 GS1_D_us GS1_D_il GS2_D_us WF1_D_il WF1_D_us WF2_D_us WF3_D_us	0.61 0.45 1.00 0.57 0.67 0.43 0.39 0.38 0.34	
DC17	-1.36	–	–	Line12_D_il1 Line13_D_il1 Line23_D_il1	0.80 1.00 0.50	
DC18	-27.7 ± j 1.1	0.2	≈1	GS1_D_us GS1_Xip GS2_D_us GS2_Xip WF1_D_us	0.44 0.86 0.51 1.00 0.49	DC grid voltage
DC19	-188 ± j 237	37	0.62	GS1_Xid GS1_D_isd GS2_Xid GS2_D_isd	0.67 0.75 0.89 1.00	current control loops
DC23	-200 ± j 225	35	0.67	WF3_Xid WF3_D_isd	0.93 1.00	
DC24	-200 ± j 225	35	0.67	GS1_Xiq GS1_D_isq	0.93 1.00	
DC29	-29.8	–	–	GS1_Xp GS2_Xp	1.00 0.86	Active and reactive power control loops
DC36	-29.8	–	–	WF3_Xq	1	

In this table, modes are sorted in four categories thanks to their associated dominant states:

- DC grid category is the one which comprises the most modes (i.e.18 modes), all DC grid elements are involved: DC cables, smoothing reactors and converter station capacitors. As already said for the point-to-point HVDC links, most of these modes correspond to complex interactions which are difficult to understand. Since there are more cables connected together these modes may correspond to very complex interactions. Most of these modes have fast dynamics (frequency oscillations over 100 Hz).
- dq-current control loop eigenvalues (from 19 to 28), are at their tuned value. Apart the current loops linked to the active power control of GS1 and GS2 which have a little bit evolved since they are a little influenced by the DC voltage control.
- Power control loop eigenvalues (from 29 to 36) are also at their tuned value. Although these modes are at their expected value these modes are participating in more than one power control loops. Note that, there are only 9 instead of 10 eigenvalues which are related to power control loops because there is one eigenvalue which is classified as DC voltage mode because it forms a complex conjugate mode with a DC voltage control loop eigenvalue. Indeed, states of active power controllers of GS1 and GS2 are among states most influenced by mode DC18 and its value is close to -30 rad/s; expected value for power control loop.

- A specific focus is given on Mode DC18, which has been classified as DC voltage mode because station capacitor states (GS1_D_us, GS2_D_us and WF1_D_us) are most influenced by this one. Moreover, it should be noted that variables states from active power controller of GS1 and GS2 are both involved in the DC grid voltage mode (GS1_Xip and GS2_Xip are among the dominant states of Mode 18). However, this mode is a pair of complex conjugate eigenvalues located close to the expected dynamics of power loop and those of the DC voltage. Nevertheless, despite appearances, the dynamics of the voltage control loop is similar to a first order transfer function. This phenomenon has already be explained during the analysis of the droop controlled VSC in Chapter 3 part 3.4.2. Note that, there is still a little difference with regard to the expected value (i.e. close to -30 rad/s), which is due to DC cables capacitors which contribute to increase the DC grid equivalent capacitor, and therefore change the DC voltage dynamics.

As conclusion, like for the point-to-point HVDC link, modes related to the DC grid have higher dynamics than modes related to converter control loops, which explains why they are uncoupled. The modes related to power control loops and to the voltage control loop are coupled because they have similar dynamics. The key point is that the DC voltage dynamics obtained by the simplified analysis in Chapter 3 is retrieved in the modal analysis.

4.3.2. Influence of the droop parameter

A parametric study is performed on the DC voltage droop parameters. Several root loci are plotted in the same figure (see Figure 4-5) in order to see modal evolution with regard to the droop parameter. The droop parameter is tested from 0.1 to 10. The theoretical time response of the DC voltage mode should be between 14 ms and 1.4 s. Root loci are distinguished by their color, the root locus with droop value set to 0.1 is in blue and root locus with droop value set to 10 are in red.

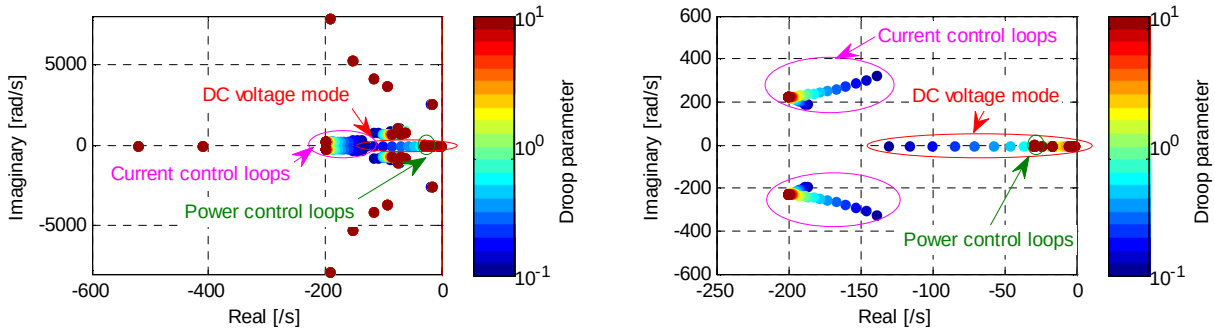

(a) Global view (b) Focus on control modes

Figure 4-5: Root locus of the five-terminal DC grid as a function of the droop value

Modes of the Table 4-3 are retrieved in Figure 4-5. Modes related to DC grid are scattered in the entire root locus while modes related to converter control loops are superimposed since converter controllers have been tuned to achieve same dynamics. In this figure, it is observed that the mode related to d-axis current loops of GS1 and GS2, the DC voltage mode and some DC grid modes (i.e. modes 6, 7, 8 and 9) are influenced by the droop parameter. The mode which is

the most influenced by the droop value is the DC voltage mode; this is consistent with the results obtained in Chapter 3 on the simplified model. Since GS1 and GS2 are configured in DC voltage droop control, it appears some evolutions with modes referenced as d-axis control loops (i.e. active power control) when the DC voltage control loop dynamics are faster than one-tenth of the current loop dynamics. Regarding DC grid modes they have small interaction with the d-axis current control loop of GS1 and GS2 modes. Other DC modes which are located further to control modes are not influenced by the DC voltage droop parameter.

Figure 4-5b is a focus on control modes in order to follow the evolution of the DC voltage mode and the current control loops modes. Thanks to participation factors the origin of the two modes initially related to the d-axis current control loops can be retrieved. The one which evolves toward the real axis involves a coupling between the d-axis control and smoothing reactors of GS1 and GS2 while the one which progresses faster toward the imaginary axis involves an interaction between the d-axis and DC converter station capacitors.

With regard to the DC voltage mode, it should theoretically move from 0.21 rad/s to 210 rad/s, but in reality it moves from 0.35 rad/s to 130 rad/s. For high droop parameter the DC voltage mode value is more or less similar to the theoretical one but for low value of droop parameter, there is a significant difference. Looking to its participation factors when droop parameter is low, d-axis control loop states are among states most influenced by the DC voltage mode.

To show how the current control loops has an effect on DC voltage dynamics, the real part of the DC voltage mode obtained by modal analysis of the full system (Full) is compared, for different droop value, with the one calculated from the simplified model found in Chapter 3 (Simplified). In the same figure it is shown the relative participation in the DC voltage mode of GS1 and GS2 d-axis current loop states (i.e. GS1 isd, GS2 isd, GS1 Xid and GS2 Xid) as a function of the droop value.

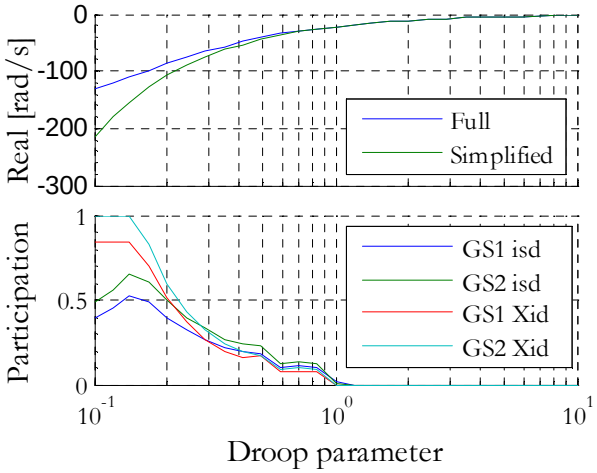

Figure 4-6: DC voltage mode evolution as a function of the droop value

In Figure 4-6, for a droop parameter higher than 0.8 (i.e. DC voltage response time of 100 ms) the value calculated with the simplified model is very close to the one obtained by modal

analysis. For a droop parameter lower than 0.8, the difference between both models becomes more and more important as the droop value is decaying.

Looking to the participation of the states in the DC voltage mode, it is confirmed that the d-axis current control loops of GS1 and GS2 are more and more involved in the DC voltage mode evolution as the droop value is decaying. This explains why the DC voltage control mode is moving ever further away to the simplified model.

Current practices in control engineering to avoid interactions between nested control loops, is to set, at least, the dynamics of the inner control loop ten times faster than the dynamics of the outer control loop. This is exactly what happens when the response time of the DC voltage becomes faster than 100 milliseconds, the outer loop, which is the voltage control loop, is interacting with the inner loop, which is the current control loop, since this one has a response time tuned at 10 milliseconds.

4.3.3. Influence of converter station capacitor values

It has been observed in Chapter 3 that converter station capacitors have a great impact on the DC voltage dynamics. Nevertheless, since converter station capacitors are participating to some modes classified as DC grid modes, it is expected that a capacitor value modification should have an impact not only on the DC voltage mode but also in DC grid modes. To evaluate this assumption, several root loci with different converter station capacitor values are plotted in the same figure. All converter station capacitor values are calculated from a common electrostatic constant (see definition in Chapter 3 part 3.2.2) which evolves from 1 millisecond to 100 milliseconds (the value used until now is 10.24 ms) while other parameters are fixed. The analysis is performed on the five-terminal DC grid, with all parameters set as default except capacitor values. Results are displayed in two figures, Figure 4-7a presents a global view of the root locus while Figure 4-7b is a view focused on control modes.

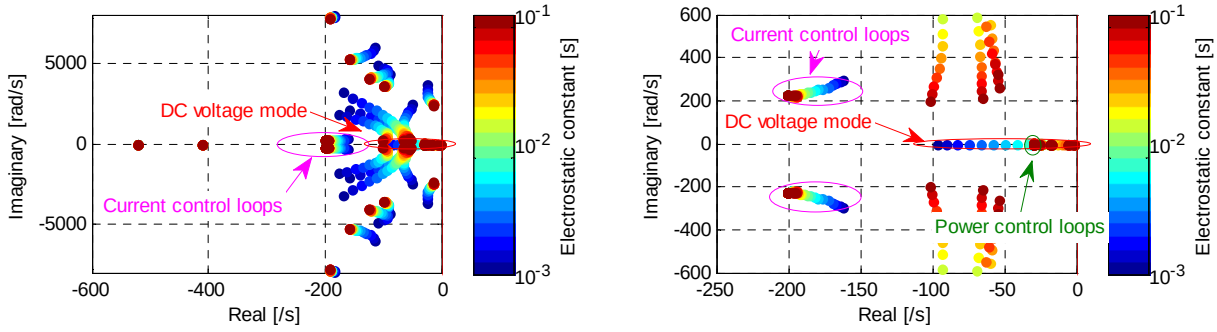

(a) Global view (b) Focus on control modes

Figure 4-7: Root loci of the five-terminal DC grid as a function of the electrostatic constant

Figure 4-7a shows more mode evolutions when changing the converter station capacitor than when changing the droop constant. These modes are associated with DC grid modes as sensed and also control modes. When looking at Figure 4-7b, the DC voltage mode is retrieved moving in the same direction, as have been wished. Also, the same phenomenon observed with the DC voltage droop constant evolution; is present with the electrostatic constant evolution; the

modes originally referred to d-axis current control loops evolve as the DC voltage dynamics is becoming faster.

Conversely to the droop case, DC modes are impacted by the capacitor values. It has been noticed that some of them stop to evolve for a certain value of electrostatic constant while others tend to become real modes.

4.4 MTDC SYSTEM INTERACTION WITH AC SYSTEM

The Matlab/Simulink® library developed at the University of Liège (ULg) has been used to model AC-DC grid [VOU04]. This library was initially developed to teach power system control and stability (i.e. angle stability, frequency control and stability, voltage control and stability). It has been chosen because it offers a large open library of power system components, it has already pre-developed standard AC networks, it could be initialized from any operating point thanks to an external power flow calculation program (also developed at ULg) called Artere, and lastly, this software is based on Matlab/Simulink® environment which offers a large flexibility for the user to modify and add new elements.

Furthermore, there is an additional m-file to achieve the modal analysis of the system. This Matlab® script uses the "linmod" function, available in the Matlab/Simulink® library, to extract the linearized state space model around an operating point from a given Matlab/Simulink® model in block-diagram from [MAT13].

The objective of this section is to trace the mode evolution of a combined AC-DC system. For this purpose, the modes of the combined AC-DC system are analyzed and compared with those of each system operating independently. Two study cases are considered:

- The MTDC system is connected to the AC system without frequency support.
- Grid side converter stations are configured with frequency droop control alike conventional units.

4.4.1. Principle of the ULg Simulink library [VOU04]

First of all, this tool is based on the quasi-sinusoidal approximation; so AC network equations represent the steady-state behavior and the part of a power system component connected to the AC network (e.g. the stator of a synchronous machine) is also represented by algebraic equations. Under the quasi-sinusoidal approximations, the network equations can be written as:

$$\begin{bmatrix} \boldsymbol{i_x} \\ \boldsymbol{i_y} \end{bmatrix} = \begin{bmatrix} \boldsymbol{G} & -\boldsymbol{B} \\ \boldsymbol{B} & \boldsymbol{G} \end{bmatrix} \begin{bmatrix} \boldsymbol{v_x} \\ \boldsymbol{v_y} \end{bmatrix} \tag{4.3}$$

Where:

$\boldsymbol{i_x}$ and $\boldsymbol{i_y}$ are the current phasor projections onto axes x and y [A] or [pu]

$\boldsymbol{v_x}$ and $\boldsymbol{v_y}$ are the voltage phasor projections onto axes x and y [V] or [pu]

$\boldsymbol{G}$ and $\boldsymbol{B}$ are the nodal conductance and susceptance matrices [S] or [pu]

Dynamic components such as loads or machines are represented by differential-algebraic equations. The originality of this tool lies in its manner to overcome the Matlab/Simulink® difficulties to deal with algebraic constraints, by splitting algebraic equations of components into one part that varies linearly with voltage and one part that does not. Each component is modeled as a Norton's equivalent, where the Norton's admittance ($\overline{y_{eq}} = g_{eq} + jb_{eq}$) relates the linear relation between the current and the voltage, and the Norton's current source ($\bar{\phi} = \phi_x + j\phi_y$) is the part of the current which does not explicitly depend on the voltage. The structure of a dynamic component connected to the AC grid is presented in Figure 4-8.

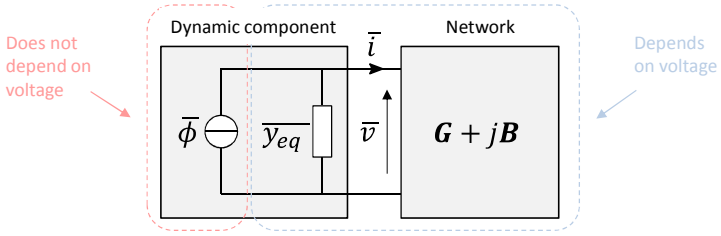

Figure 4-8: Dynamic component connected to the network

Generalizing to N components, (4.3) can be rewritten as:

$$\begin{bmatrix} \boldsymbol{\phi_x} \\ \boldsymbol{\phi_y} \end{bmatrix} - \begin{bmatrix} \boldsymbol{G_{eq}} & \boldsymbol{-B_{eq}} \\ \boldsymbol{B_{eq}} & \boldsymbol{G_{eq}} \end{bmatrix} \begin{bmatrix} \boldsymbol{v_x} \\ \boldsymbol{v_y} \end{bmatrix} = \begin{bmatrix} \boldsymbol{G} & \boldsymbol{-B} \\ \boldsymbol{B} & \boldsymbol{G} \end{bmatrix} \begin{bmatrix} \boldsymbol{v_x} \\ \boldsymbol{v_y} \end{bmatrix} \tag{4.4}$$

Where:

$\boldsymbol{\phi_x}$ and $\boldsymbol{\phi_y}$ are the x and y components of the Norton's current source, which does not depend on the network voltages [A] or [pu]

$\boldsymbol{G_{eq}}$ and $\boldsymbol{B_{eq}}$ are the conductance and susceptance matrices of components [S] or [pu]

Rearranging (4.4) leads to:

$$\begin{bmatrix} \boldsymbol{\phi_x} \\ \boldsymbol{\phi_y} \end{bmatrix} = \begin{bmatrix} \boldsymbol{G + G_{eq}} & \boldsymbol{-B - B_{eq}} \\ \boldsymbol{B + B_{eq}} & \boldsymbol{G + G_{eq}} \end{bmatrix} \begin{bmatrix} \boldsymbol{v_x} \\ \boldsymbol{v_y} \end{bmatrix} \tag{4.5}$$

In this formulation there are two separate terms; the left term comes from components which are not explicitly depending on the voltage and the right term involves a new admittance matrix which includes the contribution of components in addition to the network admittance matrix.

Figure 4-9 shows the general structure of a complete system model when it is simulated using the ULg library. Each component provides its Norton's current as well as its Norton's admittance. If the component current exclusively depends on the voltage (e.g. constant admittance load), it provides a null current vector. The whole system is solved by the Matlab/Simulink® solver directly, however, component equations (red part on the figure) are modeled as Matlab/Simulink® block-diagram while the inversion of the modified admittance matrix (4.5) (blue part on the figure) is described in Matlab® script embedded in the Matlab/Simulink® environment. In addition to operating points, the Artere program provides, automatically, the nodal admittance matrix and the Matlab® script.

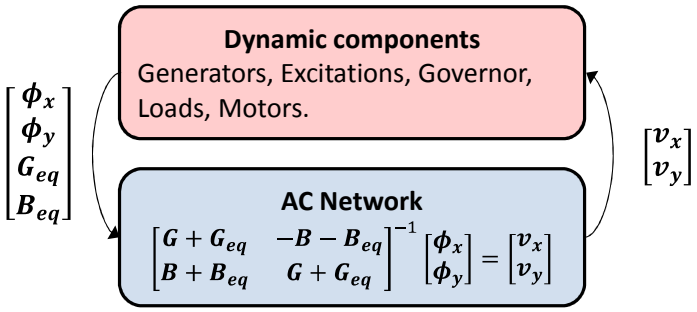

Figure 4-9: Principle of quasi-sinusoidal simulation in ULg library

4.4.2. AC grid test system

The AC system considered is presented in Figure 4-10, it is a well-known two-area system studied for inter-area oscillations [KUN94]. The inter-area oscillations are more important as the power through the tie line is important. This test system is also considered for AC-DC studies; with LCC-HVDC based transmission [KLE91], with VSC-HVDC based transmission [CHA11a], and with MTDC [PIN11] [CHA11c].

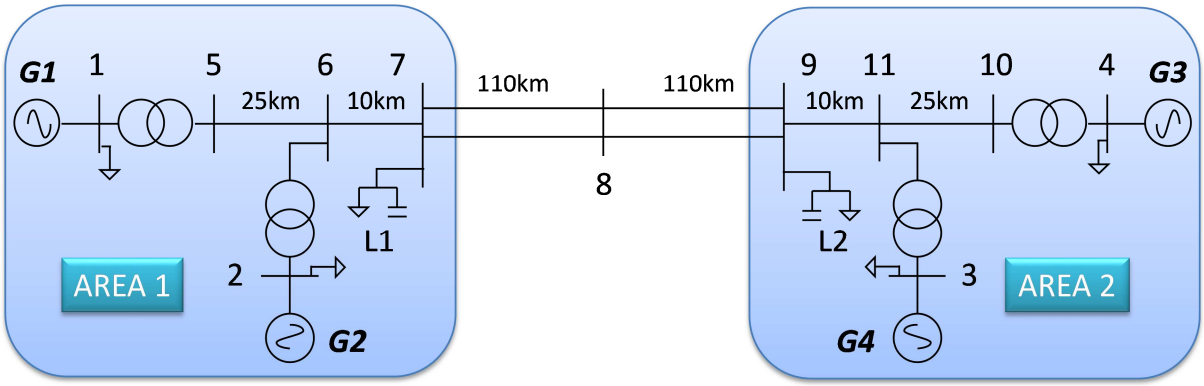

Figure 4-10: AC test system

Parameters of this test system are reported in Appendix G. The initial configuration is given in Table 4-4, it corresponds to no power transfer between the two areas.

Table 4-4: Operating point of the AC system

	Active power [MW]	Reactive power [MVar]	Voltage [kV]
G1	715	108	1.03
G2	715	82	1.01
G3	760	91	1.03
G4	715	13	1.01
L1	-1190	100	1.02
L2	-1235	250	1.03

In order to assess the effects of a future mode change, it is necessary to achieve a modal analysis on this test system with initial conditions. Mode shapes of electromechanical modes are displayed in Figure 4-11. From eigenvalues (which are not displayed) and mode shapes, classical electro-mechanical modes are identified; (from left to right) Mode 16 represents the Area 1 local

mode, Mode 17 represents the Area 2 local mode, Mode 23 represents the inter-area mode and Mode 35 represents the common mode.

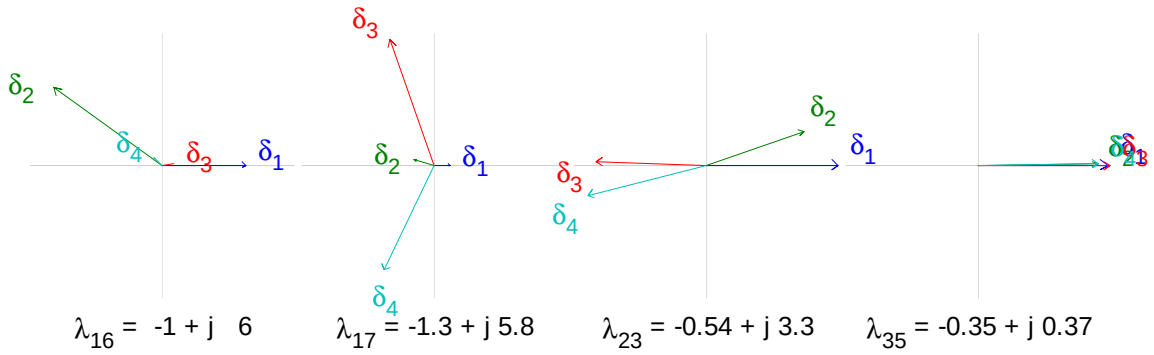

Figure 4-11: Mode shapes of the rotor angle modes – No power transfer between the two areas

To distinguish mode evolution due the integration of VSC or due to power flow change, a modal analysis is performed on the AC system alone, with a second configuration, i.e. with a 400 MW power transfer from Area 2 to Area 1. This power transfer is achieved by increasing the load L1 consumption by 400 MW and by decreasing the load L2 consumption by 400 MW. The mode shapes of electromechanical modes are displayed in Figure 4-12. As results, the value of local modes (16 and 17) has not much evolve even if their mode shape has slightly been modified. The inter-area mode is less damped and its mode shape shows more participation of G1 and G2 than G3 and G4. Moreover, rotors of G1 and G2 are not swinging against rotors of G3 and G4 in perfect opposition as they were before. Regarding the common mode there is no significant change.

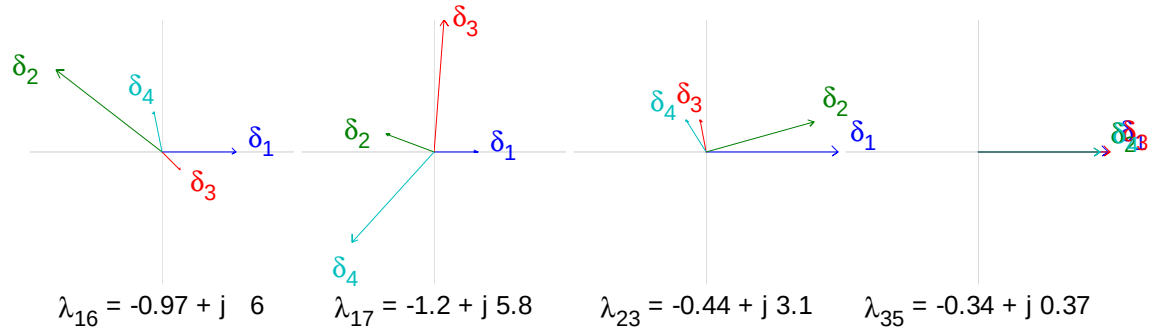

Figure 4-12: Mode shapes of the rotor angle modes – 400 MW power transfer from Area 2 to Area 1

4.4.3. Modeling a MTDC system using the ULg library

In this part, the model of a current controlled VSC connected to the AC grid is proposed. Since the AC and DC side of a VSC can be split up, only the AC side and its associated control is considered in this part. The model of a current vector controlled VSC connected to a phasor AC grid has already been developed in [ZHA10]. However, this model is not suitable for the ULg library since it is a linearized model and it does not correspond to the philosophy presented in the previous part.

The RL filtered VSC, as presented in Chapter 1 Figure 1–13, can be considered as a Thévenin's source which is voltage controlled. Therefore to be implemented in the ULg library, the VSC must be modeled as a Norton's equivalent defined by an admittance and a controlled current source:

$$\overline{y_{eq}} = g_{eq} + jb_{eq} = \frac{R_s - jX_s}{R_s^2 + X_s^2} \tag{4.6}$$

$$\bar{\phi} = \phi_x + j\phi_y = \frac{\left(v_{m_x} + jv_{m_y}\right)(R_s - jX_s)}{R_s^2 + X_s^2} \tag{4.7}$$

Where:

R_s and X_s are the VSC phase reactor elements [Ω] or [pu]

v_{m_x} and v_{m_y} are the voltage phasor at the converter side [V] or [pu]

The VSC associated with its controllers implemented in the ULg library is shown in Figure 4-13. As already mentioned in Chapter 1, the converter is controlled in the dq rotating frame. This frame is synchronized with the AC voltage phasor at the point of common coupling thanks to a PLL by controlling the q-axis grid voltage (v_{g_q}) to zero. Note that the measured voltage is filtered by a low pass filter to avoid explicit dependence between the Norton's current source and the network voltage through of the current controller. This filter is not annoying since voltage measurements are filtered in a real VSC. Differential Algebraic Equation (DAE) of the controlled VSC are described in the dq rotating frame as presented in Chapter 1. The dq voltage at converter AC side (v_{m_d},v_{m_q}) are projected onto the network reference frame (v_{m_x},v_{m_y}) and then are transformed as Norton's current source by using (4.7).

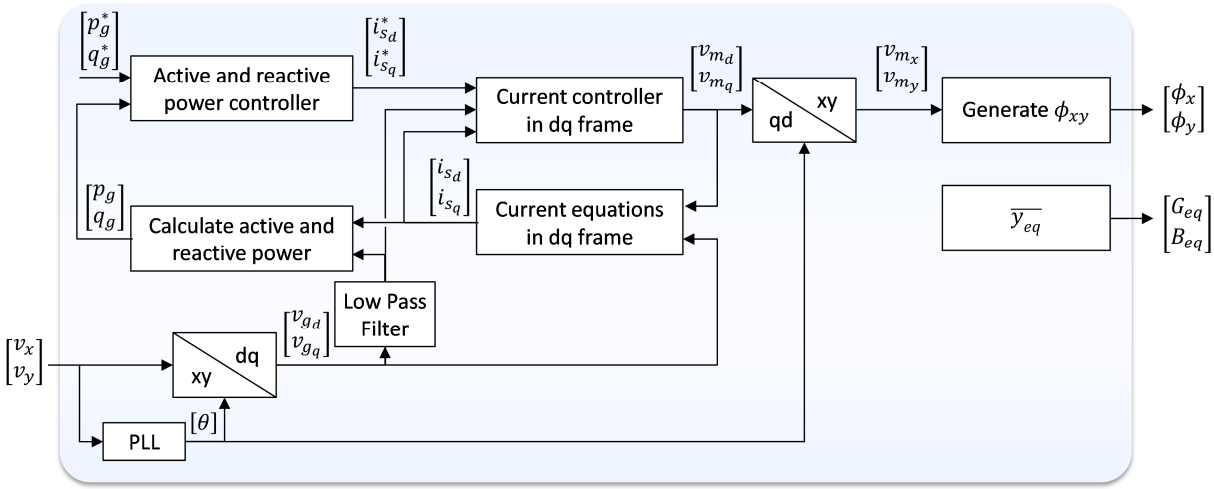

Figure 4-13: VSC model implemented in ULg library (AC side)

The model of the DC side of the converter is presented in Figure 4-14 and equations are those of Chapter 1. The DC side power is obtained by multiplying the phase reactor current and the voltage at the converter AC side. The input is the phase reactor current and the output is the DC voltage.

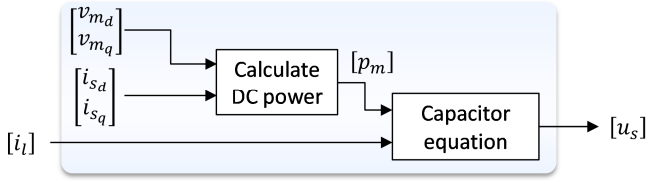

Figure 4-14:VSC model implemented in ULg library (DC side)

The connection of several converter stations to the same DC grid can be done by two different ways. The first method is shown in Figure 4-15a, the DC grid is modeled as a state space system, smoothing reactor as well as DC cables are represented by their RLC circuits. The DC grid model already developed for linearized system can be used since the DC grid equations are linear. The second method is shown in Figure 4-15b, the DC grid is modeled as DC admittance matrix, this is similar to the quasi-sinusoidal approximation since differential equations relative to the DC grid inductances and capacitors are not considered. The DC grid admittance matrix cannot be directly used since not all node voltages are provided. A reduced admittance matrix has been developed for this purpose (see Appendix J). In the following, the DC grid is modeled as state space since it gives more accurate results. However, the DC grid may be modeled by static elements when slow phenomena are considered since it enables faster simulations.

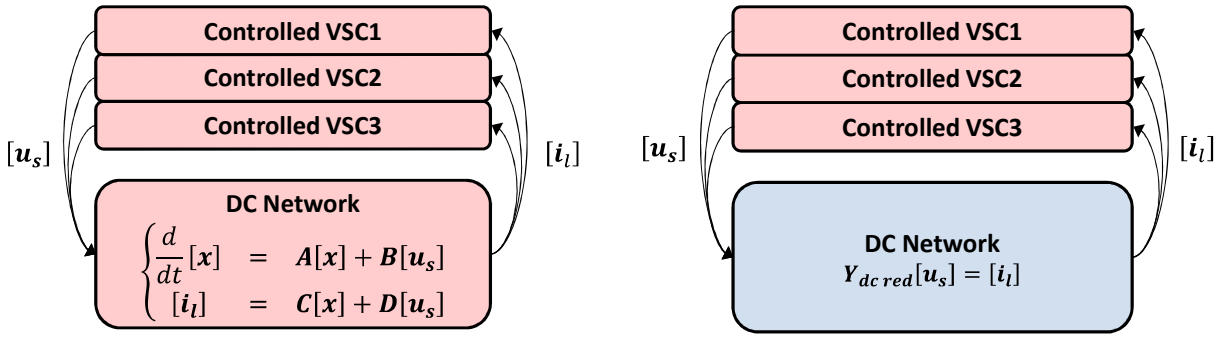

(a) DC grid modeled as state space model (b) DC grid modeled as admittance matrix

Figure 4-15: Simulation of a DC grid in ULg library

In order to validate the DC system modeling, the scenario on the five-terminal DC grid presented in part 4.2 is simulated in the ULg library. The Five-terminal DC grid is either modeled with state space DC grid (ULg1) or with an admittance matrix (ULg2). In Figure 4-16a, the DC voltage at GS1 and the active power at the PCC of GS2 are compared with the detailed model (EMTP). In Figure 4-16b, eigenvalues are compared with those obtained with the linearized model. Results obtained from both, time domain simulation and modal analysis are very similar than those previously validated. It should be noted that there are new eigenvalues which come from the PLL control loops.

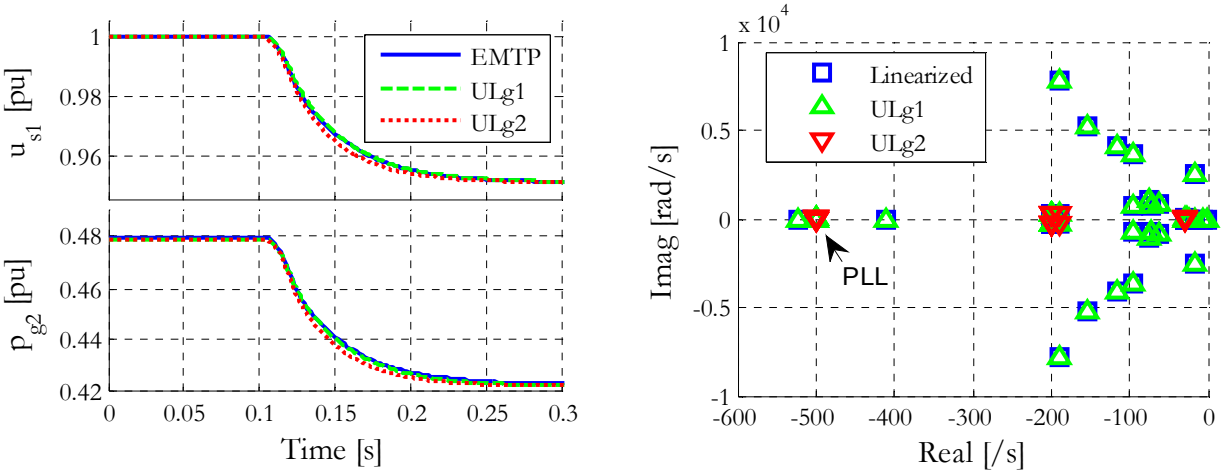

(a) Step change of 172 MW in WF5 (b) Root locus

Figure 4-16: Validation of the five-terminal DC grid modeled in the ULg library

4.4.4. Interactions of a combined AC-DC system without frequency support

In this part the AC test system is connected to the five-terminal DC grid, GS1 and GS2 are connected to node 7 and 9, respectively, as shown in Figure 4-17.

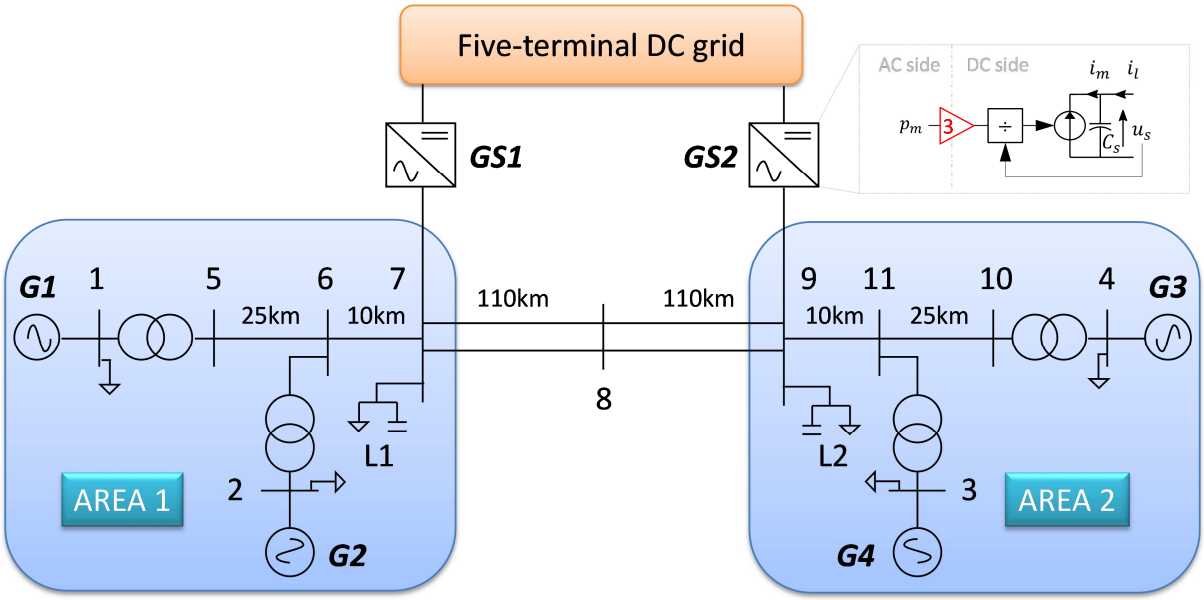

Figure 4-17: Combined AC-DC system

Nonetheless, the nominal power of GS1 and GS2 (i.e. 1320 MW and 1500 MW) cannot be handled by the AC grid. There are three possibilities to connect these two power system in the simulation. The first possibility consists in scaling up the power of the AC system, this is easy to do for the synchronous generators and load since they are defined in per unit, however, lines are designed for a specific power transfer, so it should need some expert assessments. The second dual possibility consists in scaling down the DC system, but it presents same difficulties as the first possibility. The chosen possibility consists in keeping these two systems exactly as they are.

Since an average converter model is used, it is possible to define a relation of proportionality between the AC side and the DC side. Thus, the power transferred from the AC side to the DC side is simply multiplied by a coefficient representing the AC-DC power ratio. The nominal powers of converter stations are summarized in Table 4-5. Looking at GS2 in Figure 4-7, the power measured in the AC side is multiplied by three in the DC side.

Table 4-5: AC-DC simulation – converter station nominal powers

	Nominal power [MW] (AC side)	Nominal power [MW] (DC side)
GS1	440	1320
GS2	500	1500
WF1	1440	1440
WF2	792	792
WF3	510	510

The AC-DC test system is evaluated using modal analysis for two different operating points. For both operating points, wind farms are delivering 1242 MW (i.e. 616 MW, 388 MW and 238 MW supplied respectively by WF1, WF2 and WF3). Regarding the AC grid, loads and power injections from the DC grid are calculated to have no power transfer between the two areas in one case and 400 MW of power transfer from Area 2 to Area 1 in the second case. Loads L1 and L2 as well as converter stations GS1 and GS2 are adjusted to achieve these power flows, their values are summarized in Table 4-6.

Table 4-6: Operating points in the AC grid

	L1 [MW]	L2 [MW]	GS1 [MW]		GS2 [MW]	
			AC	DC	AC	DC
Case 1 (0 MW)	1580	1240	-403	-1218	-6	-18
Case 2 (400 MW)	1580	1240	-6	-18	-403	-1218

Figure 4-18 shows the general structure of the combined AC-DC system when it is simulated using the ULg library. This figure gathers both Figure 4-9 and Figure 4-15, where grid side voltage source converter stations are the links between the Kundur's grid and the five-terminal DC grid.

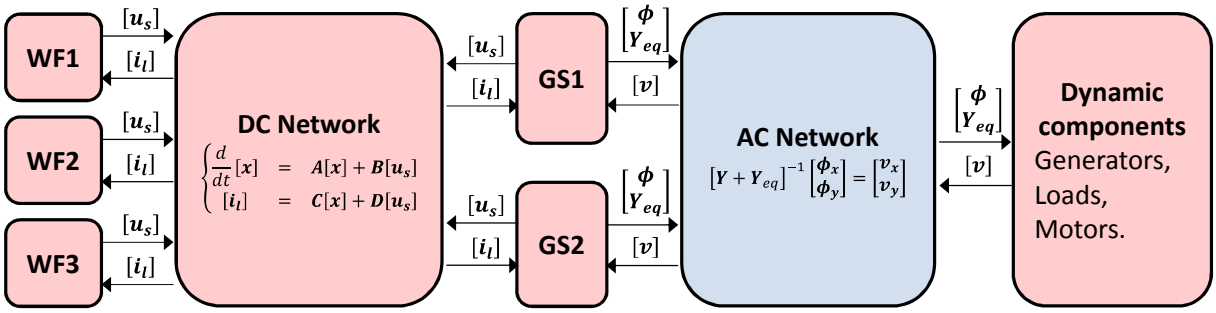

Figure 4-18: Block diagram of the combined AC-DC system in the ULg library

The Eigenvalues analysis performed on the AC-DC test system with no power transfer between both AC. AC modes of the AC system alone are retrieved in the AC-DC system at the

same values. DC modes are also at the same value than the DC grid alone. Dynamics from AC and those from DC are retrieved in the global system without any change; therefore the dynamics of the AC-DC is only a juxtaposition of both system dynamics.

The current control loop modes as well as the PLL modes are slightly modified due to AC system connection; they are marginally influenced by AC lines impedances.

In order to see the impact of power dispatch on the AC modes, mode shapes of electromechanical modes are displayed in Figure 4-19 and Figure 4-20 for both cases. In Figure 4-19, mode shapes reveal that electromechanical modes are similar to the case with no power transfer between the two zones (Figure 4-11). Mode shapes in Figure 4-20 correspond to the case with 400 MW power transfer from Area 2 to Area 1 (Figure 4-12).

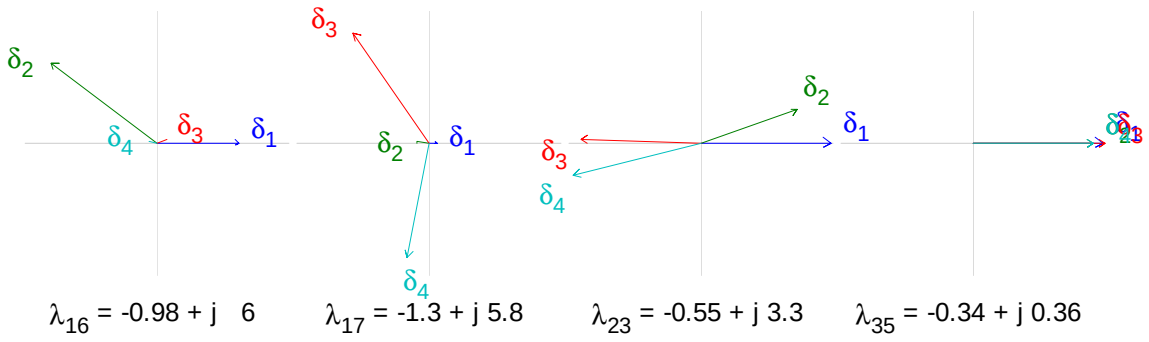

Figure 4-19: Modes shapes of the AC-DC test system without frequency support – Case 1

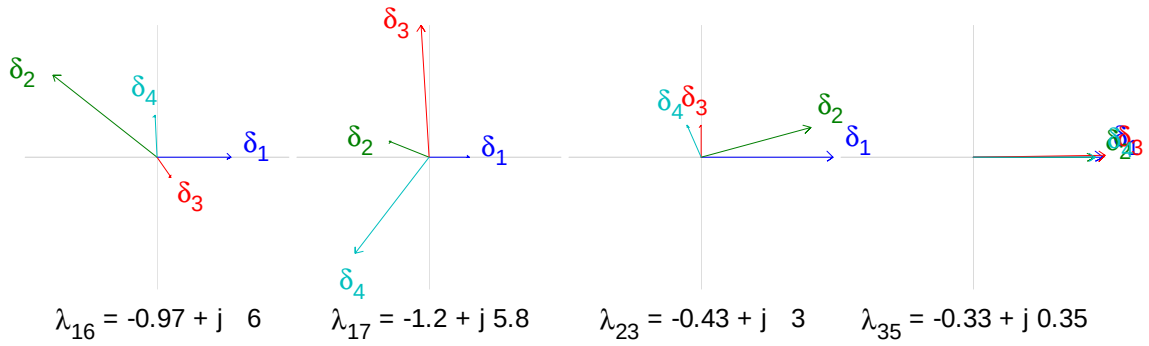

Figure 4-20: Modes shapes of the AC-DC test system without frequency support – Case 2

4.4.5. Interactions of a combined AC-DC system with frequency support

As proposed in [SIL12], a DC system can share primary reserve between asynchronous AC grids. In this section, the grid side converter stations GS1 and GS2 are embedded with frequency support in their control schemes. To do this, the power converter power set-point P_g^* is not only adjusted by the DC voltage droop control but also by the AC frequency droop. The whole controller is shown in Figure 4-21. The frequency droop parameter R determines the frequency deviation according to the output power deviation. Since the current control loop and the AC frequency control loop are nested loops, the frequency estimated by the PLL present in the converter must be filtered by a low-pass filter in order to ensure that both control loops are

decoupled. The frequency filter is chosen ten times faster than the current control loops (ω_f=35 rad/s):

$$H_f(s) = \frac{\hat{f}_f}{\hat{f}}(s) = \frac{1}{1 + \frac{s}{35}} \tag{4.8}$$

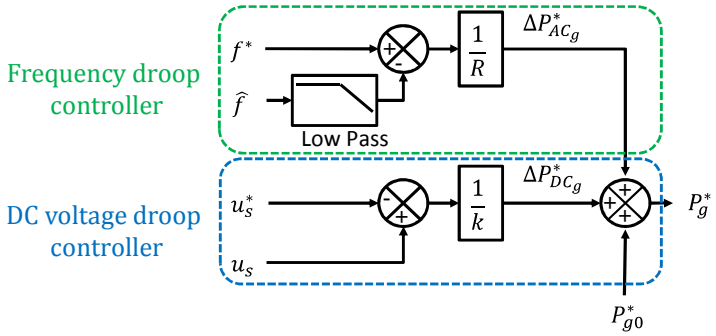

Figure 4-21: Frequency droop and DC voltage droop controller

Eigenvalues analysis is performed on the same AC-DC test system with no power transfer between both AC areas and using a frequency droop controller set at 5 % (i.e. R=0.05) on both grid side converter stations. This value is a typical value for primary frequency support and is similar value to the one used for synchronous generators (i.e. 4 %). In Table 4-7, only modes which have experienced an evolution due to the frequency support are reported.

Table 4-7: Eigenvalues of the AC-DC test system

	No Freq. Support		With Freq. Support		Comment
	Eigenvalues	Dominant States	Eigenvalues	Dominant States	
23	-0.55 ± j 3.3	G1/delta G3/delta G4/delta G1/omega G3/omega G4/omega	-0.59 ± j 3.3	G1/omega G1/delta G3/delta G4/delta G3/omega G4/omega	Inter-area mode
DC18	-28 ± j 1.2	GS1/us GS1/Xp GS2/us GS2/Xp WF1/us	-21 ± j 12	GS1/us GS1/F_w GS1/Theta_PLL GS2/us GS2/F_w GS2/Theta_PLL WF1/us WF2/us	DC voltage mode
DC19	-180 ± j 240	GS1/Xid GS1/isd GS1/isq GS1/Xiq	-280 ± j 160	GS1/Xid GS1/isd GS1/Theta_PLL GS2/Xid GS2/isd GS2/Theta_PLL GS1/control_PLL GS2/control_PLL	Current control loop modes
DC36	-490 ± j 86	GS1/Theta_PLL GS1/control_PLL	-320 ± j 440	GS1/Theta_PLL GS2/F_w GS2/isd GS2/Theta_PLL	PLL modes
DC			-24	G1/psiq2 G2/psiq2 GS1/F_w GS2/F_w	Frequency filter mode

Although, most of the modes have not been modified, there are some significant differences. Firstly, the states associated mainly with PLLs participate in more modes. They are now among the states most influenced by the mode DC19 and DC20 initially related to the d-axis current loop (i.e. active power control). In the same way, modes DC36 and DC37 which are linked to the PLL of GS1 and GS2 have now higher participation in the states of the d-axis current loop.

Electromechanical modes are faintly impacted by the frequency support, only the inter-area mode is slightly more damped (from -0.55 ± j 3.3 to -0.59 ± j 3.3).

On the other hand, the DC voltage mode (DC18) evolves slightly from -28 ± j 1.2 rad/s to -21 ± j 12 rad/s, under the effect of the frequency support. It is important to note that the states most involved in the DC voltage mode evolution were initially (i.e. without frequency support) states associated with converter power loops of GS1 and GS2 (GS1/Xd and GS2/Xd) and those associated with converter station capacitors (GS1/us, GS2/us, WF1/us, WF2/us, WF3/us) and are now states associated with converter station capacitors and also frequency filter and states associated with the PLL of GS1 and GS2 (GS1/F_w, GS1/Theta_PLL, GS2/F_w and GS2/Theta_PLL). The DC voltage mode is impacted by both the DC voltage control loop and the frequency control loop. The frequency control loop involves AC line impedances, PLL, frequency filter and the frequency controller.

The main conclusion of this investigation on the frequency droop parameter is the fact that instabilities are, admittedly, the frequency droop parameter concerns, but above all the matter of frequency measurement and frequency filter. It should be emphasized that it is not common for electromechanical mode studies on AC system since there are no frequency measurements by PLL because the frequency is directly provided by the speed of the generator. Also, the DC voltage dynamics are very sensitive to the DC system frequency support.

Parametric studies have been performed on this AC-DC test system and are presented in Appendix H to not overload this chapter.

4.4.6. Electromechanical modes of two-asynchronous areas connected by a DC system

In this part, the effect of two asynchronous AC grids connection by a DC grid is investigated. The AC system studied in the previous part is split into two asynchronous AC systems: the two areas are disconnected from each other to form two asynchronous grids. The five-terminal DC grid is still connected to the AC system at node 7 for GS1 and at node 9 for GS2, as shown in Figure 4-22.

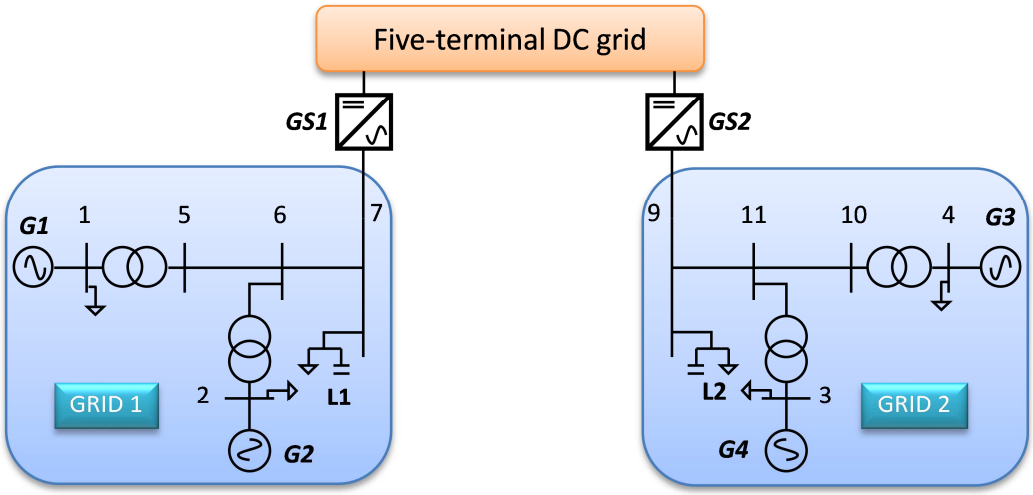

Figure 4-22: Connection of two asynchronous grids by a DC grid

Two case studies are considered:

- The DC system is not supporting the frequency
- The DC system is supporting the frequency with a frequency droop constant set to 0.05 pu/pu.

In the first case there is no frequency support from one AC grid to the other one. In the second case the two grids, share their primary reserve through the DC system.

Mode shapes of electromechanical modes are reported in Figure 4-23 when there is no frequency support and in Figure 4-24 when there is frequency support. In Figure 4-23, as expected, electromechanical modes of each grid are independent since only rotor angle states of the same grid are influenced by a given mode. From the left to the right there is the local mode of Grid 1, the local mode of Grid 2, the common mode of Grid 1 and finally the common mode of Grid 2. In Figure 4-24, the DC system is supporting the frequency, local modes have not change at all; however, the "common modes" of the two AC grids are both influenced by the other grid while they are asynchronous. Indeed, not only the states δ_{g_1} and δ_{g_2} participate in the Grid 1 "common mode" evolution, but also δ_{g_3} and δ_{g_4} in lower proportion (by definition, if only Grid 1 "common mode" is excited, states δ_{g_1} and δ_{g_2} would show an higher activity than δ_{g_3} and δ_{g_4}). The same comment can be done for the "common mode" of Grid 2. To sum up, there is the modal coupling between electromechanical modes of the two asynchronous AC grids connected by a DC system only if grid side converter stations are supporting the frequency.

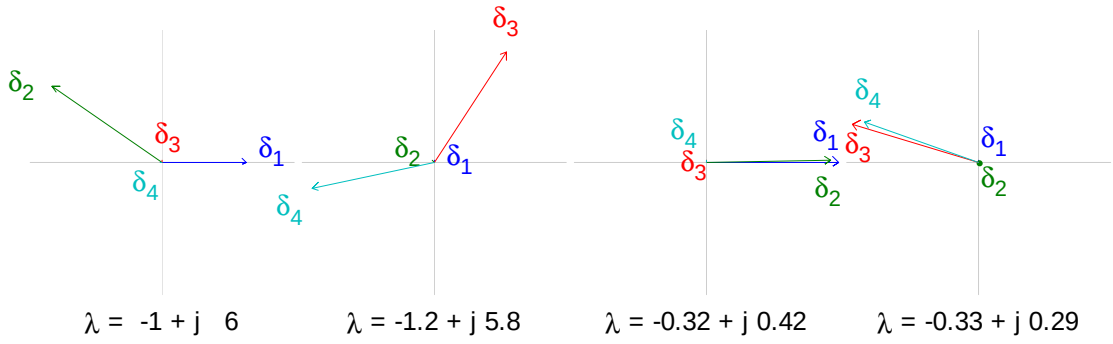

Figure 4-23: Modes shapes of the two AC grids without frequency support

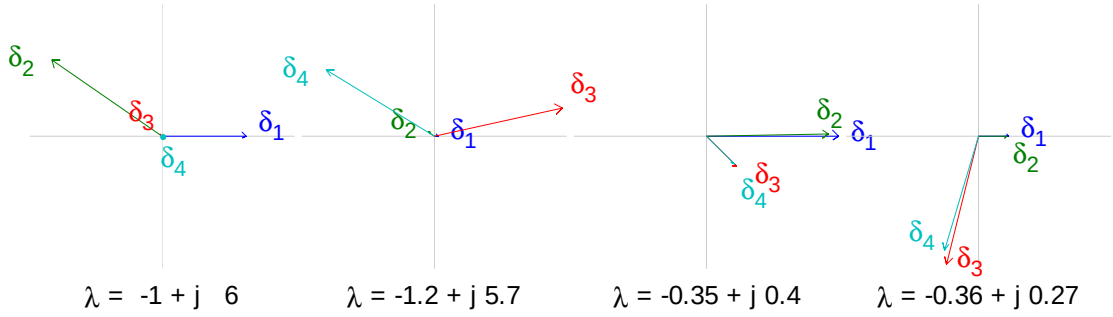

Figure 4-24: Modes shapes of the two AC grids with frequency support

4.5 CONCLUSION

In this chapter, the modeling of a Multi-terminal DC grid has been presented. The in-depth analysis performed on the DC system has shown that there is no mixes between modes from the converter station control loops and modes from the DC grid since modes from the DC grid have much higher dynamics.

The DC voltage mode identified in Chapter 3, has been retrieved among other DC system modes, it has been tracked along this chapter. As results, this mode is driven by parameters involved in the Chapter 3 simplified formula, namely DC grid capacitance and droop voltage value. However, it has been observed that its value is lower than expected when its dynamics approaches the converter station current control loop dynamics. Furthermore, even if the connection to an AC system has no impact on this mode, the frequency support from the DC grid leads to modify its dynamics.

A comparison with the results of modal analysis performed on each system independently enabled to clearly identify the changes of modes stemming from the coupling between AC and DC systems. All in all, this analysis revealed that the AC and DC modes are not strongly coupled since the dynamics of AC systems are much slower than the dynamics of DC systems.

When the DC system is supporting the frequency, electromechanical modes are a little bit influenced, nevertheless there are no mixes between modes originally referred as AC and DC modes. When connecting two asynchronous AC grids by a DC grid, it should be noted that each electromechanical mode is influenced by electromechanical states belonging to the same grid as long as there is no frequency support, while it is influenced by electromechanical states belonging to several AC grids when the DC system is supporting their frequency.

CHAPTER 5: Coordinated control

5.1 INTRODUCTION

Like for an AC system, the DC grid must be monitored and controlled to check if the system works properly and to manage power flows. This is achieved by a master controller which has a global view of the system; it supervises the whole DC grid and coordinates the converters set points. Indeed, local controls are preferred to a remote control of the DC grid power balance so as not to rely on communication (see Chapter 3), however this kind of control cannot manage power flows [BAR10]. Following system operator's orders and the scheduled power transmissions, the master controller sends references to all DC grid devices. Also, in case of contingency, it automatically finds a new stable operating point and then sends corresponding references to remaining devices. Moreover, unlike frequency in the AC system, the DC voltage is not at the same value everywhere in the DC grid due voltage DC line voltage drops, so voltage drops and transmission losses must be considered to send suitable converter settings in order to achieve a precise power flow control [HAI12].

Section 5.2 describes the role of a SCADA system and how it operates. Section 5.3 presents numerical methods used to calculate steady state operating points to find suitable set points for DC grid devices. In section 5.4, coordinated control methods are assessed for one day of wind production. In section 0, it is shown how a coordinated controller can help the system to recover a stable operating point after a severe event. In section 5.6, the DC grid coordinated controller communicates with the TSO of connected AC grid to alleviate AC congestions. Finally, this chapter ends with a conclusion which discusses benefits and limitations of coordinated controllers.

5.2 DC SCADA SYSTEM OVERVIEW

The Supervisory Control And Data Acquisition (SCADA) overview of the DC grid is shown in Figure 5-1. The SCADA system typically refers to a master terminal unit (MTU) and several remote terminal units (RTU) which are linked by data transmission media. The MTU is often a host computer which gathers information from remote devices and sends orders to them. The transmission media used to transmit the information could be physical (e.g. Ethernet, optical fiber) or wireless (e.g. radio waves, satellites). The kind of application which can be handled by the SCADA system relies on the communication speeds in combination with the time required for the data processing.

DC grid measures, operating states, alarms are gathered and analyzed by the DC SCADA system and then relevant information are displayed on a control panel for the DC grid system operator. The SCADA system is composed of Human-Machine Interface (HMI) which can translates system operators' orders into commands for devices. Thus, the operator can turn on or off converters, change power and voltage references, connect disconnect lines or converters.

The DC grid scheduled power transfers have been established in advance to plan the desired power transits between different AC areas and the distribution of the forecasted wind power production. This can be obtained either on an energy pool market or by a planning process realized by TSOs and DC grid operators. The planning program is sent to the SCADA system to fulfill the scheduled power injections.

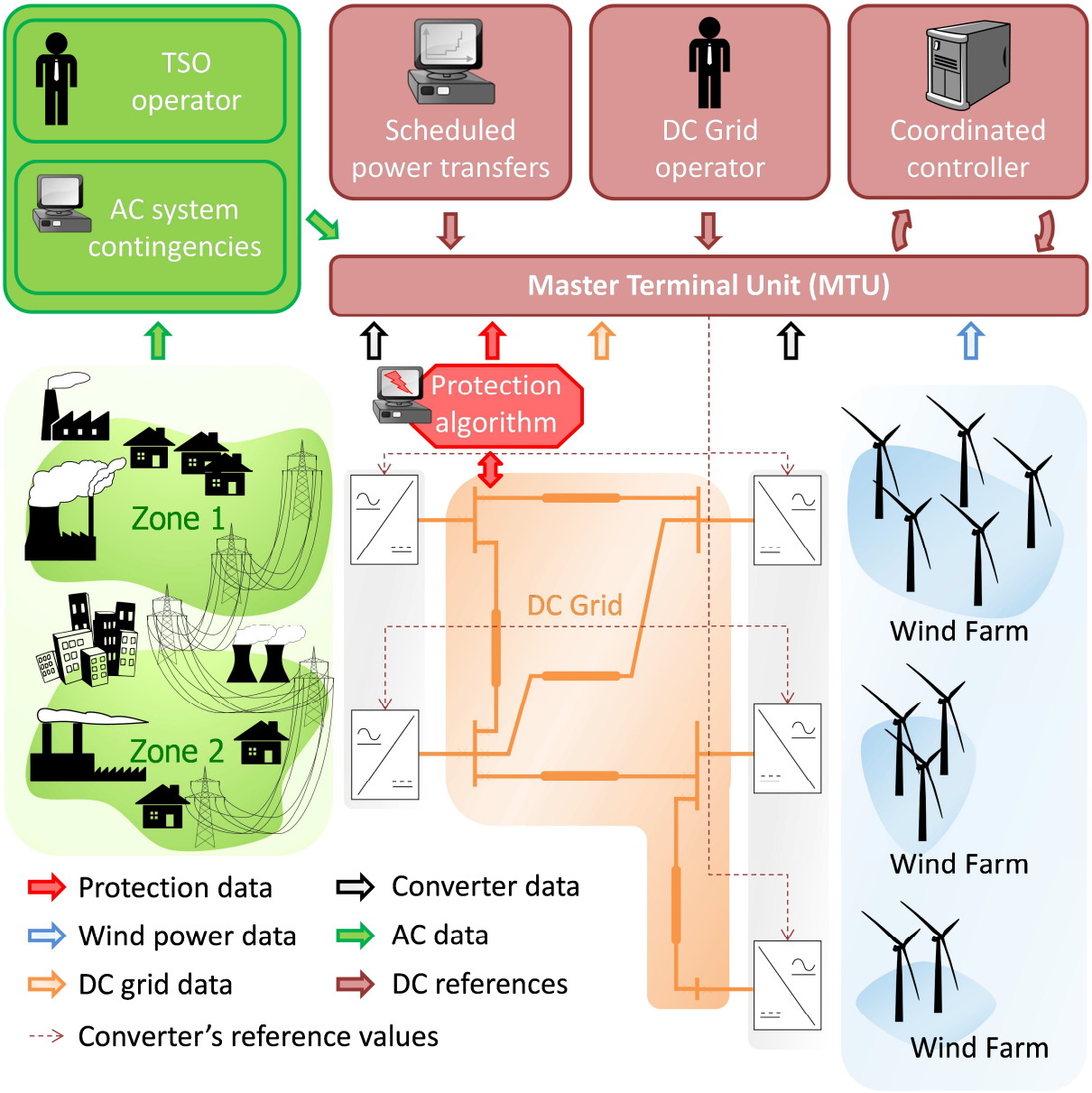

Figure 5-1: General overview of the DC SCADA system

In a real situation, wind power production does not exactly match the prediction. To solve this problem, the possible wind power production is also sent to the MTU system which, in turn, sends it with the scheduled program to the coordinated controller. This one computes converter's references in order to deliver the wind power to AC areas and to respect as much as possible the power injection program. This will be detailed later.

The DC protection algorithm is not a part of the SCADA system because of communication latency; data processing speed are not fast enough. Hence, a dedicated device is used for that purpose; it is described in the following part. Nevertheless, this device can communicate information on the protection status and on events which have occurred in the DC grid to the MTU.

The SCADA system also allows exchanging information between TSOs of AC areas and DC grid. In the same way, information of AC grid contingencies can be sent to the DC SCADA system which adjusts automatically the set points of the affected on-shore grid side converters.

5.3 POWER FLOW CALCULATION ON MTDC GRIDS

5.3.1. DC admittance

The objective of this part is to obtain automatically the DC grid admittance matrix of any topology to solve directly DC grid Kirchhoff's laws. For static calculations the DC grid is only represented by its resistive elements. As an example the five-terminal topology is represented in Figure 5-2, conductor cable losses are represented by a series resistance (R_{ij}) and insulation losses by a shunt resistance (R_{ii}). The cable conductance is split and equally distributed at the two cable ends. The shunt resistance at each terminal represents the sum of haft-conductance of connected cables. In this figure the losses of the smoothing reactor are also taken into account (R_{SRi}). In practice the power flow is mainly driven by line resistances, shunt resistances and smoothing reactor resistances are not preponderant. Firstly, for the sake of simplicity only the positive cable is considered and the ground potential is taken to be at zero volt. The generalization to two poles will be presented afterward.

The sign conventions are defined as follows:

- Ground potential is zero volt
- Node voltage is the difference between the node potential and the ground potential. In case of two-poles (i.e. symmetric monopolar or bipolar) transmission, the node voltage is the difference, at the corresponding node, between the potential of the positive cable and the potential of the negative cable.
- Line currents are defined, in the positive cable by the current flowing from the first node (first subscript) towards the second node (second subscript). For two-poles the current through the negative cable is in the opposite direction.
- Injected currents are the ingoing currents in the node for positive cable and outgoing currents for negative cables.
- Line powers are the power flowing at the first node (first subscript) towards the second node (second subscript). For two-pole transmission, the power flow is the sum of the power flows in the positive cable and in the negative cable.
- Injected powers are the ingoing powers in one node. For two-pole transmission, the injected power is the sum of the injected powers in the positive cable and in the negative cable.

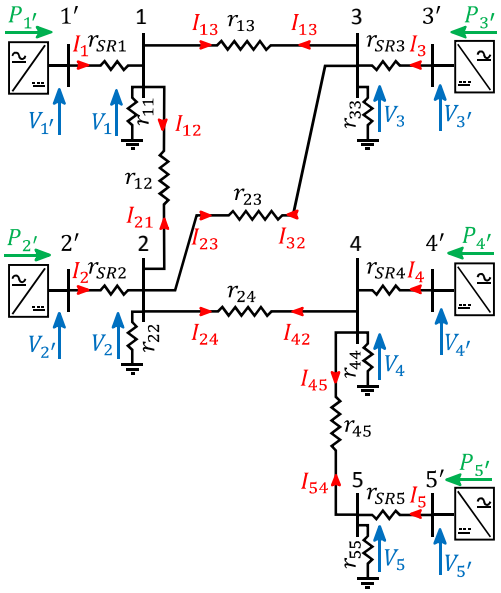

Figure 5-2: Static representation of the five-terminal DC grid

At each terminal, the algebraic sum of branch currents plus the current through the shunt resistance is null, so the injected current is defined as follows:

$$I_i = \sum_{\substack{j=1 \\ j \neq i}}^{n} I_{ij} + I_{ii} \tag{5.1}$$

Where

I_i is the injected current at the ith terminal

I_{ij} is the branch current between ith and jth terminals

I_{ii} is the current through the shunt resistance

n is the node number

The previous equation can be rewritten using the DC grid resistances and node voltages:

$$I_i = \sum_{\substack{j=1 \\ j \neq i}}^{n} \frac{1}{R_{ij}} (V_i - V_j) + \frac{V_i}{R_{ii}} \tag{5.2}$$

Considering the whole DC grid, the previous relation can be written in a matrix form:

$$\boldsymbol{I} = \boldsymbol{Y}\,\boldsymbol{V} \tag{5.3}$$

Where

$\boldsymbol{I}$ is a vector containing injection currents

$\boldsymbol{Y}$ is the admittance matrix

$\boldsymbol{V}$ is a vector containing node voltages

The admittance matrix $\boldsymbol{Y}$ is filled by:

$$\begin{cases} Y_{ij} = -\dfrac{1}{R_{ij}} & \forall i \neq j \\ Y_{ii} = \displaystyle\sum_{k=1}^{n} \dfrac{1}{R_{ij}} \end{cases} \quad (5.4)$$

If there is no link between the two stations, the resistance is infinite and therefore the admittance value is null. Since the link between terminal i and terminal j is defined by the resistor R_{ij} which is identical to R_{ji}, the admittance matrix is symmetric. Each element of the admittance matrix diagonal (Y_{ii}) is the sum of all connected admittances.

Solving negative and positive pole configurations leads to solve the problem twice: once for the positive pole and once again for the negative pole. If both poles have similar parameters and no asymmetric studies are considered (e.g. no pole to ground fault), voltages and injected currents have same magnitude in opposite direction. Hence, in that case the system can be solved once, either on the positive or the negative pole.

5.3.2. DC steady-state calculation

The DC admittance matrix allows solving directly Kirchhoff's laws; this is useful to simulate the DC grid. However, usually the system operator knows the voltages at some terminals and currents at others, therefore, the admittance matrix cannot be simply used. In [JOV09a] and [MAY10], they rearrange equations in order to set the voltage level at least at one node and to impose current injections for others. The system resolution gives injection currents for known node voltages and voltages for known currents.

Theory

In this part, the DC network is generalized to a n node network, with l known voltages and $n - l$ known injected currents. For the sake of clarity, current and voltage vectors are sorted, firstly filled by the unknown currents and secondly by unknown voltages. Nevertheless the method works as well with an unordered matrix. The ordered matrix equation of the DC network is presented below.

$$\begin{bmatrix} I_1 \\ \vdots \\ I_l \\ I_{l+1} \\ \vdots \\ I_n \end{bmatrix} = \begin{bmatrix} Y_{11} & \ddots & Y_{1l} \\ \vdots & \ddots & \vdots \\ \vdots & \ddots & \vdots \\ \vdots & \ddots & \vdots \\ \vdots & \ddots & \vdots \\ Y_{n1} & \ddots & Y_{nl} \end{bmatrix} \begin{bmatrix} Y_{1\,l+1} & \ddots & Y_{1n} \\ \vdots & \ddots & \vdots \\ \vdots & \ddots & \vdots \\ \vdots & \ddots & \vdots \\ \vdots & \ddots & \vdots \\ Y_{n\,l+1} & \ddots & Y_{1n} \end{bmatrix} \begin{bmatrix} V_1 \\ \vdots \\ V_l \\ V_{l+1} \\ \vdots \\ V_n \end{bmatrix} \quad (5.5)$$

The first step consists in splitting the current and voltage vectors in two parts in order to separate known from unknown variables. Then the new two admittance matrices are simplified by setting zeros at the unused part:

$$\begin{bmatrix} I_1 \\ \vdots \\ I_l \\ 0 \\ \vdots \\ 0 \end{bmatrix} + \begin{bmatrix} 0 \\ \vdots \\ 0 \\ I_{l+1} \\ \vdots \\ I_n \end{bmatrix} = \begin{bmatrix} Y_{11} & \ddots & Y_{1l} \\ \vdots & \ddots & \vdots \\ \vdots & \ddots & \vdots \\ \vdots & \ddots & \vdots \\ \vdots & \ddots & \vdots \\ Y_{n1} & \ddots & Y_{nl} \end{bmatrix} \begin{bmatrix} 0 \end{bmatrix} \begin{bmatrix} V_1 \\ \vdots \\ V_l \\ 0 \\ \vdots \\ 0 \end{bmatrix} + \begin{bmatrix} 0 \end{bmatrix} \begin{bmatrix} Y_{1\,l+1} & \ddots & Y_{1n} \\ \vdots & \ddots & \vdots \\ \vdots & \ddots & \vdots \\ \vdots & \ddots & \vdots \\ \vdots & \ddots & \vdots \\ Y_{n\,l+1} & \ddots & Y_{1n} \end{bmatrix} \begin{bmatrix} 0 \\ \vdots \\ 0 \\ V_{l+1} \\ \vdots \\ V_n \end{bmatrix} \quad (5.6)$$

The second step consists in moving to the left the unknown voltages and doing the opposite for the known currents:

$$\begin{bmatrix} I_1 \\ \vdots \\ I_l \\ 0 \\ \vdots \\ 0 \end{bmatrix} - \begin{bmatrix} 0 & \cdots & \begin{matrix} Y_{1\,l+1} & \ddots & Y_{1n} \\ \vdots & \ddots & \vdots \\ \vdots & \ddots & \vdots \\ \vdots & \ddots & \vdots \\ Y_{n\,l+1} & \ddots & Y_{1n} \end{matrix} \end{bmatrix} \begin{bmatrix} 0 \\ \vdots \\ 0 \\ V_{l+1} \\ \vdots \\ V_n \end{bmatrix} = \begin{bmatrix} Y_{11} & \ddots & Y_{1l} \\ \vdots & \ddots & \vdots \\ \vdots & \ddots & \vdots \\ \vdots & \ddots & \vdots \\ Y_{n1} & \ddots & Y_{nl} \end{bmatrix} \begin{bmatrix} 0 \\ \vdots \\ V_l \\ 0 \\ \vdots \\ 0 \end{bmatrix} - \begin{bmatrix} 0 \\ \vdots \\ 0 \\ I_{l+1} \\ \vdots \\ I_n \end{bmatrix} \tag{5.7}$$

The third step consists in summing the two parts of each side to get a unique vector of unknowns in the left and known values in the right. After this operation the previous equation looks like

$$\left[\begin{array}{ccc|ccc} 1 & & 0 & & & \\ & \ddots & & & & \\ 0 & & 1 & & & \\ \hline 0 & \cdots & 0 & & & \\ & \ddots & & & & \\ 0 & \cdots & 0 & & & \end{array}\right] \begin{bmatrix} -Y_{1\,l+1} & \ddots & -Y_{1n} \\ \vdots & \ddots & \vdots \\ \vdots & \ddots & \vdots \\ \vdots & \ddots & \vdots \\ -Y_{n\,l+1} & \ddots & -Y_{1n} \end{bmatrix} \begin{bmatrix} I_1 \\ \vdots \\ I_l \\ V_{l+1} \\ \vdots \\ V_n \end{bmatrix} = \begin{bmatrix} Y_{11} & \ddots & Y_{1l} \\ \vdots & \ddots & \vdots \\ \vdots & \ddots & \vdots \\ \vdots & \ddots & \vdots \\ Y_{n1} & \ddots & Y_{nl} \end{bmatrix} \left[\begin{array}{ccc} 0 & \cdots & 0 \\ & \ddots & \\ 0 & \cdots & 0 \\ \hline -1 & & 0 \\ & \ddots & \\ 0 & & -1 \end{array}\right] \begin{bmatrix} V_1 \\ \vdots \\ V_l \\ I_{l+1} \\ \vdots \\ I_n \end{bmatrix} \tag{5.8}$$

Finally, the unknowns are solved by inverting the left matrix of the previous equation:

$$\begin{bmatrix} I_1 \\ \vdots \\ I_l \\ V_{l+1} \\ \vdots \\ V_n \end{bmatrix} = \left[\begin{array}{ccc|ccc} 1 & & 0 & & & \\ & \ddots & & & & \\ 0 & & 1 & & & \\ \hline 0 & \cdots & 0 & & & \\ & \ddots & & & & \\ 0 & \cdots & 0 & & & \end{array}\right] \begin{bmatrix} -Y_{1\,l+1} & \ddots & -Y_{1n} \\ \vdots & \ddots & \vdots \\ \vdots & \ddots & \vdots \\ \vdots & \ddots & \vdots \\ -Y_{n\,l+1} & \ddots & -Y_{1n} \end{bmatrix}^{-1} \begin{bmatrix} Y_{11} & \ddots & Y_{1l} \\ \vdots & \ddots & \vdots \\ \vdots & \ddots & \vdots \\ \vdots & \ddots & \vdots \\ Y_{n1} & \ddots & Y_{nl} \end{bmatrix} \left[\begin{array}{ccc} 0 & \cdots & 0 \\ & \ddots & \\ 0 & \cdots & 0 \\ \hline -1 & & 0 \\ & \ddots & \\ 0 & & -1 \end{array}\right] \begin{bmatrix} V_1 \\ \vdots \\ V_l \\ I_{l+1} \\ \vdots \\ I_n \end{bmatrix} \tag{5.9}$$

From (5.9), topologies with passive nodes (i.e. with no converter connected) can be easily handled. In fact, passive nodes are considered as current known nodes with a current set at zero.

Once all injected currents or nodes voltage are known, currents through lines and shunt resistors can be easily retrieved:

$$\begin{cases} I_{ij} = \dfrac{(V_i - V_j)}{R_{ij}} & \forall j \neq i \\ I_{ii} = \dfrac{V_i}{R_i} \end{cases} \tag{5.10}$$

The injected power is obtained by using the scalar product between the current vector and the voltage vector.

$$\boldsymbol{P} = \boldsymbol{V} \cdot \boldsymbol{I} \tag{5.11}$$

Where, the · symbol denotes the element-by-element multiplication, and $\boldsymbol{P}$ is a vector containing the injected power at each node.

The power transmitted at node i towards node j is calculated by using the power line relation:

$$P_{ij} = V_i I_{ij} = \frac{V_i(V_i - V_j)}{R_{ij}} \tag{5.12}$$

And the power through shunt resistors:

$$P_{ii} = V_i I_{ii} = \frac{V_i^2}{R_{ii}} \tag{5.13}$$

If there are positive and negative cables, both with same characteristics, the steady state calculation can be done only on positive cables with resistor matrix of positive cables. The result of the positive cable can be used directly for the negative as power vector is the same, current and voltage vectors have same value with opposite sign. Therefore, to handle symmetrical monopole configurations, the system is solved only on the positive pole and powers and voltages are simply multiplied by two.

Numerical application

The steady state calculation is tested on the five-terminal DC grid (symmetrical monopole configuration) with the following inputs:

- DC voltage of node $1'$ is set at ±320 kV
- Injected current of node $2'$ is $I_2 = -1200\ A$
- Injected current of node $3'$ is $I_3 = 950\ A$
- Injected current of node $4'$ is $I_4 = 600\ A$
- Injected current of node $5'$ is $I_5 = 380\ A$

DC grid data are reported in Appendix C.2. Results of the steady state calculations are the node voltages, injected currents and injected powers, they are displayed in Table 5-1.

Table 5-1: Steady state results (node)

Node	Voltage [kV]	Injected Current [A]	Injected Power [MW]
1	640	0	0
2	640.2	0	0
3	640.5	0	0
4	640.5	0	0
5	641.2	0	0
1'	640	-723.5	-463
2'	640.2	-1200	-768.3
3'	640.5	950	608.5
4'	640.5	600	384.3
5'	641.2	380	243.7

Results are checked thanks to a simulation, using a permanent voltage source for the fixed voltage node and current sources for fixed current nodes, results are identical.

The steady state calculation can also give current and power transfers through lines. The power transfers are displayed in matrix form in Table 5-2.

Table 5-2: Steady state results (Power transfer)

P_{ij}	1	2	3	4	5	1'	2'	3'	4'	5'
1	1.1	-170.5	-293.7	0	0	463	0	0	0	0
2	170.5	1	-313.5	-626.3	0	0	768.3	0	0	0
3	293.9	313.6	1	0	0	0	0	-608.5	0	0
4	0	626.5	0	0.6	-242.9	0	0	0	-384.3	0
5	0	0	0	243.2	0.5	0	0	0	0	-243.7
1'	-463	0	0	0	0	0	0	0	0	0
2'	0	-768.3	0	0	0	0	0	0	0	0
3'	0	0	608.5	0	0	0	0	0	0	0
4'	0	0	0	384.3	0	0	0	0	0	0
5'	0	0	0	0	243.7	0	0	0	0	0

The power transfer matrix enables to see the power transfer through cables, when there is no cable between two nodes the power transfer is obviously null.

Diagonal elements are the cable conductance losses whereas extra-diagonal elements are transmission power transfers. The transmission line losses which are due to cable resistivity are retrieved from the sum of line input power minus the line output powers (i.e. cable losses $= P_{ij} - P_{ji}$). The total losses are 5.2 MW, they represent 0.4 % of the wind power production, their origins are displayed in Table 5-3.

Table 5-3: Losses in the DC grid

	Losses [MW]	[%]
Smoothing reactors	0.07	1.3
Cable conductance	4.19	81
Cable resistance	0.92	17.7
Total	5.2	100

As results, losses due to cable conductance are larger than losses due to cable resistance, and smoothing reactor losses are minor. These results should however be treated with caution as the line resistance is underestimated (see Chapter 3 | 3.2.3) and the power flow is not at its maximum.

5.3.3. Newton-Raphson DC load flow

TSOs are dealing with power instead of currents since they are managing energy transfer. Load flow programs are used for this purpose; they solved the following non-linear formula:

$$\boldsymbol{P = V \cdot I = V \cdot (Y\,V)} \tag{5.14}$$

NR equations

In this part, the NR algorithm is applied to a DC grid load flow. A DC load flow program is simpler than an AC load flow because there are fewer variables: no reactive power and no voltage angle.

This work is strongly inspired by [BEE11] to retrieve power flow equations and power flow algorithm, however the purpose is different. Indeed, the objective of Jef Beerten's work is to calculate the steady state after a disturbance while the objective of this work is to calculate set points for converter stations in order to achieve the desired power flow.

In the same way as previously, typically nodes are classified in two groups, constant voltage or constant power. The voltage nodes are stiffly maintained at constant voltage whereas the voltages of power nodes are unknown. The NR algorithm minimizes the mismatch between the power injections obtained from a given voltage map which is updated by the algorithm and the wanted power injections at power nodes. The power mismatch vector at the k[th] iteration is:

$$\boldsymbol{\Delta P}_{(idx\,P)}^{(k)} = \boldsymbol{P}_{(idx\,P)}^{*} - \left(\boldsymbol{V}_{(idx\,P)}^{(k)} \cdot \boldsymbol{Y}_{(idx\,P)} \boldsymbol{V}_{(idx\,P)}^{(k)}\right) \tag{5.15}$$

Where:

(k) is the iteration number

$(idx\,P)$ is the indexes of constant power nodes

$\boldsymbol{P}_{(idx\,P)}^{*}$ is the reference power vector for constant power nodes

Following NR method the voltage correction vector at constant power nodes is given by:

$$\left(\frac{\boldsymbol{\Delta V}}{\boldsymbol{V}}\right)_{(idx\,P)}^{(k)} = \left(\boldsymbol{J}^{(k)}\right)^{-1} \boldsymbol{\Delta P}_{(idx\,P)}^{(k)} \tag{5.16}$$

Where $\boldsymbol{J}^{(k)}$ is the Jacobian matrix which contains voltage partial derivative over power injection. They are obtained from the power injection definition which is:

$$P_i = V_i \sum_{j=1}^{n} Y_{ij} V_j = V_i \left(\sum_{\substack{j=1 \\ j \neq i}}^{n} Y_{ij} V_j + Y_{ii} V_i \right) \tag{5.17}$$

Therefore, the terms of the Jacobian matrix are defined by:

$$\begin{cases} J_{ij} = V_j \dfrac{\partial P_i}{\partial V_j} = V_j V_i Y_{ij} & \forall i \neq j \\ J_{ii} = V_i \dfrac{\partial P_i}{\partial V_i} = V_i \left(\displaystyle\sum_{\substack{k=1 \\ k \neq i}}^{n} Y_{ik} V_k + 2 V_i Y_{ii} \right) \end{cases} \tag{5.18}$$

Putting (5.17) into (5.18):

$$\begin{cases} J_{ij} = V_j \dfrac{\partial P_i}{\partial V_j} = V_j I_j Y_{ij} & \forall i \neq j \\ J_{ii} = V_i \dfrac{\partial P_i}{\partial V_i} = P_i + V_i^2 Y_{ii} \end{cases} \tag{5.19}$$

The Jacobian matrix can be directly obtained with the following equation:

$$\boldsymbol{J^{(k)}} = diag\left(\boldsymbol{P}_{(idx\,P)}^{(k)}\right) + \boldsymbol{Y}_{(idx\,P)} \cdot \boldsymbol{V}_{(idx\,P)}^{(k)} \left(\boldsymbol{V}_{(idx\,P)}^{(k)}\right)^{T} \tag{5.20}$$

NR algorithm

The load Flow with NR algorithm is given in Figure 5-3.

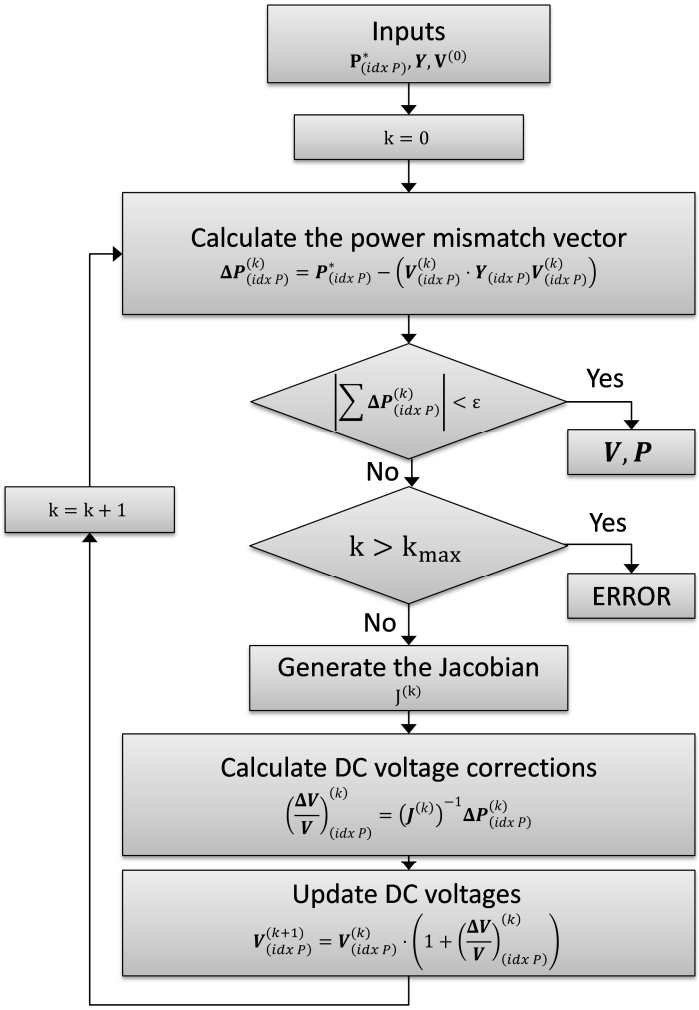

Figure 5-3: Load flow with NR algorithm

The inputs of the program are:

- DC network admittance matrix ($\boldsymbol{Y}$)
- Indexes of constant voltage nodes ($idx\ V$)
- Indexes of constant power nodes ($idx\ P$)
- Tolerance convergence threshold (ε)
- Maximum number of iterations (k_{max})
- Power reference of constant power nodes ($\mathbf{P}^{*}_{(idx\,P)}$)

  Passive nodes are considered constant power nodes with the specified power set at zero.
- Initial voltage vector. ($\mathbf{V}^{(0)}$)

  Voltage vector is filled by specified voltage for constant voltage nodes ($idx\ V$) and by the nominal voltage for others ($idx\ P$).

If the algorithm converges the outputs are:

- The updated voltage vector ($\boldsymbol{V}$)
- The power injection vector ($\boldsymbol{P}$)

Numerical application

Even if mathematically several nodes can be of DC voltage type, in practice only one is considered. Indeed, if there is more than one DC voltage type node, the node power injections are not known for these buses, while if there is only one, almost all node power injections are known; only DC losses which are reported on the slack bus are not known. The load flow algorithm is tested on the five-terminal DC grid with the following inputs:

- DC voltage of node $1'$ is set at ±320 kV
- Injected power of node $2'$ is $P_2 = -758\ MW$
- Injected power of node $3'$ is $P_3 = 616\ MW$
- Injected power of node $4'$ is $P_4 = 384 MW$
- Injected power of node $5'$ is $P_5 = 238\ MW$

The load flow algorithm converges in two iterations (Tolerance threshold 100 W). Results are displayed in Table 5-4.

Table 5-4: Load flow results (node)

Node	Voltage [kV]	Injected Current [A]	Injected Power [MW]
1	640	0	0
2	640.3	0	0
3	640.5	0	0
4	640.5	0	0
5	641.2	0	0
1'	640	-741.9	-474.8
2'	640.2	-1183.9	-758
3'	640.5	961.7	616
4'	640.5	599.6	384
5'	641.2	371.2	238

The power flow algorithm gives the expected results, power at constant power buses are retrieved and the voltage of node $1'$ is still at 640 kV. Results are checked through a time domain simulation, using a permanent voltage source for the fixed voltage node and current sources for fixed current nodes.

5.3.4. DC load flow with power sharing capability

Context

Let's recall that the load flow algorithm is a tool used in the control center to calculate proper references to converter stations in real time. In AC systems, it is well known that there are differences between the scheduled load program and the reality. These differences are handled in the first time by the primary control (i.e. frequency droop control) which ensures the power balance and then by the secondary control which brings back the frequency to its nominal value

and restores border power exchanges. The secondary control consists in sending new power references to some units which are participating to the secondary control at regular time intervals (e.g. 15 minutes). The secondary control is slower than the primary control in order not to interact with it. The TSO prescribes participation to the secondary control at production unit which are participating to it according to their rating [BOR13].

The coordinated control has a similar role in the DC system, its objective is to send new references to converter stations to reestablish the DC voltage at nominal value and maintain the power flow as scheduled when it is possible. The DC grid is often unable to fulfill the scheduled program because of some uncertainties:

- Wind power forecast error
- Unavailability of wind farm
- Unavailability of on-shore station

Using the previous classic load flow algorithm all power uncertainties are borne by the constant voltage bus. Like for primary control and secondary control, it seems better to divide up this power deviation among more than one converter stations. Therefore; a modified load flow algorithm is proposed in order to dispatch the power mismatch between several substations, in accordance to predefined power sharing coefficient called participation to the coordinated control.

This algorithm has the ability to find new set points in order to:

- Share the wind power forecast error to several onshore converter stations
- Share the power deviation due to unavailability of one converter station
- Limit the wind power injection if on-shore converter stations cannot accept more power.

Theory

To fulfill this task, a new term related to power deviation is added to the power reference of each station. All converter stations have an initial power reference (P^*), and some of them can adjust their reference to balance the DC grid power flow. The final powers delivered by converter stations are given by the following formula:

$$\boldsymbol{P} = \boldsymbol{P}^* + \frac{\boldsymbol{\alpha}}{\sum \boldsymbol{\alpha}} P_{dev} \tag{5.21}$$

Where:

$\boldsymbol{P}$	is a vector containing delivered powers,
$\boldsymbol{P}^*$	is a vector containing initial power references of all nodes including the constant voltage node,
$\boldsymbol{\alpha}$	is a vector containing the relative participation of each station,
P_{dev}	is the power balance error.

Unlike the previous method, the power flow of power controlled nodes cannot be guaranteed if their alpha parameter is not null ($\alpha_i \neq 0$). Depending on the value of α_i, a part of

the power balance error is allocated to this node. The power balance error is a new unknown which must be solved by a modified load flow algorithm.

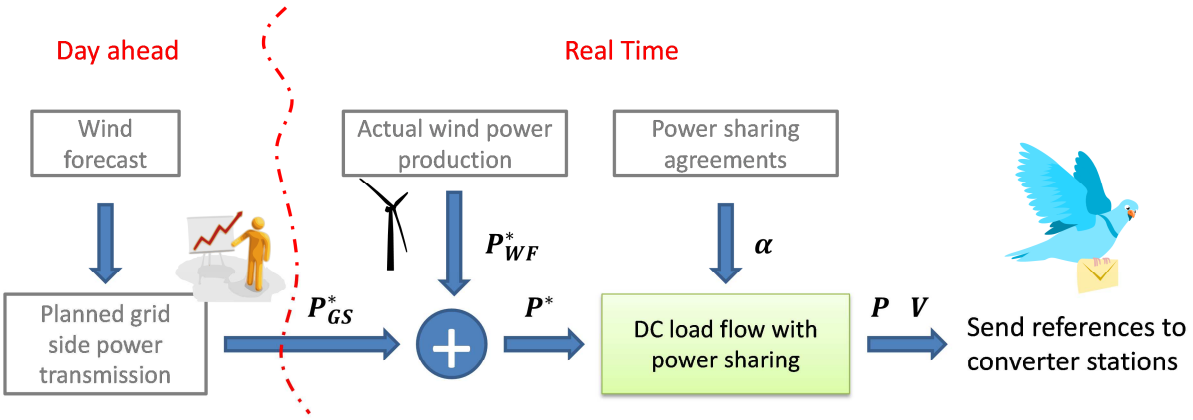

Figure 5-4: Operation scheme of DC load flow with power sharing capability

Figure 5-4 shows the normal operation scheme of the coordinated controller when it is equipped with a DC load flow with power sharing capability. When the system operator wants the whole wind power harvested to be carried on the shore, the power reference vector (P^*) is filled by the actual wind power production (P^*_{WF}) for wind farm converter stations and by the planned power transfer (P^*_{GS}) for grid side converter stations. The power balance error is shared according to the participation $\boldsymbol{\alpha}$ to the coordinated control. The participation of a given station depends on the participation of other stations, i.e. the higher the α coefficient of a station, the larger the portion of the power deviation taken by this station. The stations which have a null participation parameter act as conventional power nodes. The particular case where there is only one converter which has a non-null α parameter is similar as the previous DC load flow.

Vector $\boldsymbol{\alpha}$ may be adjusted according to the objective, for instance if all the wind power must be carried to shore, only the grid side converter stations must participate to the coordinated control. Conversely, if the grid side converter stations are saturated, the wind farm must participate and grid side converter stations shall have a null participation, thus wind power production is limited.

The DC load flow must be adapted to take into account the new unknown (P_{dev}). The mismatch power vector (5.15) is modified as follows:

$$\boldsymbol{\Delta P}^{(k)} = \left(\boldsymbol{P}^* + \frac{\boldsymbol{\alpha}}{\sum \boldsymbol{\alpha}} P_{dev}^{(k)}\right) - \left(\boldsymbol{V}^{(k)} \cdot \boldsymbol{Y}\, \boldsymbol{V}^{(k)}\right) \tag{5.22}$$

The correction of the new unknown (ΔP_{dev}) is introduced into the correction vector as follows:

$$\begin{bmatrix} \Delta P_{dev}^{(k)} \\ \left(\frac{\boldsymbol{\Delta V}}{\boldsymbol{V}}\right)^{(k)}_{(idx\ NV)} \end{bmatrix} = \left(\boldsymbol{J}^{(k)}\right)^{-1} \boldsymbol{\Delta P}^{(k)} \tag{5.23}$$

Where:

ΔP_{dev} is the power deviation correction

$(idx\ NV)$ is the indexes of not fixed voltage nodes

As a basic principle of linear algebra, the number of linearly independent equations must be equal to the number of unknowns to find the system solution. Therefore, the power mismatch vector concerns all nodes while traditionally the power of the slack bus is not considered. For the same reason, voltage corrections are given for all nodes except one, the one where the voltage is fixed by the operator.

To solve this linear system, the Jacobian is also modified. Partial derivatives of the first column express the sensitivity of the power deviation on the node mismatch powers. They are defined as follows:

$$J_{i1} = \frac{\partial P_i}{\partial P_{dev}} = -\frac{\alpha_i}{\sum \boldsymbol{\alpha}} \tag{5.24}$$

Partial derivatives of other columns are referred to the Jacobian used by typical DC load flow (5.19).

Algorithm

This advanced load flow program is similar to the NR based typical load flow algorithm with the exception of the power deviation value. The flow chart of the modified load flow is presented in Figure 5-5.

The inputs of the program are:

- DC network admittance matrix ($\boldsymbol{Y}$)
- Indexes of constant voltage nodes
- Indexes of not fixed voltage nodes ($idx\ NV$)
- Power reference vector($\mathbf{P}^*$)
  Passive nodes are considered as constant power nodes with specified power set at zero.
- Power sharing vector ($\boldsymbol{\alpha}$)
  Passive nodes as well as constant power nodes are set at zero.
- Initial voltage vector. ($\mathbf{V}^{(0)}$)
  Voltage vector is filled by specified voltage for the fixed voltage node and by the nominal voltage for others.
- Tolerance convergence threshold (ε)
- Maximum number of iterations (k_{max})

If the algorithm converges the outputs are:

- The updated voltage vector ($\boldsymbol{V}$)
- The power injection vector ($\boldsymbol{P}$)

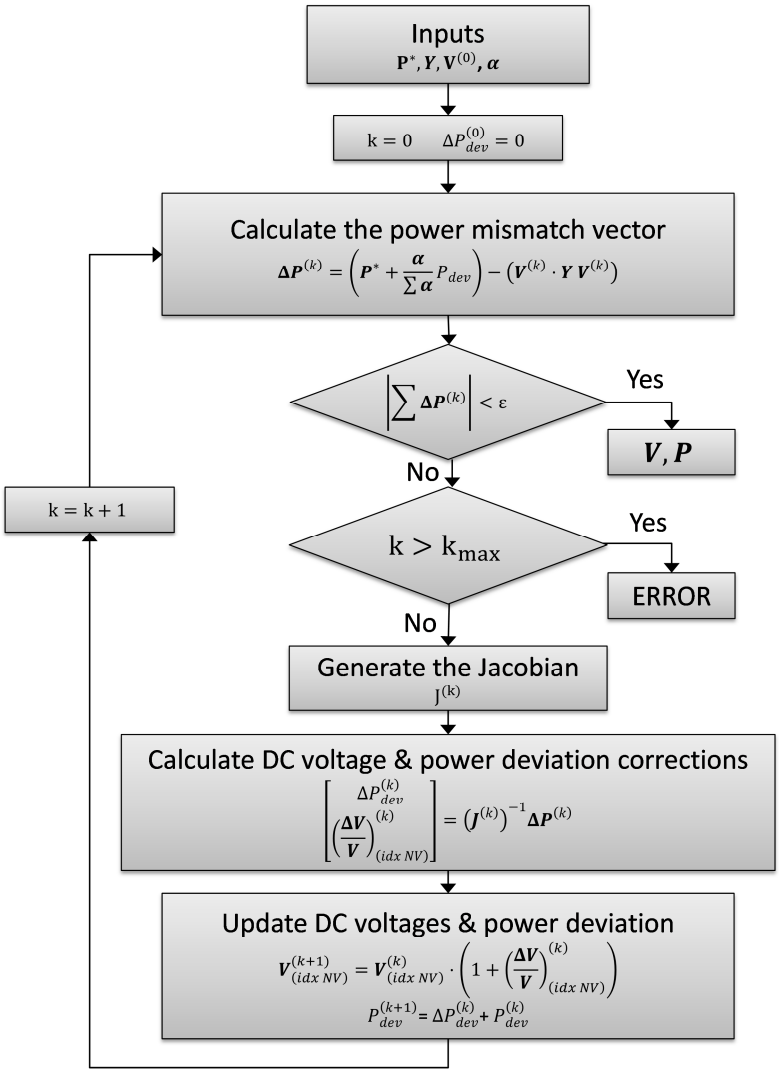

Figure 5-5: DC load flow with power sharing capability

Numerical application

The operation of this algorithm is explained by the way of a small scenario. The day ahead, on the electricity pool market, the schedule wind production was 600 MW for the first wind farm (i.e. converter station n°3), 400 MW for the second wind farm (i.e. converter station n°4) and 200 MW for the third wind farm (i.e. converter station n°5). As result of the electricity pool market the AC grid connected at the converter station n°1 takes 700 MW and the rest for the AC grid connected at the converter station n°2, that is 500 MW. Furthermore, since the second grid is stronger than the first one, it was agreed by both TSOs that wind power forecasted errors are twice more allocated to converter station 2 than converter station 1. The next day, the wind production was not exactly at the forecasted value: the first wind farm was delivering 616 MW, the second wind farm 384 MW and the third wind farm 238 MW.

The load flow with power sharing capability allows finding references which fulfills the aforementioned conditions. To solve this problem the input data are filled as follows:

- DC voltage of node $1'$ is set at ±320 kV

- Injected power of node $1'$ is $P_1 = -700\ MW$
- Injected power of node $2'$ is $P_2 = -500\ MW$
- Injected power of node $3'$ is $P_3 = 616\ MW$
- Injected power of node $4'$ is $P_4 = 384MW$
- Injected power of node $5'$ is $P_5 = 238\ MW$
- Stations 1&2 are participating to the coordinated control, station 2 participates twice more than the station 1: $\alpha_1 = 1, \alpha_2 = 2$

The load flow algorithm converges in two iterations (Tolerance threshold 100 W). Results are displayed in Table 5-5.

Table 5-5: Load flow results (node)

Node	Voltage [kV]	Injected Current [A]	Injected Power [MW]
1	640	0	0
2	640.5	0	0
3	640.7	0	0
4	640.7	0	0
5	641.4	0	0
1'	640	-1110.7	-710.9
2'	640.5	-814.6	-521.7
3'	640.7	961.5	616
4'	640.7	599.4	384
5'	641.4	371	238

Power flow computation gives the expected results, power value at constant power nodes are retrieved and the voltage of node $1'$ is still at 640 kV. The original power balance error is given by:

$$\begin{aligned} P_{dev} &= (-710.9 + 700) + (-521.7 + 500) \\ &= -10.9 - 21.7 = -32.6\ MW \end{aligned} \quad \textbf{(5.25)}$$

The power deviation due to the scheduled error is -32.6 MW, stations 1 takes 1/3 and the station 2 takes 2/3, as requested by the system operator.

After the load flow calculation, the control center sends a power reference of -710.9 MW to converter station n°1 and a power reference of -521.7 MW to converter station n°2.

5.4 STRATEGY IN NORMAL OPERATION

5.4.1. Simulation of the five-terminal DC grid

The five-terminal DC grid is simulated during one day (Figure 5-6). Wind power profiles as well as planned grid side power transfers are the inputs of the simulation. The simulation is achieved on Matlab/Simulink®. Converters are simulated as averaged model with inner and outer controllers and the DC grid is simulated using the reduced admittance matrix ($Y_{dc\,red}$) presented in Appendix J. The DC grid could be simulated using the DC grid state space model but the simulation speed is far slower than with the admittance matrix while results are similar.

The DC grid is simulated in the same condition as in Chapter 4, grid side stations are droop controlled and wind farm stations deliver the whole wind power. The droop parameter is set at 0.82 for both onshore stations (i.e. response time of 100ms).

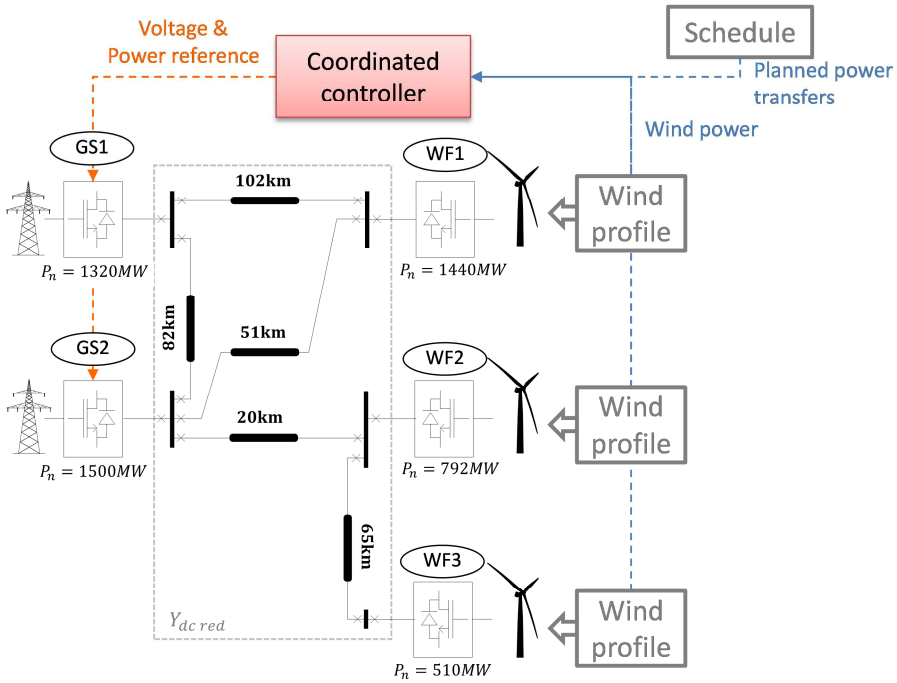

Figure 5-6: Simulation of the five-terminal DC grid

The coordinated controller is embedded in the Matlab/Simulink® simulation using a special block called "S-Function", which enables to integrate Matlab® functions, such as the load flow program. It receives as inputs the wind power production from each wind farm and the scheduled power transfer of onshore converters. The DC voltage of GS1 is imposed at 1 pu. The coordinated controller calculates the new references at given instants and sends power and voltage references to grid side converter stations.

5.4.2. Wind power profiles

Simulated wind power production is obtained from real wind power production data of three wind farms located in the same area close to the shore. These data are 10-minute production data, given in percent of the wind farm nominal power. These data are scaled to the nominal power of each wind farm (i.e. 1440 MW, 792 MW and 510 MW for respectively wind farm 1, 2 and 3).

To be simulated with a time step lower than ten minutes, data are interpolated each 6 seconds using a cubic interpolation method to avoid derivative discontinuities. Results are plotted for 1 day of production in Figure 5-7a and zoomed for two hours in Figure 5-7b. Square symbols are the given data, lines are the interpolated data.

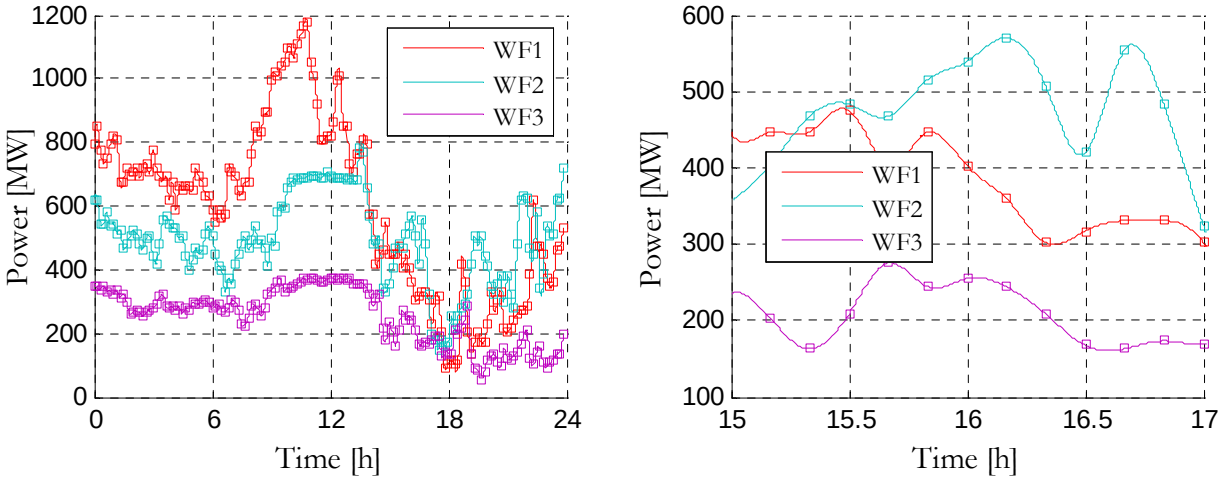

(a) 24 hours (b) 2 hours

Figure 5-7: Wind power production

5.4.3. Scheduled power transfer

Because DC losses are neglected, the sum of input and output powers must be null. Since there are at least two grid side injection points, the power transfer is not forced (?). So using the wind power production schedule, AC grid TSOs and the DC grid operator can plan the power injection program one day ahead. This injection program must remain compatible with the operating limits, such as substation rating and transmission cable ampacities (Cable overcurrent is not treated in this work but will have to be considered in further studies).

For simulation needs, the wind power forecast is generated from production data. The forecasted wind power is generated from the normal distribution with sliding 1 hour window mean wind data values and a standard deviation of 10%. On Figure 5-8a, the wind power production data is solid line and the forecasted is dotted line.

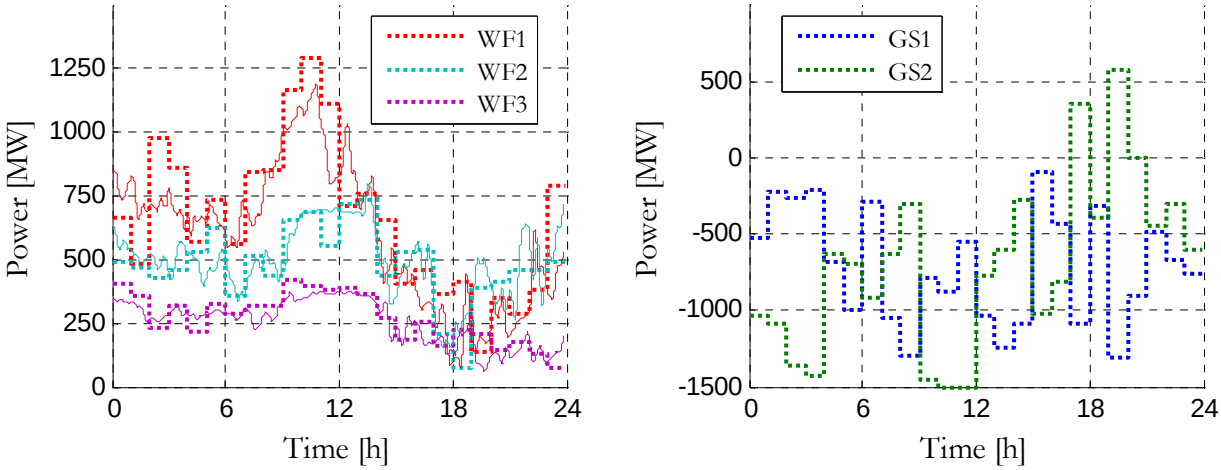

(a) Wind power forecast (b) Planned grid power transfer

Figure 5-8: Planned DC grid power exchanges

The power injection at the first grid side point is obtained from a uniform distribution between 0 and its nominal power. The power injection of the second is set to balance the DC grid power injection. If the power injection of the second one is higher than the substation's nominal power, the planned power transfer is set at the substation's nominal power and the power injection of the first station is set at a value which balances the DC grid. The planned grid power transfer is plotted in Figure 5-8b.

5.4.4. Simulation of one day

Without coordinated control

The first simulation is performed without the coordinated control, the power reference of a wind farm station is the actual wind power production and the power reference of a grid side stations is the planned power transfer, presented in the previous paragraph (Figure 5-8b). DC voltage and DC power are plotted in Figure 5-9. In Figure 5-9b dotted lines are the planned values, solid lines are the simulated values. DC power injections of wind farm converter stations are not reported because there is no change from Figure 5-8a.

In Figure 5-9b, grid side power transfers are close to the ones planned by TSOs, the forecast error is shared by both onshore stations; however the DC voltage exceeds the limits.

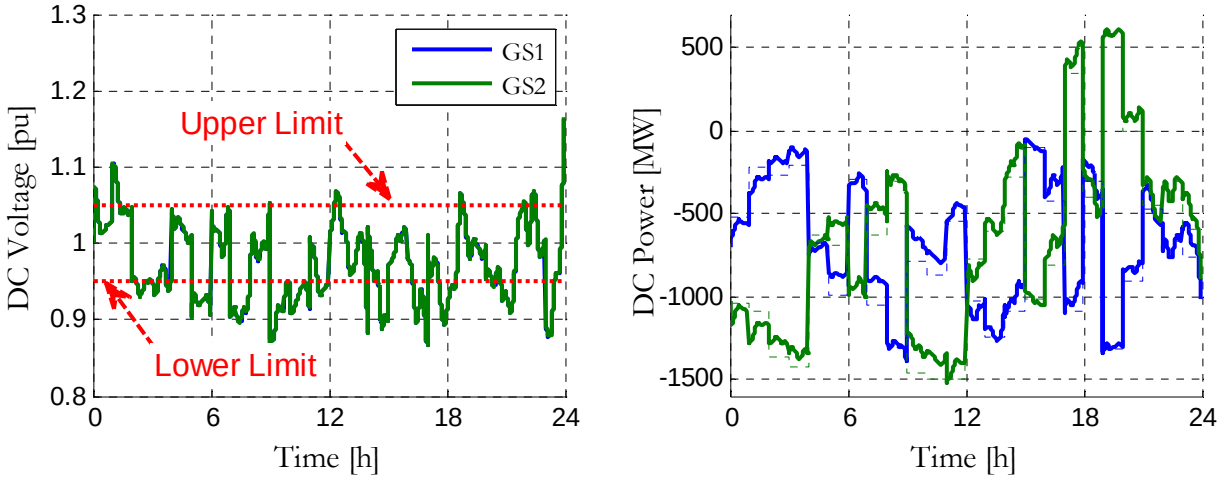

(a) DC voltage (b) DC power

Figure 5-9: Simulation of one day – without the coordinated control

With coordinated control without power sharing capability

The coordinated controller sends new references to grid side converters. References are the DC voltage reference and the power reference that are calculated using a classical load flow, the GS1 station is the slack bus and the power reference of GS2 is the power transfer forecast. The power reference input vector of the load flow algorithm is filled by the scheduled on-shore power transfer and the actual wind power production. Two case studies are simulated: in the first case references are sent each ten minutes and in the second case references are sent each minute. Results are respectively plotted in Figure 5-10 and in Figure 5-11.

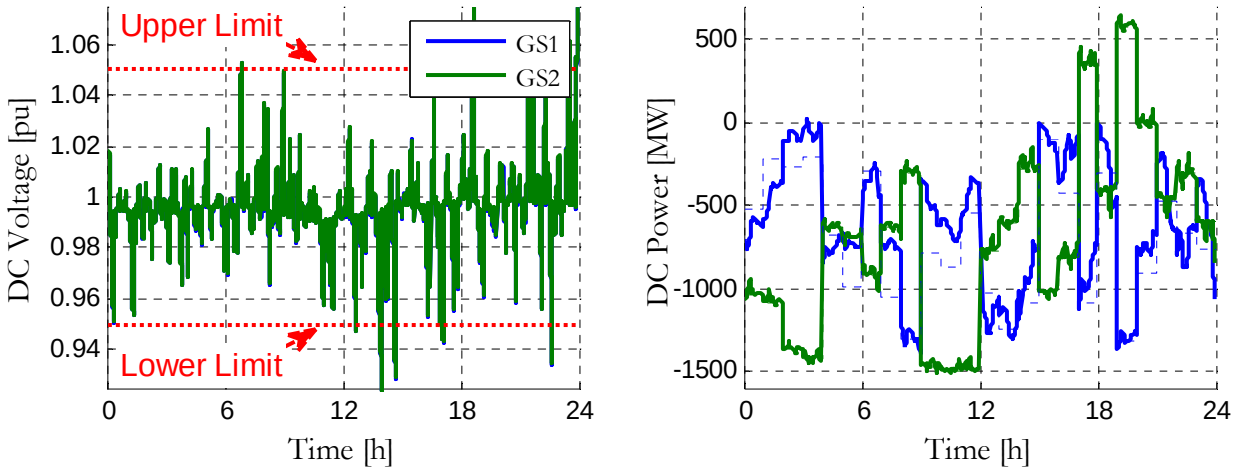

(a) DC voltage (b) DC power

Figure 5-10: Simulation of one day – load flow without power sharing – each 10 minutes

The DC voltage returns close to its nominal value after each refreshment of the references. If phase reactor converter losses had been considered in the power flow program, the DC voltage would return exactly to the nominal value after reference sending. For both cases the power injection of the GS2 station matches the reference, while the GS1 balances the DC grid power flow. The case where references are sent each ten minutes is more fluctuating than the case where references are sent each minute. In the first case the DC voltage is mainly between bounds while in the second case the DC voltage is very close to the nominal DC voltage.

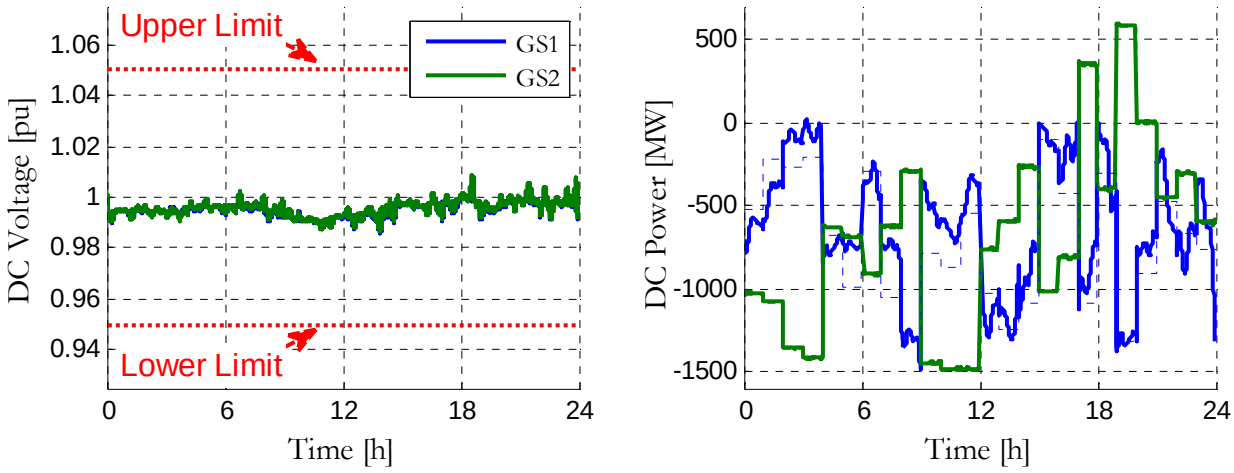

(a) DC voltage (b) DC power

Figure 5-11: Simulation of one day – load flow without power sharing – each 1 minute

With coordinated control with power sharing capability

In this part the coordinated control sends new references to grid side converters each minute, as in the previous paragraph. However the converter control uses the load flow with power sharing capability instead of the classical power flow. The power reference input vector of the load flow algorithm is filled by the scheduled on-shore power transfer and the actual wind

power production. In this case, the power sharing parameters are set at the same value for both grid side converter stations and set at null value for all wind farm converter stations.

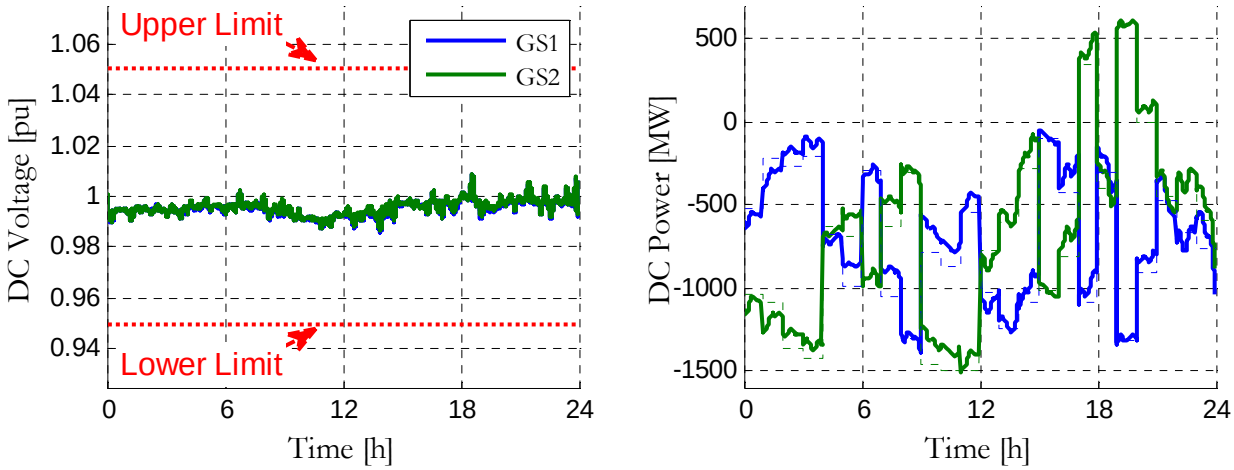

(a) DC voltage (b) DC power

Figure 5-12: Simulation of one day – load flow with power sharing – each minute

In Figure 5-12, the DC voltage profile is comparable from the previous case. As expected, the power schedule error is shared between both onshore converter stations.

5.4.5. Sensibility to the grid parameters

In reality the model of the DC grid and the real DC grid are not exactly the same, due to several reasons such as resistance deviation owing to temperate change. To see the impact of the model error, the previous scenario is simulated with same parameters, except that in the model, the resistance of the cable between the two grid side converter stations is 50 % more resistive than reality (i.e. 0.66 Ω instead of 0.43 Ω). The difference with regard to the previous case is plotted in Figure 5-13.

The peaks observed on the DC power deviation plot are not substantial at all, since they are the result of small time mismatches between the two simulations performed with variable steps. Beyond that, there are no significant changes with regard to the ideal case. The DC voltage is a little bit higher because the operating point moves on the droop characteristic toward higher voltage to compensate the load flow error which has overestimated DC grid losses. Nonetheless, DC grid losses are not significant therefore power references are close to the ideal ones, so the DC voltage drops are not so significant.

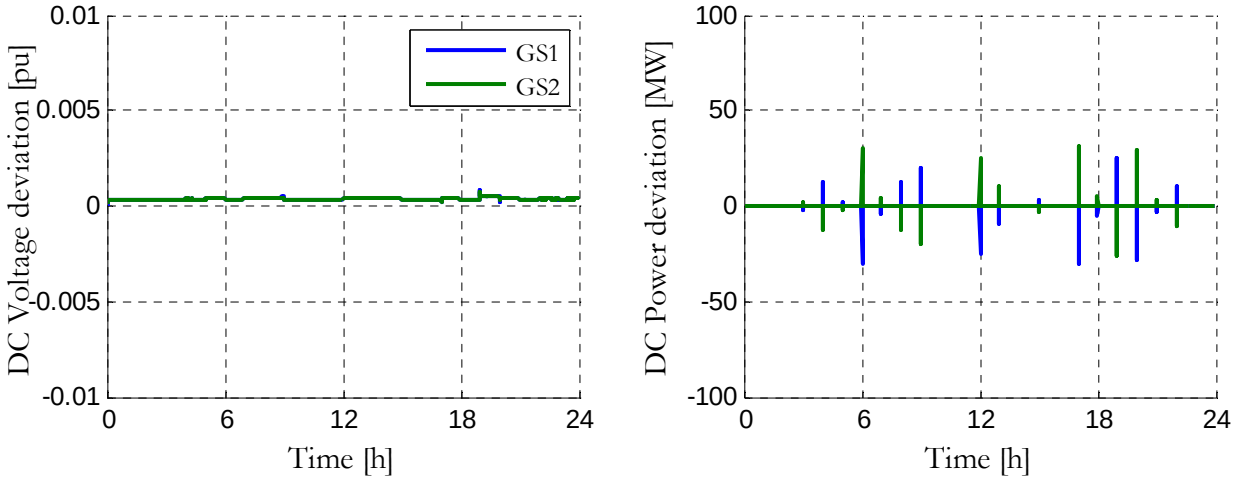

(a) DC voltage deviation (b) DC power deviation

Figure 5-13: Simulation of one day – load flow with power sharing – each minute – model with error

5.4.6. Loss of communication

The coordinated controller relies on communication data. A communication failure can occur during the DC grid operation. In that case converters keep their old references until the communication link is restored. As an example a loss of communication is simulated twice during one hour. Results are plotted in Figure 5-14.

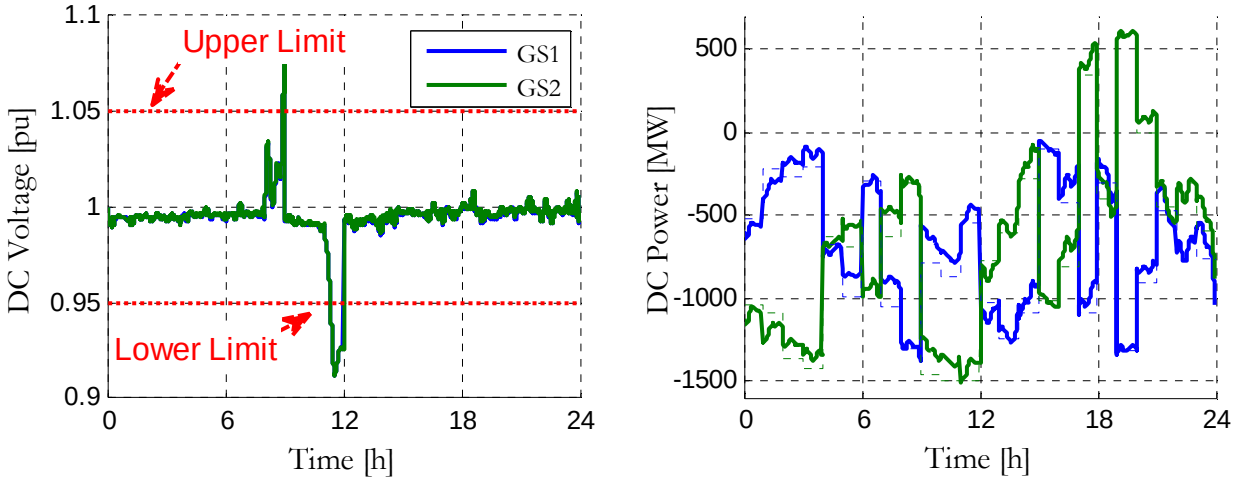

(a) DC voltage (b) DC power

Figure 5-14: Loss of communication between 8 and 10 o'clock and then between 11 and 12 o'clock

During the communication loss the DC voltage is controlled by the droop control method which does not rely on communication, using the latest set points as references. As expected, the DC voltage level is raising when wind power is increasing and the DC voltage level is falling when the wind power is decreasing. When the communication is back the DC voltage level regains its nominal value. Since the droop control principle is to share the power deviation

between the two onshore stations like the coordinated control, the power curves obtained with both simulations are similar.

5.5 SYSTEM RESTORATION AFTER AN EVENT

New references must be sent to converter stations after a major event, such as a station trip, to get a chance to stay in operation. For that purpose the coordinated control monitors alarms and checks if no system limits are exceeded. If a limit is reached the coordinated controller calculates a new operating point with the remaining devices and sends to them new set points. The coordinated controller takes some time to detect an abnormal operation, to calculate the new operating point and to send references to converter stations. During this time, the DC system is controlled by the local control strategy, presented in the Chapter 3. In this chapter, the voltage limits are arbitrarily set at ± 5 %, short term limits (i.e. less than 500 ms) are not considered since they are the matter of local control.

The patent taken out by ABB [NUQ12] is based on this idea. A remote controller monitors the DC grid and when it detects a disruption, it identifies the fault and then calculates new set points for converter stations in order to get a stable operating point. In the patent, the sharing of power deviation due to the converter station outage among remaining converter stations is also considered. Unlike this patent which is based on an optimal power flow which ensures that set points do not exceed limits, the presented method is based on a simple load flow algorithm which has a power flow sharing capability. This method enables to take into account the power transfer schedule and the forecast error. This suits well when the DC grid connects wind farms. Furthermore, the ABB's patent method is focused on disruptions in the DC grid while the presented method regularly calculates and sends new references even when the DC grid operates properly.

The scheme of the coordinated control is shown in Figure 5-15. The coordinated control calculates new references after a given time (i.e. cyclic operation) or is triggered just after a disruption, such as overvoltage condition. The TSO preferences are considered, it includes the actual wind power production, the power transmission schedule and the wanted power deviation sharing. Then a new load flow is achieved in order to have new set points. If power references of grid side converter stations do not exceed power limits they are sent. If the power reference of one station exceeds the nominal power of that station, the nominal power is set as reference and its participation to the coordinated control is set at zero. A new load flow is achieved with new parameters. The load flow algorithm needs at least one station actively participating to the coordinated control. If all grid side converter stations are at their limits, the wind power injection must be limited. This is achieved by making all wind farms participate to the coordinated control. The power references obtained by the load flow algorithm are the limits for wind power production.

It should be noted that currently this coordinated controller never checks the transmission cable ampacities. With the considered topology, the cables should not be overloaded as long as converter station nominal powers are not exceeded. However, for another topology or if a cable is lost the coordinated controller should be equipped with an additional feature which handles over-currents through cables.

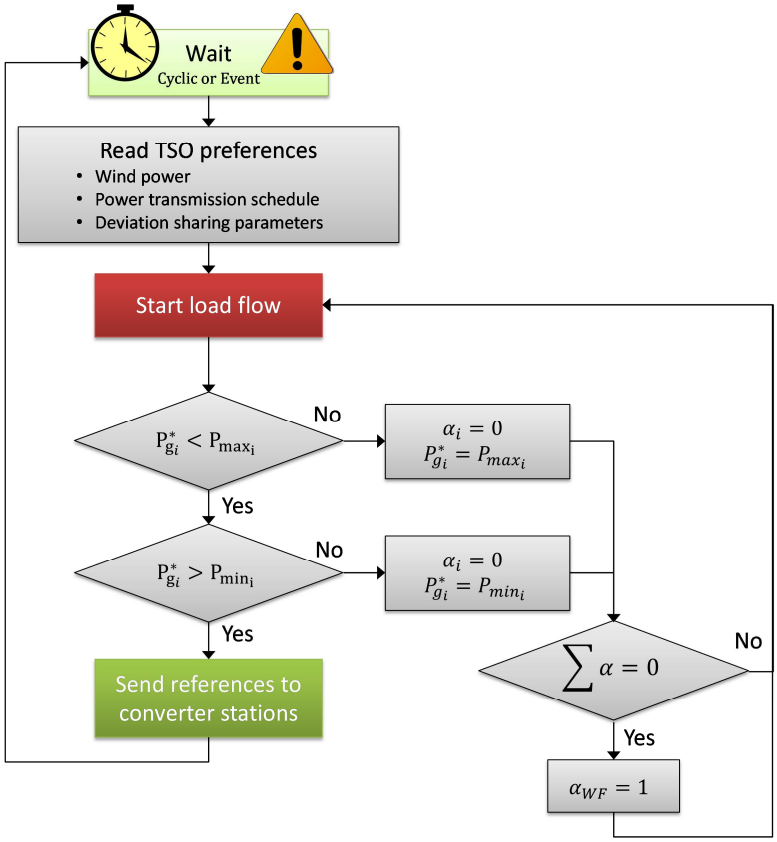

Figure 5-15: Coordinated control scheme

The coordinated control is tested for three different events:

- Outage of WF1 converter station
- Outage of GS1 converter station with low wind production
- Outage of GS1 converter station with high wind production

For these tests, converter station power references are saturated at the station nominal power and are also ramp rate limited at 9 pu per second. In a first time, the coordinated control sends references 500 ms after it detects that voltage level is out of bounds.

Results from the first scenario are plotted in Figure 5-16. When WF3 is tripped the two droop controlled stations decrease their power flow to maintain the DC grid power balance. Once the power balance is obtained the DC voltage is stabilized at 0.82pu. When the coordinated controller detects a voltage under the lower limits it calculates and sends new references to the two grid side converter stations taking into account that WF1 converter station is out of service. Then the DC voltage returns to its nominal value and the power flow of the two grid side converter stations is at the same value than the one obtained by the droop method because the power sharing is equivalent in both controls. Nonetheless there is a little power transient just after the references have been sent; this corresponds to the time for the voltage to get back to the reference level. Lower ramp rate limits lead to lower power deviations when changing references but the transient would be longer for both power and voltage.

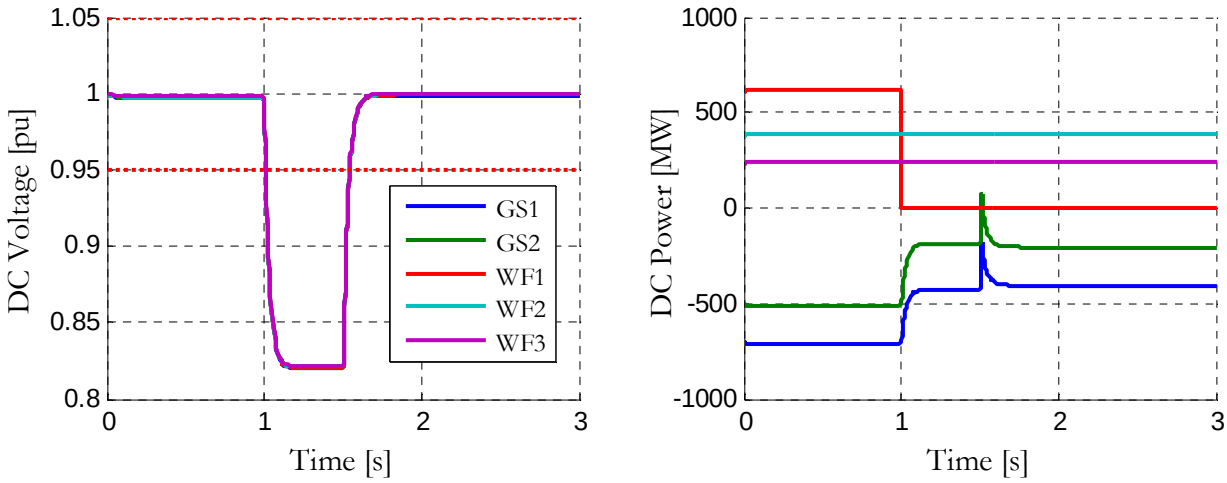

(a) DC voltage (b) DC power

Figure 5-16: Coordinated control test – WF1 outage

Results from the second scenario are plotted in Figure 5-17. When the first grid side converter stations is tripped, only the second grid side converter station balances the DC power flow, because this is the only one which is equipped with droop control. The DC voltage grows and stops at a stable level at 1.37 pu when the whole power is compensated by the second grid side converter station. 500 ms after, the coordinated controller sends a new power reference to GS2. As for the previous scenario the DC voltage returns to nominal, the active power is at the same level than the one given by the droop control and there is a transient due to the time needed for the voltage restoration. The response time is slower than when WF1 is tripped because, in that case, only GS2 is still controlling the DC voltage.

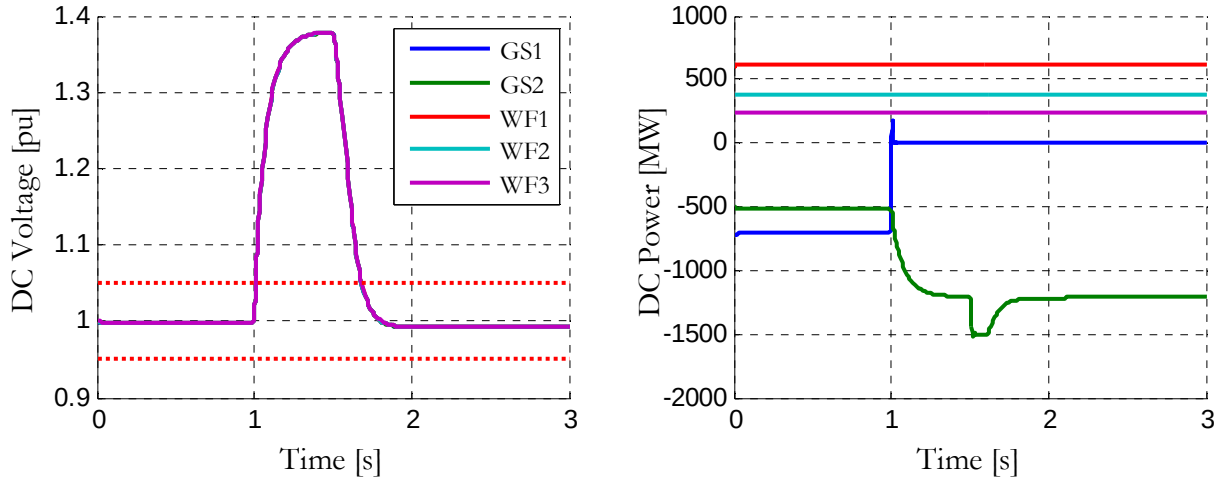

(a) DC voltage (b) DC power

Figure 5-17: Coordinated control test (500 ms) – GS1 outage – low wind power production

Until now, following steady state criterions, the loss or excess of power can be handled by stations which are equipped with voltage droop controller. The third scenario consists in a tripping of the GS1, like the previous scenario but this time the wind power cannot be handled by only GS2.

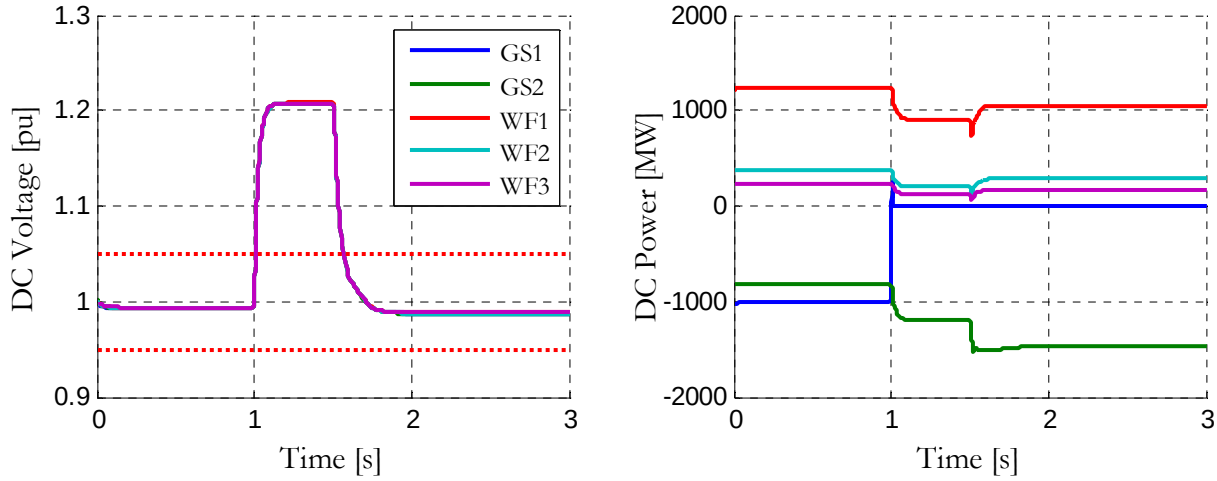

(a) DC voltage (b) Legend b

Figure 5-18: Coordinated control test (500 ms) – GS1 outage – high wind power production – wind farms are equipped with dead-band droop controller

As said in Chapter 3, wind farms can participate in the droop control scheme when the DC voltage exceeds a given limit. For instance, the third scenario is simulated with wind farms equipped with dead band droop controller with dead band set at 2 % of voltage deviation (see chapter 3). Simulation results are plotted in Figure 5-18. Thanks to the participation of wind farm to the droop control, the power delivered by GS2 is not saturated. After 500 ms the coordinated controller sends new references which optimize the wind power transfer by setting the maximal power for onshore stations and curtailing wind power injections at the maximum that the DC grid can handle. The wind power curtailment is defined according to the wind farm rating.

As conclusion, the coordinated control is not a tool which enables N-1 situation, because its dynamics is much slower than the local control. Therefore the N-1 situation is more dealing with primary control strategy. The coordinated control is instead a tool which restores the system under normal condition once the system has already been stabilized.

5.6 ALLEVIATE AC CONGESTIONS

Until now the AC system is considered as a slack bus; the AC grids absorb the power flow from the DC grid without restriction. In some cases the planned program cannot be applied because of contingencies on the AC grid. The power injected from the DC grid to the AC grid may be limited owing to, for instance, a line overloaded on the AC grid. Sometimes, AC grids needs more power because of a lack of production. Also, if the DC grid is connected at several injection points to the same AC grid, the power can flow through the DC grid in order to alleviate AC congestions. In case of sudden event, the control center of the AC grid must interact with the DC grid coordinated controller in real time, to change the power injections.

To illustrate this point, an AC system composed of two AC areas is considered (see Figure 5-19). The power transfer from an area to the other can either flow by the two parallel AC lines or by the DC grid. The AC lines between AC areas have a power rating of 400MW each. The AC

system is monitored and controlled in a control center which can communicate with the DC grid coordinated controller.

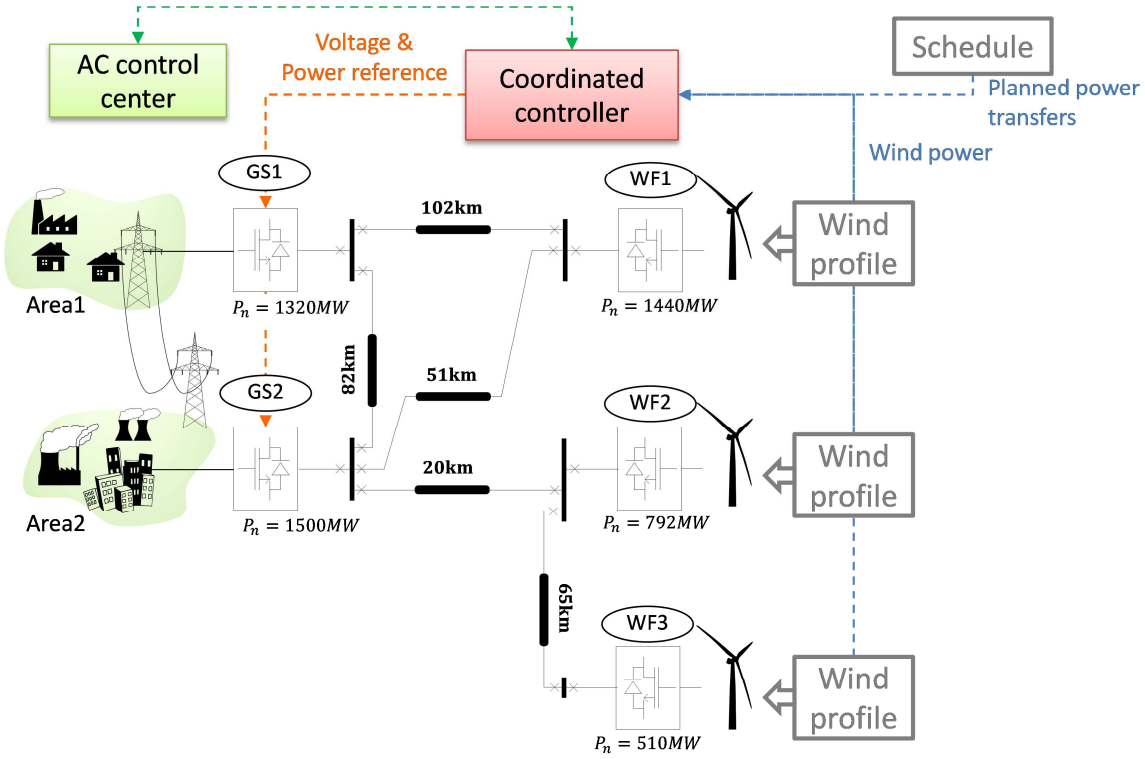

Figure 5-19: Simulation of the five-terminal DC grid with AC grid

In the TWENTIES work package WP5 a special protection scheme (SPS) is started on the DC grid when a contingency is detected on the AC grid. The SPS consists in pre-established control actions which enable to cope with an emergency situation. For instance, in case of overload in an onshore line, the SPS sends curtailment references to offshore wind farms. In this work, no pre-established plan are proposed, the DC load flow algorithm is used to provide new converter station settings.

The scenario simulated to show how the DC grid can support the AC system is the outage of one of the AC transmission lines between two areas at 6 o'clock. Before the event, area 1 was providing 600 MW to area 2. Once the transmission line is tripped the remained transmission line is overloaded of 200 MW, therefore the AC control center asks the DC grid coordinated control to transmit 200 MW from converter station GS1 to GS2. Results are compared with results without reference change (dotted lines).

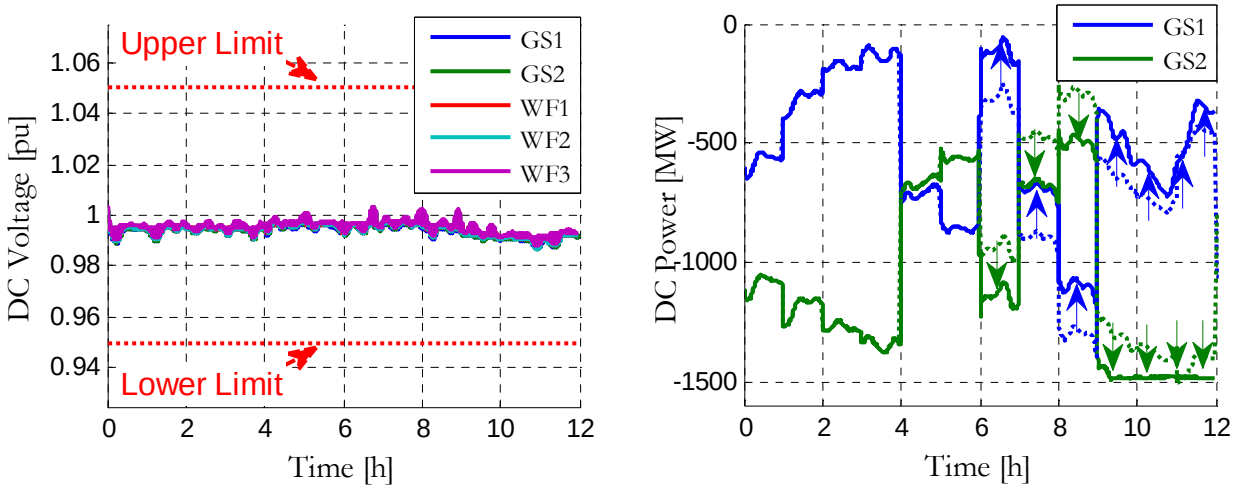

(a) DC voltage (b) DC power

Figure 5-20: Alleviate AC contingency

In Figure 5-20a, the DC voltage is not impacted by this power flow change. In Figure 5-20b, after 6 o'clock the grid side power injections do not follow the scheduled program, because the program is changed owing to the request from the AC grid control center. If the program was not changed the power flows would be the dotted lines. The new planned production is translated of 200 MW for GS1 and translated of -200 MW for GS2. After 9 o'clock the additional transfer of 200 MW cannot be achieved because the wanted power injection is higher than the converter rating (i.e. 1500 MW for converter GS2), therefore the power reference of GS2 is set at its nominal value and GS1 acts as a slack bus.

5.7 CONCLUSION

The coordinated control allows managing power flows in the DC grid for normal and emergency situations. In normal operation the coordinated controller enables to:

- maintain the DC voltage within a nominal range when the DC grid is in droop control scheme,
- dispatch the wind power following a transmission scheduled program,
- share forecast errors according to pre-established participation coefficients,
- interact with AC grids power dispatch requirements.

Following an event such as a station trip, the coordinated controller can send new references to help the DC system returning into normal operation. However, in N-1 converter station operational limits are exceeded, which suggests that N-1 capability could not be solved by the coordinated controller as long as the communication speed is not fast enough.

CHAPTER 6: Experimental Study

6.1 MOTIVATION AND CHAPTER OUTLINE

The concept of DC grid is widely addressed in the literature, but it has never been tested since such DC grids do not exist yet. As already mentioned in the introduction, this work is a part of the TWENTIES DEMO 3 project which aims to demonstrate the feasibility of a DC grid by experimental tests. However, it was impossible to conduct tests with a full-scale demonstrator for cost and technical reasons. As an intermediary step, in the L2EP facility, a low-voltage DC grid has been built to assess the control and protection schemes.

This DC grid mock-up is a low scale equivalent of the five-terminal DC grid topology studied in Chapter 4 and Chapter 5. It is a 250 V pole-to-pole voltage mock-up which is based on the Hardware In the Loop (HIL) principle; one part of the system is simulated by an hybrid real time simulator which is plugged to physical elements, namely converters, cables, DC breaker.

The mock-up is designed in such a way that it:

- reflects at best what would be the behavior of a future DC grid,
- provides enough flexibility to test different DC and AC network topologies,
- offers facilities to test and compare different control laws as presented in Chapter 3,
- could be monitored and controlled from a remote supervisor to test coordinated control strategies as presented in Chapter 5,
- can be affected by a pole-to-pole short-circuit on the physical cables, offering a test bench to implement DC protection algorithms [DES13].

This chapter is organized as following: first part (6.2) deals with the mock-up components descriptions and designs while the second part (6.3) shows the experimental results. Finally, this chapter ends with a global conclusion (6.4) on the mock-up limitations and its added value.

6.2 MOCK-UP DESCRIPTION

The development of this mock-up has taken approximately 1 year and a half and has mobilized one post doc full time, partly 2 PhD students, two engineers, two professors and the support from RTE France staff. In this subsection, the description and the design of the main equipment is given in detail.

6.2.1. Methodology to scale a DC grid

To reflect at best the behavior of a high voltage DC grid, a special attention was paid during the design process to have a homothetic design of major components constituting the DC grid. For the design of this mock-up two main aspects have been required:

- The dynamics of the DC grid mock-up must be equal to the full scale one to assess power management operations
- Wave propagation speed in the low-scale cables should be similar to real one to evaluate protection scheme performances.

Converter station design

Theoretical studies achieved in simulation have shown that the converter control loop dynamics as well as the DC capacitor values have a great influence on the DC grid behavior. The structure and control basics of the VSC have been previously described in Chapter 1.

Converter stations used in the mock-up are 2-level converters associated with a LCL filter for mitigating the current harmonics on the AC side and DC capacitor and smoothing reactors on the DC side, see Figure 6-1. The equivalence between high power converter and the mock-up converter can be easily achieved thanks to the per unit transformation.

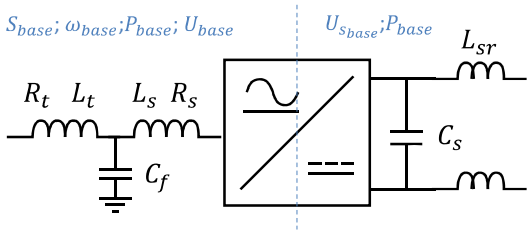

Figure 6-1: single-line diagram of a Mock-up converter station

In Chapter 3, it has been demonstrated that energy stored in the DC system characterizes its dynamics. Therefore, the value of the mock-up converter station capacitor must be designed so that the electrostatic constant as introduced in Chapter 3 part 3.2.2. Is the same than a full-scale converter. The same approach can be applied for the smoothing reactor design:

$$H_L = \frac{1}{2} L_{SR} \frac{I_{base}^2}{P_{base}} = \frac{1}{2} L_{SR} \frac{P_{base}}{U_{base}^2} \quad \textbf{(6.1)}$$

Physical converter stations on the mockup are rated at 3 kVA-2.5 kW. Their design is based on data from a 1077 MVA-1000 MW converter station. Passive component values are summarized in Table 6-1. It should be noted that the LCL filter capacitor is not based on per unit conversion, but it is calculated to achieve a desired cut-off frequency.

Table 6-1: Per unit approach for converter station design

	Parameter	High power converter value	Per unit value	Mock-up converter value
AC side	S_{base}	1077 MVA	1 pu	3 kVA
	U_{base}	320 kV	1 pu	125 V
	LCL cut-off frequency	500 Hz	–	1 kHz
	R_s	0.48 Ω	0.005 pu	0.026 Ω
	L_s	45 mH	0.15 pu	2.5 mH
	R_t	0.48 Ω	0.005 pu	0.026 Ω
	L_t	45 mH	0.15 pu	2.5 mH
	C_f	4.47 µF	–	20.4 µF
DC side	$U_{s\,base}$	640 kV	1 pu	250 V
	P_{base}	1000 MW	1 pu	2500 W
	C_s	50 µF	10.24 ms	819 µF
	L_{SR}	10 mH	1.10^{-2} ms	610 mH

In order to validate the scaling methodology the same simple off-line simulation is carried out for the high and low voltage converters. For this test, the VSC is connected to an infinite voltage bus on the AC side and to a resistance in the DC side, see Figure 6-2a. This resistance was calculated to achieve, at nominal voltage, a consumption of fifty per cent of the nominal power. To maintain the DC voltage, both converter stations are droop controlled with droop value set at 0.82 pu/pu. Thus the dynamics of the DC grid are defined by the capacitor value.

In Figure 6-2b, the scenario consists in the connection of a new resistive load of 16 pu at t=0.1 s and its disconnection at t=0.2 s. Results from the low-voltage converter and from its high voltage counterpart are shown in per unit of their DC side base in order to be compared. Power and voltage curves from the simulation of each converter are very close; therefore the scaling methodology is validated.

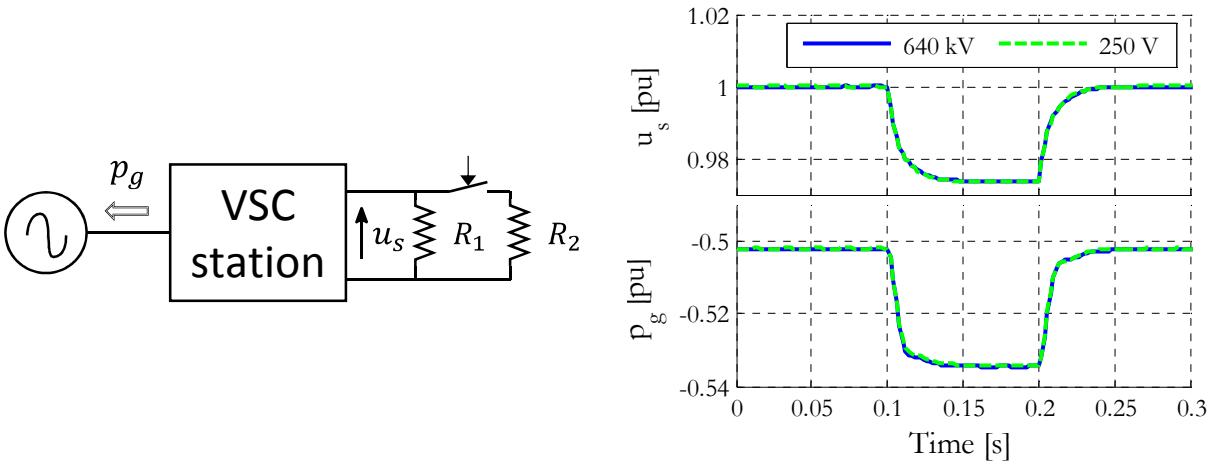

(a) test system (b) time domain results

Figure 6-2: Validation of the VSC scaling methodology

Two physical two-level VSCs (3000 VA – (AC) 125 V – (DC) 250 V) based on the aforementioned methodology have been developed. This converter station is shown in Figure 6-3. The low level control has been implemented on a DSP F28335; it includes PWM signal generation, current control in the dq frame, power control, DC voltage control and a software based overcurrent and overvoltage protections. It receives measure signals from voltage and current sensors and sends control signals to IGBT gates and to protections relays. The gateway with the SCADA system is ensured by a Beckhoff PLC. Also, the PLC manages the initialization and shutdown sequences.

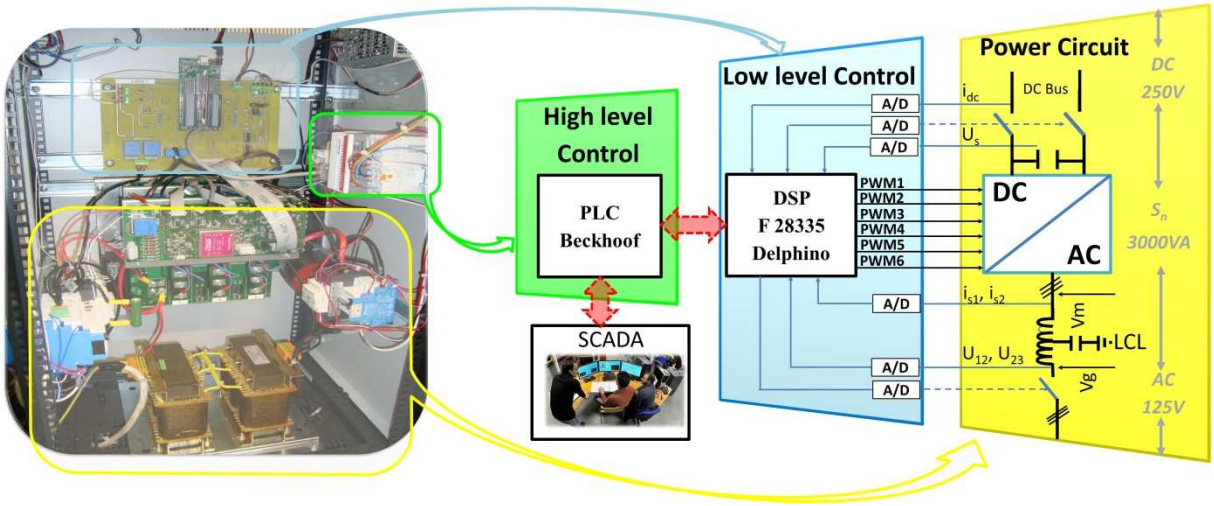

Figure 6-3: Physical VSC and its control architecture

Cable design

To assess the protection scheme, the DC cable should ensure wave propagation, hence it is not possible to emulated DC cable by a simple RLC circuit, such as Π equivalent like it is done in [EGE12]. Therefore, DC cable is emulated by a low-scale coaxial cable, as shown in Figure 6-4, to have similar propagation time than the corresponding high voltage cable. The copper section of the core was chosen to achieve a voltage drop no larger than 5 % per cable for a current of 10 amps and nominal voltage of 125 V. Nexans has proposed to use cables with copper sections of 10mm² and 25mm² which leads to a maximal length of 2 km and 5 km to stay within the voltage bounds. As these cables must be installed in a limited space and for cost reasons, their total length has been limited to 15 km (i.e. 7.5 km per pole).

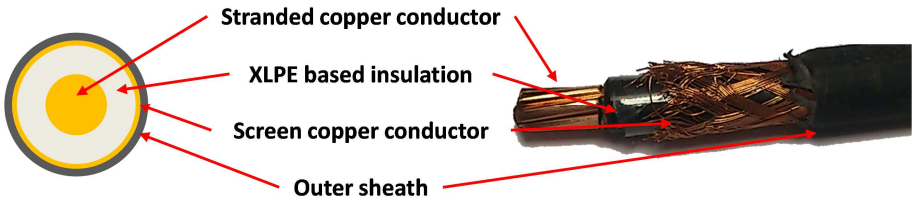

Figure 6-4: low-voltage coaxial DC cable

The theoretical wave speed through a coaxial cable is given by the well-known formula:

$$\sigma = \frac{1}{\sqrt{LC}} \tag{6.2}$$

Table 6-2 summarized the propagation time obtained for both cables. As results, both cables have same propagation speed, the theoretical propagation time for 5 km is 25 µs and for 2 km it is 10 µs.

Table 6-2: Theoretical propagation time through low - voltage cables

	Cable section [mm²]	Cable length [km]	Linear capacitance [µF/km]	Linear inductance [µH/km]	Propagation speed [km/s]	Propagation time [µs]
MPRXCX25	25	5	0.42	61	$1.98\ 10^5$	25
MPRXCX10	10	2	0.32	79	$1.98\ 10^5$	10

6.2.2. Mock-up general overview

As introduced before, it was not possible to develop a unitary scale MTDC to perform tests on it. To assess control performance and to test fault detection algorithm a hybrid simulation has been developed at the L2EP Lab. The overview of the five-terminal DC grid mock-up is presented in Figure 6-5.

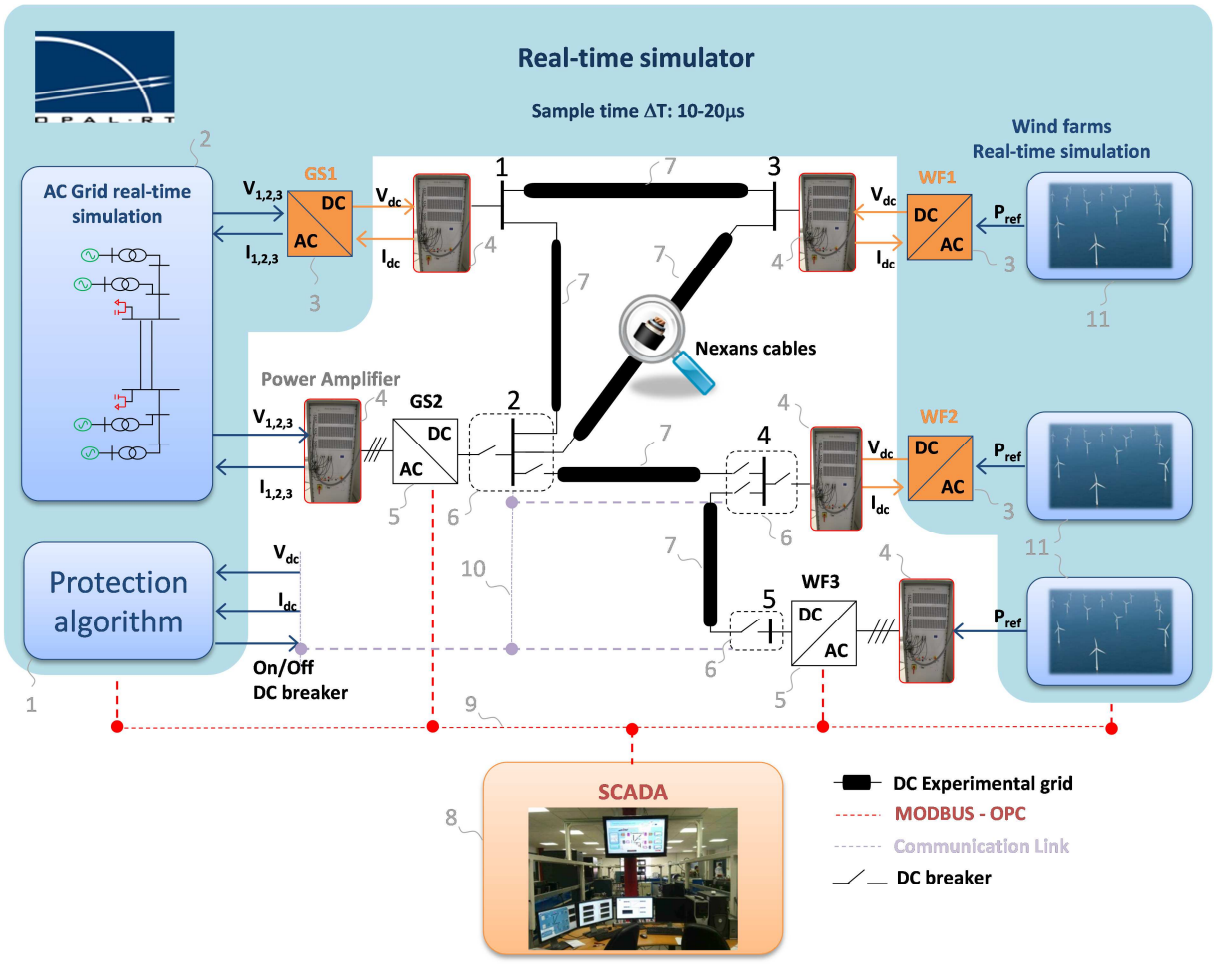

Figure 6-5: Mock-up general overview

The mock-up is divided in two main parts; one physical part in the center of the figure and one virtual part is implemented in a real-time simulator, this latter is highlighted by a blue shape in the background. The interface between physical devices and the real time simulator analog outputs is achieved thanks to several high-bandwidth AC or DC power amplifiers (4). It should

be observed, that power amplifiers are either dealing with AC quantities (Node 2 and Node 5) or dealing with DC quantities (Node 1, Node 3 and Node 4).

There are two physical VSCs (5), five low voltage DC cables, each composed by two symmetrical poles (7) and DC low voltage beakers (6) amongst physical devices. There are three virtual VSCs (3), one AC grid simulated (2) and three virtual wind farms (11) are simulated in the same real time simulator: Opal-RT®. The protection algorithm (1) is embedded in another real time simulator in order to guaranty separate operation between the protection algorithm and the simulation. The communication between DC breakers (6) and the protection algorithm is provided by an independent medium (10). Finally the DC system is monitored and controlled by a SCADA system (8) which receives information from VSCs or the real-time simulator and then sends set points to them thanks to a media using MODBUS or OPC as communication protocol (9).

The protection algorithm as well as the DC breakers are not the subject of this study, this has been treated by Justine Descloux during her PhD [DES13]. It should be noted that DC breakers are an association of 2 IGBTs and diodes to obtain a four quadrant switch. By nature, such devices experiment unwanted voltage drops which are significant at low voltage scale; hence the DC grid power flow is widely impacted. Therefore, to carry out tests on power dispatch, DC breakers are shunted to avoid their inherent voltage drops.

6.2.3. Mock-up power flow

In reality, the final five-terminal DC grid topology described in Chapter 4 was obtained from the mock-up topology. The initial test system was proposed in TWENTIES D11.1 [NGU12], it was a five-terminal DC grid with the same DC grid architecture, three wind farms and two onshore converter stations, but cable lengths and station nominal powers were different.

On the mock-up, the lengths of the cables have been revised to deal with a set of cable drums delivered by Nexans. It has been also decided to assign the 25 mm² section to the meshed part and the 10 mm² section to the antenna part. The final cable arrangement is shown in Figure 6-7a.

The cables are laid in a room on their drums (see Figure 6-6a) since it is more convenient for the storage and it increases the direct inductance and therefore increases the propagation time. In Table 6-3, measurements on LC parameters performed at 1 kHz are reported, and new propagation speed are calculated for each cable. For instance the propagation time of the cable D is 285 μs instead of 11 μs if the cable would be unrolled. Thus, it has similar propagation time order than the corresponding real HVDC XLPE cable (i.e. 2500 mm² – 320 kV – 100 km long) which has a propagation time close to 500 μs.

Owing to connection resistances, in junction box for instance (see Figure 6-6b), the resistances of the DC cables are not exactly at their theoretical value. So the DC resistances were also measured for each DC cable by a DC ohmmeter, results are reported in Table 6-3.

(a) Arrangement of cable drums

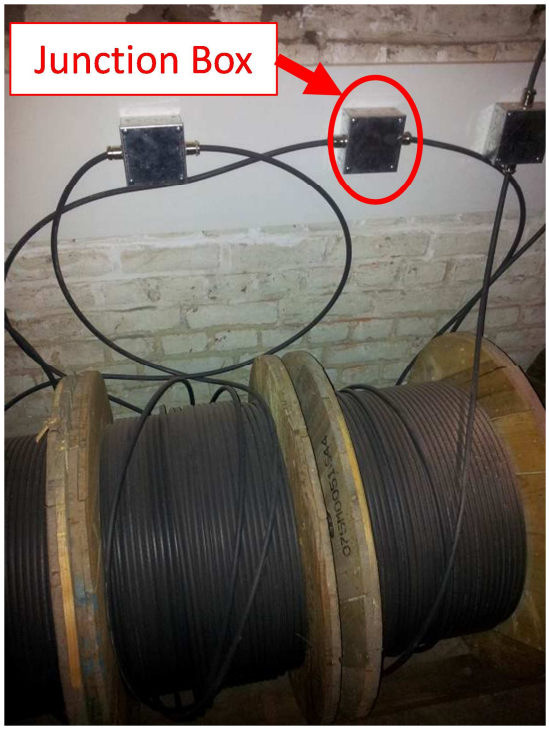

(b) Junction between two cable sections

Figure 6-6: Cable-laying

Table 6-3: Measured cable data – per pole

Link	Number of drums	Cable section [mm²]	Drum length [m]	Total cable length [km]	Total resistance [Ω]	Total inductance [mH]	Total capacitance [µF]	Propagation time [µs]
A	2	25	227	0.45	0.43	17.3	0.19	57
B	5	25	227	1.14	1.01	43.1	0.47	142
C	8	25	227	1.82	1.46	69.0	0.74	228
D	10	25	227	2.27	1.77	86.3	0.93	285
E	9	10	161	1.45	2.52	58.7	0.46	570

The nominal power of each station has been obtained from a specific scenario performed on the mock-up. It is required that the voltage deviation between the highest voltage level and the lowest voltage level should be below 10 % in normal operation. Thanks to the steady state algorithm presented in Chapter 5, and new cable data directly measured on the mock-up, a scenario which satisfies the voltage drop requirements has been found. To obtain this scenario, GS1 one has been set at the nominal voltage level (i.e. 250 V) and WF3 has been set at the highest voltage level (i.e. 275 V). The current through GS2 has been imposed at 10 A, and currents from WF1 and WF2 have respectively been defined at 8.5 A and 4.5 A to get a convenient power flow. The power flow is shown in Figure 6-7b.

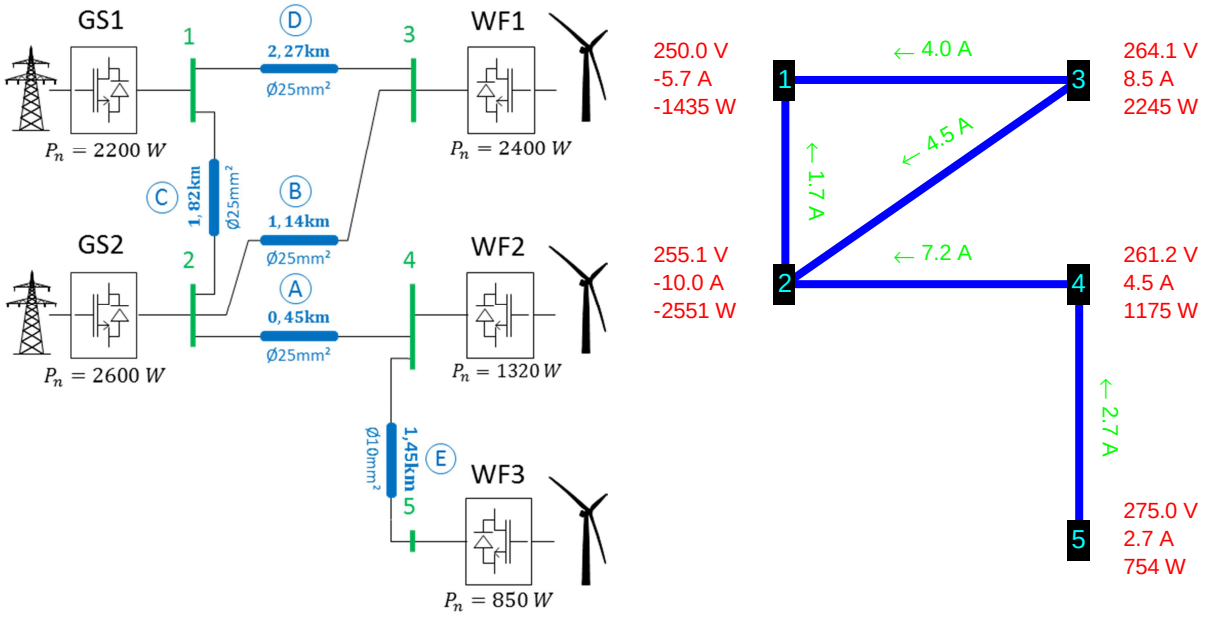

(a) Mock-up cable arrangement (b) DC mock-up power flow overview

Figure 6-7: Mock-up arrangement and nominal scenario

This scenario has been considered to define the nominal power of each converter station; the nominal power of each station is sized close to the power flow scenario apart from GS1 which is more powerful to be able to take a part of the power currently delivered to the AC grid by GS2. The nominal apparent power is sized 5 % upper than the nominal active power. Nominal powers defined for the mock-up converter stations are displayed in Table 6-4.

Table 6-4: Mock-up load flow and station nominal power

	DC Voltage [V]	DC currents [A]	Power [W]	Nominal Power [W]	Nominal apparent power [VA]
GS1	250	-5.7	-1435	2200	2310
GS2	255	-10	-2551	2600	2730
WF1	264	8.5	2245	2400	2520
WF2	261	4.5	1175	1320	1386
WF3	275	2.7	754	850	892.5

6.2.4. Mock-up storage

As highlighted all along this work, capacitors are key components for the DC grid dynamics, consequently special attention has been paid to have homothetic capacitor values. As said in part 6.2.1, mock-up converter station capacitors are designed to have same electrostatic constant than a unitary scale VSC (i.e. around 10 ms). From nominal power of converter stations and a 10 ms electrostatic constant the desired capacitor values are calculated. However, it is not possible to get the exact capacitor values for physical converters (Node 2 and Node 5) since capacitors are sold as normalized values.

Moreover, because of the failure of a high-bandwidth power amplifier connected at Node 4, this one has been replaced by another power-amplifier with a lower bandwidth. Since this spare power amplifier could not follow the DC voltage dynamics, notably in case of DC fault, it has been current controlled directly connected to a physical capacitor.

The values of capacitors implemented in the mock-up are reported in Table 6-5. It should also be pointed out that physical capacitors have a tolerance of 20 %.

Table 6-5: Converter station capacitor implemented in the mock-up

	Type	Nominal DC voltage [V]	Nominal power [W]	Electrostatic constant [ms]	Desired capacitor value [µF]	Capacitor value [µF]
GS1	Virtual	250	2200	10	721	721
GS2	Physical	250	2600	10	852	1100 (±20 %)
WF1	Virtual	250	2400	10	786	786
WF2	Virtual	250	1320	10	433	440 (±20 %)
WF3	Physical	250	850	10	279	270 (±20 %)

6.2.5. AC system simulated in real time

In order to show how DC grid can participate to AC ancillary services, grid side converter stations are connected to the same AC grid as presented in the second part of Chapter 4. It has been simulated in real time in the Opal-RT® simulator.

In this system, the simulated AC grid is dealing with hundreds of megawatts while the mock-up is dealing with thousands of watts. To face this problem a scale factor is considered between the power extracted to the DC grid and the one injected into the AC grid. In the simulated AC grid, grid side converter stations are replaced by power injector sources.

6.2.6. Overview of the SCADA system

Objectives of the DC SCADA system

The role of the SCADA system is not considered in this part since it has already been discussed in Chapter 5. The SCADA must act as a dispatching center, it should be able to:

- monitor quantities of each converter station,
- monitor the states of each component,
- change control mode of each converter station,
- send references to each station local controller,
- send suitable converter set points to reach a wanted power flow,
- recalculate automatically converter orders after an event to return to normal operation,
- monitor and control AC grids,
- start and stop wind power production,

- start and stop stations, even from the scratch,
- trigger DC fault,
- clear DC fault and protection algorithm alarms.

Management of the mock-up signals

The mock-up communication scheme is presented in Figure 6-8. The MTU is equipped with PcVue software that allows the development of the HMI. The communication between devices is made through an Ethernet network. The communication protocol OPC was chosen to achieve the communication between multivendor devices: PcVue server, Beckhoff PLC, the OPAL-RT® and other client computers. A Beckhoff PLC is embedded in each converter stations to be employed as a gateway between a home-made protocol over RS232 serial communication and the OPC over the Ethernet network. The latency of the SCADA system is one second. Figure 6-8 summarizes the different informations which are exchanged between the MTU and RTUs.

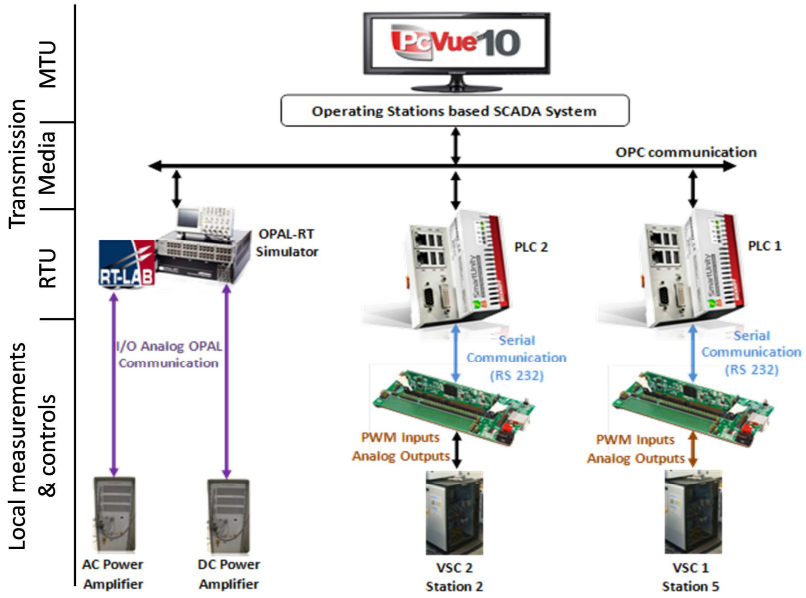

Figure 6-8: Mock-up communication scheme

Table 6-6: Information exchanged by the SCADA system and the devices

Device	Inputs	Outputs
Physical Converter	• Control mode • Active power and DC voltage set points • Turn on/off signal	• Status • Currents, power, voltage
Simulated Converter	• Control mode • Active power and DC voltage set points	• Currents, power, voltage
Short circuit generator	• Short circuit impedance • Turn on/off signal	• Status
Breaker	• Turn on/off signal	• Status • Currents
AC grid	• AC generator voltage set points • AC generator power set points • Power of loads	• Power flow • Voltage map

HMI description

A HMI based on PcVue environment has been developed to serve as interface between the DC grid and the system operator. A screenshot of this HMI is shown in Figure 6-9. This HMI displays the states of each converter, their control modes, their power flow and their DC bus voltage. The HMI allows the mock-up operator to define the converter control mode, the power and voltage set point. From this control interface, it is also possible to trigger faults in the DC grid by pushing the lightning button. Since the protection algorithm is not embedded in the SCADA system, this one is fully independent. Only the states of the protection algorithm as well as the states of DC breakers are displayed each second, at the same time than other information.

It is possible for the operator to choose between manual control and automatic control. Choosing manual control ("stop coordinated control") means that the set points sent to converter station are those defined by the operator while choosing the automatic control ("coordinated control") means a load flow program is running in background to automatically find and refresh converter station set points. Converter states are checked by the load flow program in order to adjust accordingly the power flow. Moreover, once the information dealing with a DC grid problem is known by the SCADA system, such as converter station outage or overvoltage limit reached, the SCADA program runs a new load flow in order to retrieve as fast as possible a suitable operating point.

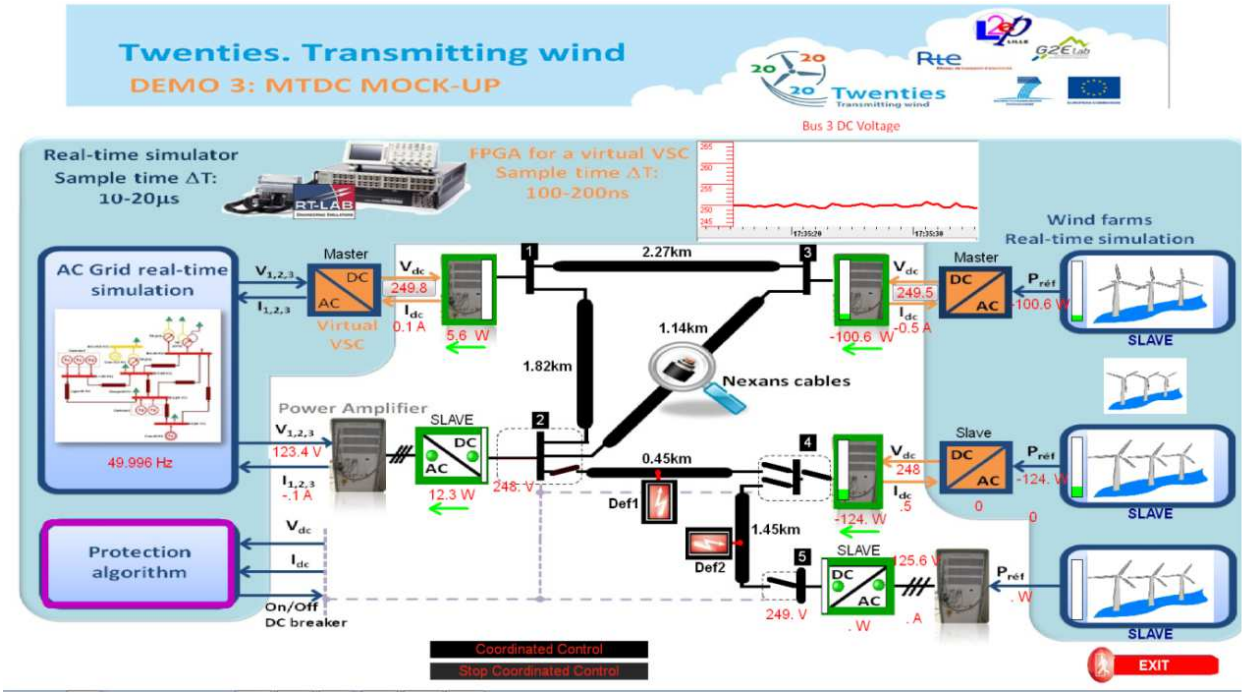

Figure 6-9: Screenshot of the HMI

6.3 EXPERIMENTAL RESULTS

6.3.1. Assessment of the droop control

Mock-up results

This test is focused on the DC voltage dynamics when the DC grid is subjected to a severe power change. The objective is to assess both simulation models and the first order transfer function found in Chapter 3. To do this, the DC system is first stabilized at an operating point and then a fast power reference change is applied at WF1.

For this test, converters stations control strategy is:

- GS1 and GS2 are droop controlled with droop value set at 0.82 pu/pu
- WF1, WF2, WF3 control their power flow at constant value

Before the event:

- The power reference of GS1 is 560 W
- The DC voltage reference of GS1 is 250 V
- The power reference of GS2 is 400 W
- The DC voltage reference of GS2 is 253 V
- The power reference of WF1 is -600 W
- The power reference of WF2 is -300 W
- The power reference of WF3 is -300 W

The scenario is a sudden power reference change from -600 W to 0 W at WF1. The rate of change of the reference is limited at 30 kW/s. In Figure 6-10, powers and voltages of all converter stations are reported. For GS1, GS2 and WF1 powers are measured on the AC side while for WF2 and WF3 powers are measured on the DC side.

In Figure 6-10, powers and voltages are stable before the power variation (before 0.3 s). However, the measured power at the DC side of WF3 (Figure 6-10e) is -230 W instead of the expected -300 W because of the physical VSC, mainly switching losses which are around 70 W. Losses of the second physical converter (GS2) are estimated at 70 W too, but they are not visible on these results because power measurements are on the AC side. The power ramp variation on WF1 is visible in Figure 6-10c. In Figure 6-10a and Figure 6-10b, the power balance is achieved by both grid side converter stations (GS1 and GS2) with similar proportion. Since the power variation leads to a power deficit the DC voltage map decreases and stabilizes at a lower value. The DC voltage dynamics are around the expected 100 ms response time.

An offline simulation has been carried out on EMTP-RV® with the mock-up parameters in order to validate the models. In order to have the same power injected and extracted from the DC grid, power references of GS2 and WF3 were modified to take into consideration switching losses of real converter stations. Thus the power reference of GS2 is set at 470 W and the one of WF3 is set at -230 W. Simulation results are displayed in green dotted lines and compared to experimental results.

Before and after the event, steady state voltages and powers are very close in both cases. The DC voltage of all stations and the power deviations of droop controlled stations are similar. Regarding the dynamics there is a little difference which could be explained by the cable model since cables are replaced by simple resistances for simulation.

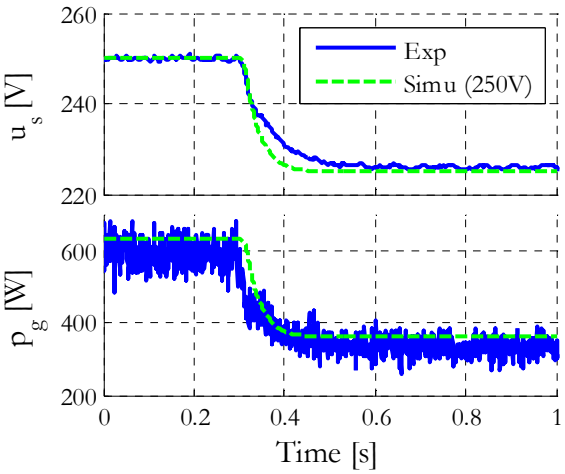

(a) GS1

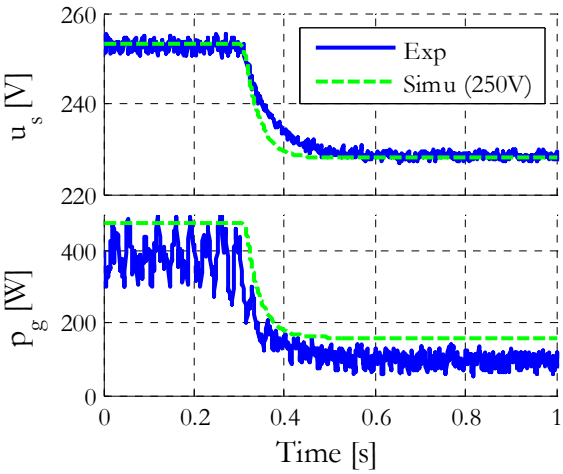

(b) GS2

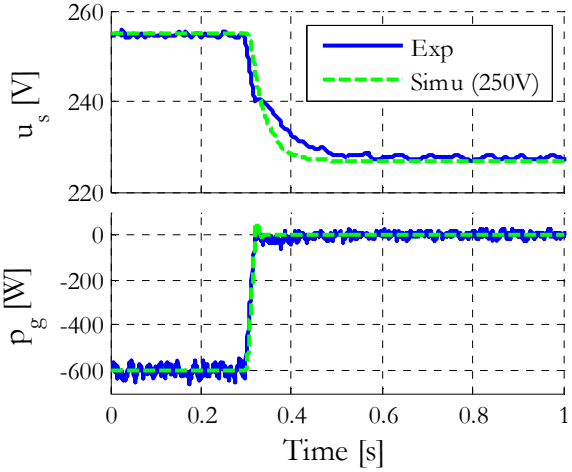

(c) WF1

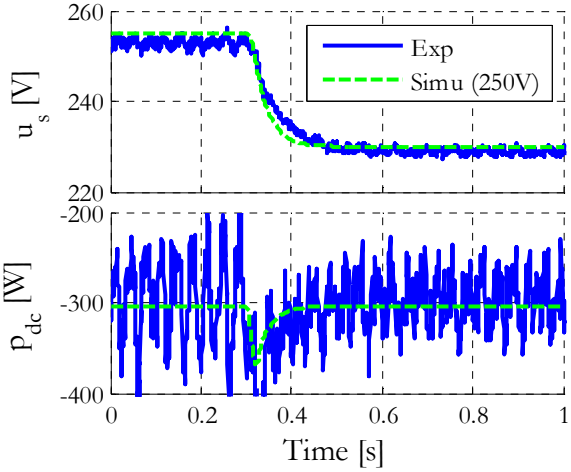

(d) WF2

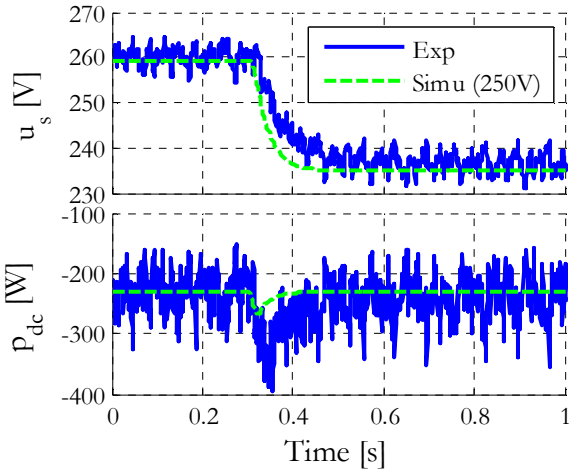

(e) WF3

Figure 6-10: Experimental results of a step power change of 600 W on WF1 – Comparison with results from off-line simulation of the mock-up

Comparison with the high voltage DC grid

First and foremost, the aim of this mock-up is to represent a high voltage MTDC grid. To be sure that it is representative of a full-size system; the above experimental results are compared to the off-line simulation results performed with an equivalent 640 kV MTDC grid.

In this part, the five-terminal DC grid presented in chapter 4 is considered. In this simulation, converters are modeled by their average equivalent model since the observed dynamics are not in the range of their switching frequency. Also, to be accurate, cables are represented by their wideband model which includes the coupling between the screen and the core conductor. Finally, powers controlled by converter stations are defined in accordance to the power flows of the mock-up converters.

Table 6-7 summarizes nominal powers and the steady state node voltages and powers. In this table, data which are written between brackets are per unit values with regard to the nominal voltage level, or with regard to the converter station nominal power. For this simulation the powers of GS2, WF1, WF2 and WF3 are imposed while GS1 is defined as a slack bus. Therefore, in per unit, the voltage of GS1 is equal in both cases and the powers of other stations are rigorously identical. The power delivered by GS1 is quite similar in both cases, therefore, even if DC grid losses are more important, the dynamic difference is not really significant, and should not alter results on control strategies. However, as expected the DC voltage map, in per unit, is fairly different, for instance the DC voltage at Node 5 is 4% higher than the nominal value in the mock-up while in the 640 kV DC grid the DC voltage is only 0.1 % higher. Hence, the droop control strategy which relies on local voltage measurement may differ.

Table 6-7: Comparison of the mock-up a high voltage DC grid – Load flow results

	Low voltage (Mock-up)			High voltage		
	Nom. power [W]	Power [W]	Voltage [V]	Nom. power [MW]	Power [MW]	Voltage [kV]
GS1	2200	630 (0.28)	250.0 (1.00)	1320	384 (0.25)	640.0 (1.00)
GS2	2600	482 (0.19)	253.2 (1.01)	1560	290 (0.19)	640.2 (1.00)
WF1	2400	-600 (0.25)	255.1 (1.02)	1440	-360 (0.25)	640.4 (1.00)
WF2	1320	-300 (0.23)	255.0 (1.02)	792	-180 (0.23)	640.4 (1.00)
WF3	850	-230 (0.27)	259.4 (1.04)	510	-138 (0.27)	640.8 (1.00)

In Figure 6-11, experimental results from the mock-up are superimposed on simulation results from a 640 kV equivalent DC grid. An equivalent scenario to the previous experimental test is simulated. In this figure results are compared in per unit. The dynamics of both voltages and powers are very close; the small difference can come from the capacitors of real converters which cannot be exactly at the designed value because of the standardized capacitor values. The voltage and power deviations are very similar.

Since the droop value considered in this test is not very steep (82 % of voltage change leads to 100 % of power change) conversely to a droop value such as 5 %. (5 % of voltage change leads to 100 % of power change), the DC power flow dispatch is not really impacted by the voltage drops through the cables.

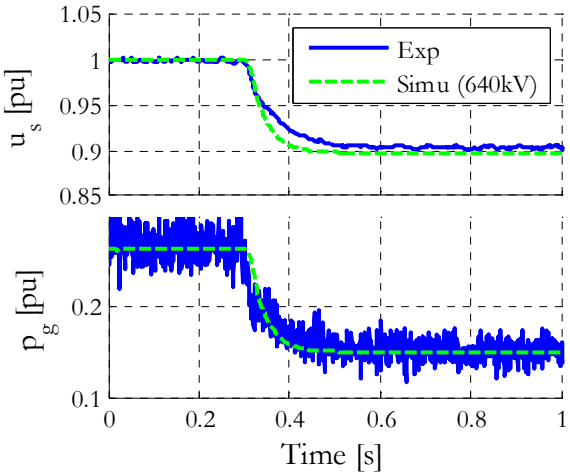

(a) GS1

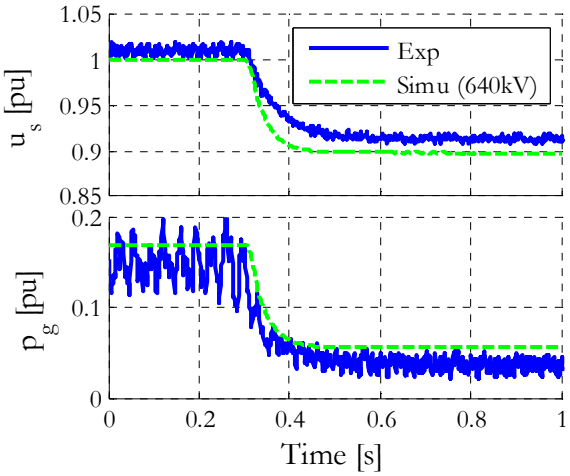

(b) GS2

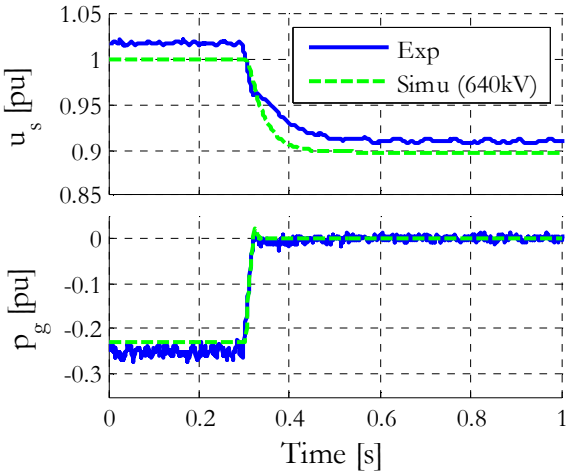

(c) WF1

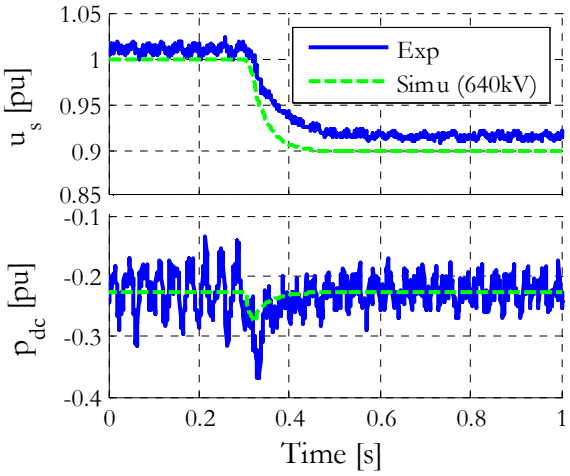

(d) WF2

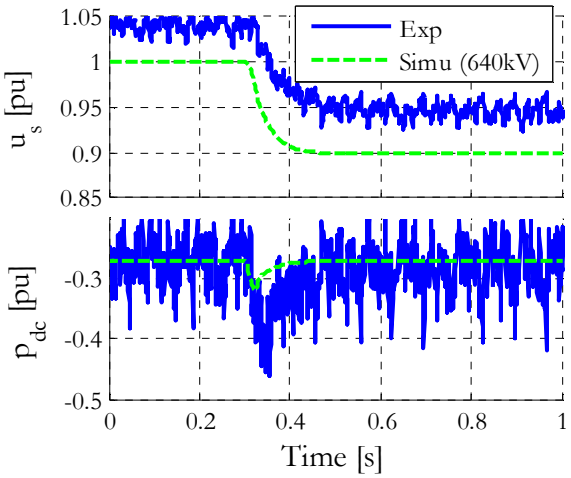

(e) WF3

Figure 6-11: Experimental results of a step power change of 0.25 pu on WF1 – Comparison with results from off-line simulation of a high voltage MTDC grid

6.3.2. Assessment of the coordinated control

This part should assess off-line simulation results obtained in Chapter 5 by doing tests on the hybrid DC grid mock-up.

Normal operation

To present the benefits of the coordinated controller, wind farm converter stations follow wind power profiles. One day of wind power production used in Chapter 5 is scaled down to the mock-up converter station nominal power.

To see what happens if there is no coordinated controller, same scenario is tested without this controller. For this test, the wind power profiles are set at 20 % of their values to avoid too large voltage deviations. The 24 h wind farm production profiles are simulated in 15 minutes in order to performed experimental tests in one quarter instead of one day. Since the wind farm production profiles have slow changes, this has no influence on the results. In the following, even though experimental results are obtained in 15 minutes, results are displayed as a function of the time of wind farm production profiles. For this test:

- GS1 and GS2 are droop controlled with droop value set at 0.82 pu/pu
- The power reference of GS1 is 0 W
- The DC voltage reference of GS1 is 250 V
- The power reference of GS2 is 0 W
- The DC voltage reference of GS2 is 250 V

In Figure 6-12, the power injected at wind farm stations is shared between GS1 and GS2 thanks to the droop control. The power extracted by GS2 is a bit higher than GS1 because the nominal power of GS2 is slightly larger than GS1. The DC voltage depends on the amount of power injected by wind farms; the more the power the higher the voltage. The DC voltage has already reached 275 V, i.e. 25 % over the nominal voltage, even with a power reduced to 20%.

Now considering a coordinated controller, the converter station references are computed by the Load Flow program with power sharing capability (see Chapter 5 part 5.3.3) which is performed on Matlab® client. The OPC protocol is used for the communication between the SCADA system (PCVue) and Matlab®. The Matlab® client retrieves information available on the SCADA server about:

- the actual power production of wind farm converter stations
- the desired voltage level for GS1 set at 250 V
- the states of each converter station

Each five seconds the SCADA system changes a variable to indicate to the Matlab client that it could start a new load flow. Once references are calculated, the Matlab® client overwrites the converter set points on the SCADA Server. These set points located on the SCADA server are sent to the converter station each 100 ms; i.e. the communication speed between converter stations and the SCADA system.

The Load Flow program has the DC grid admittance matrix which corresponds to the DC grid topology with measured resistances. To have a similar effect as the droop control which is defined in per unit, power sharing coefficients of GS1 and GS2 are not exactly equal since they do not have the same power rating. The sharing coefficients are:

- GS1: $\alpha_{GS1} = 1$
- GS2: $\alpha_{GS2} = 1.18$ ($\alpha_{GS2} = \alpha_{GS1} \frac{P_{n_{GS2}}}{P_{n_{GS1}}}$)
- WF1, WF2 and WF3: $\alpha_{WF} = 0$

As said before, there are extra losses due to converter switching losses. These losses cannot be handled by the load flow program since it works with power injected in the DC side while converter station powers are controlled in AC side. As a quick solution to this problem, roughly estimated converter losses are deducted before the load flow solving and then added to the power references.

In Figure 6-13, the same wind production profiles are tested with the coordinated controller. Profiles are also accelerated with the same speed as for the previous case, therefore the new operating points which are calculated each 5 s corresponds to time steps of 8 min if the production profile time scale is considered. The power profiles of grid side converter stations are similar to the case without coordinated controller since power sharing coefficient have been chosen to share power in the same way as for the droop control strategy. Nonetheless, there is a slight difference which is explained by the losses compensation mechanism on GS2 which induces a power displacement on that station. The main difference is on the DC voltage map which is very close to the nominal voltage, each 8 min the voltage of GS1 returns to the reference value.

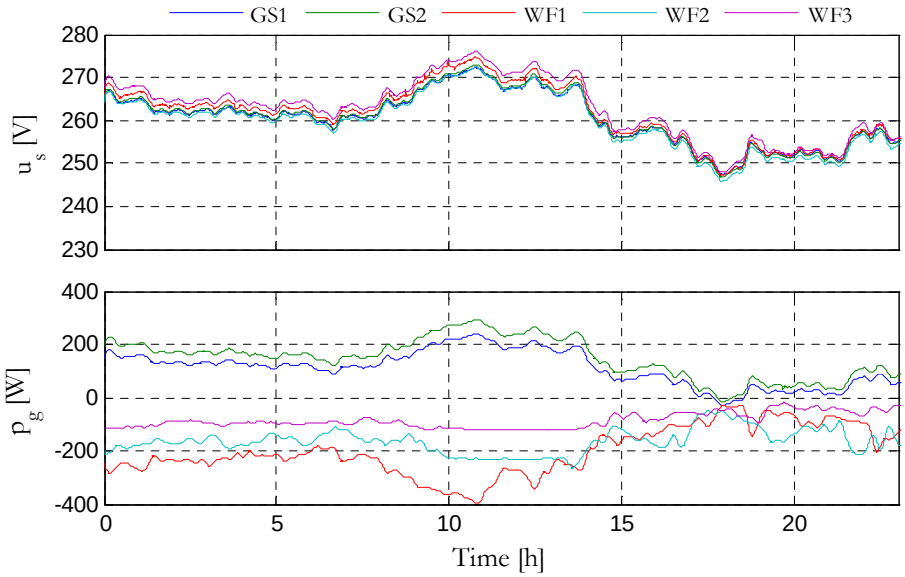

Figure 6-12: Experimental measure of 1 day of wind power production without the coordinated controller

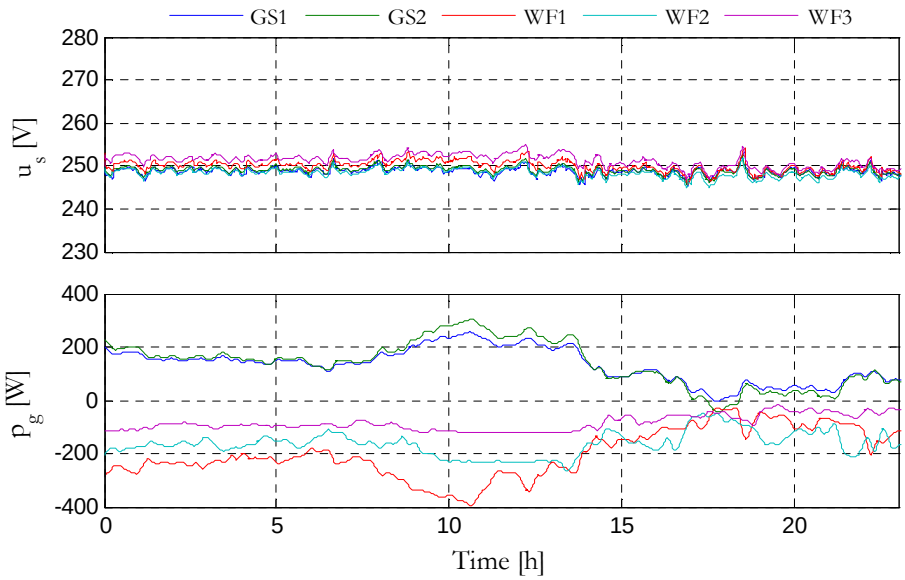

Figure 6-13: Experimental results of 1 day of wind power production with coordinated controller

Follow-up of the planned grid injection program

In Chapter 5, it was shown by off-line simulations that grid side converter stations can follow a planned AC grid injection program. To do this, the injection program grid used in Chapter 5 is scaled down to the nominal powers of the mock-up grid side converter stations.

In Figure 6-14, the previous scenario is tested with grid side power references filled by the injection program (dotted curves). The DC voltage looks like the previous case; the DC voltage is still close to the nominal value. Conversely to the previous case, grid side power transfers attempt to follow the schedule program instead of just sharing a part of wind power production. It is observed that power through grid side converters are further from the schedule program than off-line simulation results displayed in Chapter 5. This is due to mock-up losses, notably those of physical converters, which are higher in proportion than the 640 kV test system and are not considered in the creation of the schedule injection program. Moreover, it should be noticed that planned injection program is better followed by GS1 than by GS2 since there is more losses in GS2 which is a physical converter than in GS1 which is simulated.

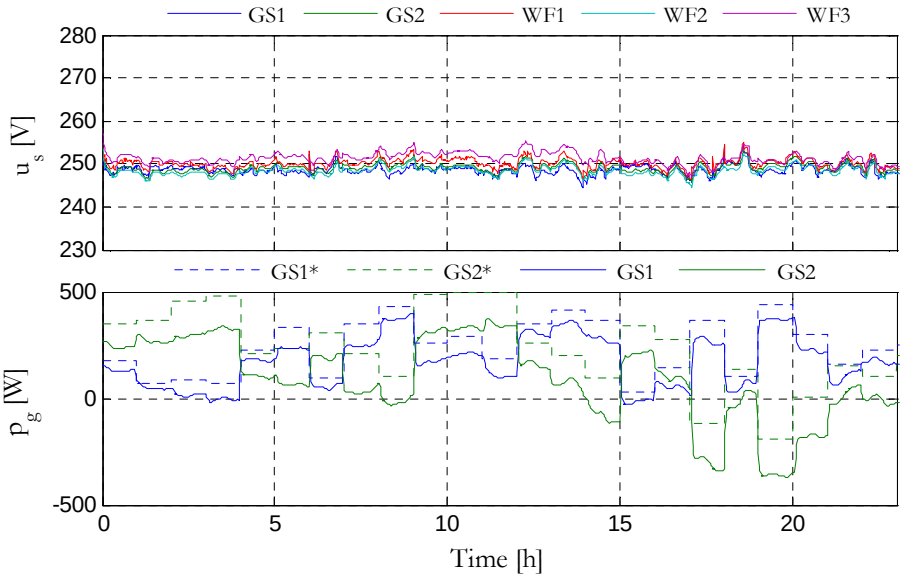

Figure 6-14: Experimental measurement of 1 day of wind power production with coordinated controller – Using a plan for grid side power injection

Alleviation of AC congestions

In section 5.6, it was shown that DC system can alleviate AC congestions on AC grid request in real time. To assess this functionality the Kundur's grid is connected to the mock-up grid side converter, like in Chapter 4. The nominal power of GS1 (resp.GS2) converter station is 400 MW (resp. 470 MW) on the AC side and 2200 W (resp. 2600 W) on the mock-up.

In Figure 6-15, the wind production profiles are the same as in previous cases, however this time an AC grid is connected behind the converter stations. To simulate an overloaded transmission line between the two AC areas, the load located in Area 2 is steeply increased and, in the meantime, the load located in the Area 1 is decreased while the generator productions are not modified. Once the limit of 300 MW is exceeded between Area 1 and Area 2 ($P_{A1 \rightarrow A2}$), the supervisor of the AC system asks the DC SCADA system to change quickly its grid side power injections in order to induce a 100 MW decrease on the transmission line. To do this, the DC SCADA system launches a new load flow to compute new converter station set points with:

- Power sharing coefficients for GS1 is 1,
- Power sharing coefficients for GS2 is 1.18,
- the power reference of GS1 is set at -100 MW (-550 W),
- the power reference of GS2 is set at +100 MW (+550 W),
- the power references of wind farm converter stations follow wind profile production.

The DC voltage map is not shown in this figure since it is similar to previous cases with coordinated controller. Powers delivered by GS1 and GS2 to the AC system are equivalent to Figure 6-13, until the AC system asks the DC system to change its power flows. To alleviate the AC transmission line between the two areas there is an offset of - 550 W (-100 MW) for GS1 and +550 W (+100 MW) for GS2 while powers injected by wind farm converter stations do not

change. This offset leads to decrease of 100 MW the power transmitted through the AC line between the two areas.

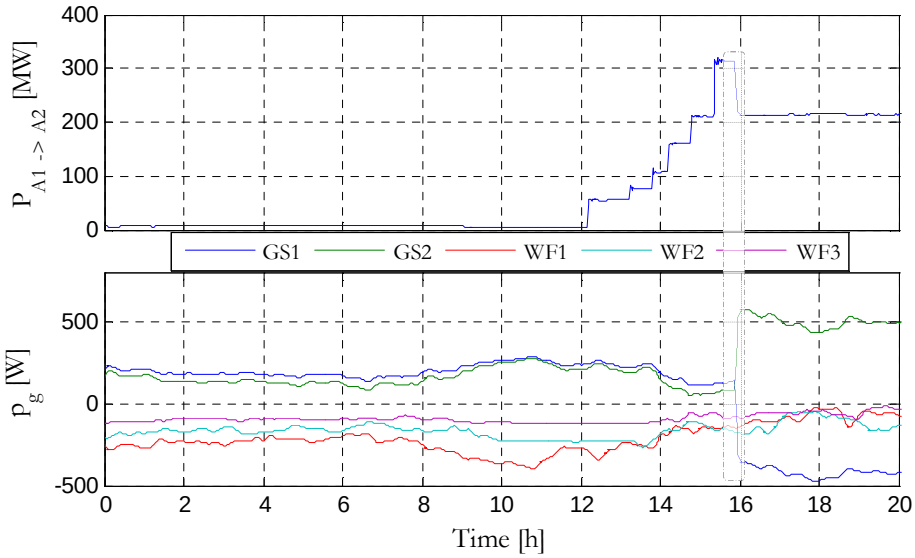

Figure 6-15: Experimental measurement of 1 day of wind power production with coordinated controller – Alleviation of an AC congestion

System restoration after a converter outage

It was suggested in Part 5.5 that the coordinated controller can reestablish normal operation after a severe event such as a station tripping. Two tests were carried out to assess this feature; one for an offshore station tripping and another for a grid side station tripping. It is easier and more accurate to trip real converter stations since breakers and firing-pulse inhibition do not have to be simulated. Before achieving these tests, it was checked that the loss of power flow of the tripped station does not lead to too much voltage deviation to avoid damages on DC grid components.

For these tests, the primary control strategy is tuned in the same way as in previous cases; grid side converters are droop controlled and wind farm converter stations maintain constant power. The coordinated controller updates grid side converter station references each 5 s and it is set to share the power harvested by wind farms between GS1 and GS2 in respect with their power rating, like for the previous test without the scheduled program. Before computing new set points, the coordinated controller checks if the converter is in operation or not. As shown in Figure 5-15, if the converter is out of operation, it is not taken into account in the coordinated control.

In Figure 6-16, results of the WF3 tripping test are shown. At 5 s, the WF3 is tripped and the power balance is provided by the two grid side converter stations which are droop controlled. At about 7 s, the coordinated controller sends new power and voltage references to GS1 and GS2, this leads to restore the DC voltage at nominal value without any power variation. There is no power variation since the power sharing parameters have been set to do the same thing as the droop control power sharing.

In Figure 6-17, results of the GS2 tripping are displayed. For this test, power injection from wind farms have been decreased again to avoid devastating overvoltage when the GS2 will be tripped. Conversely to the simulation test performed in Chapter 5 Part 5.5, wind farm converter stations are not equipped with dead band droop control to help the DC voltage to remain between bounds. At 5 s, GS2 is tripped and the whole power which was flowing through it is fully reported on GS1. At around 8 s, the coordinated controller sends new references to GS1, and therefore the DC voltage goes back to nominal value and the power delivered by GS1 is almost not impacted.

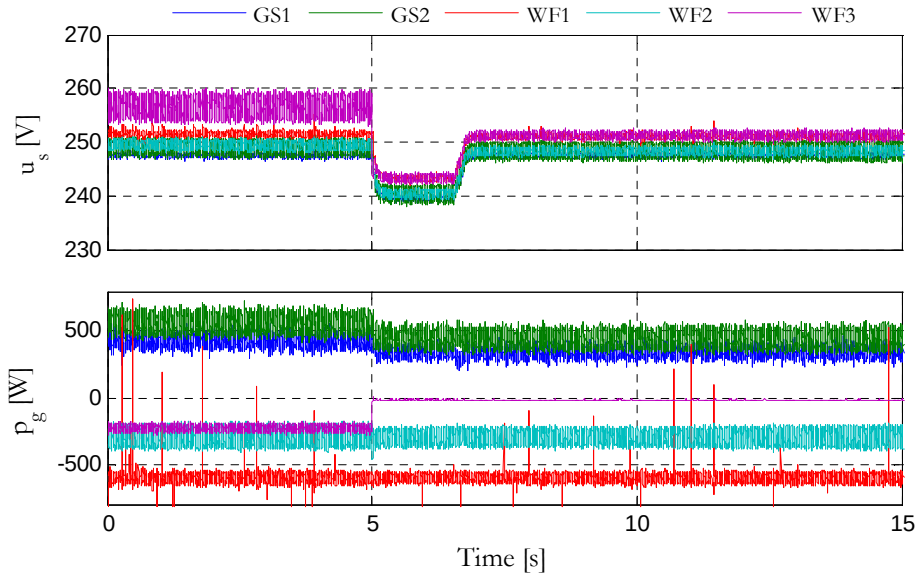

Figure 6-16: Outage of a wind farm converter station

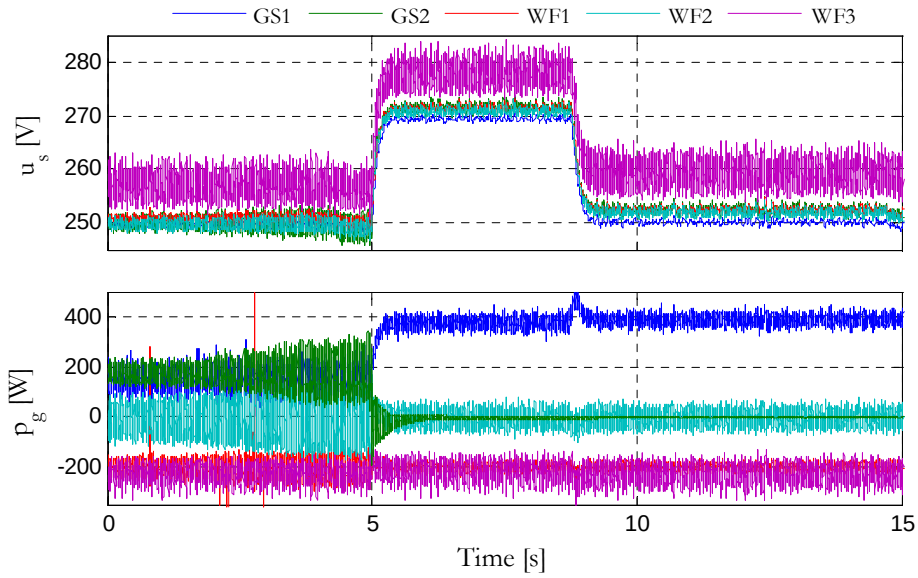

Figure 6-17: Outage of a grid side converter station

6.4 CONCLUSION

The architecture and the different equipment of a unique and novel hybrid low-voltage DC grid mock-up suitable for testing control strategies as well as DC fault protection scheme have been presented in this chapter. The objective of this work was to develop a demonstrator with experimental proof to assess offshore DC grid performances. The TWENTIES Demo3 mock-up provides an interesting intermediate and flexible step between off-line simulations and on site demonstrator. On the 3rd of April 2013, experimental tests were presented to the European Commission during a public demonstration which took place in the L2EP laboratory.

Tests which are carried out on this mock-up are fairly reflective of the reality since during the design phase, a methodology was set up to have a homothetic low-scale system to represent at best a high voltage DC grid. Thanks to this approach, the dynamics of the DC grid are well represented. Thus, the considerations on the DC voltage dynamics discussed in previous chapters have been experimentally retrieved. Also, since the control of each converter station is local and independent, it confirms that primary control strategies, such as the DC voltage droop control, work properly without synchronization and communication.

The management of the DC grid is provided by a SCADA system which enables the DC grid operator to monitor and interact with the DC system in real time. Thus, it is now possible to observe how the DC grid behaves when an operator remotely starts or shutdowns a station or changes a reference. Since measures and set points of converters are gathered at the same centralized computer, coordinated control algorithms could be tested. Tests performed with the coordinated controller have shown its effectiveness; either for automatically dispatching power flows or regulating the DC voltage level.

Moreover, owing to connection of a Real Time Simulator to the DC grid mock-up, the impact of the connection of a DC grid to an AC grid can be assessed with various AC topologies, such as how DC grid can alleviate AC contingencies.

Finally, thanks to the physical low voltage shield cables which give similar propagation time than real HVDC cables, a DC fault protection algorithm have been tested and validated in the PhD thesis of Justine Descloux.

In conclusion, this mock-up has some limitations because of the low-scale: voltage drops through cables are too large in proportion and real converter stations have too much loss and generate a lot of noise. Nevertheless, despite these flaws, as one of the first experimental DC grid, this mock-up has already shown extremely valuable results and will undoubtedly be further upgraded to help the development of future DC grids.

CONCLUSION

Nowadays, political leaders and all relevant actors in the society are looking for solutions to produce energy with a low impact on the environment. In this context, installing new solar, wind and hydro power plants seems to be one of solutions. Nonetheless, these sources are not as flexible as traditional ones since they cannot be installed anywhere as they need a favorable production location and citizens often do not want such installations close to their homes. Additionally, renewable energy sources often exhibits an intermittent behavior, which can be smoothed by considering an energy mix and a production from different areas. For that purpose and also to improve electricity trading between countries, existing transmission lines must be reinforced and new interconnections must be built. As mentioned in Chapter 1, to connect offshore wind farms located further than 50 km from the shore and improve power transfer between countries across the sea, DC transmission is the only feasible solution. As cost-effective solution and reliability enhancement, DC grids are expected to improve the transmission flexibility and the accommodation capacity of green energy towards the load centers which are located within actual AC grids.

Such DC grids do not exist yet and their control and protection shall be developed. The TWENTIES DEMO3 project was launched to assess the main drivers for the development of multi-terminal HVDC grids. As part of the TWENTIES Work Package 11, this work aims to assess control strategies to manage DC grids and to test them on a reduced scale demonstrator. For reliability reasons, the proposed DC grid control structure does not rely on fast communication and remain in operation with a loss of communication. In fact, in this study, converter stations are locally controlled by their associated control loops and by another level which enables to balance the DC grid power flows at any time. The system restoration at nominal operating points and the power dispatching is provided by a centralized coordinated controller which sends new set points to converter stations at longer time frame.

In Chapter 1, the comparison of both LCC and VSC technologies leads to choose VSC; since recent advances made in power electronics, VSCs are becoming more and more reliable, flexible and efficient. Conversely to LCC, they can be connected to passive or weak AC grids (e.g. wind farms), can control quickly, smoothly and independently active and reactive powers and can easily reverse their power flow. For all these reasons, VSC technologies are considered as the best candidate for DC grids. In the last part of Chapter 1, the classical control of VSC is presented. It is composed of the current control scheme in the dq frame, the active and reactive power controllers, the DC voltage controller, as well as the operating limits.

One of the objectives of this work was to evaluate the stability of control strategies. In the same way as for AC power system stability problems, the small signal stability analyses were considered. A linearized model of the system has to be developed, this is presented in Chapter 2; the small signal model of DC system is developed, first, component by component and then a method to aggregate these models is presented. The linearization of the VSC is given step by step. First, the linear model of the current controlled VSC is detailed, and then the linear model of the power controlled VSC, and finally the linear model of DC voltage controlled VSC. All these models have been successfully validated by a time domain simulation which compares the linear model against an accurate model simulated in the EMTP-RV® software. Also, in this chapter, a novel linear simplified cable model is proposed. The comparison with accurate

Wideband cable model proves that classical Π models are not appropriate to represent the cable behavior in the bandwidth of converter control loop dynamics. This investigation leads to a new cable model suitable to assess control stability. This model includes the coupling between the core and the screen conductors. This chapter ends by an example of point-to-point HVDC link to introduce the method of small signal stability analysis.

In Chapter 3, the analogy between AC systems and DC systems reveals that the inertia constant of rotating machines can be compared to an electrostatic constant which represents the converter station capacitor. Since this electrostatic constant is much lower than the inertia constant, it results that the storage which stabilizes the system during disturbances is lower in DC grids. Then a literature review on DC grid control strategies leads to choose the DC voltage droop method since the burden of voltage control and power balance is shared among several stations. This method is particularly interesting when there are several stations connected to onshore grids.

The objective of the second part of Chapter 3 was to explain the behavior of the DC grid when it is droop controlled. To this end, the DC grid was simplified to keep only the main drivers which influence the DC voltage and the power transfer. This simplification leads to a first order transfer function which involves the converter station droop parameters as well as the converter station capacitor values. Thanks to this approach, considerations on the DC voltage dynamics have been easily found:

- Increasing the droop parameters leads to slow the DC voltage dynamics and increase the relative voltage deviation caused by a given power deviation.
- Increasing the converter station DC capacitor values leads to slow down the DC voltage dynamics.

Based on these results, a methodology to design the droop value was developed; the DC voltage dynamics is tuned by adjusting the droop parameters to achieve a slower dynamics than converter station current control loops and therefore obtain a smooth control. However, having a response time around 100 ms leads to high droop values and high voltage deviations for a given power variation. It has been observed that if the DC voltage has to remain between $\pm 5\,\%$ bounds, then the maximal power deviation manageable in the DC grid is much lower than the nominal power of one converter station. It implies the impossibility of the DC system to keep the required performance when this converter suddenly fails. Then a discussion on the voltage limits, the DC voltage dynamics and the converter station capacitor values was undertaken to state explicitly how the maximal admissible power deviation could be improved. As a reflection on this, increasing the converter station capacitor values and pushing up DC voltage boundaries is the best way to enable more power deviation. To illustrate this point, the value of capacitors needed to enable "N-1 converter condition" is calculated on a three-terminal DC grid, this leads to multiply by 20 the value of actual VSC capacitors.

Chapter 4 deals with the stability of MTDC grids; it relies on the models developed in Chapter 2. The modal analysis of a five-terminal DC grid shows that DC cable modes are dissociated from converter control modes since they have different dynamics. Modes of power and current control loops are retrieved at their expected values. The DC voltage modes are

plotted as a function of the droop parameter and the converter station capacitor value. It results that for slow DC voltage dynamics (i.e. 10 times slower than current control loop dynamics) the DC voltage mode is exactly at the value given by the simplified model found in Chapter 3. However, for faster dynamics, the eigenvalues obtained by modal analysis with the full system are slower than the roots of the simplified model. The interaction between current control loops and voltage control loop explains this phenomenon.

The second part of this chapter is focused on AC-DC interactions. Modal analyses are used to prove interactions between the five-terminal DC grid and a generic AC grid. The methodology employed consists in studying the modes of each system separately and then analyzing the modes of the combined AC-DC system. Apart from PLL modes, modes of the full system are a juxtaposition of modes of both systems. Having the DC grid participating to the frequency support leads to slightly change the DC voltage mode since the DC voltage control loops is modified. Electromechanical modes are not impacted by the connection of a DC grid if there is no frequency participation and are slightly modified with frequency participation.

Considering two asynchronous AC grids connected by a DC grid, their electromechanical modes remain independent as long as there is no frequency support from the DC grid. If the DC grid participates to the frequency support, electromechanical modes involve mechanical states of both areas.

The coordination of local control is presented in Chapter 5. The proposed coordinated controller aims to maintain the system in normal operation, to ensure the desired power transfer and restore the system in normal operation after an event. The coordinated controller sends regularly new set points to converter stations; power and voltage for droop controlled stations and only power for power controlled stations. As it has an action time scale much higher than DC grid dynamics, only steady state behavior is considered. Since with a classical load flow algorithm, the system inherent losses and the prediction errors are both reported on a slack bus, a new load flow algorithm was developed to dispatch these errors on several buses. The performances of coordinated controller were tested with one day of wind power production. The comparison of both results with and without the coordinated controller shows the effectiveness of this control. The trip of a station was also tested, it has shown that the coordinated controller enables to restore the system under normal operation but it cannot solve N-1 situation because of its time frame.

Finally, the experimental validations of control principles developed in this work have been presented in Chapter 6. Since it was impossible to conduct tests with a full-scale demonstrator, a hybrid small scale DC grid connected to a virtual AC grid was developed. A homothetic design has been considered to represent at best a high voltage system. Once compared in per unit, simulation of both converter stations controlled in droop has shown very close results, even if they have really different levels of voltage and power. DC cables were especially chosen for their propagation speed to be able to test a protection plan, so their behavior is not really similar to real HVDC cable; they are too resistive in proportion.

Despites excessive voltage drops through cables, results obtained on the mock-up and those obtained by simulation of the full-scale system exhibits very close dynamics, similar to a

first order transfer function. Thus the simplified approach of Chapter 3 is validated by this experimentation. Also, thanks to a centralized supervisor it was possible to implement a coordinated control algorithm which is physically independent from the local control. Tests performed with the coordinated controller have shown its effectiveness; either for automatically dispatching power flows or regulating the DC voltage level.

As main contribution, this work has emphasized the DC grid dynamics when this one is droop controlled. Also, it has shown the effectiveness of a centralized controller to manage local and independent control without fast communication.

Future works will focus on the following list:

- Consider MMC instead of PWM based 2-level VSC since voltage excursion and current control dynamics may be different.
- Consider more complex wind farms models to verify how they can change their power flow, either if they are droop controlled or if they participate to the frequency support of onshore AC grids.
- Have a discussion between converter station manufacturers and TSOs to know what could be the dynamics of power variations in normal and emergency situation. The DC voltage dynamics depends on it.
- Lead an investigation on DC grid variant control methods: Dead band droop method and piecewise droop method.
- Trace modes on parametric studies with only relevant modes to avoid getting lost among a large number of modes.
- Consider dynamic AC line model to verify if there is no interaction between converter control loops and AC line resonances.
- Assess robustness of control strategies should be considered. Nonlinear methods and predictive control methods should help assessing the stability over an operating range conversely to modal analyses which are focused on only one operating point.
- Improve the coordinated controller:
    - Develop a DC power flow which includes VSC losses.
    - Develop a coordinated control which redispatches power flow if powers through cables exceed their limits.
- Test if the coordinated control could be used for the frequency support. Indeed, in view of frequency support dynamics, the coordinated controller could be used instead of a frequency droop on grid side converter stations. Thus, the system modes must change.
- Improve the mock-up:
    - Increase the nominal voltage of the mock-up to decrease the relative voltage drops.
    - Improve the efficiency of physical VSCs to be more representative of high voltage converter.
    - Improve the robustness of the mock-up to be able to test the mock-up at nominal power without risk of damage, notably on power amplifiers.

REFERENCES

[ABB06] "HVDC Light power cables - Submarine and land power cables," ABB, Technical brochure - HVC 2GM5001-gb 3000, Apr. 2006.

[ABB13] "5SNA 2000K450300 - StakPak IGBT Module," ABB, Data Sheet, 2013.

[ADA12a] GP Adam, SJ Finney, K Bell, and BW Williams, "Transient capability assessments of HVDC voltage source converters," in *Power and Energy Conference at Illinois (PECI), 2012 IEEE*, pp. 1-8, 2012.

[AIN67] J.D. Ainsworth, "Discussion on Harmonic instability between controlled static convertors and a.c. networks," *Proceedings of the Institution of Electrical Engineers*, vol. 114, no. 12, pp. 949-957, 1967.

[ALS11] A. M. Alsseid, D. Jovcic, and A. Starkey, "Small signal modelling and stability analysis of multiterminal VSC-HVDC," in *Proc. 2011-14th European Conf. Power Electronics and Applications (EPE 2011)*, pp. 1-10, 2011.

[AND02] BR Andersen, L Xu, PJ Horton, and P Cartwright, *Topologies for VSC transmission.*: IET, vol. 16, 2002.

[AND05] B. Andersen et al., "VSC transmission," CIGRE WG B4.37, Technical Brochure, May 2005.

[ASP11] G. Asplund, "HVDC Grid Feasibility Study," CIGRE B4.52, Technical Brochure, Dec. 2011.

[BAD12] Babak Badrzadeh, "Power conversion systems for modern ac–dc power systems," *European Transactions on Electrical Power*, vol. 22, no. 7, pp. 879-906, 2012. [Online]. http://dx.doi.org/10.1002/etep.611

[BAH07] M. P. Bahrman and B. K. Johnson, "The ABCs of HVDC transmission technologies," *IEEE Power and Energy Magazine*, vol. 5, no. 2, pp. 32-44, 2007.

[BAH08] M.P. Bahrman, "HVDC transmission overview," in *Transmission and Distribution Conference and Exposition, 2008. T&D. IEEE/PES*, pp. 1-7, 2008.

[BAL12] B Jayant Baliga, *Advanced high voltage power device concepts*, Springer New York ed.: Springer Science+ Business Media, 2012.

[BAR10] C. D Barker and R. Whitehouse, "Autonomous converter control in a multi-terminal HVDC system," in *Proc. ACDC AC and DC Power Transmission 9th IET Int. Conf*, pp. 1-5, 2010.

[BEE11] Jef Beerten, Dirk Van Hertem, and Ronnie Belmans, "VSC MTDC systems with a distributed DC voltage control - A power flow approach," in *Proc. IEEE Trondheim PowerTech*, pp. 1-6, 2011.

[BEE13] Jef Beerten, "Modeling and Control of DC Grids," KU Leuven - Science,

Engineering and Technologies, Ph.D. dissertation, 2013.

[BER00] François BERNOT, "Composants de l'électronique de puissance," *Techniques de l'ingénieur Alimentations et électronique de puissance*, vol. base documentaire : TIB283DUO., no. ref. article : e3960, Aug. 2000, fre.

[BOR13] P. Bornard, M. Pavard, and G. Testud, "Réseaux d'interconnexion et de transport : réglages et stabilité," *Techniques de l'ingénieur Réseaux électriques de transport et de répartition*, vol. base documentaire : TIB263DUO., no. ref. article : d4092, 2013, fre.

[CHA11a] R.N. Chaudhuri and B. Chandhuri, "Impact of Wind Penetration and HVDC Upgrades on Dynamic Performance of Future Grids," in *IEEE Power and Energy Society - General Meeting*, 2011.

[CHA11c] N. R. Chaudhuri, R. Majumder, B. Chaudhuri, and Jiuping Pan, "Stability Analysis of VSC MTDC Grids Connected to Multimachine AC Systems," *IEEE Transactions on Power Delivery*, vol. 26, no. 4, pp. 2774-2784, 2011.

[CHA13] N. R. Chaudhuri, R. Majumder, and B. Chaudhuri, "System Frequency Support Through Multi-Terminal DC (MTDC) Grids," *IEEE Transactions on Power Systems*, vol. 28, no. 1, pp. 347-356, 2013.

[CHA13a] N. R. Chaudhuri and B. Chaudhuri, "Adaptive Droop Control for Effective Power Sharing in Multi-Terminal DC (MTDC) Grids," *IEEE Transactions on Power Systems*, vol. 28, pp. 21-29, 2013, Early Access.

[CIG10] "Voltage Source Converter (VSC) HVDC for Power Transmission– Economic Aspects and Comparison with other AC and DC Technologies," CIGRE WG B4-46, Technical Brochure, Oct. 2010.

[COL10] S. Cole, "Steady state and dynamic modelling of VSC HVDC systems for power system simulation," Katholieke Universiteit Leuven – Faculteit Ingenieurswetenschappen, Katholieke Universiteit Leuven – Faculteit Ingenieurswetenschappen, Ph.D. dissertation, DOI: ISBN 978-94-6018-239-6, September 2010.

[COL10a] S. Cole, J. Beerten, and R. Belmans, "Generalized Dynamic VSC MTDC Model for Power System Stability Studies," *IEEE Transactions on Power Systems*, vol. 25, no. 3, pp. 1655-1662, 2010.

[DEC11] J.D. Decker and P. Kreutzkamp, "Offshore Electricity Grid Infrastructure in Europe : A Techno-Economic Assessment," 3E , dena, EWEA, ForWind, IEO, NTUA, Senergy, SINTEF, OffshoreGrid's final report, Oct. 2011.

[DES12] J. Descloux et al., "HVDC Meshed grid : Control and Protection of a Multiterminal HVDC System," in *CIGRE General Session, Paris, France*, 2012.

[DES12a] O. Despouys, "Offshore DC Grids: Inpact of Topology on Power Flow Control," in *IET proc. in the 10th International Conference on AC and DC Power Transmission, Birmingham*, 2012.

[DES13] (2013, June) Desertech Fundation. [Online]. http://www.desertec.org

[DES13a] J. Descloux, "Protection contre les courts-circuits des réseaux à courant continu de forte puissance," École Doctorale Électronique, Électrotechnique, Automatique et Traitement du Signal de Grenoble - Laboratoire de Génie Électrique de Grenoble (G2Elab), Ph.D. dissertation, Sep. 2013.

[DIE12] C. Dierckxsens et al., "A distributed DC voltage control method for VSC MTDC systems," *Electric Power Systems Research*, vol. 82, no. 1, pp. 54-58, 2012. [Online]. http://www.sciencedirect.com/science/article/pii/S0378779611001933

[DOR08] J. Dorn, H. Huang, and D. Retzmann, "A new Multilevel Voltage-Sourced Converter Topology for HVDC Applications," , Paris, France, 2008.

[EIR11] "EirGrid Grid Code - Version 4.0," EirGrid, Tech. rep., Dec. 2011. [Online]. http://clients.rte-france.com/lang/fr/clients_producteurs/mediatheque_client/dtr.jsp

[EMT12] Jean Mahseredjian, "EMTP-RV help," PowerSys, 2012.

[ENE09] "An Analysis of Offshore Grid Connection at Kriegers Flak in the Baltic Sea," Energinet.dk, Svenska Kraftnät, Vattenfall Europe Transmission, Tech. rep., May 2009.

[ENT10] "Ten year network development plan 2010-2020," ENTSO-E, Tech. rep., 2010. [Online]. http://www.entsoe.eu

[ENT11] ENTSOE, "Offshore Transmission Technology," ENTSOE, Tech. rep., Nov. 2011. [Online]. www.entsoe.eu

[EUR08] Commission of the European Communities, *20 20 by 2020: Europe's Climate Change Opportunity: Communication from the Commission to the European Parliament, the Council, the Economic and Social Committee and the Committee of the Regions*. Bruxelles: Official Publications of the European Communities, 2008. [Online]. http://eur-lex.europa.eu/LexUriServ/LexUriServ.do?uri=CELEX:52008DC0030:EN:HTML:NOT

[EUR12] Europacable, "Introduction to HVDC Subsea Cables," Europacable, Tech. rep., July 2012. [Online]. www.europacable.com

[FIC09] N. Fichaux, J. Wilkes, F. Van Hulle, and Cronin A., "Oceans of Opportunity," EWEA (European Wind Energy Association), Tech. rep., 2009.

[FRI13] (2013, June) Friends of the Supergrid. [Online].

http://www.friendsofthesupergrid.eu

[GON12a] Francisco Gonzalez-Longatt and Juan Manuel Roldan, "Effects of dc voltage control strategies of voltage response on multi-terminal HVDC following a disturbance," in *Universities Power Engineering Conference (UPEC), 2012 47th International*, pp. 1-6, 2012. [Online]. http://ieeexplore.ieee.org/xpls/abs_all.jsp?arnumber=6398553

[GRU99] R. Grunbaum, B. Halvarsson, and A. Wilk-Wilczynski, "FACTS and HVDC Light for power system interconnections," in *Power Delivery Conference, Madrid, Spain*, pp. 1-18, 1999.

[HAI08] T.M. Haileselassie, M. Molinas, and T. Undeland, "Multi-Terminal VSC-HVDC System for Integration of Offshore Wind Farms and Green Electrification of Platforms in the North Sea," in *Nordic Workshop on Power and Industrial Electronics*, vol. 4, p. 12, June 2008.

[HAI08a] T.M. Haileselassie, "Control of Multi-terminal VSC-HVDC Systems," Norwegian University of Science and Technology, Department of Electrical Power Engineering, Master's thesis, 2008. [Online]. http://urn.kb.se/resolve?urn=urn:nbn:no:ntnu:diva-8933

[HAI09a] T. Haileselassie, "Control of multiterminal HVDC transmission for offshore wind energy," , pp. 1-7, September 2009.

[HAI12] T.M. Haileselassie and K. Uhlen, "Precise Control of Power Flow in Multiterminal VSC-HVDCs Using DC Voltage Droop Control," in *Proc. IEEE Power and Energy Society General Meeting*, 2012.

[HAN03] T.L. Hanley, R.P. Burford, R.J. Fleming, and K.W. Barber, "A general review of polymeric insulation for use in HVDC cables," *Electrical Insulation Magazine, IEEE*, vol. 19, no. 1, pp. 13-24, 2003.

[HOL92] Joachim Holtz, "Pulsewidth modulation-a survey," *IEEE Transactions on Industrial Electronics*, vol. 39, no. 5, pp. 410-420, 1992.

[IEE13] IEEE Global History Network. (2013, Apr.) www.ieeeghn.org. [Online]. http://www.ieeeghn.org/wiki/index.php/Milestone-Nomination:Eel_River_Back-to-Back_High_Voltage_Direct_Current_Converter_Station,_1972

[INE11] "INELFE," Press Release, January 2011. [Online]. http://www.energy.siemens.com/us/en/power-transmission/hvdc/hvdc-plus/references.htm#content=2014%20INELFE%2C%20France-Spain

[INE12] "Inelfe chooses Prysmian and Siemens to build the new power line between France and Spain," Press release, June 2012. [Online]. www.inelfe.eu

[JAC10] B. Jacobson, P. Karlsson, G. Asplund, L. Harnefors, and T. Jonsson, "VSC-HVDC

transmission with cascaded two-level converters," in *Cigre, France, Paris*, 2010.

[JOV09a] D. Jovcic, "Power flow study in DC Grids, considering nominal operation and under DC faults," University of Aberdeen, Tech. rep., Oct. 2009.

[KAL12] G. O. Kalcon, G. P. Adam, O. Anaya-Lara, S. Lo, and K. Uhlen. (2012) Small-Signal Stability Analysis of Multi-Terminal VSC-Based DC Transmission Systems.

[KAR02] P. Karlsson, "DC Distributed Power Systems-Analysis, Design and Control for a Renewable Energy System," Lund University, Department of Industrial Electrical Engineering and Automation, Ph.D. dissertation, ISBN: 918893425X, 2002.

[KLE91] M. Klein, G. J. Rogers, and P. Kundur, "A fundamental study of inter-area oscillations in power systems," *IEEE Transactions on Power Systems*, vol. 6, no. 3, pp. 914-921, 1991.

[KOC08] I. Kocar, J. Mahseredjian, and G. Olivier, "Weighting Method for Transient Analysis of Underground Cables," *IEEE Transactions on Power Delivery*, vol. 23, no. 3, pp. 1629-1635, jul. 2008.

[KUN04] P. Kundur et al., "Definition and classification of power system stability IEEE/CIGRE joint task force on stability terms and definitions," *IEEE Transactions on Power Systems*, vol. 19, no. 3, pp. 1387-1401, Aug. 2004.

[KUN94] P. Kundur, N.J. Balu, and M.G. Lauby, *Power system stability and control.*: McGraw-Hill Professional, 1994.

[LAT11] Héctor F. Latorre, "Modeling and Control of VSC-HVDC Transmissions," KTH Royal Institute of Technology, School of Electrical Engineering, Electric Power Systems, Stockholm, Sweden, Ph.D. dissertation, 2011.

[LES03] A. Lesnicar and R. Marquardt, "An innovative modular multilevel converter topology suitable for a wide power range," in *Proc. IEEE Bologna Power Tech*, vol. 3, 2003.

[LEV12] F. Leveque, L. Meeus, I. Azevedo, M. Saguan, and Glachant J-M., "Offshore Grids: Towards a Least Regret EU Policy," Final Report - Topic 5 - Think, DOI: 10.2870/35516, 2012. [Online]. http://think.eui.eu

[LIN98a] M. Lindgren, "Modeling and Control of Voltage Source Converters connected to the grid," Electrical and Computer Engineering Chalmers University of Technology, CHALMERS UNIVERSITY OF TECHNOLOGY, Ph.D. dissertation, 1998.

[LIU11a] C.-C Liu et al., "Preliminary Analysis of HVDC Networks for Off-Shore Wind Farms and Their Coordinated Protection," Status report for European Commission, Deliverable D5.1. FP7 Twenties project EC-GA n° 249812, May 2011.

[LON90] Willis F Long et al., "Application aspects of multiterminal DC power transmission,"

IEEE Transactions on Power Delivery, vol. 5, no. 4, pp. 2084-2098, 1990.

[MAC11] N. M. MacLeod, C. D. Barker, and Totterdell A. J., "From concept to reality; the development of a multi-level VSC HVDC converter," , Italy, Bologna, 2011.

[MAT13] Mathworks. (2013, Sep.) R2013b Documentation. [Online]. www.mathworks.com

[MAY10] L. Mayron-de-Olivera-Pinto, "Gestion de réseau à courant continu à multi terminaux, analyse et traitement des défauts," INP-ENSEEIHT, Institut National Polytechnique de Toulouse, Master's thesis, 2010.

[MON12] Pascal Monjean, "Optimisation de l'architecture et des flux énergétiques de centrales à énergies renouvelables offshore et onshore équipées de liaisons en continu," l'École Nationale Supérieure d'Arts et Métiers, Ph.D. dissertation, September 2012.

[NAK99] T. Nakajima and S. Irokawa, "A control system for HVDC transmission by voltage sourced converters," in *Proc. IEEE Power Engineering Society Summer Meeting*, vol. 2, pp. 1113-1119, 1999.

[NEG06] N. Barberis Negra, J. Todorovic, and T. Ackermann, "Loss evaluation of HVAC and HVDC transmission solutions for large offshore wind farms," *Electric Power Systems Research*, vol. 76, no. 11, pp. 916-927, 2006.

[NGU11] S. Nguefeu et al., "Accomodation of offshore wind farms: an opportunity for the development of HVDC grids," in *4th European Conference on HV and MV Substation Equipment*, 2011.

[NUQ12] R. Nuqui, J. Pan, K. Srivastava, and T. Jonsson, "Coordinated control of multi-terminal HVDC system," no. 20120092904, April 2012.

[OKB12] M.H. Okba, M.H. Saied, M. Z. Mostafa, and T. M. Abdel-Moneim, "High voltage direct current transmission - A review, part I," in *Energytech, IEEE*, pp. 1-7, 2012.

[PER12] Jaime Peralta, Hani Saad, Sébastien Dennetière, Jean Mahseredjian, and Samuel Nguefeu, "Detailed and averaged models for a 401-level MMC--HVDC system," *IEEE Transactions on Power Delivery*, vol. 27, no. 3, pp. 1501-1508, 2012.

[PIN11] G. Pinares, "Undersatnding the Operation of HVDC grids," in *Cigre 2011, Bologna*, 2011.

[PRE13] Robin Preece, "A probabilistic approach to improving the stability of meshed power networks with embedded HVDC lines," University of Manchester, Ph.D. dissertation, 2013. [Online]. https://www.escholar.manchester.ac.uk/api/datastream?publicationPid=uk-ac-man-scw:186981&datastreamId=FULL-TEXT.PDF

[PRI11] E. Prieto-Araujo, F. D. Bianchi, A. Junyent-Ferre, and O. Gomis-Bellmunt, "Methodology for Droop Control Dynamic Analysis of Multiterminal VSC-HVDC

Grids for Offshore Wind Farms," *IEEE Transactions on Power Delivery*, vol. 26, no. 4, pp. 2476-2485, 2011.

[SAK83] T. Sakurai, K. Goto, S. Irokawa, K. Imai, and T. Sakai, "A New Control Method for Multiterminal HVDC Transmission Without Fast Communications Systems," *IEEE Transactions on Power Apparatus and Systems*, no. 5, pp. 1140-1150, 1983.

[SEK00] N. Seki, "Field testing of 53 MVA three-terminal DC link between power systems using GTO converters," in *Proc. IEEE Power Engineering Society Winter Meeting*, vol. 4, pp. 2504-2508, 2000.

[SEL12] R.L. Sellick and M. Akerberg, "Comparison of HVDC Light (VSC) and HVDC Classic (LCC) site aspects, for a 500MW 400kV HVDC transmission scheme," in *10th IET International Conference on AC and DC Power Transmission (ACDC 2012)*, pp. 1-6, 2012.

[SHA11] R. Sharma, "Electrical structure of future offshore wind farms with a HVDC transmission connection," Department of Eletrial Engineering, Centre for Eletric Tehnology (CET), Tehnical University of Denmark, Lyngby Denmark, Ph.D. dissertation, 2011.

[SIE11] "High voltage direct current transmission-proven technology for power exchange," SIEMENS, Brochure from SIEMENS, 2011.

[SIL12] B. Silva, C. L. Moreira, L. Seca, Y. Phulpin, and J. A. Pecas Lopes, "Provision of Inertial and Primary Frequency Control Services Using Offshore Multiterminal HVDC Networks," *IEEE Transactions on Sustainable Energy*, vol. 7, pp. 800-808, 2012.

[SWI07] S. Swingler et al., "Statistics of AC underground cable in power networks," CIGRE WG B1.07, Technical Brochure, 2007.

[TAY07] R. Taylor, "HVDC Projects Listing," Working Group on HVDC and FACTS Bibliography and Records (DC and Flexible AC Transmission Subcommittee of the IEEE Transmission and Distribution Committee), Report, 2007.

[TEE09] S. P. Teeuwsen, "Simplified dynamic model of a voltage-sourced converter with modular multilevel converter design," in *Proc. IEEE/PES Power Systems Conf. and Exposition PSCE '09*, pp. 1-6, 2009.

[TEN13] Tennet. (2013, June) BorWin1 project: First DC power link between an offshore wind park and the very-high voltage grid. [Online]. http://www.tennet.eu/de/en/grid-projects/offshore-projekte/borwin1.html

[TWE11] C.-C Liu et al., "Preliminary Analysis of HVDC Networks for Off-Shore Wind Farms and Their Coordinated Protection," Status report for European Commission, Deliverable D5.1. FP7 Twenties project EC-GA n° 249812, Mar. 2011.

[TWE11a] D. Cirio et al., "Principles of an optimal operation of the AC/DC interconnected power systems – Specification of the requirements for the HVDC grid (DCG) injections to the AC grid," Status report for European Commission, Deliverable D5.2b. FP7 Twenties project EC-GA n° 249812, Dec. 2011.

[TWE13] "TWENTIES project," TWENTIES, Final report for EWEA, FP7 Twenties project EC-GA n° 249812, Oct. 2013. [Online]. www.twenties-project.eu

[UCT04] "Operation Handbook," UCTE, Tech. rep., 2004.

[VEC11] Aurélien Vécrin, "Réseaux électriques à courant continu pour l'intégration des énergies renouvelables dans les réseaux alternatifs : Stabilité statique et dynamique," Université Lille 1, Master's thesis, 2011.

[VOU04] C.D. Vournas, E.G. Potamianakis, C. Moors, and T. Van Cutsem, "An educational simulation tool for power system control and stability," *Power Systems, IEEE Transactions on*, vol. 19, no. 1, pp. 48-55, feb. 2004.

[VRA12] T.K. Vrana, L. Zeni, and O. B. Fosso, "Active Power Control with Undead-Band Voltage \& Frequency Droop for HVDC Converters in Large Meshed DC Grids," in *EWEA Conference, Copenhagen,* April 2012.

[WAN12] W. Wang, M. Barnes, and O. Marjanovic, "Droop Control modelling and Analysis of Multi-terminal VSC-HVDC for Offshore Wind Farms," in *IET proc. in the 10th International Conference on AC and DC Power Transmission, Birmingham*, 2012.

[WIK13] Wikipedia, the free encyclopedia. (2013, Apr.) wikipedia.org. [Online]. http://en.wikipedia.org/wiki/Ren%C3%A9_Thury

[XU09] L. Xu, L. Yao, and M. Bazargan, "DC grid management of a multi-terminal HVDC transmission system for large offshore wind farms," in *Proc. Int. Conf. Sustainable Power Generation and Supply SUPERGEN '09*, pp. 1-7, 2009.

[YAO08] Wei Yao, Jinyu Wen, Shijie Cheng, and Haibo He, "Modeling and simulation of VSC-HVDC with dynamic phasors," in *Proc. Third Int. Conf. Electric Utility Deregulation and Restructuring and Power Technologies DRPT 2008*, pp. 1416-1421, 2008.

[YAZ10] Amirnaser Yazdani and Reza Iravani, *Voltage-Sourced Converters in Power Systems.*: Wiley, 2010.

[ZHA10] L. Zhang, "Modeling and control of VSC-HVDC links connected to weak systems," ROYAL INSTITUTE OF TECHNOLOGY - SCHOOL OF ELECTRICAL ENGINEERING - ELECTRICAL MACHINES AND POWER ELECTRONICS, Ph.D. dissertation, 2010.

APPENDIXES

A. CONVERTER DATA

A simplified single-line diagram of the substation and its associated controllers is presented in Figure A-1. It is a classical LCL filtered substation controlled in dq synchronous frame. This converter station is used as reference. The converter controllers are presented in Chapter 1 part 1.3.

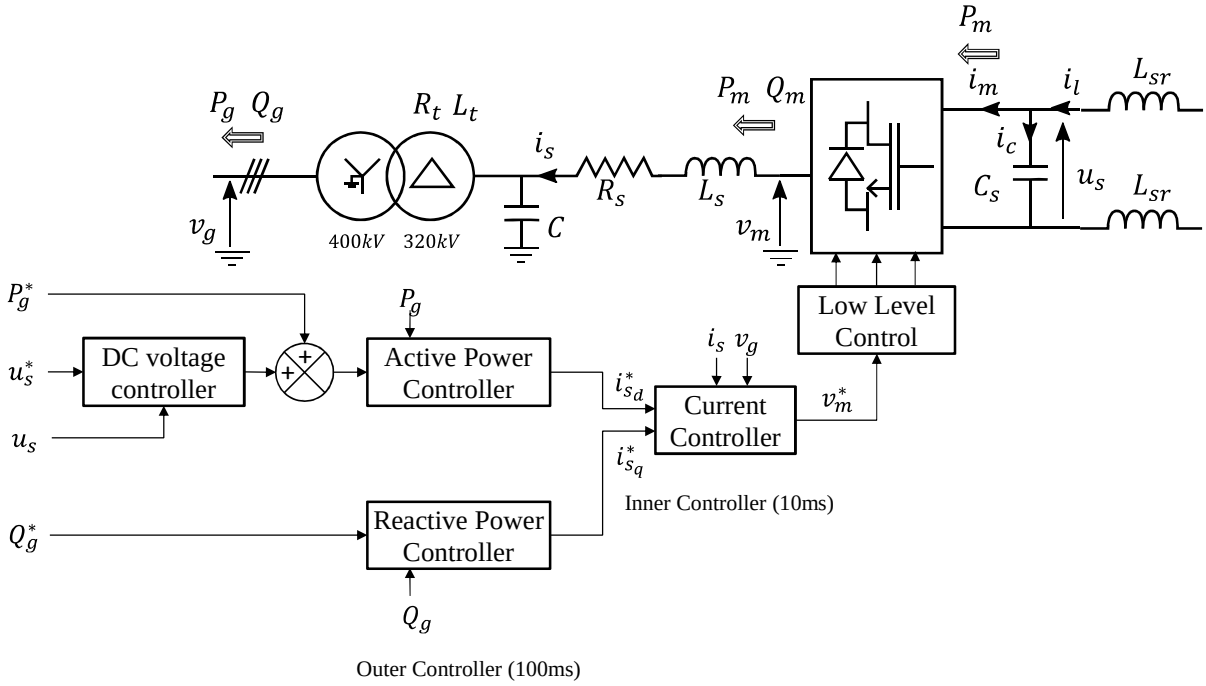

Figure A-1 : Converter

Table A-1 : HVAC Cable parameters

	Parameter	High power converter value	Per unit value
AC side	S_{base}	1077 MVA	1 pu
	U_{base}	320 kV	1 pu
	LCL cut-off frequency	500 Hz	–
	R_s	0.48 Ω	0.005 pu
	L_s	45 mH	0.15 pu
	R_t	0.48 Ω	0.005 pu
	L_t	45 mH	0.15 pu
	C_f	4.47 µF	–
DC side	$U_{s\,base}$	640 kV	1 pu
	P_{base}	1000 MW	1 pu
	C_s	50 µF	10.24 ms
	L_{SR}	10 mH	1.10^{-2} ms

B. CONTROLLER TUNING

B.1. Current controller tuning

The PI current controller has following form:

$$C_i(s) = k_{p_i} + \frac{k_{i_i}}{s} \tag{B.1}$$

The current controller in the dq frame, presented in Chapter 1 part 1.3.1 is arranged as the d-axis and q-axis are fully decoupled. The transfer function of the current control is the same for both axes, the d-axis current control loop transfer function is given:

$$\frac{i_{s_d}}{i_{s_d}^*}(s) = \frac{1 + \frac{k_{p_i}}{k_{i_i}} s}{1 + \frac{k_{p_i} + R_s}{k_{i_i}} s + \frac{L_s}{k_{i_i}} s^2} \tag{B.2}$$

PI controllers are tuned considering the pole placement method, the denominator of this transfer function is compared to a desired characteristic equation whose the dynamics are known:

$$P(s) = 1 + \frac{2\zeta}{\omega_n} s + \frac{1}{\omega_n^2} s^2 \tag{B.3}$$

Where:

ζ Is the damping ratio

ω_n Is the natural frequency [rad/s]

A step response of this second order polynomial is presented in Figure B-2 for two damping values and for desired response time at 5 % of 1 s, i.e. the system output must enter between bounds of ±5 % of the final value one second after the input step. The damping ratio defines the overshoot while the natural frequency is about dynamics. There is second order abacus which enables to find the natural frequency as function to the desired response time at 5% and a damping ratio. Typically, the value of damping ratio is set at 0.7 to achieve a 5% overshoot and at 1 to have no overshoot. For these values, the natural frequency is obtained by:

$$\begin{aligned} \omega_n &= \frac{3}{t_{r_i 5\%}} \quad if\ \zeta = 0.7 \\ \omega_n &= \frac{5}{t_{r_i 5\%}} \quad if\ \zeta = 1 \end{aligned} \tag{B.4}$$

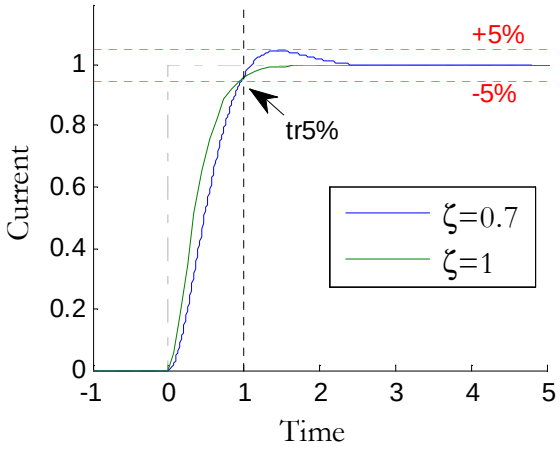

Figure B-2 : Step response for different damping values and same response time

The controller parameters are tuned for the current transfer function characteristic polynomial to fit the desired polynomial:

$$k_{i_i} = L_s \omega_n^2 \tag{B.5}$$

$$k_{p_i} = 2\zeta\omega_n L_s - R \tag{B.6}$$

B.2. Power controller tuning

The PI power controller has following form:

$$C_p(s) = k_{p_p} + \frac{k_{i_p}}{s} \tag{B.7}$$

To tune the power controller, it is considered that the response time of the power control loops is set at least ten times slower than those of current control loops, so current control loops dynamics can be neglected and replaced by a simple unitary gain. In these conditions, the power control loop presented in Chapter 1 part 1.3.2 can be defined by the following transfer function:

$$\frac{p_g}{p_g^*}(s) = \frac{1 + \frac{k_{p_p}}{k_{i_p}} s}{1 + \frac{1 + k_{p_p}}{k_{i_p}} s} \tag{B.8}$$

This transfer function can be assimilated at a first order transfer function of time constant τ_p. Controller parameters are tuned to achieve a desired response time:

$$k_{i_p} = \frac{1}{\tau_p} \tag{B.9}$$

$$k_{p_p} = 0 \tag{B.10}$$

B.3. Voltage controller tuning

The PI DC voltage controller has following form:

$$C_v(s) = k_{p_v} + \frac{k_{i_v}}{s} \tag{B.11}$$

Similarly to the power control, the dynamics of the DC voltage control loop must be at least ten times slower than current control loop dynamics to avoid interactions between both control loops. Once the dynamics of current control loop is neglected, the voltage control loop presented in Chapter 1 part 1.3.3 and considering an IP controller (see Figure 2–7b in Chapter 2 part 2.2.3) can be defined by the following transfer function:

$$\frac{u_s}{u_s^*}(s) = \frac{1}{1 + \frac{k_{p_v}}{k_{i_v}} s + \frac{C_s}{k_{i_v}} s^2} \tag{B.12}$$

The controller parameters are tuned for the voltage transfer function characteristic polynomial to fit the desired second order polynomial:

$$k_{i_v} = C_s \omega_n^2 \tag{B.13}$$

$$k_{p_v} = 2\zeta \omega_n C_s \tag{B.14}$$

B.4. PLL tuning

The rotating frame is synchronized with the AC voltage phasor at the point of common coupling. At this node, the three phase voltages may be written as:

$$\begin{aligned} v_{g_a}(t) &= V_g \sqrt{2}\, sin(\delta_g) \\ v_{g_b}(t) &= V_g \sqrt{2}\, sin(\delta_g - {}^{2\pi}/_{3}) \\ v_{g_c}(t) &= V_g \sqrt{2}\, \sin(\delta_g - {}^{4\pi}/_{3}) \\ \delta_g &= \omega t \end{aligned} \tag{B.15}$$

The Phase Lock Loop (PLL) enables retrieving the voltage phase angle (δ_g). To this purpose, Figure B-3 recalls the classical arrangement of a synchronous reference frame PLL, where the q component is controlled at zero.

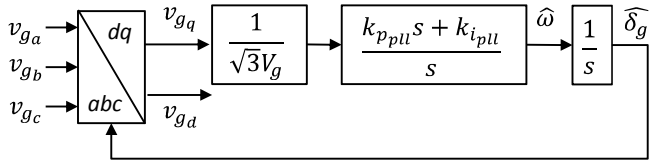

Figure B-3 : Synchronous reference frame PLL scheme

The PLL response time can be obtained by linearizing the relationship between the estimated angle ($\widehat{\delta_g}$) and the exact voltage angle (δ_g). The following transfer function is easily found:

$$\frac{\Delta\widehat{\delta_g}}{\Delta\delta_g} = \frac{1 + \frac{k_{p_{pll}}}{k_{i_{pll}}} s}{1 + \frac{k_{p_{pll}}}{k_{i_{pll}}} s + \frac{1}{k_{i_{pll}}} s^2} \tag{B.16}$$

The controller parameters are tuned for the PLL transfer function characteristic polynomial to fit the desired second order polynomial:

$$k_{i_{pll}} = \omega_n^2 \quad \textbf{(B.17)}$$

$$k_{p_{pll}} = 2\zeta\omega_n \quad \textbf{(B.18)}$$

C. CABLE

C.1. Cable data

Each DC transmission is associated with two cables, one for the positive pole and one for the negative pole. They are buried beneath the ground. Electrical data are calculated thanks to the EMTP-RV® routine, main parameters are summarized in Table C-2.

Table C-2 : Cable parameters (calculated at 10 µHz)

	Cable 320 kV 2500 mm²	Cable 320 kV 500 mm²
Cable section [mm²]	2500	500
Nominal current [A]	1800 – 2700	700 – 1100
Core resistance [mΩ/km]	5.3	3.1
Screen resistance [mΩ/km]	60.2	88.2
Core inductance [mH/km]	3.6	3.8
Screen inductance [mH/km]	3.5	3.6
Core-screen mutual inductance [mH/km]	3.5	3.6
Core-to-ground conductance [µS/km]	0.06	0.04
Core-to-ground capacitance [µF/km]	0.24	0.15

C.2. Five-terminal DC grid cable data

Transmission cable parameters of the five-terminal DC grid are summarized in Table C-3. These data are derived from Table C-2, they correspond to the positive pole and take into account parallel cables. The resistance of smoothing reactors is chosen at 10 mΩ for each station.

Table C-3 : Cables parameters of the five-terminal DC grid (positive pole)

Bus "From"	Bus "To"	Length [km]	Resistance [Ω]	Conductance [µS]
1	2	82	0.44	5
1	3	102	0.55	6.2
2	3	51	0.27	3.1
2	4	20	0.11	1.2
4	5	65	1	5

D. CONCEPT OF SMALL-SIGNAL STABILITY ANALYSES [KUN94]

D.1. Eigenvalues

Small-signal stability is the ability of a system to reach a stable operating point after a small disturbance. The system has to be linearized for the analysis purpose. In fact, a power system can be described by a set of differential algebraic equations (DAE) which could be non-linear. However considering only small variations around an operating point, the system can be linearized using the Taylor's series, which could be limited to the first order by neglecting terms of degree two and higher. Thus, the system can be described by a state space form:

$$\begin{cases} \Delta\dot{x} = \boldsymbol{A}\Delta x + \boldsymbol{B}\Delta u \\ \Delta y = \boldsymbol{C}\Delta x + \boldsymbol{D}\Delta u \end{cases} \quad \textbf{(D.19)}$$

Where

Δx is the state vector (dimension n)

Δu is the input vector (dimension r)

Δy is the output vector (dimension m)

A is the state matrix (dimension $n \times n$)

B is the input matrix (dimension $n \times r$)

C is the output matrix (dimension $r \times n$)

D is the feed-forward matrix (dimension $m \times r$)

The time response of this system is given by

$$\Delta x(t) = e^{\boldsymbol{A}(t-t_0)}\Delta x(t_0) + \int_{t_0}^{t} e^{\boldsymbol{A}(t-v)}\boldsymbol{B}\Delta u(v)dv \quad \textbf{(D.20)}$$

From **(D.20)**, two terms are identified, one which does not depend on input, called the free motion and the second which is related to inputs. It can be noticed that time response converges only if eigenvalues of A have negative real parts. At this operating point the modes of the system are retrieved by eigenvalues which are n non-trivial solutions of the following equation:

$$\boldsymbol{A}\phi_i = \lambda_i\phi_i \quad \textbf{(D.21)}$$

Where

λ_i is the ith eigenvalue

ϕ_i is the ith right eigenvector associated to the ith eigenvalue (dimension n)

Real eigenvalue corresponds to a non-oscillatory mode. When it is positive the mode is unstable, it grows with aperiodic manner. Complex eigenvalues of the system are always available in the form of pairs of complex conjugate, because the state-space of a physical system is always real. Writing complex conjugate eigenvalues as follows:

$$\lambda_{i,j} = \sigma \pm j\omega \quad \textbf{(D.22)}$$

Where the frequency of oscillation is given by:

$$f = \frac{\omega}{2\pi} \quad \textbf{(D.23)}$$

And the damping is expressed in a form of damping ratio:

$$\zeta = \frac{-\sigma}{\sqrt{\sigma^2 + \omega^2}} \quad \textbf{(D.24)}$$

This damping ratio represents the rate of amplitude decay of the oscillation. In some ways, it expresses the number of oscillations to reach a certain rate of decay. Therefore, more its value is close to one, more oscillations are damped, if its value is negative, the corresponding mode will be unstable. In power system, it is often said that a damping of 5% is the last acceptable limit.

D.2. Eigenvectors

From eigenvalues, the free motion is given by:

$$\frac{d\boldsymbol{z}}{dt} = \begin{bmatrix} \lambda_1 & & 0 \\ & \lambda_2 & \\ 0 & & \lambda_n \end{bmatrix} \boldsymbol{z} \quad \textbf{(D.25)}$$

Where

$\mathbf{z}$ Is the transformed state vector (dimension n)

Unlike the initial free motion system there is no cross-coupling between states, variables of z are directly associated to the system modes. However this is a mathematical representation which does not have a physical sense. The relation between modes and physical system is retrieved by right eigenvectors which have been used to uncouple the system. They represent a linear combination between the original states which are often referred to physical behavior and the transformed states which are related to system's modes:

$$\boldsymbol{\Delta x} = [\boldsymbol{\phi_1} \quad \boldsymbol{\phi_2} \quad \dots \quad \boldsymbol{\phi_n}]\, \boldsymbol{z} \quad \textbf{(D.26)}$$

If only one mode is excited, activity of each original state is given by:

$$\Delta x_k = \boldsymbol{\phi_i}(k) z_i \quad if\ z_l = 0 \quad \forall\, l \neq i \quad \textbf{(D.27)}$$

The right eigenvector enables to measure the activity of original states with regards to the corresponding mode.

In same way, to quantify influences of original states on modes, a new vector is introduced, it is called left eigenvector, it is defined as follows:

$$\boldsymbol{\psi_i}\, \boldsymbol{\phi_i} = 1 \quad \textbf{(D.28)}$$

This new vector enables to write **(D.26)** in opposite direction

$$\boldsymbol{z} = [\boldsymbol{\psi_1^T} \quad \boldsymbol{\psi_2^T} \quad \dots \quad \boldsymbol{\psi_n^T}]^{\mathrm{T}} \boldsymbol{\Delta x} \quad \textbf{(D.29)}$$

Thus, the ith mode is the result of a linear combination of all original states:

$$z_i = \sum_{k=1}^{n} \boldsymbol{\psi_i}(k) \boldsymbol{\Delta x}(k) \quad \textbf{(D.30)}$$

The right eigenvector allows quantifying the contribution of each original state on the corresponding mode.

D.3. Mode shapes

The mode shape is a graphical representation of the right eigenvector; it enables to plot on a complex plan the activity of original states with regards to one mode. For instance, the mode shape of the ith mode is shown in Figure D-4.a. Two states are participating in this mode (Δx_1

and Δx_2). The modulus of the component of the ith right eigenvector ($\boldsymbol{\phi_i}$) relatives to the state Δx_1 is higher than the modulus of the component of $\boldsymbol{\phi_i}$ relatives to the state Δx_2, so Δx_1 participates more in the mode λ_i than Δx_2. Both right eigenvector components are almost in opposite direction, therefore they the two systems which are represented by states Δx_1 and Δx_2 are acting one against the other. It should be noted that, only states of same nature can be compared to have a physical interpretation of this diagram.

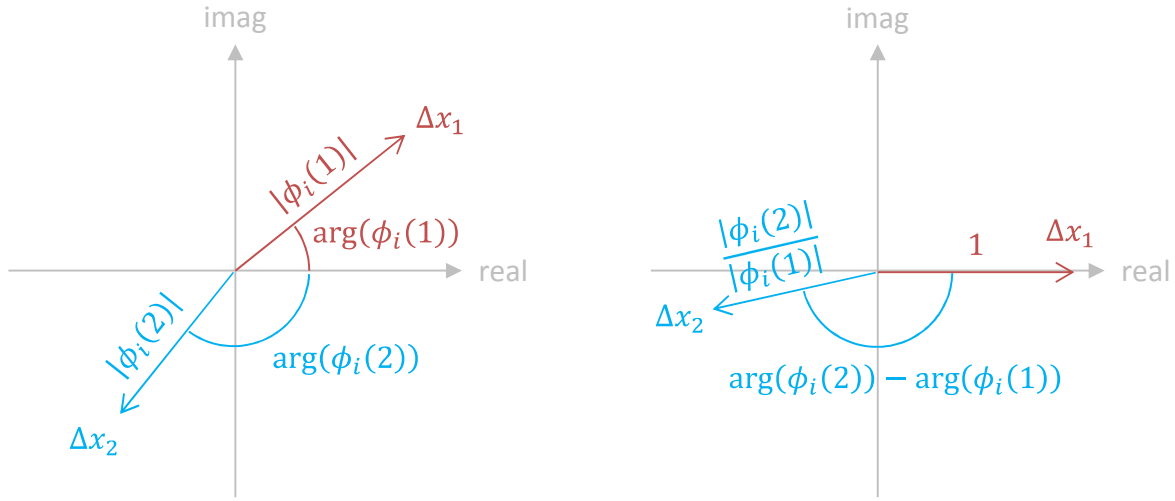

(a) Not normalized (b) Normalized

Figure D-4 : Mode shapes of ith mode

By definition, these vectors could have different lengths and positions, only their relative lengths and positions are important. In practice, the longest vector is set at 1, and other vector lengths are normalized from its length. Also the angle of the first vector is arbitrarily set at 0 and other vector angles are defined from its angle.

D.4. Participation factors

In power system analysis, eigenvalues are computed and then original states which are most influenced by less damped modes are retrieved thanks to the right eigenvectors. The influence comparison can be easily done when states denotes same quantity, such as rotor speed, but when the same mode cause an activity on states of different natures, it is difficult to draw conclusions. To overcome this problem, the participation factor is introduced:

$$p_{ki} = \phi_i(k)\psi_i(k) \tag{D.31}$$

This parameter, without unit, gives the sensibility of the kth mode on the ith states. These parameters are normalized in order to have the highest participation factor equal to one. Thanks to this tool the sensibility of physical variables to the dynamic of a defined mode can be compared, whether or not variables are same nature.

E. STATE SPACE MODELING

E.1. Model association principles

If we consider two elementary states space models which are links by their inputs and outputs as follow:

$$\begin{cases} \frac{d}{dt}[X_1] = A_1X_1 + B_1U_1 \\ \frac{d}{dt}[X_2] = A_2X_2 + B_2U_2 \\ Y_1 = C_1X_1 + D_1U_1 \\ Y_2 = C_2X_2 + D_2U_2 \\ U_1 = T_{12}Y_2 \\ U_2 = T_{21}Y_1 \end{cases} \quad \textbf{(E.32)}$$

These two systems can be concatenated in a global state space which has the following form:

$$\begin{cases} \frac{d}{dt}\begin{bmatrix} X_1 \\ X_2 \end{bmatrix} = \begin{bmatrix} A_{11} & A_{12} \\ A_{21} & A_{22} \end{bmatrix}\begin{bmatrix} X_1 \\ X_2 \end{bmatrix} + \begin{bmatrix} B_{11} & B_{12} \\ B_{21} & B_{22} \end{bmatrix}\begin{bmatrix} U_1 \\ U_2 \end{bmatrix} \\ \begin{bmatrix} Y_1 \\ Y_2 \end{bmatrix} = \begin{bmatrix} C_{11} & C_{12} \\ C_{21} & C_{22} \end{bmatrix}\begin{bmatrix} X_1 \\ X_2 \end{bmatrix} + \begin{bmatrix} D_{11} & D_{12} \\ D_{21} & D_{22} \end{bmatrix}\begin{bmatrix} U_1 \\ U_2 \end{bmatrix} \end{cases} \quad \textbf{(E.33)}$$

The global state space contains all states, all inputs and all outputs of previous elementary state space model. By developing (E.32), the elements which fill new matrices can be retrieved:

$$\frac{d}{dt}[X_1] = A_1X_1 + B_1U_1 + B_1T_{12}Y_2 \quad \textbf{(E.34)}$$

$$\frac{d}{dt}[X_1] = A_1X_1 + B_1U_1 + B_1T_{12}C_2X_2 + B_1T_{12}D_2U_2 + B_1T_{12}D_2T_{21}Y_1 \quad \textbf{(E.35)}$$

$$\frac{d}{dt}[X_1] = A_1X_1 + B_1U_1 + B_1T_{12}C_2X_2 + B_1T_{12}D_2U_2 + B_1T_{12}D_2T_{21}C_1X_1 \quad \textbf{(E.36)}$$

In the same manner:

$$\frac{d}{dt}[X_2] = A_2X_2 + B_2U_2 + B_2T_{21}C_1X_1 + B_2T_{21}D_1U_1 + B_2T_{21}D_1T_{12}C_2X_2 \quad \textbf{(E.37)}$$

Regarding outputs equations:

$$Y_1 = C_1X_1 + D_1U_1 \quad \textbf{(E.38)}$$

$$Y_2 = C_2X_2 + D_2U_2 \quad \textbf{(E.39)}$$

Once equations are developed, it is easy to fill matrices of the whole state space, this is presented in Figure E-5.

$$\frac{d}{dt}[X_1] = \underbrace{A_1X_1}_{A_{11}} + \underbrace{B_1U_1}_{B_{11}} + \underbrace{B_1T_{12}C_2X_2}_{A_{12}} + \underbrace{B_1T_{12}D_2U_2}_{B_{12}} + B_1T_{12}D_2T_{21}C_1X_1$$

$$\frac{d}{dt}[X_2] = \underbrace{A_2X_2}_{A_{22}} + \underbrace{B_2U_2}_{B_{22}} + \underbrace{B_2T_{21}C_1X_1}_{A_{21}} + \underbrace{B_2T_{21}D_1U_1}_{B_{21}} + B_2T_{21}D_1T_{12}C_2X_2$$

$$Y_1 = \underbrace{C_1X_1}_{C_{11}} + \underbrace{D_1U_1}_{D_{11}}$$

$$Y_2 = \underbrace{C_2X_2}_{C_{22}} + \underbrace{D_2U_2}_{D_{22}}$$

Figure E-5 : Model association principles with two elementary state space models

It should be noted that we assumed that there is never a system which is linked by more than two D matrices.

E.2. Overview of the state space creation routine

The whole state space model is built step-by-step. Firstly each elementary state space model is built and stored. In the meantime, some information about the state space name, its input names, output names, states names, and names of devices connected are all saved. Next these information are used to build input-output connection matrices, and finally to build the whole state space.

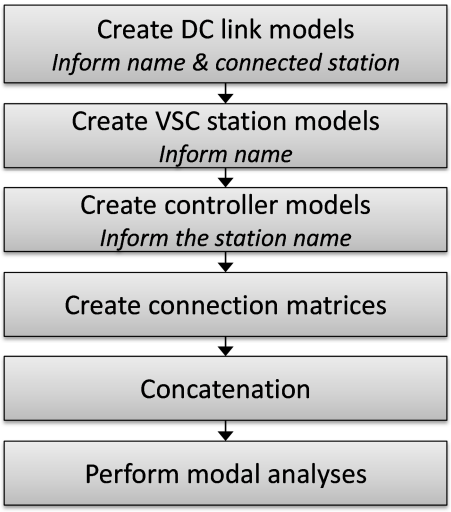

Figure E-6 : state space creation routine overview

E.3. Connection matrix creation

Connection matrices enable to define the link between inputs of one model to outputs of another model (see Chapter 2 part 2.4.1). Once the all elementary state space models are built, a function read stored information two models by two models, checks if they are connected. If they are, the function examines what these two models represent and create a suitable connection matrix. Otherwise, an empty matrix defined the link between both systems.

For instance, we consider the connection of the active power controller as shown in Figure E-7. The active power controller state space model has 3 inputs (the active power reference and the d-axis current and the grid voltage) and 1 output (the d-axis current reference). The vector current controlled VSC state space model has 4 inputs (the d-axis current reference, the q-axis current reference, the current flowing through the smoothing reactor and the grid voltage) and 3 outputs (the DC voltage, the d-axis current and the q-axis current). Therefore the d-axis current reference is the output of the active power controller and the input of the vector current controlled VSC. The d-axis current is the output of the vector current controlled VSC and the input of the active power controller.

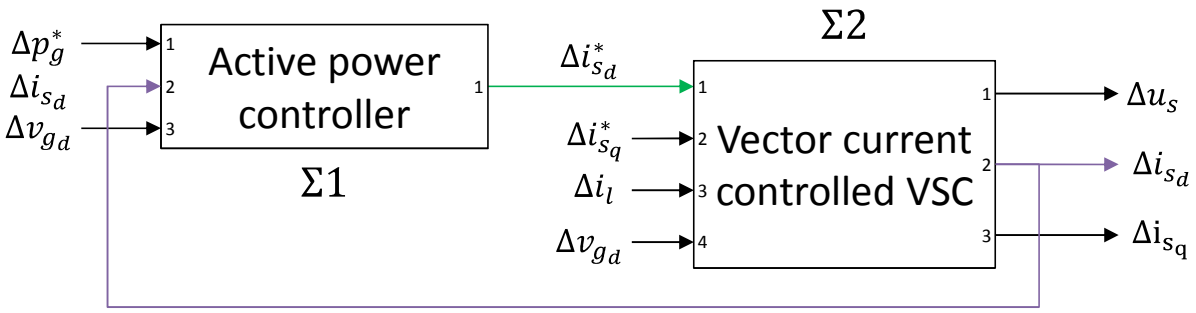

Figure E-7 : Connection of the active power controller to the vector current controlled VSC

According to established links between both elementary state space models, the connection matrix which links the output of the active power controller model (Σ1) to the inputs of the current controlled VSC model (Σ2), is defined as:

$$T_{12} = \begin{bmatrix} 1 \\ 0 \\ 0 \\ 0 \end{bmatrix} \quad \textbf{(E.40)}$$

And the connection matrix which links the outputs of the current controlled VSC model (Σ2) to the inputs of the active power controller model (Σ1), is defined as:

$$T_{21} = \begin{bmatrix} 0 & 0 & 0 \\ 0 & 1 & 0 \\ 0 & 0 & 0 \end{bmatrix} \quad \textbf{(E.41)}$$

E.4. Model association routine

The model association routine gathers all elementary state space models to a global state space model. The routine executes the model association principles presented in E.1. The algorithm is presented in Figure E-8. Once the whole state space model is built, i.e. A, B, C and D matrices are built. Next, the B and D matrices are simplified. In a first time, elementary state space model inputs which are associated to the outputs of another elementary states space model

are deleted. In a second time, if there is the same input for different elementary state space models, the contribution of this input is gathered in only one column to have only one input in the global state space model (for instance the two elementary state space models presented in Figure E-7, have a common input (Δv_{g_d})).

Create A matrix	**Fill diagonal elements** $A_{ii} = A_i$
	Fill extra-diagonal elements $T_{ij} \neq 0 \rightarrow A_{ij} = B_i T_{ij} C_j$
	Add contribution from D matrix $T_{ij} \neq 0 \;\&\&\; D_j \neq 0 \;\&\&\; T_{jk} \neq 0 \rightarrow A_{ik} = A_{ik} + B_i T_{ij} D_j T_{jk} C_k$
Create B matrix	**Fill diagonal elements** $B_{ii} = B_i$
	Add contribution from D matrix $T_{ij} \neq 0 \;\&\&\; D_j \neq 0 \rightarrow B_{ij} = B_i T_{ij} D_j$
Create C matrix	**Fill diagonal elements** $C_{ii} = C_i$
Create D matrix	**Fill diagonal elements** $D_{ii} = D_i$
Simplify B and D matrices	**Delete unused inputs** $B(:, idx_i) = 0 \qquad D(:, idx_i) = 0$
	Gather same inputs $B(:, idx_i) = B(:, idx_i) + B(:, idx_j) + B(:, idx_k)$ $B(:, idx_j) = 0 \qquad B(:, idx_k) = 0$ $D(:, idx_i) = D(:, idx_i) + D(:, idx_j) + D(:, idx_k)$ $D(:, idx_j) = 0 \qquad D(:, idx_k) = 0$

Figure E-8 : Model association algorithm

E.5. States nomenclature

D_uc1	Capacitor voltage at node 1 (DC cable)
D_uc2	Capacitor voltage at node 2 (DC cable)
D_il1	Core inductor current (DC cable)
D_il2	Screen inductor current (DC cable)
D_ilf1	Current through the feeder inductor 1 (DC cable)
D_ilf2	Current through the feeder inductor 2 (DC cable)
Xid	d-axis integral controller (Station)

D_isd	d-axis current (Station)
Xiq	q-axis integral controller (Station)
D_isq	q-axis current (Station)
D_us	DC voltage (Station)
Xp	Integral of active power controller (Station)
Xq	Integral of reactive power controller (Station)
D_il	Current through the smoothing reactor (Station)
Xv	Integral of DC voltage controller (Station)

F. MODAL ANALYSIS OF THE FIVE-TERMINAL DC GRID

F.1. Eigenvalues of the five-terminal DC grid

The next table presents all eigenvalues of the five-terminal DC grid, apart the ones which have real part lower than -1.10^3 rad/s.

Table F-4 : Eigenvalues of the five-terminal DC grid

	eigenvalues	Freq.	Damp.	Dominant States		Comment
1	-191 ± j 7820	1240	0.024	Line24_D_il1 Line45a_D_uc1 Line45b_D_uc1	1.00 0.40 0.40	DC grid
2	-153 ± j 5280	840	0.029	Line12_D_uc2 Line23_D_uc1 Line23_D_il1 Line45a_D_uc2 Line45a_D_il1 Line45b_D_uc2 Line45b_D_il1 WF3_D_il	0.77 0.48 0.71 1.00 0.79 1.00 0.79 0.84	
3	-117 ± j 4140	658	0.028	Line13_D_uc2 Line13_D_il1 Line23_D_uc2 Line23_D_il1 WF1_D_il WF3_D_il	1.00 0.49 0.50 0.73 0.51 0.37	
4	-94.2 ± j 3680	585	0.026	Line12_D_uc1 Line12_D_il1 Line13_D_uc1 Line13_D_il1 GS1_D_il WF2_D_il WF3_D_il	0.72 1.00 0.90 0.57 0.61 0.41 0.61	
5	-16.7 ± j 2560	408	0.0065	Line12_D_uc1 Line13_D_uc1 Line13_D_uc2 GS1_D_il GS2_D_il WF1_D_il WF2_D_il	0.51 0.63 0.44 1.00 0.45 0.68 0.33	
6	-75.3 ± j 1060	169	0.071	WF2_D_us WF2_D_il WF3_D_us WF3_D_il	1.00 0.90 0.93 0.54	
7	-63.1 ± j 839	134	0.075	Line24_D_il1 GS2_D_us GS2_D_il WF2_D_us WF3_D_us	0.36 1.00 0.99 0.46 0.53	
8	-71.8 ± j 701	112	0.1	Line13_D_il1 GS1_D_us GS1_D_il WF1_D_us WF1_D_il	0.32 0.63 0.37 1.00 0.71	
9	-95.2 ± j 686	109	0.14	Ligne12_D_il1 Ligne23_D_il1 GS1_D_us GS1_D_il GS2_D_us GS2_D_il WF1_D_us WF2_D_us WF3_D_us	0.61 0.45 1.00 0.57 0.67 0.43 0.39 0.38 0.34	

10	-409	0	1	Ligne12_D_il2 Ligne13_D_il2 Ligne23_D_il2	0.80 1.00 0.50	
11	-522	0	1	Ligne45a_D_il1 Ligne45a_D_il2 Ligne45b_D_il1 Ligne45b_D_il2	0.32 1.00 0.32 1.00	
12	-24.6	0	1	Ligne45a_D_il2 Ligne45b_D_il2	1.00 1.00	
13	-6.16	0	1	Ligne45a_D_il1 Ligne45a_D_il2 Ligne45b_D_il1 Ligne45b_D_il2	1.00 0.32 1.00 0.32	
14	-17.2	0	1	Ligne12_D_il2 Ligne13_D_il2	1.00 0.38	
15	-17.3	0	1	Ligne23_D_il2 Ligne24_D_il2	0.34 1.00	
16	-17.3	0	1	Ligne13_D_il2 Ligne23_D_il2 Ligne24_D_il2	0.40 1.00 0.75	
17	-1.36	0	1	Ligne12_D_il1 Ligne13_D_il1 Ligne23_D_il1	0.80 1.00 0.50	
18	-27.7 ± j 1.1	0.246	1	GS1_D_us GS1_Xp GS2_D_us GS2_Xp WF1_D_us	0.44 0.86 0.51 1.00 0.49	DC grid voltage
19	-188 ± j 237	37.6	0.62	GS1_Xid GS1_D_isd GS2_Xid GS2_D_isd	0.67 0.75 0.89 1.00	d-axis current loops
20	-198 ± j 219	34.9	0.67	GS1_Xid GS1_D_isd GS2_Xid GS2_D_isd	0.95 1.00 0.72 0.76	
21	-200 ± j 225	35.8	0.67	WF1_Xid WF1_D_isd WF1_Xiq WF1_D_isq	0.58 0.63 0.93 1.00	
22	-200 ± j 225	35.8	0.67	WF2_D_isd WF2_Xiq WF2_D_isq	0.31 0.93 1.00	
23	-200 ± j 225	35.8	0.67	WF3_Xid WF3_D_isd	0.93 1.00	
24	-200 ± j 225	35.8	0.67	GS1_Xiq GS1_D_isq	0.93 1.00	q-axis current loops
25	-200 ± j 225	35.8	0.67	GS2_Xiq GS2_D_isq	0.93 1.00	
26	-200 ± j 225	35.8	0.67	WF1_Xid WF1_D_isd WF1_Xiq WF1_D_isq	0.93 1.00 0.58 0.63	
27	-200 ± j 225	35.8	0.67	WF2_Xid WF2_D_isd WF2_D_isq	0.93 1.00 0.31	
28	-200 ± j 225	35.8	0.67	WF3_Xiq WF3_D_isq	0.93 1.00	
29	-29.8	0	1	GS1_Xp GS2_Xp	1.00 0.86	active and reactive power loops
30	-29.8	0	1	WF2_Xp	1	
31	-29.8	0	1	WF3_Xp	1	

32	-29.8 ± j 3e-014	6E-15	1	GS1_Xq GS2_Xq WF1_Xp	0.48 0.80 1.00
33	-29.8 ± j 3e-014	6E-15	1	GS2_Xq WF1_Xq WF1_Xp	1.00 0.56 0.97
34	-29.8	0	1	WF2_Xq	1
35	-29.8	0	1	WF3_Xq	1

F.2. DC grid modeled by an admittance matrix

It has been observed that modes associated with the DC grid are uncoupled as regards to modes associated with converter control loops. The objective of this part is to show the influence of the DC grid model on modes classified as converter control loop modes. For this purpose, DC cables as well as smoothing reactors are modeled by their resistive elements which can be modeled as an admittance matrix only (see Appendix J). This is the same principle than the quasi-sinusoidal approximation in AC system, transmission line are modeled by their steady state behavior. With this modelling, there is no DC cable and smoothing reactor state variables, therefore it is expected to have no mode classified as DC grid modes.

The overall five-terminal DC grid state space with an admittance matrix instead of DC cable state space has only 35 state variables: five converter stations with 7 states (i.e. 8 states minus 1 because there is no smoothing reactor). The eigenvalues of this system are plotted and compared with those of the Five-terminal with DC cables modeled as state space (see Table F-4) in Figure F-9a. A zoom is realized around the DC grid voltage mode in Figure F-9b. Eigenvalues of the system modeled with state space DC grid are represented by red crosses and those of the system modeled with DC grid admittance are represented by blue squares.

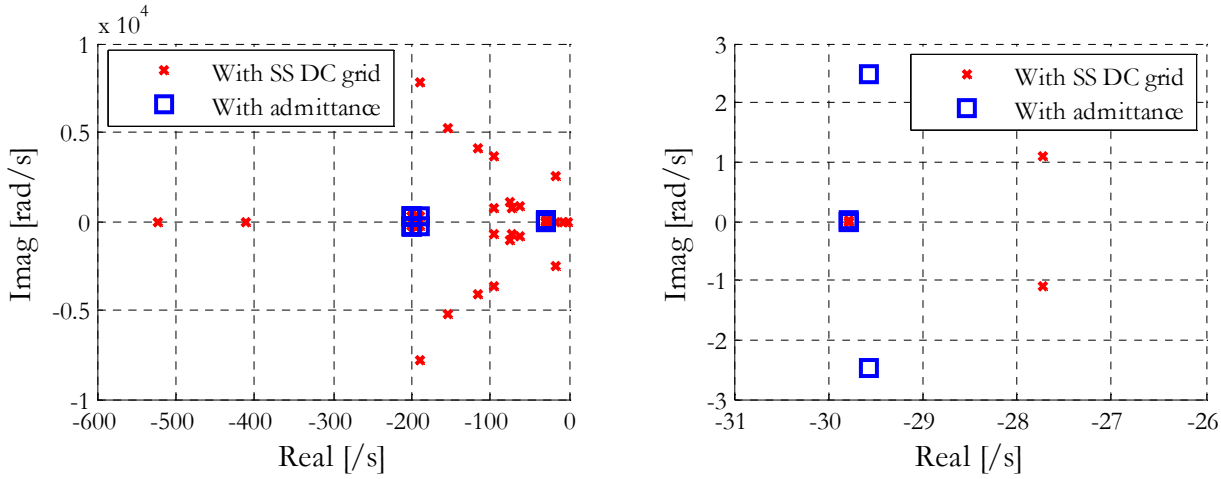

(a) Full size (b) Zoom on the DC voltage mode

Figure F-9 : Root loci of the Five-terminal DC grid with admittance matrix for DC gird

In Figure F-9a, the modes related to current control loops and power control loops are at the same location in both root locus. Focusing on the DC voltage mode (Figure F-9b), it has been observed a slight difference; -29.6 ± j 2.5 instead of -27.7 ± j 1.1 rad/s, which confirms that DC cable capacitors play a role on the DC voltage dynamics.

As a general comment, the DC grid static model is sufficient and accurate for studies which are dealing with power dispatch in normal operation. Indeed, DC grid modes have very fast dynamics, and as long as they are not excited by fast operations or sudden events, the DC grid behaves like a purely resistive circuit.

F.3. Influence of the smoothing reactors

To limit the current ripple and protect the converter against DC grid faults, smoothing reactors are added at each converter between the converter capacitor and DC cables, on the positive and negative poles. In [DES13], it is demonstrated that smoothing reactors limit the faulted current ramp rate (i.e. lower di/dt) and the maximal current is smaller, therefore there is more time for the protection scheme to detect and isolate the fault before reaching the converter diode maximal current. High value of inductors are beneficial to the protection point of view, however this changes the DC grids modes and may make the system oscillates more, and in the worst case it could lead to instabilities.

To assess the DC grid stability, the system eigenvalues are plotted with smoothing reactor values from 10 mH (the default value) and 1 H. The analysis is performed on the five-terminal DC grid, with all parameters set as default except smoothing reactor values which are changed for all converter stations. Results are displayed in two figures, the Figure F-10a presents a global view of the root locus while Figure F-10b is a view focused on control modes.

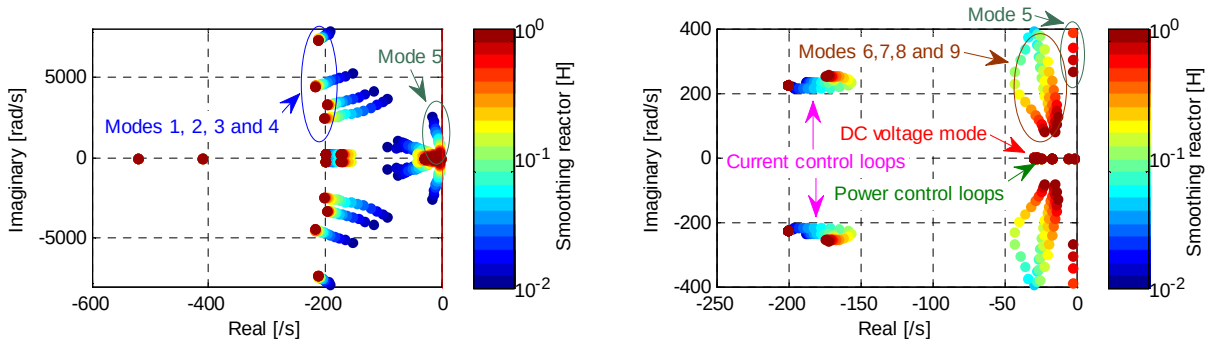

(a) Global view (b) Focus on control modes

Figure F-10 : Root loci of the five-terminal DC grid as function of the smoothing reactor value

As the smoothing reactor values are increasing, modes assimilated to DC cables are evolving in the same direction as if the DC capacitor values would increase. This confirms the participation factor analysis, which says that these modes are made of LC resonant circuits. Even if modes 5, 6, 7, 8 and 9 are evolving toward the real axis in direction to the real part there is no unstable mode, even for higher smoothing reactor values.

Looking at Figure F-10b, as expected, the DC voltage mode is not influenced by the smoothing reactors. However, the current control loop modes are a little bit influenced, which is quite surprising since there is no clear links between smoothing reactors and converter station control loops. The participation factor analysis informs that GS1 and GS2 capacitors as well as smoothing reactors are participating in the mode originally referred as current control mode when it is at the most remote value from the original one. Knowing the undamped natural frequency of the current loop is 300 rad/s and recalling converter station capacitor values are

66 µF and 75 µF for the GS1 and GS2, respectively. The case when the current control loops should be the most influenced by the LC resonant circuit which is defined by:

$$L_{SR_i} = \frac{1}{300^2 \times C_{s_i}} \quad \textbf{(F.42)}$$

To obtain a resonant frequency at 300 rad/s, the smoothing reactor should be equal to 148 mH for GS1 or 168 mH for GS2. These values are consistent with results obtained by the root locus since the mode initially related to GS1 and GS2 current control loop is at the most remote position for smoothing reactor values between 110 mH and 180 mH.

G. PARAMETERS OF THE AC TEST SYSTEM

The AC system considered is presented in Figure G-11, is taken from [KUN94]. This test system was provided by the ULg .Small impedances of 108 MW are added close to generators in order to implement it in RTLab® (similar to Matlab/SimPowerSystem® environment).

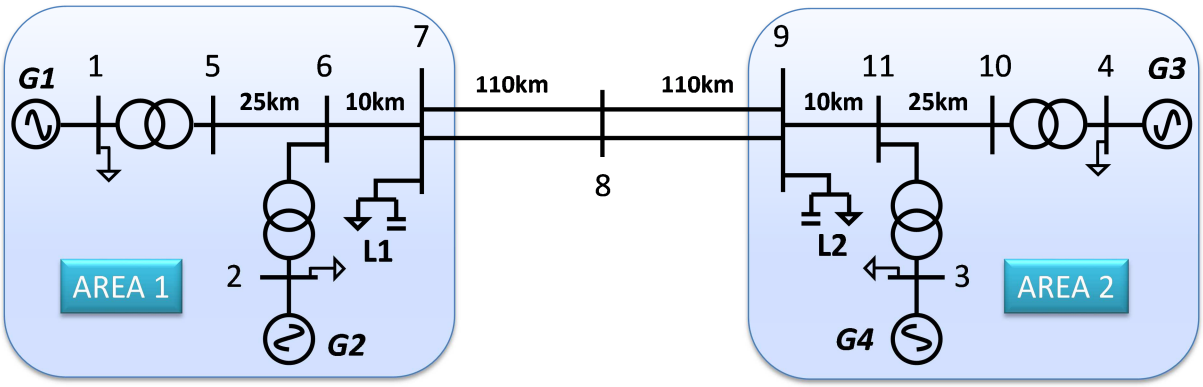

Figure G-11 : AC test system

Table G-5 : Generator data

Nominal values		
	$S_N = 900MVA$	$V_N = 20\ kV$
Electrical and mechanical data		
$X_d = 1.8$	$X_q = 1.7$	$H = 6.5s$
$X'_d = 0.3045$	$X'_q = 0.5747$	$X_l = 0.2$
$X''_d = 0.25$	$X''_q = 0.25$	$R_a = 0.02$
$T'_d = 1.63s$	$T'_q = 0.1826s$	
$T''_d = 0.0294s$	$T''_q = 0.0232s$	
$T'_{d0} = 9.636s$	$T'_{q0} = 0.54s$	
$T''_{d0} = 0.0359s$	$T''_{q0} = 0.0533s$	

Table G-6 : AC line data

$V_b = 230\ kV$	$S_b = 100\ MVA$
$r = 0.0001\ pu/km$	$x_l = 0.001\ pu/km$

Table G-7 : Transformer data

$V_{1N} = 20\ kV$	$V_{2N} = 320\ kV$	$S_N = 900\ MVA$	$X = 15\ \%$

G.1. AC State nomenclature

omega	Generator angular frequency
delta	Generator angular position
psif	Rotor field inductor
psid1	Rotor d-axis damper
psiq1	Rotor q-axis damper 1
psiq2	Rotor q-axis damper 2
lead	PSS lead transfer function
washout	PSS washout transfer function
zsr	Governor
dbp	Turbine low pressure stage
dmp	Turbine medium pressure stage
dhp	Turbine high pressure stage
exciter	Generator exciter
Vfilter	Voltage filter
deriv feed	Derivative feed-back (voltage control)

H. FURTHER AC-DC MODAL ANALYSES

H.1. Sensitivity towards frequency droop parameter

Eigenvalues are computed for different values of frequency droop parameter in order to observe the sensibility of the modes on this parameter. Knowing no interactions have been identified between DC grid modes and AC system modes, the DC grid is modeled as an admittance matrix to limit the number of eigenvalues. The modal analysis is performed for frequency droop parameter set from 0.01 to 100 pu/pu for both grid side stations. When the frequency droop is set at 0.01 pu/pu converter stations are participating more than conventional units and when it is set at 100 pu/pu there is almost no frequency support from converters.

In Figure H-12, there are four different root-locus views, one displays the whole eigenvalues, another is focused on the DC voltage mode, another in electromechanical modes and the last one in the common mode.

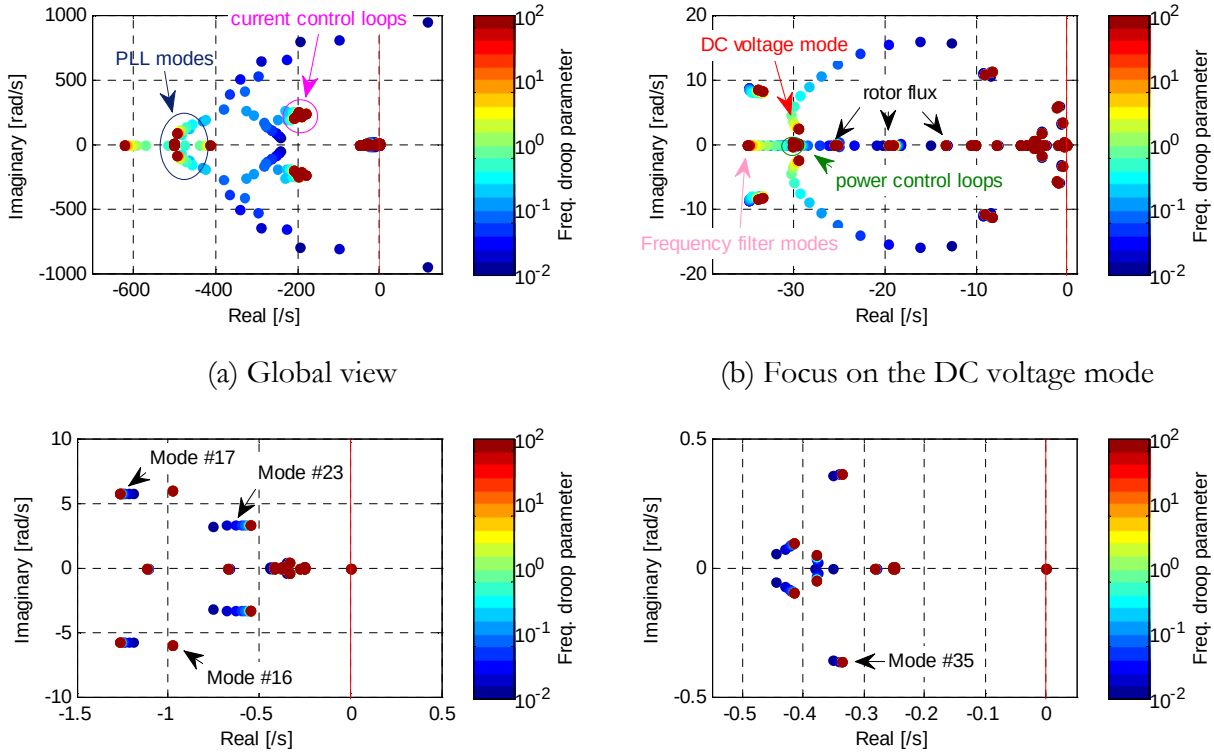

(a) Global view

(b) Focus on the DC voltage mode

(c) Focus on electromechanical modes

(d) Focus on the common mode

Figure H-12 : Sensitivity towards the frequency droop parameter

In the global view (Figure H-12a), PLL modes and current control loops modes are clearly identifiable. Modes identified as PLL modes are moving toward the instable region. For low value of frequency droop constant (i.e. Converter stations are actively supporting the frequency) the system is unstable because of PLL, frequency filter and current control loop interactions (information revealed by participation factor analysis).

Looking at (Figure H-12b), as expected the DC voltage mode is very influenced by the frequency droop parameter. Unlike its evolution caused by the voltage droop parameter, it does not evolve on the real axis; associated with the frequency filter mode, they form a complex

conjugate mode. When there is no frequency support from the DC system, frequency filter mode and DC voltage mode are at their original values (i.e. -35 rad/s and -28 ± j 1.2 rad/s). As soon as the DC system supports more the AC frequency, the DC voltage mode is combined with frequency filter mode to from a complex conjugate mode. Other modes related to converter station power loops or AC modes are fairly impacted by the DC grid frequency support.

Regarding electromechanical modes (Figure H-12c and Figure H-12d), some of them are influenced by the frequency droop parameter. The damping of the inter-area mode (Mode 23) is improved as the frequency support is higher. Conversely, the damping of Area 2 local mode (Mode 17) is worse. The Area 1 local mode (Mode 16) is not influenced at all while the common mode (Mode 35) damping is slightly improved.

H.2. Sensitivity towards frequency droop parameter when wind farm are participating to the DC voltage control

The objective of this part is to show how modes are influenced by the frequency droop parameters when a wind farm is participating to the DC voltage control. Results are compared with those obtained with the previous case. It should be noted that the participation of one other converter station would change the DC voltage dynamics if the DC voltage droop gain is not updated. Therefore the DC voltage droop parameter of GS1, GS2 and WF1 has been set at 1.25 in order to achieve a theoretical response time of 100 ms (similar to the previous case).

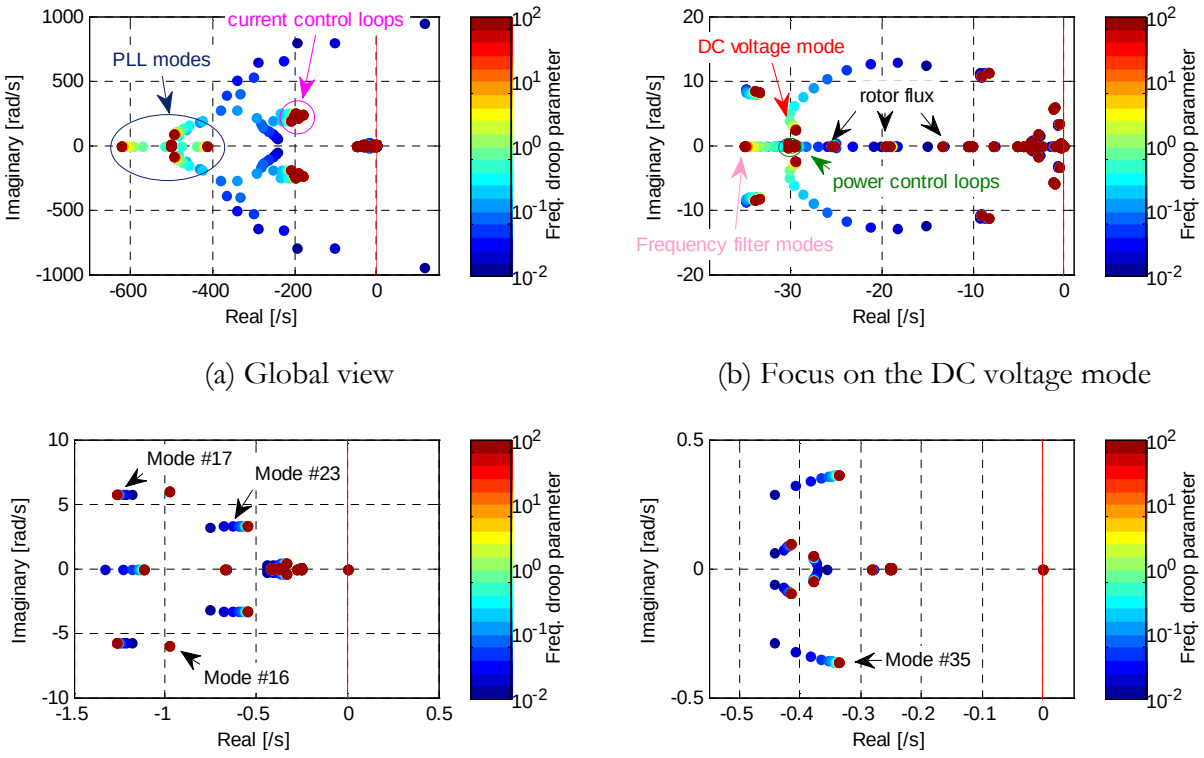

(a) Global view

(b) Focus on the DC voltage mode

(c) Focus on electromechanical modes

(d) Focus on the common mode

Figure H-13 : Sensitivity towards the frequency droop parameter when wind farm are participating to the DC voltage control

In Figure H-13, the same parametric test as in H.1 is performed. Results are similar than those obtained in H.1, except the common mode which is better damped when increasing the frequency support. This seems logical since the wind farm contributes to the frequency control by the way of the voltage control.

I. NEWTON RAPHSON METHOD

Classically, load flow solutions are solved using Newton-Raphson (NR) algorithm. It is an iterative method used to solve nonlinear problems. This method finds successively better approximation of the roots of a function. This method is based on the Taylor's theorem, the system is linearized around an operating point at each iteration. The derivative is used to bring closer to the roots value. For instance, given a function f over the variable x and its derivative f'. Starting from an initial point x_0 the better approximation x_1 which satisfies $f(x_1) = b$ is:

$$b - f(x_0) = f'(x_0)(x_1 - x_0) \tag{I.43}$$

Rewriting (I.43) to find the correction Δx in function to the result mismatch Δf:

$$\Delta x^{(1)} = \frac{\Delta f^{(0)}}{f'^{(0)}} \tag{I.44}$$

The upper script in parenthesis means the iteration number. Normally, more the number of iterations is high more the variable is close to the root value. The algorithm stops when the results mismatch is under a given tolerance value. The NR method is illustrated in Figure I-14.

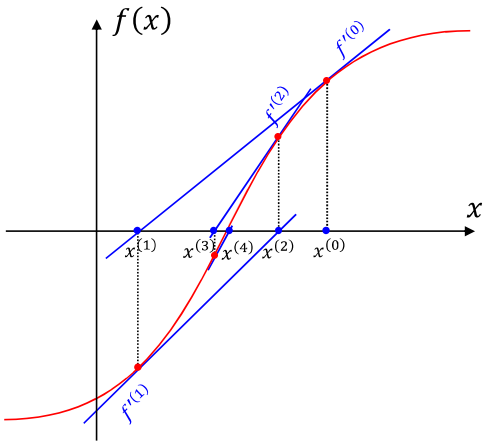

Figure I-14 : Illustration of the NR method

J. REDUCED ADMITTANCE MATRIX

J.1. Motivation

To simulate the DC grid by resistive elements, the following equation has to be solved:

$$\boldsymbol{I = YV} \tag{J.45}$$

Where:

$\boldsymbol{Y}$ is the reduced admittance matrix
$\boldsymbol{I}$ is the node injection current vector
$\boldsymbol{V}$ is the node voltage vector

To be able to solve this equation, all node voltages should be known, however, in simulation only converter station capacitor voltages are known and the voltage of passive nodes are not known. In this appendix, a new admittance matrix which considers only active nodes is developed.

J.2. Theory

As said in Chapter 5 part 5.3.2 passive nodes are considered as injected currents nodes set at zero amps. When the DC grid is simulated, passive nodes are not interesting and so they could be suppressed of the admittance matrix. From the DC steady-state calculation presented in Chapter 5 part 5.3.2 and considering that all nodes which are current nodes are set to zero amps, (5.9) can be simplified as follows:

$$\begin{bmatrix} I_1 \\ \vdots \\ I_l \\ V_{l+1} \\ \vdots \\ V_n \end{bmatrix} = \left[\begin{array}{c|c} \boldsymbol{Y_{red}} & \boldsymbol{X_{12}} \\ \hline \boldsymbol{X_{21}} & \boldsymbol{X_{22}} \end{array}\right] \begin{bmatrix} V_1 \\ \vdots \\ V_l \\ 0 \\ \vdots \\ 0 \end{bmatrix} \tag{J.46}$$

Where

$\boldsymbol{Y_{red}}$ is the reduced admittance matrix
$\boldsymbol{X_{21}}$ is the matrix useful to retrieve voltages of passive nodes
$\boldsymbol{X_{12}}$ & $\boldsymbol{X_{22}}$ are useless matrices

J.3. Numerical application

The same scenario than the one used in Chapter 5 part 5.3.2 is considered to validate the reduced admittance matrix. Results are displayed in Table J-8; node voltages are the inputs and injected currents are the outputs. Results are identical to those obtained in Chapter 5 part 5.3.2.

Table J-8 : Steady-state results with reduce impedance matrix (node)

Node	Voltage [kV]	Injected Current [A]	Injected Power [MW]
1'	640	-723.5	-463
2'	640.2	-1200	-768.3
3'	640.5	950	608.5
4'	640.5	600	384.3
5'	641.2	380	243.7

Modélisation Dynamique et Commande des Réseaux à Courant Continu Multi-Terminaux Haute Tension

Résumé :
Cette thèse porte sur le contrôle et la stabilité de réseaux à Courant Continu (CC) Multi-Terminaux de Haute Tension pour le raccordement des parcs éoliens en mer à plusieurs points d'injection terrestres. Ce travail aborde à la fois les méthodes de contrôle d'équilibrage des puissances entrantes et sortantes du réseau CC et les méthodes de réglage coordonné pour diriger les flux d'énergie en accord avec les Gestionnaires du Réseau de Transport (GRT).
L'étude bibliographique sur les méthodes de contrôle des réseaux CC a permis de choisir la méthode de statisme de tension. Une analyse approfondie a mise en évidence l'influence de la pente du statisme et les éléments de stockage sur la dynamique du réseau CC, cela a conduit à une méthodologie pour dimensionner le statisme. L'analyse modale a été utilisée pour évaluer la stabilité du réseau CC et pour déterminer les origines des interactions entre réseaux à courant alternatif et CC.
Parce que le contrôle primaire agit à un niveau local, un contrôleur maître est proposé pour diriger les flux d'énergie dans le réseau CC. En considérant un état statique, ce contrôleur calcule les références à envoyer aux stations de conversion afin de restaurer le système à sa valeur nominale et de satisfaire les demandes du GRT.
Enfin, les méthodes développées théoriquement ont été évaluées sur une maquette hybride où les réseaux alternatifs sont simulés en temps réel et des câbles CC et convertisseurs sont représentés physiquement. Les éléments de cette maquette sont dimensionnés homothétiquement par rapport à un système de taille réelle. Cette maquette est contrôlée par un système de supervision dans lequel le réglage coordonné est implémenté.

Mots clés :
Réseau Multi Terminaux à Courant Continu, Réseau Haute Tension à Courant Continu, Simulation hybride, Convertisseur source de tension, Interactions entre réseaux alternatifs et continus, System de supervision et d'acquisition de donnés, Maquette de réseau DC, Contrôle, Modélisation, Analyse Modale

Dynamic Modeling and Control of Multi-Terminal HVDC Grids

Abstract:
This thesis deals with control and stability of Multi terminal HVDC (MTDC) grid used to connect wind farms to several onshore injection points. This work discusses both the primary control methods to provide DC grid power balance and coordinated control methods to dispatch power as scheduled by TSOs.
The literature review on primary control methods allows choosing the droop voltage method as the best candidate to control the DC grid. An in-depth analysis highlights the influence of the droop parameter and the DC storage elements on the DC grid dynamics and this leads to a methodology to size the droop parameter. Next the stability of DC grid alone is assessed by small signal stability analyses. Also, interaction origins between AC and DC systems are traced using modal analysis.
Since, primary control act as converter level using local measurements, a master controller is proposed to manage the DC grid power flows. Based on steady study state considerations, this controller computes references to send to converter stations in order to restore the system at nominal value and to satisfy TSOs wishes: interconnections schedule power transits and wind power sharing.
Finally, methods theoretically developed are assessed on a multi terminal mock-up. This is an hardware-in-the-loop mock-up where AC systems are simulated in real time and cables and some converters are real at low scale. The low scale mock-up is homothetic to a full scale system: electrical elements are the same in per unit, DC storage is also homothetic and converter's controllers are tuned to achieve identical time responses. The mock-up is monitored by a SCADA system in which the coordinated control is implemented.

Key words:
Multi Terminal DC (MTDC), High Voltage Direct Current (HVDC), Hardware-In-the-Loop (HIL) Simulation, Voltage Source Converter (VSC), Interactions AC-DC, SCADA, DC grid mock-up, Control, Modeling, Modal Analysis